Curriculum Vitae of Ralf Cuntze *comprising his* Scientific Findings

Prof. Dr.-Ing. habil. Ralf Cuntze VDI, Ralf_Cuntze@t-online.de

Retired from industry, MAN-Technologie, Augsburg, and from Composites United

Engineer and hobby scientist:

application-oriented with a touch for material modelling and with the hope to be some bridge-builder between mechanical and civil engineering (construction).

Hobbies: exploring the world, nature photography, gardening, mountaineering, cyclamen breeding, etc.

This was my LIFE.

1939 born Sept 8 in Erfurt. Survived bombing at Erfurt and a machine gun fire at the war's end

1964: Dipl.-Ing. Civil Engineering CE (construction, ***TU Hannover***). 1968: Dr.-Ing. in Structural Dynamics (CE). 1978: Dr.-Ing. habil. Venia Legendi in Mechanics of Lightweight Structures (TU-M)

1980-1983: Lecturer at Universität der Bundeswehr München: on 'Fracture Mechanics' in the construction faculty and 1990-2002 on 'Composite Lightweight Design' in aerospace faculty

1987: Full professorship 'Lightweight Construction', *not started in favor of industry*

1998: Honorary professorship at Universität der Bundeswehr München

1968-1970: FEA-programming (***DFVLR*** at the airport Essen/Mühlheim)

1970-2004: MAN-Technologie (München , Augsburg). Headed the Main Department 'Struct. and Thermal Analysis'. 50 years of life with Fibers CarbonF, AramidF, GlassF, BorF, Bs(basalt)F.

*Theoretical fields of work: structural dynamics, finite element analysis, rotor dynamics, structural reliability, partial/deterministic safety concepts, material modeling and model validation, fatigue, fracture mechanics, design development 'philosophy' & design verification

*Mechanical Engineering applications at ***MAN***: ARIANE 1-5 launcher family (design of different parts of the launcher stages, inclusively Booster) Cryogenic Tanks, High Pressure Vessels, Heat Exchanger in Solar Towers (GAST Almeria) and Solar Field, Wind Energy Rotors (GROWIAN Ø103 m, WKA 60, AEROMAN. Probably the first world-wide wind energy conferences organized in 1979, 1980 with Dr.Windheim), Space Antennas, Automated Transfer Vehicle (Jules Verne, supplying the space station ISS), Crew Rescue Vehicle (CMC application) for ISS, Carbon and Steel Gas-Ultra-Centrifuges for Uranium enrichment. Filament Winding theory. Material Databank etc.

*Civil Engineering applications: Supermarket statics, armoring plans, pile foundation, 5th German climbing garden (1980 designed, concreted and natural stone-bricked)

1971-2010: Co-author of ***ESA/ESTEC***-Structural Materials Handbook, Co-author and first convener of the ESA-Buckling Handbook and co-author in Working Groups WGs for ESA-Standards 'Structural Analysis', 'High Pressure Vessels' (metals and composites) and 'Safety Factors'

1972–2015, ***IASB***: Luftfahrt-Technisches Handbuch HSB 'Fundamentals and Methods for Aeronautical Design and Analyses'. Author and Co-author of numerous HSB sheets and about

2006-2008 co-transfer with co-translation of the HSB aerospace structural handbook into its present English version.

1980-2011: **Surveyor/Advisor** for German BMFT (MATFO, MATEC), BMBF (LuFo) and DFG

1980-2006: **VDI Guideline 2014**, co-author of Parts 1 and 2, Beuth Verlag '*Development of Fiber-reinforced Plastic Components';* Part 3 *'Analysis*', editor/convener/co-author

1986 and 1889: One week **FRP-lecture** on composite design in Pretoria, SA

2000-2013: World-Wide-Failure-Exercises **WWFE** on Uni-directional fiber-reinforced materials (UD) strength: WWFE-I (*2D stress states)* non-funded winner against institutes of the world, WWFE-II (*3D states*) top-ranked

2009-2021 linked to ***Carbon Composites e.V***. at Augsburg, later ***Composites United CU e.V.*** and to TUDALIT Dresden. Since 2011 working on the light weight material Fiber-reinforced (polymer) Carbon Concrete. **Founded and headed the working groups**: (1) 2009: 'Engineering' linked to the WG Non-Destructive Testing and the WG Connection Technologies, mechanical engineering. (2) 2010: 'Composite Fatigue'. In 2010 the author held an event that was excellently attended by international speakers. (3) 2011: 'Design Dimensioning (*Auslegung, Bemessung*) and Design Verification (*Nachweis*)' mainly for carbon concrete. This working group was the foundation stone for the later specialist network ***CU Construction***, aiming at *"Fiber-based lightweight construction*". (4) 2017: 'Automated fabrication in construction including serial production' *("3D-Print")*. (5) 2020, 2021: Forum 'Carbon concrete for practice' at 'Ulm Concrete Days'

2010: Founder of the Germany-wide Working Group BeNa to base fatigue life prediction 'embedded lamina-wise' in order to become more general in future fatigue life design

2019:***GLOSSAR.** "Fachbegriffe für Kompositbauteile - *technical terms for composite parts*". Springer2019. Edited at suggestion of carbon concrete colleagues to improve mutual understanding

2022: **Life-Work Cuntze - a compilation from the author's papers, presentations, published and non-published design sheets and project works in industry* (850 Pages, more design work-related)

2023: **Design of Composites using Failure-Mode-Concept-based tools - from Failure Model Validation to Design Verification*. Mechanics of Composite Materials, Vol. 59, No. 2, May, 2023, pp. 263-282. **Minimum Test Effort-based Derivation of Constant-Fatigue-Life curves, displayed for the brittle UD composite materials*. Mechanics of Composite Materials, Springer, Advanced Structured Materials, Vol.199, 107–146, draft. *Cuntze R and Kappel E: *Benefits, applying Tsai's Ideas 'Trace', 'Double-Double' and 'Omni Failure Envelope' to Multiply UD-ply composed Laminates?* * *UD-Strength Failure criteria: Which one should I take*? 19 p.

Preprints, drafts are fully open for the public and downloadable from
** https://www.carbon-connected.de/Group/Prof.Ralf.Cuntze or from Research Gate*

1) *The presented novel scientific ideas invite for discussion.*
2) *The author's research works were never funded.*
3) *The author asks for forgiveness in advance for inaccuracies, as he cannot get anyone to proofread.*

Of course, the text content in the scientific chapters would have deserved a revision and harmonization, but the author is already 85.

Chapters

1 Creation of the ‘Failure Mode Concept’ (FMC, about 1996) 6

2 *Interaction of Stresses* by the application of Strength Failure Criteria 9

3 Material Symmetry and ‘Generic’ Number 10

4 Direct use of a Friction Value μ in the SFCs of Isotropic and UD materials 11

5 Material stressing effort Eff (Werkstoffanstrengung) 13

6 So-called ‘Global’ SFCs and (failure mode-linked) ‘Modal’ SFCs 14

7 Collection of Derived SFCs, Interaction of Failure Modes and a Multi-fold Mode 16

8 Validity Limits of UD SFC Application → Finite Fracture Mechanics (FFM) 21

9 ‘Curiosities’ regarding Classical Material Mechanics 23

10 Automated Generation of Constant Fatigue Life curves considering Mean Stress Effect 26

11 Evidencing 120°-symmetrical Failure Bodies of Brittle and Ductile Isotropic Materials 33

12 Completion of the Strength Mechanics Building 39

13 Safety Concept in Structural Engineering Disciplines 40

14 Nonlinear Stress-Strain relationships, Beltrami Theory with Change of Poisson’s Ratio ν 47

15 A measurable parameters’-based ‘Extended-Mises’ Model instead of a ‘Gurson’ Model? 58

16 Note on Continuum (micro-)Damage Mechanics (CDM) 72

17 Multi-scale Structural modelling with Material Modelling and some Analysis 80

18 Some Lessons Learned from Testing and from Evaluation of Test Results 86

19 2D-Laminate Design: Direct Determination of Tsai’s ‘Omni principal FPF strain failure envelopes 90

20 Note on Criticality of Fiber Micro-Fragments and Dusts of CFR-Plastic/CFR-Concrete 95

21 A novel Determination of the Residual Strength *R*res, non-cracked, Fatigue Phase 2 101

22 Full Mohr Envelope $\tau_{nt}(\sigma_n)$, Derivation of $\Theta_{fp}(\sigma_n)$ and of Cohesive shear Strength 106

23 Replacing fictitious Model Parameters $a_{\perp\perp}, a_{\perp||}$ by measurable Friction Values μ 113

24 Fracture Bodies of Normal Concrete, UHPC and Foam 117

25 Accurate Mohr-Coulomb Curve and Cohesive shear Strength R^{τ} of Brittle Isotropic materials 128

26 Mapping 2D and 3D Test Results of Concrete and Rocks applying Confining Stresses 133

27 UD-Strength Failure criteria: Which one should I take? 147

28 Technical Terms, Laminate Description, Material Stressing Effort *Eff* 156

29 Miscelleaneous 163

30 Glossary book, Contributions to Handbooks, Guidelines etc. 167

31 References since 2000 and Acknowledgement 179

32 Affiliations .... **Fehler! Textmarke nicht definiert.**

33 Documenting Hobbies: Globetrotter, Hiking, Photography, sparrows & alpine-cyclamen ‘breeding’ .... **Fehler! Textmarke nicht definiert.**

34 Resume .... **Fehler! Textmarke nicht definiert.**

This document comprises results of the author’s **never funded, non-supported research work** performed in the vacant time at industry and as retired person. He assumes no liability for damages resulting from application.

Findings of the author during his long-lasting Research Activities

Novel simulation-driven product development shifts the role of physical testing to virtual testing, to simulation, respectively. This requires High Fidelity and therefore the use of reliable material models. *Simulation means: Imitation of the operation of a real-world process and model adaption due to test information by performing many analyses.*

Basic desire of the macro-scopically working structural engineer is a material model linked to an ideally homogeneous material which might be isotropic or anisotropic. Connecting desire is: Be provided with a clear Strength Mechanics Building in order to get a cost-saving basis due to only analyze and test what is really physically necessary.

For the 3D-Demonstration of Strength are required - *nowadays practically a must regarding the usual 3D FEA stress output* – validated 3D Strength Failure Criteria (SFC) rendered by 3D failure bodies to firstly perform Design Dimensioning and to finally achieve Design Verification. All this is targeted in the following elaboration. Pre-information on the basic focus here, UD material:

*The following figure displays some of the different strengthening fibers applied in construction, and a comparison of a standard Carbon Fiber with a human hair.

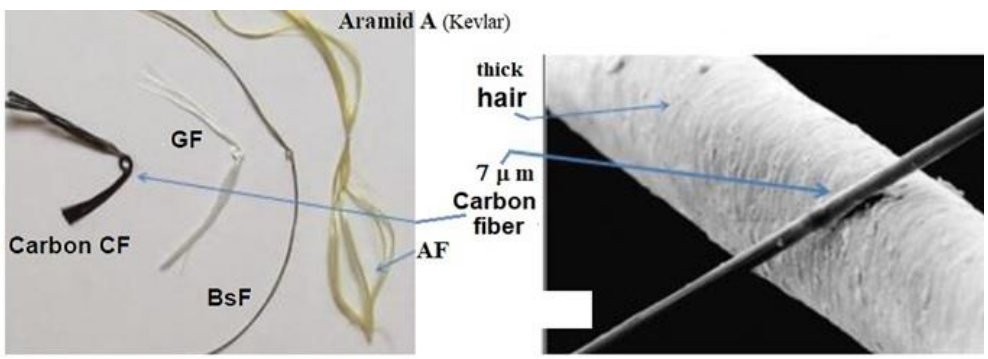

Glass GF (AR glass= alcali-resistant in concrete) **Basalt BsF** (alcali-resistant in concrete by ZrO_2)

*And the next figure shall provide for the applied stringent failure mode thinking the observed 5 failure modes faced with Uni-directional fiber-reinforced materials.

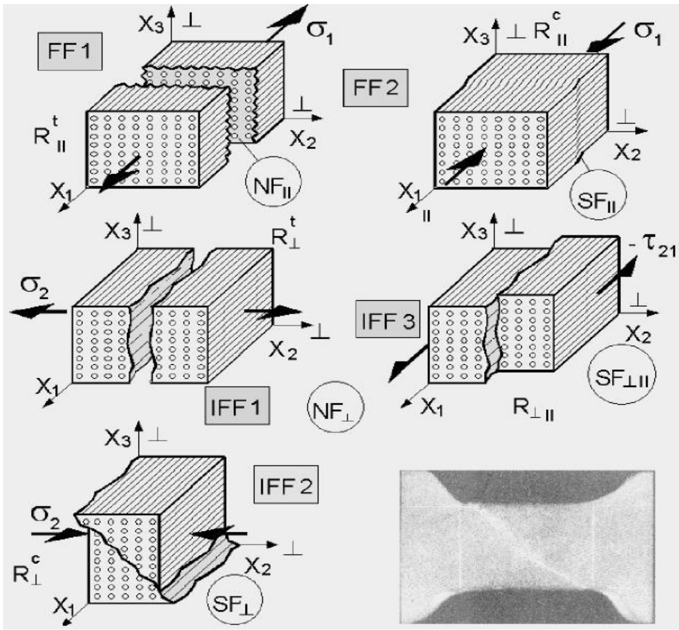

In the above context:
Two basic features are faced by the structure-designing engineers, three types of surfaces

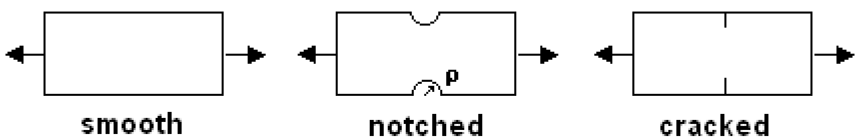

and the behavior of the material, whether it is brittle (about $R^c > \approx 3 \cdot R^t$) or ductile.

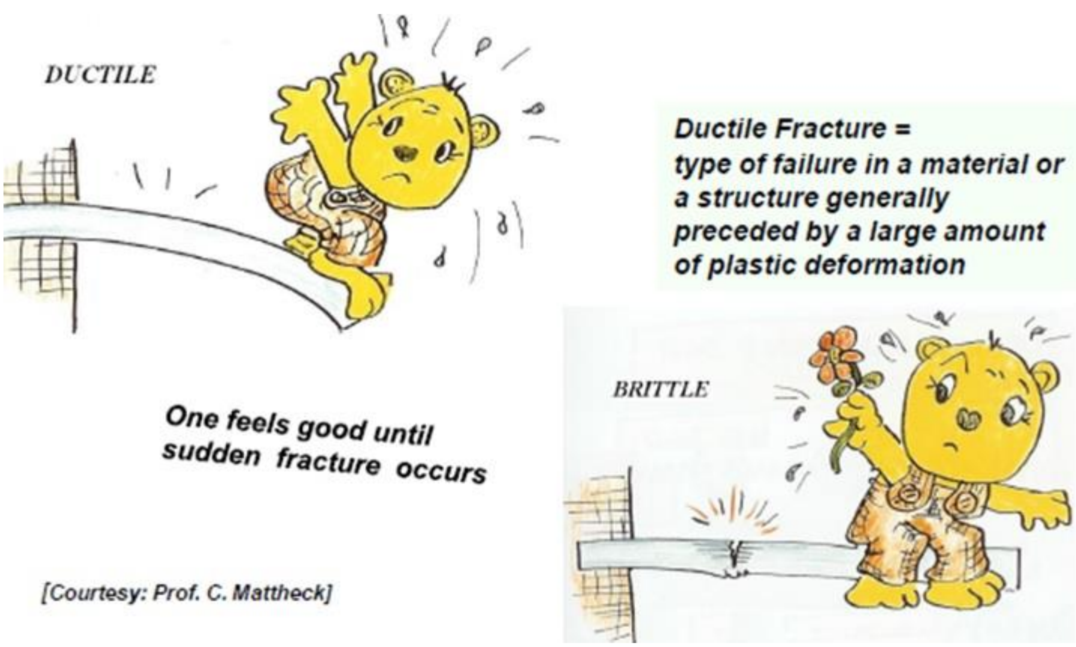

Basic focus here: Smooth type structural parts.

1 Creation of the ‘Failure Mode Concept’ (FMC, about 1996)

***Aim**: Creation of a Static & Cyclic Strength Mechanics Building as basis for all material and of practical, physically-based SFCs.*

Being since 1970 in the industrial composite business the author tried to firstly sort out in regular discussions with Alfred Puck applicable SFCs for UD materials. Puck developed in 1990 his Hashin-based Action-plane Inter-Failure-Failure SFC which was included in 2006 into the VDI 2014 guideline, sheet 3 (editor Cuntze).
Working with practically all material types the author was encouraged to find a Concept for all the material families isotropic, UD and further orthotropic ones including dense with porous materials.

The finally developed so-called Failure-Mode-Concept (FMC) incorporates a rigorous thinking in failure modes and can be briefly described by the FMC features, derived about 1995, which were the basis for the development of Cuntze’s macro-mechanical SFCs:

- Each failure mode represents 1 independent failure mechanism and thereby represents 1 piece of the complete failure surface.
- A failure mechanism at the lower micro-scopic mode level shall be considered in the applied desired macro-scopic SFC
- Each failure mechanism or mode is governed by 1 basic strength *R*, only (witnessed!)
- Each failure mode can be represented by 1 SFC.

This further includes:

* Failure mode-wise mapping,
* Stress invariant’s-based formulation,
* Equivalent stress generation,
* Each neat failure mode is governed by just one strength R^{mode}, witnessed for ductile and brittle materials, and
* All SFC model parameters are measurable entities! Each SFC represents a failure surface, therefore for the originator the FMC will be the foundation upon which he physically based SFCs generated.

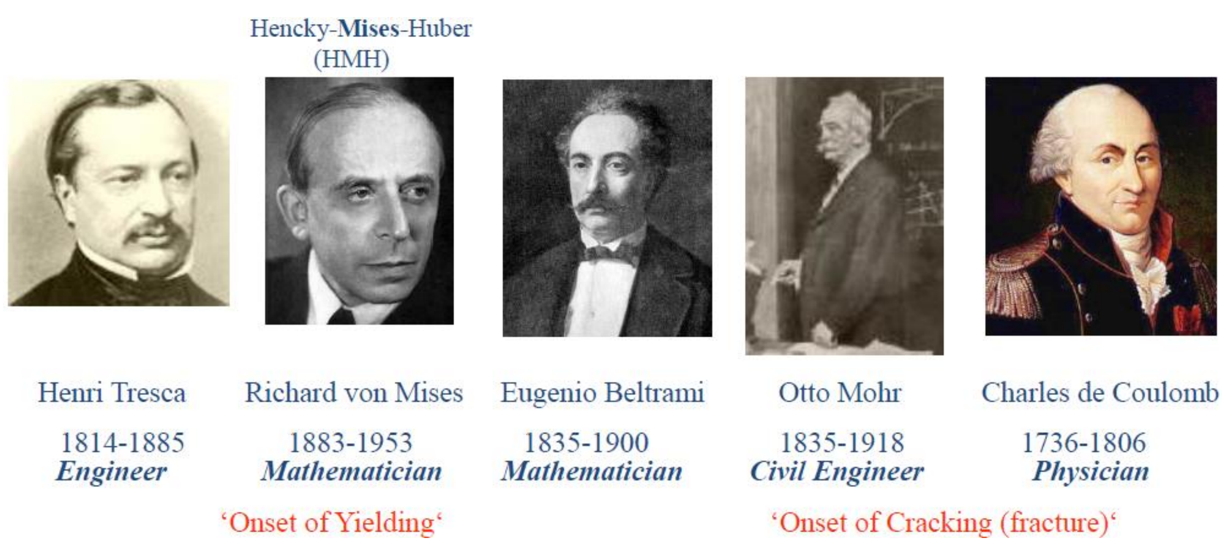

Fig.1-1: Some pioneers which set up strength failure hypotheses (ductile, brittle)

In the case of brittle materials the failure surface is the surface of a fracture failure body. Such a surface is determined by the peaks or ends of all failure stress vectors. The surface is mathematically defined by a Failure function *F,* which becomes 1 at 'Onset-of-Failure'. $F = 1$ is the formulation of the SFC (*mathematically, we write a condition*). *Fig.1-1* above presents the pioneers in the isotropic SFC field.

The author's idea was to create physically-based SFCs and to note his Lessons Learned *LL* during the elaboration. The FMC was originally derived for UD materials because there was the big demand at that time. The employed stress invariants shall be presented via isotropic knowledge:

Beltrami, Schleicher et al. assumed at initiation of yield that the strain energy (denoted by *W*) in a solid cubic element of a material will consist of two portions:

$$W = \int \{\sigma\}\{\varepsilon\}\, d\{\varepsilon\} = W_{Vol} + W_{shape} \quad \text{with} \quad \{\sigma\} = (\sigma_1, \sigma_2, \sigma_3, \tau_{23}, \tau_{13}, \tau_{12})^T .$$

Including Hooke's law in the case of a ***transversely-isotropic*** (UD solid) the expression will take the form, using s_{ik} := compliance coefficients, E:=elasticity modulus, ν:=Poisson's ratio,

$$W = [s_{11}\cdot\sigma_1^2 + s_{22}\cdot\sigma_2^2 + s_{33}\cdot\sigma_3^2 + s_{44}\cdot\tau_{23}^2 + s_{55}\cdot(\tau_{12}^2 + \tau_{13}^2)] / 2 + s_{12}\cdot(\sigma_1\,\sigma_2 + \sigma_1\,\sigma_3) +$$

$$s_{23}\cdot\sigma_2\,\sigma_3 = \underbrace{\frac{I_1^2}{2\cdot E_{\|}}}_{\text{volume}} + \underbrace{\frac{I_2^2\cdot(1-\nu_{\perp\perp})}{4\cdot E_{\perp}}}_{\text{volume}} - \underbrace{\frac{\nu_{\perp\|}\cdot I_1\cdot I_2}{E_{\|}}}_{\text{volume}} + \underbrace{\frac{I_3}{2\cdot G_{\|\perp}}}_{\text{shape}} + \underbrace{\frac{I_4\cdot(1+\nu_{\perp\perp})}{4\cdot E_{\perp}}}_{\text{shape}} .$$

with the invariants $I_1 = \sigma_1,\; I_2 = \sigma_2 + \sigma_3\;;\; I_3 = \tau_{31}^2 + \tau_{21}^2\;;\; I_4 = (\sigma_2 - \sigma_3)^2 + 4\tau_{23}^2\;;$

$$I_5 = (\sigma_2 - \sigma_3)\,(\tau_{31}^2 - \tau_{21}^2) - 4\tau_{23}\,\tau_{31}\,\tau_{21}.$$

In the ***isotropic*** case analogously follows, however simpler,

$$W = \left[\underbrace{\frac{1-2\nu}{3} I_1^{iso\,2}}_{\text{volume}} + \underbrace{\frac{2+2\nu}{3} 3J_2^{iso}}_{\text{shape}}\right] / 2E$$

with $I_1^{iso} = \underline{f(\sigma)} = \sigma_I + \sigma_{II} + \sigma_{III}\,,\;\; 6\cdot J_2^{iso} = \underline{f(\tau)} = (\sigma_I - \sigma_{II})^2 + (\sigma_{II} - \sigma_{III})^2 + (\sigma_{III} - \sigma_I)^2,$

It is known, both portions in the bracket above are used to formulate a failure function

$$F = \underbrace{c_1\cdot\frac{(1-2\nu)\cdot I_1^{iso\,2}}{3\bar{R}^2}}_{\text{volume}} + \underbrace{c_2\cdot\frac{(2+2\nu)\cdot 3J_2^{iso}}{3\bar{R}^2}}_{\text{shape}} .$$

Fig. 1-2 below displays for the 2 material families above the physically-based choice of invariants:

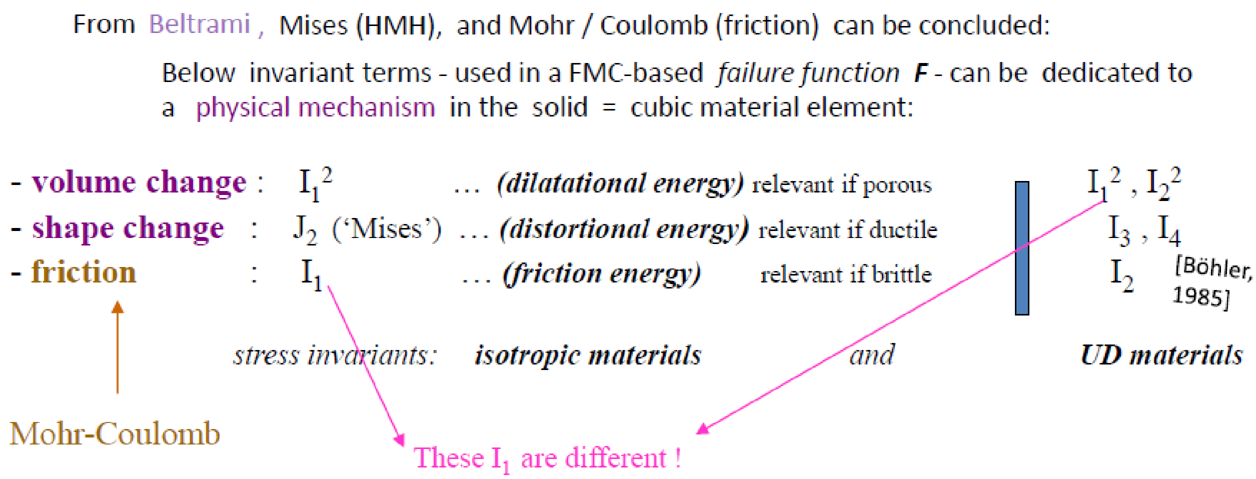

Fig.1-2: Reasons for choosing invariants when creating FMC-based SFCs

Exemplarily, the isotropic SFC model, spanning up the fracture body in the compression domain, shall be used for demonstration. The complete SFC reads:

$$\text{Shear Fracture SF,}\quad I_1 < 0: \quad F^{SF} = F^{\tau} = c_1 \cdot \frac{6 \cdot J_2}{2 \cdot \bar{R}^{c2}} \cdot \Theta_{\tau} + c_2 \cdot \frac{I_1}{\bar{R}^c} + c_3 \cdot \left(\frac{I_1}{\bar{R}^c}\right)^2 .$$

Herein, the first part of the SFC represents the shape change, the second the friction effect, the third the volume change and the non-circularity parameter Θ_{τ} describing the inherent, nevertheless often not known 120°-symmetry of the failure bodies of isotropic brittle and ductile material, too (see a later chapter).

Above invariants can be formulated in 3D structural component stresses, in principal stresses and in Mohr stresses, which will become essential when deriving a stress state-caused fracture angle and the so-called cohesive strength..

Note, please: Strength notations

R means strength (resistance) in general and further Strength Design Allowable used for Design Verification. $\bar{R}$ means average strength used for modelling, mapping of the course of test data.

LL: *Similarly behaving materials possess the same shape of a fracture body using the same SFC!*

2 *Interaction of Stresses* by the application of Strength Failure Criteria

***Aim**: Provision of a failure mode-based stress-interaction ('Modal') and not a mathematical global one.*

The derivation of the FMC-based SFCs builds up on the hypotheses of Beltrami, Hencky-Mises-Huber (HMH) and Mohr-Coulomb. Therefore the depicted SFC approaches consider, that the solid material element may experience, generated from different energy portions, a shape change (HMH), a volume change and friction. FMC-based SFCs will be given for a large variety of isotropic brittle structural materials such as porous Concrete Stone, Normal Concrete, UHPC sandstone, monolithic ceramics and for the transversely-isotropic fiber-reinforced polymers Lamina (ply, lamella) and finally orthotropic fabrics inclusively fabric ceramics, see [*CUN22, Cun23a,24b*].

Since two decades the author believes in a macroscopically-phenomenological 'complete classification' system, where all strength failure types are included, see the figure below. In his assumed system several relationships may be recognized: (1) Shear stress yielding SY, followed by Shear fracture SF considering 'dense' materials. For porous materials under compression, the SF for dense materials is replaced by Crushing Fracture CrF. (2) In order to complete a mechanical system beside SY also NY should exist. This could be demonstrated by PMMA (plexiglass) with its chain-based texture showing NY due to crazing failure under tension and SY in the compression domain, [see *subsection 9.1 or CUN22,§4.1*]. The right side of the scheme outlines that a full similarity of the 'simpler' isotropic materials with the transversely-isotropic UD materials exists.

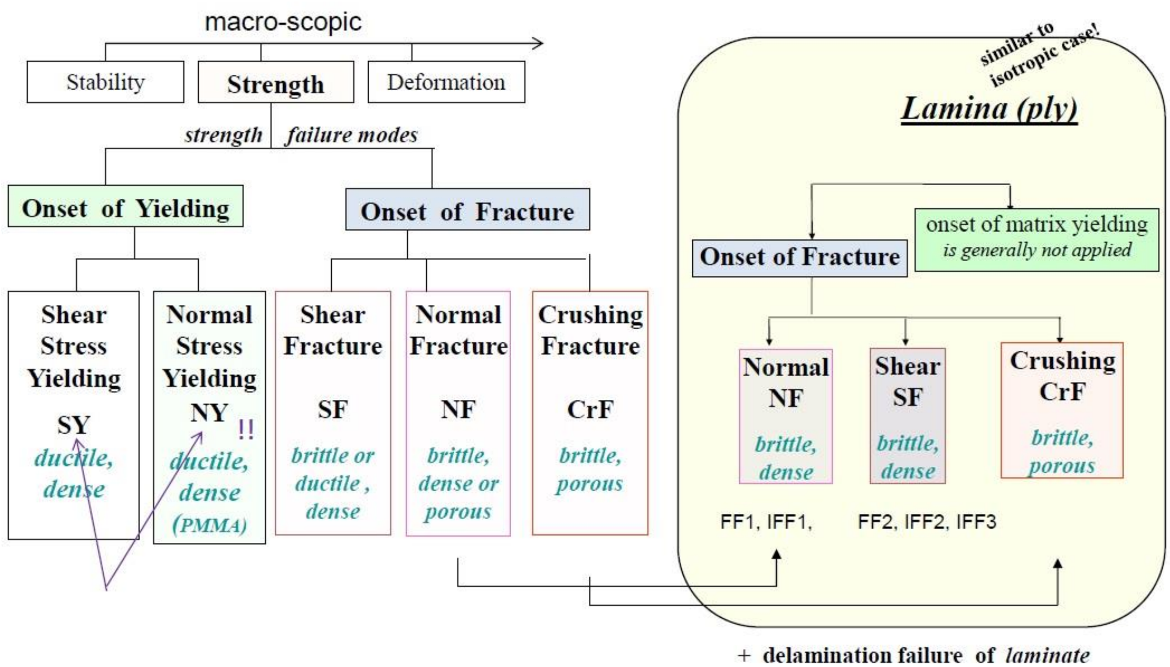

Fig.2-1.: Scheme of macro-scopic strength failure types and modes of isotropic materials and transversely-isotropic UD-materials (Cuntze1998)

LL:

** Failure behavior of Fiber-Reinforced materials is similar to isotropic ones*

** Principally, instead of stress-based SFC, strain-based SFC might be applied if the full stress-strain history is accurately considered. However, just limit strain conditions are used in pre-dimensioning (§22), because the certification process is stress-based.*

3 Material Symmetry and ‘Generic’ Number *(material inherent?)*

***Aim**: Consideration of the available material knowledge.*

During the derivation of the FMC a closer look at material symmetry facts was taken whereby the question arose: “Does a material symmetry–linked Generic Number exist with a number 2 for isotropic and 5 for UD materials?

Under the design-simplifying presumption “Homogeneity is a permitted assessment for the material concerned” and regarding the respective material tensors, it follows from material symmetry that the number of strengths equals the number of elasticity properties!
Fracture morphology gives further evidence: Each strength property corresponds to a distinct strength failure mode and to a distinct strength failure type, to Normal Fracture (NF) or to Shear Fracture (SF). This seems to mean, that a characteristic number of quantities is fixed: 2 for isotropic material and 5 for the transversely-isotropic UD lamina (≡ lamellas in civil engineering). Hence, the applicability of material sym*metry involves that in general just a minimum number of properties needs to be measured* (benefits:& test cost + time) which is helpful when setting up strength test programs. ⇒ Witnessed material symmetry knowledge seems to tell: “There might exist a ‘generic’ (*term was chosen by the author*) material inherent number for”:

Isotropic Material: of **2**
- 2 e*lastic ‘constants’, 2 strengths, 2 strength failure modes fracture* (NF with SF) and 2 fracture mechanics modes (defined as modes, where crack planes do not turn)
- *1 physical parameter (such as the coefficient of thermal expansion CTE, the coefficient of moisture expansion CME, and the friction value μ, etc.)*

Transversely-Isotropic Material: of **5** for the these basically brittle materials
- 5 e*lastic ‘constants’, 5 strengths, 5 strength failure modes fracture* (NFs with SFs)
- *2 physical parameters (CTE, CME, $\mu_{\perp\perp}$, $\mu_{\perp\|}$ etc.).*

Orthotropic Material: of **9** (6).

This looks to be proven by the investigation of Normal Yielding NY of plexiglass and (*theoretically*) by a compressive fracture toughness K_{IIcr}^{c} for a brittle material with an ideally homogeneous state at the crack tip [see *section 9 or CUN22§4*].

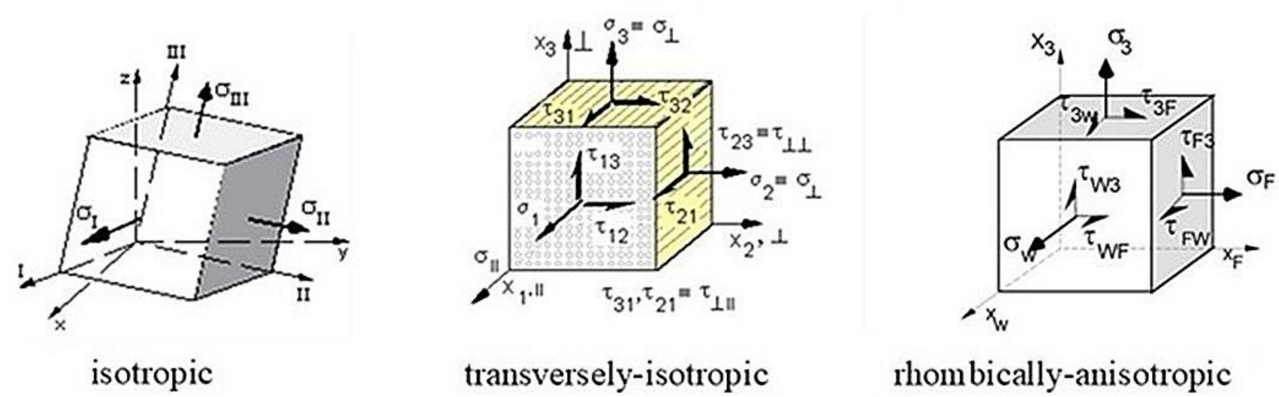

$\{\sigma\} = (\sigma_x, \sigma_y, \sigma_z, \tau_{yz}, \tau_{xz}, \tau_{xy})^T$ $\{\sigma\} = (\sigma_1, \sigma_2, \sigma_3, \tau_{23}, \tau_{13}, \tau_{21})^T$ $\{\sigma\} = (\sigma_W, \sigma_F, \sigma_3, \tau_{3F}, \tau_{3W}, \tau_{FW})^T$

Fig.3-1: Presentation of the stresses faced with the envisaged three material families

***LL:** A ‘generic’ number seems to be inherent for the different material families, as the author found.*

4 Direct use of a Friction Value μ in the SFCs of Isotropic and UD materials

Aim: *Direct use of the measurable μ instead of applying a μ-hiding friction model parameter*.

Mohr-Coulomb acts. Therefore, in the case of compressed brittle materials the effect of friction is to capture, which usually is performed by 'fictitious' friction-linked model parameters. Such a model parameter for friction, here the a or the b in the SFC, can be replaced by the measured μ.
In order to achieve this, the very challenging task to transform an SFC in structural stresses into a SFC in Mohr stresses had to be successfully to be performed [*Cun23c, Annex2*]. Ultimately, an engineer prefers the application of a measurable and physically understandable value μ, especially, because it does not scatter that much, and this is essential in design.
For isotropic materials this direct use is depicted in *Table 4-1*.

Table 4-1, Isotropic materials: Simple 2D formulation

Assumption: Fracture failure body is rotationally symmetric like Mises yield body.

$$I_1 = (\sigma_I + \sigma_{II} + 0) = f(\sigma), \quad 6J_2 = (\sigma_I - \sigma_{II})^2 + (\sigma_{II} - 0)^2 + (0 - \sigma_I)^2 = f(\tau)$$

* Normal Fracture NF, $I_1 > 0$ ↔ * Shear Fracture SF, $I_1 < 0$

Strength Failure Criterion (SFC), mode interaction exponent $m = 2.7$, $\mu = 0.2$

$$Eff^{NF} = \frac{\sqrt{4J_2 - I_1^2/3} + I_1}{2 \cdot R^t} = \frac{\sigma_{eq}^{NF}}{\bar{R}^t} \leftrightarrow Eff^{SF} = \frac{c_2^{SF} \cdot I_1 + \sqrt{(c_2^{SF} \cdot I_1)^2 + 12 \cdot c_1^{SF} \cdot 3J_2}}{2 \cdot R^c} = \frac{\sigma_{eq}^{SF}}{\bar{R}^c}.$$

$$c_1^{SF} = 1 + c_2^{SF}, \; c_2^{SF} = (1 + 3 \cdot \mu)/(1 - 3 \cdot \mu) \text{ from } \mu = \cos(2 \cdot \theta_{fp}^{c} {}^\circ \cdot \pi / 180).$$

$$Eff = [(Eff^{NF})^m + (Eff^{SF})^m]^{m^{-1}} \rightarrow f_{RF} = 1/Eff.$$

For UD material, this is executed within the full SFC set in the *Table 4-21*:

Table 4-21, UD materials: 3D SFC formulations for FF1, FF2 and IFF1, IFF2, IFF3and 2D

FF1: $Eff^{\|\sigma} = \breve{\sigma}_1 / \bar{R}_{\|}^t = \sigma_{eq}^{\|\sigma} / \bar{R}_{\|}^t$ with $\breve{\sigma}_1 \cong \varepsilon_1^t \cdot E_{\|}$ (matrix neglected)

FF2: $Eff^{\|\tau} = -\breve{\sigma}_1 / \bar{R}_{\|}^c = +\sigma_{eq}^{\|\tau} / \bar{R}_{\|}^c$ with $\breve{\sigma}_1 \cong \varepsilon_1^c \cdot E_{\|}$

IFF1: $Eff^{\perp\sigma} = [(\sigma_2 + \sigma_3) + \sqrt{\sigma_2^2 - 2\sigma_2 \cdot \sigma_3 + \sigma_3^2 + 4\tau_{23}^2}\,] / 2\bar{R}_{\perp}^t = \sigma_{eq}^{\perp\sigma} / \bar{R}_{\perp}^t$

IFF2: $Eff^{\perp\tau} = [a_{\perp\perp} \cdot (\sigma_2 + \sigma_3) + b_{\perp\perp}\sqrt{\sigma_2^2 - 2\sigma_2\sigma_3 + \sigma_3^2 + 4\tau_{23}^2}\,] / \bar{R}_{\perp}^c = \sigma_{eq}^{\perp\tau} / \bar{R}_{\perp}^c$

IFF3: $Eff^{\perp\|} = \{[b_{\perp\|} \cdot I_{23-5} + (\sqrt{b_{\perp\|}^2 \cdot I_{23-5}^2 + 4 \cdot \bar{R}_{\perp\|}^2 \cdot (\tau_{31}^2 + \tau_{21}^2)^2}\,] / (2 \cdot \bar{R}_{\perp\|}^3)\}^{0.5} = \sigma_{eq}^{\perp\|} / \bar{R}_{\perp\|}$

$$\{\sigma_{eq}^{\text{mode}}\} = (\sigma_{eq}^{\|\sigma}, \sigma_{eq}^{\|\tau}, \sigma_{eq}^{\perp\sigma}, \sigma_{eq}^{\perp\tau}, \sigma_{eq}^{\|\perp})^T, \quad I_{23-5} = 2\sigma_2 \cdot \tau_{21}^2 + 2\sigma_3 \cdot \tau_{31}^2 + 4\tau_{23}\tau_{31}\tau_{21}$$

Inserting the compressive strength point $(0, -\bar{R}_{\perp}^c) \rightarrow a_{\perp\perp} \cong \mu_{\perp\perp} / (1 - \mu_{\perp\perp})$, $b_{\perp\perp} = a_{\perp\perp} + 1$

from a measured fracture angle $\rightarrow \mu_{\perp\perp} = \cos(2 \cdot \theta_{fp}^c {}^\circ \cdot \pi / 180)$, for 50° $\rightarrow \mu = 0.174$.

$b_{\perp\|} = 2 \cdot \mu_{\perp\|}$. Typical friction value ranges: $0 < \mu_{\perp\|} < 0.25$, $0 < \mu_{\perp\perp} < 0.2$.

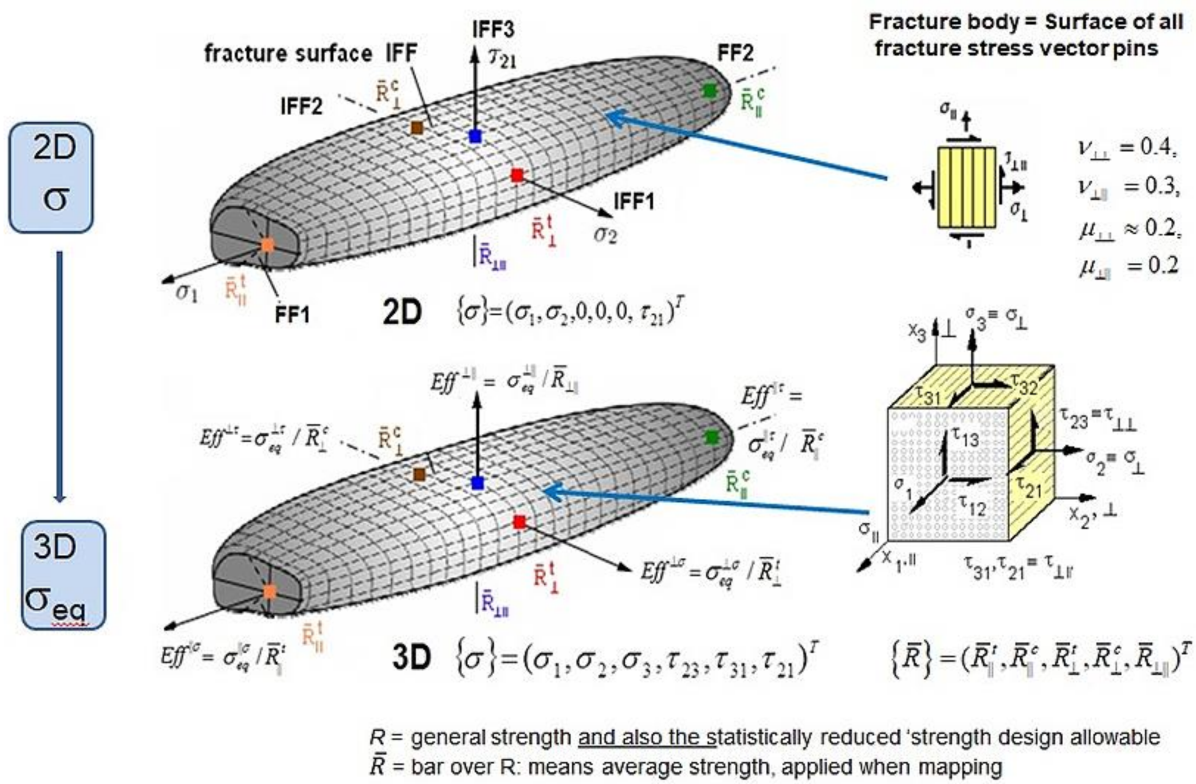

Fig.4-2: From a 2D failure body to a 3D failure body by replacing stresses by equivalent stresses

The upper figure displays the UD failure body as the visualization of the associated SFC set. The lower figure documents that if moving from the ply *stresses* to the mode-linked *equivalent ply stresses* one keeps the same UD failure body, usable now as 3D failure body!

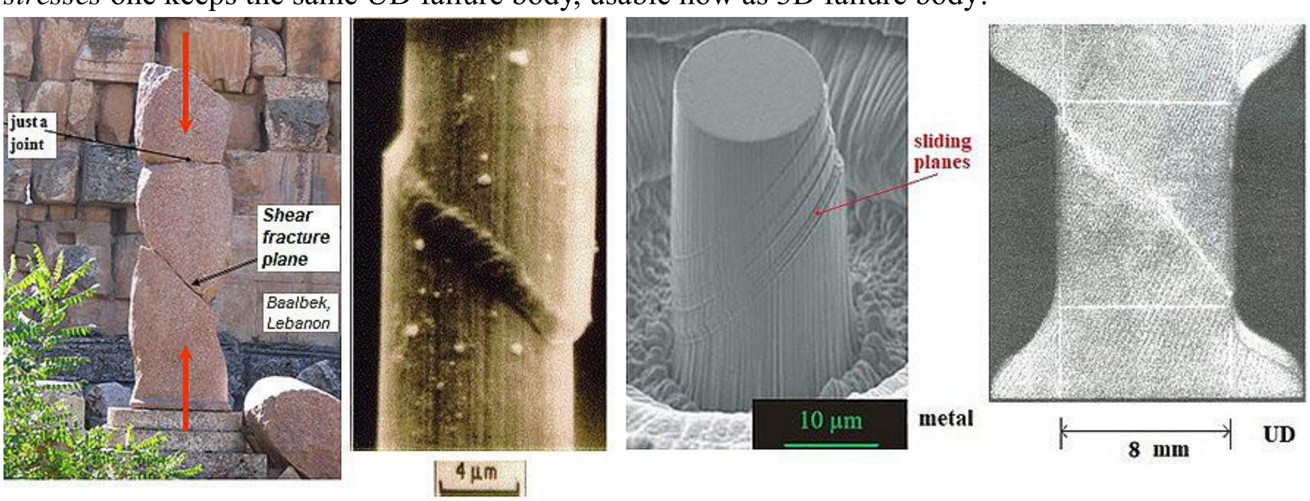

Fig.4-3,Friction driven shear fracture planes at extreme length scales.anes : Facture angles of the brittle materials Rock material, Carbon fiber [K. Schulte, TU Hamburg-Harburg], Ductile metal compression cut from a single crystal (deformed pillar after compression testing. Monnet, G. & Pouchon, M. A. (2013), Determination of the so-called critical resolved shear stress and the friction stress in austenitic stainless steels by compression of pillars extracted from single grains', Mater. Letters 98, 128-130) and laterally compressed UD-CFRP

LL:

* *Often, SFCs employ just strengths and no friction value. This is physically not accurate and the undesired consequence in Design Verification is: The Reserve Factor may be not on the safe side..*
* *In contrast to the 'doing': Friction must and can now be directly considered by the measured µ*
* *Friction occurs similarly over the scales.*

5 Material stressing effort Eff (Werkstoffanstrengung)

***Aim**: Generation of a physical basis for the interaction of failure modes and for an excellent understanding of a failure body (Eff = 100%) with multi-axial strength (capacity) values.*

If several failure modes are activated by the stress state then the application of the so-called *material stressing effort Eff* is very helpful (*in German: Werkstoffanstrengung. This artificial name had to be created in the World Wide Failure Exercise on UD-SFCs, together with the UK-organizers, because an equivalent term to the excellent German term is not known in English*).

The full *Eff* consists of all mode portions Eff^{mode}. It works analogous to 'Mises'

$$Eff^{\text{yield mode}} = \sigma_{eq}^{\text{Mises}} / R_{0.2} \rightarrow Eff^{\text{fracture mode}} = \sigma_{eq}^{\text{fracture mode}} / R \ .$$

The contribution of each single Eff^{mode} informs the designing engineer about the importance of the single portions in the SFC and thereby about the critical failure driving mode and thereby outlining the design-driving mode.

Whereas the structural engineer is more familiar with the equivalent stress the material engineer prefers above 'material stressing effort' *Eff*. The terms are linked by $\sigma_{\text{eq}}^{\text{mode}} = Eff^{\text{mode}} \cdot R^{\text{mode}}$.

The use of *Eff* supports 'Understanding the multi-axial strength capacity of materials', see *Fig.13-4*:

For instance, 3D-compression stress states have a higher bearing capacity, but the value of *Eff* nevertheless stays at 100%. Consequently, this has nothing to do with an increase of a (*uniaxial*) technical strength *R* which is a fixed result of a Standard!

The following fracture test result of a brittle concrete impressively shows how a slight hydrostatic pressure of 6 MPa increases the strength capacity in the longitudinal axis from 160 MPa up to 230 MPa - 6 MPa = 224 MPa. Thereby, the benefit of 3D-SFCs–application could be proven as the fracture stress states below depict both the Effs are 100% :

$$\sigma_{\text{fr}} = (\sigma_I\,,\ \sigma_{II}\,,\ \sigma_{III}\,)_{\text{fr}}^{\ \text{T}} = (-160,\ 0,\ 0\,)^{\text{T}}\,\text{MPa} \Leftrightarrow (-224-6,\ -6,\ -6\,)^{\text{T}}\,\text{MPa}$$

Because both the *Eff*s are 100% for $(-160,\ 0,\ 0)^T$ and for $(-224-6,\ -6,\ -6)^T$ [*CUN, §5.5*] !

This can be transferred to the quasi-isotropic plane of the transversely-isotropic UD-materials, $\sigma_2 - \sigma_3$, see [*Cun23c*], and to the orthotropic CMC fabric, when beside shear τ_{WF} the compressive stress σ_W^c acts together with σ_F^c and both activate friction on the sides [*Cun24b*].

LL:

The physically clear-based quantity Eff gives an impressive interpretation of what 100% strength capacity in 1D- 2D- and 3D stress states physically really means.

6 So-called 'Global' SFCs and (failure mode-linked) 'Modal' SFCs, Mode-interaction

Aim: *Shortly explaining the difference of 'Global' and 'Modal' SFCs.*

There are a lot of possibilities to generate SFCs. *Fig.6-1* presents a survey:

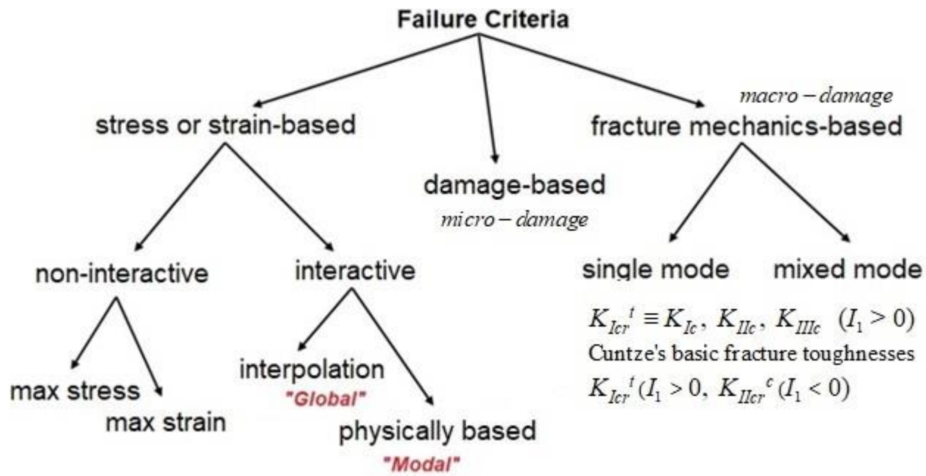

Fig.6-1: Possibilities to generate SFCs when following Klaus Rohwer [Rohwer K.: *Predicting Fiber Composite Damage and Failure*. Journal of Composite Materials, published online 26 Sept. 2014 (online version of this article can be found at: http://jcm.sagepub.com/content/early/2014/09/26/0021998314553885]

Present so-called interacting SFCs are a sub-part, which can be basically separated into two groups, 'global' and 'modal' ones. The HMH yield failure condition is a modal SFC that captures just one failure mode. The author choose the term global as a "play on words" to modal and to being self-explaining. Global SFCs describe the full failure surface by one single mathematical equation. This means that for instance a change of the UD *tensile* strength $\bar{R}_{\perp}^{t}$ affects the failure curve in the *compression* domain, where no physical impact can be. Global SFCs couple physically different failure modes whereas modal SFCs describe each single failure mode and therefore will better map the course of test data and not lead to a wrong Reserve Factor in any mode domain:

1 Global SFC $\quad F(\{\sigma\},\{R\}) = 1 \quad$ *mathematically 'married' modes*

Set of Modal SFCs $\quad F(\{\sigma\},\{R^{\text{mode}}\}) = 1 \quad$ *single mode formulations.*

In the case of modal SFCs (*such as the FMC-based ones*) also equivalent stresses can be computed, like 'isotropic Mises', $\quad \{\sigma_{\text{eq}}^{\text{mode}}\} = \left(\sigma_{eq}^{||\sigma},\ \sigma_{eq}^{||\tau},\ \sigma_{eq}^{\perp\sigma},\ \sigma_{eq}^{\perp\tau},\ \sigma_{eq}^{||\perp}\right)^{T}$.

and this is advantageous for design decisions. Within a 'global' SFC formulation all modes are mathematically married. This has a very bad impact: Each change, coming from a new test information for any pure mode, has an effect on all other independent failure modes and might include some redesign, see the full change of the ZTL-curve in *Fig.6-2*. Such a bad impact is never faced using a 'modal' formulation, like the FMC one.

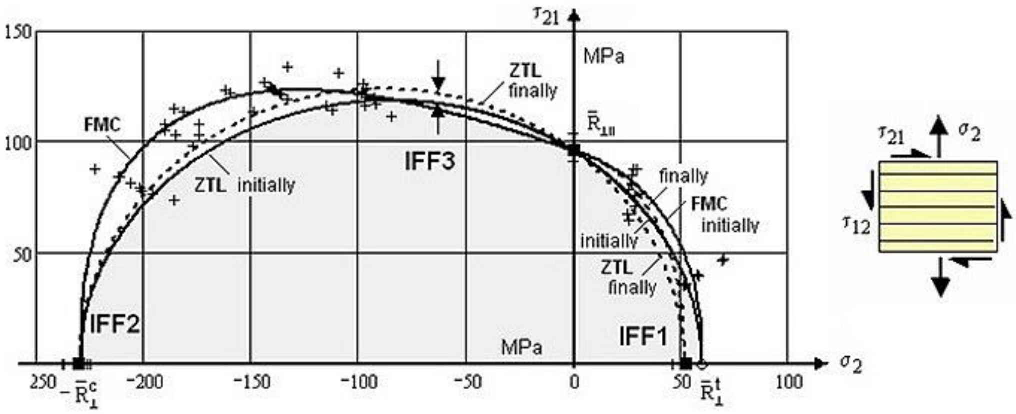

ZTL: global

$$\frac{\sigma_2{}^2}{\overline{R}_\perp^t \cdot \overline{R}_\perp^c} + \sigma_2 \cdot \left(\frac{1}{\overline{R}_\perp^t} - \frac{1}{\overline{R}_\perp^c}\right) + \frac{\tau_{21}{}^2}{\overline{R}_{\perp\|}} = 1$$

FMC: modal

$$\left(\frac{\sigma_2}{\overline{R}_\perp^t}\right)^m + \left(\frac{-\sigma_2}{\overline{R}_\perp^c}\right)^m + \left(\frac{|\tau_{21}|}{\overline{R}_{\perp\|} - \mu_{\perp\|} \cdot \sigma_2)}\right)^m = 1$$

Fig.6-2: Modelling example, impact of a novel test information in the mode IFF1 considering a global (ZTL-SFC, still used in the HSB) and a modal SFC,

Considering the shortcomings of 'global' UD SFCs, my friend John Hart-Smith cited:

"It is scientifically incorrect to employ polynomial interaction failure models (the 'global' ones)***, if the mechanism of failure changes"!***

Of course, a modal FMC-approach requires an interaction in all the mode transition zones. This is performed by a probabilistic approach, using a 'series failure system' in the transition zone of adjacent modes NF with SF, reading

$$Eff \;=\; \sqrt[m]{(Eff^{\text{mode }1})^m \;+\; (Eff^{\text{mode }2})^m \;+\; ....} = 1 = 100\% \qquad \textit{for} \quad \text{Onset-of-Failure}$$

and applying a mode interaction exponent *m,* also termed rounding-off exponent, the size of which is high in case of low scatter and vice versa. The value of *m* is obtained by curve fitting of test data in the transition zone of the interacting modes. Experience delivered that $2.5 < m < 2.9$.

With the FMC-based SFCs for the three 'material families' available multi-axial fracture test data were mapped by the author to validate the SFCs being the mathematical descriptions of the envisaged fracture failure models. For a large variety of materials the associated fracture bodies were displayed in later chapters with distinct cross–sections of them, for instance for the isotropic applications: Principal stress plane, octahedral stress plane and tensile and meridian planes. Various links or interrelationships between the materials could be outlined.

LL:

* *So-called 'Global' SFCs couple physically different failure modes whereas the Modal SFCs describe each single failure mode and therefore will better map the course of test data and not lead to a wrong Reserve Factor*
* *Here, global and modal have a similar level of abstraction, as in the case of stability the terms 'global' and 'local' have*
* *Similarities between the materials could be found*
* *The surface of the failure body reads: F = 1, for a 'global' formulation and Eff = 1 for a 'modal' formulation.*

7 Collection of Derived SFCs, Interaction of Failure Modes and a Multi-fold Mode

7.1 Presentation of the derived Failure Mode Concept-based Strength Failure Criteria

Aim: *Provision of SFCs which were derived on the same concept basis.*

For the mentioned three material families the associate SFCs are tabled on the following pages:

I a : 3D-isotropic SFCs of dense Isotropic Materials *for* ***NF*** *and* ***SF****, 120°-rotational symmetry*

2 modes → 2 SFCs, is in line with 'generic' number according to the FMC.

Normal Fracture NF for $I_1 > 0$ ↔ Shear Fracture SF for $I_1 < 0$

$$F_\sigma^t = F^{NF} = c^{NF} \cdot \Theta^{NF} \cdot \frac{\sqrt{4J_2 \cdot \Theta^{NF} - I_1^2/3} + I_1}{2 \cdot \bar{R}^t} = 1 \quad \leftrightarrow \quad F_\tau^c = F^{SF} = c_{1\Theta}^{SF} \cdot \frac{6J_2 \cdot \Theta^{SF}}{2\bar{R}^{c2}} + c_{2\Theta}^{SF} \cdot \frac{I_1}{\bar{R}^c} = 1$$

$$Eff^{NF} = c^{NF} \cdot \frac{\sqrt{4J_2 \cdot \Theta^{NF} - I_1^2/3} + I_1}{2 \cdot \bar{R}^t} = \frac{\sigma_{eq}^{NF}}{\bar{R}^t} \leftrightarrow Eff^{SF} = \frac{c_{2\Theta}^{SF} \cdot I_1 + \sqrt{(c_{2\Theta}^{SF} \cdot I_1)^2 + c_{1\Theta}^{SF} \cdot 12J_2 \cdot \Theta^{SF}}}{2 \cdot \bar{R}^c} = \frac{\sigma_{eq}^{SF}}{\bar{R}^c}.$$

If a failure body is rotationally symmetric, then $\Theta = 1$ like for the neutral or shear meridian.

A two-fold acting mode makes the rotationally symmetric fracture body 120°-symmetric and is modelled by $\Theta(J_3)$ using the invariant J_3 and Θ as non-circularity function with d as non-circularity parameter

$$\Theta^{NF} = \sqrt[3]{1 + d^{NF} \cdot \sin(3\vartheta)} = \sqrt[3]{1 + d^{NF} \cdot 1.5 \cdot \sqrt{3} \cdot J_3 \cdot J_2^{-1.5}}, \Theta^{SF} = \sqrt[3]{1 + d^{SF} \cdot 1.5 \cdot \sqrt{3} \cdot J_3 \cdot J_2^{-1.5}}$$

Lode angle ϑ, here set as $\sin(3 \cdot \vartheta)$ with 'neutral' shear meridian angle set $\vartheta = 0°$;

tensile meridian angle 30° $\rightarrow \Theta^{NF} = \sqrt[3]{1 + d^{SF} \cdot (+1)}$; compr. merid. angle -30° $\rightarrow \Theta^{SF} = \sqrt[3]{1 + d^{SF} \cdot (-1)}$.

Equation of the fracture failure body: $Eff = [(Eff^{NF})^m + (Eff^{SF})^m]^{m^{-1}} = 1 = 100\%$ total effort

$$Eff = \sqrt[m]{(c^{NF} \cdot \frac{\sqrt{4J_2 \cdot \Theta^{NF} - I_1^2/3} + I_1}{2 \cdot \bar{R}^t})^m + (\frac{c_{2\Theta}^{SF} \cdot I_1 + \sqrt{(c_{2\Theta}^{SF} \cdot I_1)^2 + c_{1\Theta}^{SF} \cdot 12J_2 \cdot \Theta^{SF}}}{2 \cdot \bar{R}^c})^m} = 1.$$

Curve parameter relationships obtained by inserting the compressive strength point (0, $-\bar{R}^c$, 0):

* Rotationally symmetric: $c_1^{SF} = 1 + c_2^{SF}$, $d^{SF} = 0$, friction parameters are equal $c_2^{SF} \equiv c_{2\Theta}^{SF}$

$c_2^{SF} = c_{2\Theta}^{SF} \approx (1 + 3 \cdot \mu)/(1 - 3 \cdot \mu)$ from $\mu = \cos(2 \cdot \theta_{fp}^c \,° \cdot \pi / 180)$ and for 50° $\rightarrow \mu = 0.174$.

* 120°-rotationally symmetric: $c_{1\Theta}^{SF} = 1 + c_2^{SF} \cdot \sqrt[3]{1 + d^{SF} \cdot (-1)}$ with

c^{NF}, Θ^{NF} from the two points $(\bar{R}^t, 0, 0)$ and $(\bar{R}^{tt}, \bar{R}^{tt}, 0)$ or by a minimum error fit, if data,

c^{SF}, Θ^{SF} from the two points $(-\bar{R}^c, 0, 0)$ and $(-\bar{R}^{cc}, -\bar{R}^{cc}, 0)$ or by minimum error fit .

A paraboloid serves as closing cap $\frac{I_1}{\sqrt{3} \cdot \bar{R}^t} = s^{cap} \cdot (\frac{\sqrt{2J_2 \cdot \Theta^{NF}}}{\bar{R}^t})^2 + \frac{\max I_1}{\sqrt{3} \cdot \bar{R}^t}.$

$$I_1 = (\sigma_I + \sigma_{II} + \sigma_{III}) = f(\sigma), \quad 6J_2 = (\sigma_I - \sigma_{II})^2 + (\sigma_{II} - \sigma_{III})^2 + (\sigma_{III} - \sigma_I)^2 = f(\tau)$$

$$27J_3 = (2\sigma_I - \sigma_{II} - \sigma_{III}) \cdot (2\sigma_{II} - \sigma_I - \sigma_{III}) \cdot (2\sigma_{III} - \sigma_I - \sigma_{II}) .$$

I b : 3D-isotropic SFCs of dense Isotropic Materials for NF and SF, 120°-rotational symmetry

Table I b collects all information necessary to design dimension a porous isotropic material like a foam or a concrete stone. These materials experience *120°-rotational symmetry*.

'Porous' isotropic material: SFC formulations for NF and CrF, 120°-rotational symmetry

Normal Fracture NF for $I_1 > 0$ $\leftrightarrow$ Crushing Fracture CrF for $I_1 < 0$

$$F^{NF} = c^{NF} \cdot \Theta^{NF} \cdot \frac{\sqrt{4J_2 \cdot \Theta^{NF} - I_1^2/3} + I_1}{2 \cdot \bar{R}^t} = 1 \leftrightarrow F^{CrF} = c^{CrF} \cdot \Theta^{CrF} \cdot \frac{\sqrt{4J_2 \cdot \Theta^{CrF} - I_1^2/3} + I_1}{2 \cdot \bar{R}^c} 1$$

$$Eff^{NF} = c^{NF} \cdot \frac{\sqrt{4J_2 \cdot \Theta^{NF} - I_1^2/3} + I_1}{2 \cdot \bar{R}^t} = \frac{\sigma_{eq}^{NF}}{\bar{R}^t} \leftrightarrow Eff^{CrF} = c^{CrF} \cdot \frac{\sqrt{4J_2 \cdot \Theta^{CrF} - I_1^2/3} + I_1}{2 \cdot \bar{R}^c} = \frac{\sigma_{eq}^{CrF}}{\bar{R}^c}.$$

If a failure body is rotationally symmetric, then $\Theta = 1$ like for the neutral or shear meridian, respectively. A 2-fold acting mode makes the rotationally symmetric fracture body 120°-symmetric and is modelled by using the invariant J_3 and Θ as non-circularity function with d as non-circularity parameter

$$\Theta^{NF} = \sqrt[3]{1 + d^{NF} \cdot \sin(3\vartheta)} = \sqrt[3]{1 + d^{NF} \cdot 1.5 \cdot \sqrt{3} \cdot J_3 \cdot J_2^{-1.5}} \leftrightarrow \Theta^{CrF} = \sqrt[3]{1 + d^{CrF} \cdot 1.5 \cdot \sqrt{3} \cdot J_3 \cdot J_2^{-1.5}}$$

Lode angle ϑ, here set as $\sin(3 \cdot \vartheta)$ with 'neutral' (shear meridian) angle $\vartheta = 0°$ ($\rightarrow \Theta = 1$);

tensile meridian angle $30° \rightarrow \Theta^{NF} = \sqrt[3]{1 + d^{NF} \cdot (+1)}$; compr. mer. angle $-30° \rightarrow \Theta^{CrF} = \sqrt[3]{1 + d^{CrF} \cdot (-1)}$.

Mode interaction $\rightarrow$ Equation of the fracture body: $Eff = [(Eff^{NF})^m + (Eff^{SF})^m]^{m^{-1}} = 1 = 100\%$

$$Eff = \sqrt[m]{\left(c^{NF} \cdot \frac{\sqrt{4J_2 \cdot \Theta^{NF} - I_1^2/3} + I_1}{2 \cdot \bar{R}^t}\right)^m + \left(c^{CrF} \cdot \frac{\sqrt{4J_2 \cdot \Theta^{CrF} - I_1^2/3} + I_1}{2 \cdot \bar{R}^c}\right)^m} = 1.$$

Curve parameter relationships obtained by inserting the compressive strength point $(0, -\bar{R}^c, 0)$:

* Rotationally symmetric $\Theta = 1$: $d^{SF} = 0$, $c_{1\Theta}^{SF} = 1 + c_2^{SF}$
* 120°-rotat. symmetric $\Theta \neq 1$: $c_{1\Theta}^{SF} = 1 + c_2^{SF} \cdot \sqrt[3]{1 + d^{SF} \cdot (-1)}$, with

  c^{NF}, Θ^{NF} from the two points $(\bar{R}^t, 0, 0)$ and $(\bar{R}^{tt}, \bar{R}^{tt}, 0)$ or by minimum error fit, if data available,

  c^{CrF}, Θ^{CrF} from the two points $(-\bar{R}^c, 0, 0)$ and $(-\bar{R}^{cc}, -\bar{R}^{cc}, 0)$ or by minimum error fit.

The failure surface is closed at both the ends: A paraboloid serves as closing cap and bottom

$$\frac{I_1}{\sqrt{3} \cdot \bar{R}^t} = s^{cap} \cdot \left(\frac{\sqrt{2J_2 \cdot \Theta^{NF}}}{\bar{R}^t}\right)^2 + \frac{\max I_1}{\sqrt{3} \cdot \bar{R}^t} \quad , \quad \frac{I_1}{\sqrt{3} \cdot \bar{R}^t} = s^{bot} \cdot \left(\frac{\sqrt{2J_2 \cdot \Theta^{CrF}}}{\bar{R}^t}\right)^2 + \frac{\min I_1}{\sqrt{3} \cdot \bar{R}^t}$$

Slope parameters s are determined connecting the respective hydrostatic strength point with the associated point on the tensile and compressive meridian, $\max I_1$ must be assessed whereas $\min I_1$ can be measured. $\bar{R}^t$ is normalization strength.

II : 3D-SFCs of (quasi-)Brittle Dense UD Materials

5 modes → 5 SFCs, is in line with 'generic' number according to the FMC. IFF1 generates a straight line in the stress plane!

FF1: $Eff^{\|\sigma} = \breve{\sigma}_1 / \bar{R}_{\|}^t = \sigma_{eq}^{\|\sigma} / \bar{R}_{\|}^t$ with $\breve{\sigma}_1 \cong \varepsilon_1^t \cdot E_{\|}$ (matrix neglected)

FF2: $Eff^{\|\tau} = -\breve{\sigma}_1 / \bar{R}_{\|}^c = +\sigma_{eq}^{\|\tau} / \bar{R}_{\|}^c$ with $\breve{\sigma}_1 \cong \varepsilon_1^c \cdot E_{\|}$

IFF1: $Eff^{\perp\sigma} = [(\sigma_2 + \sigma_3) + \sqrt{\sigma_2^2 - 2\sigma_2 \cdot \sigma_3 + \sigma_3^2 + 4\tau_{23}^2}\,] / 2\bar{R}_{\perp}^t = \sigma_{eq}^{\perp\sigma} / \bar{R}_{\perp}^t$

IFF2: $Eff^{\perp\tau} = [a_{\perp\perp} \cdot (\sigma_2 + \sigma_3) + b_{\perp\perp}\sqrt{\sigma_2^2 - 2\sigma_2\sigma_3 + \sigma_3^2 + 4\tau_{23}^2}\,] / \bar{R}_{\perp}^c = \sigma_{eq}^{\perp\tau} / \bar{R}_{\perp}^c$

IFF3: $Eff^{\perp\|} = \{[b_{\perp\|} \cdot I_{23-5} + (\sqrt{b_{\perp\|}^2 \cdot I_{23-5}^2 + 4 \cdot \bar{R}_{\perp\|}^2 \cdot (\tau_{31}^2 + \tau_{21}^2)^2}\,] / (2 \cdot \bar{R}_{\perp\|}^3)\}^{0.5} = \sigma_{eq}^{\perp\|} / \bar{R}_{\perp\|}$

$$\{\sigma_{eq}^{\text{mode}}\} = (\sigma_{eq}^{\|\sigma},\ \sigma_{eq}^{\|\tau},\ \sigma_{eq}^{\perp\sigma},\ \sigma_{eq}^{\perp\tau},\ \sigma_{eq}^{\|\perp})^T, \quad I_{23-5} = 2\sigma_2 \cdot \tau_{21}^2 + 2\sigma_3 \cdot \tau_{31}^2 + 4\tau_{23}\tau_{31}\tau_{21}$$

Inserting the compressive strength point (0, $-\bar{R}_{\perp}^c$) → $a_{\perp\perp} \cong \mu_{\perp\perp} / (1 - \mu_{\perp\perp})$, $b_{\perp\perp} = a_{\perp\perp} + 1$

from a measured fracture angle → $\mu_{\perp\perp} = \cos(2 \cdot \theta_{fp}^{c}{}^\circ \cdot \pi / 180)$, for 50° → $\mu = 0.174$.

$b_{\perp\|} \cong 2 \cdot \mu_{\perp\|}$. Typical friction value ranges: $0 < \mu_{\perp\|} < 0.25$, $0 < \mu_{\perp\perp} < 0.2$.

Interaction Equation:

$$Eff^m = [(\sigma_{eq}^{\|\sigma} / \bar{R}_{\|}^t)^m + (\sigma_{eq}^{\|\tau} / \bar{R}_{\|}^c)^m + (\sigma_{eq}^{\perp\sigma} / \bar{R}_{\perp}^t)^m + (\sigma_{eq}^{\perp\tau} / \bar{R}_{\perp}^c)^m + (\sigma_{eq}^{\perp\|} / \bar{R}_{\perp\|})^m]$$

or $Eff = \sqrt[m]{(Eff^{\text{mode }1})^m + (Eff^{\text{mode }2})^m + \ldots} = 1 = 100\%$ *for* Onset-of-Failure .

As abbreviation, $I_2 \cdot I_3 - I_5 = I_{23-5}$ is used. In the equations above, $\bar{R}$ denotes an average = typical strength value that should be used for the stress-strain curves in stress and deformation analysis. In the design verification the statistically reduced strength values are applied. The superscripts ^{t}, ^{c} stand for tensile, compressive. The superscripts $^\sigma$ and $^\tau$ mark the type of fracture failure whether it is caused by a tensile stress (Normal Fracture, NF, 'cleavage') or a shear stress (Shear Fracture, SF), e.g. due to a compressive normal stress $\sigma_{\|}^c$ or a transverse normal stress $\sigma_{\perp}^c$.

Failure activated in two directions is considered by adding a multi-fold failure term, proposed in [*Awa78*] for isotropic materials. It can be applied to brittle UD material in the transversal (quasi-isotropic) plane as well.

For the 2D-case, a simplified friction modelling (IFF3) is possible:

$Eff^m = [(Eff^{\|\sigma})^m + (Eff^{\|\tau})^m + (Eff^{\perp\sigma})^m + (Eff^{\perp\tau})^m + (Eff^{\perp\|})^m]$ with the mode portions inserted, 2D,

$$Eff = [(\frac{(\sigma_1 + |\sigma_1|)}{2 \cdot \bar{R}_{\|}^t})^m + (\frac{(-\sigma_1 + |\sigma_1|)}{2 \cdot \bar{R}_{\|}^c})^m + (\frac{\sigma_2 + |\sigma_2|}{2 \cdot \bar{R}_{\perp}^t})^m + (\frac{-\sigma_2 + |\sigma_2|}{2 \cdot \bar{R}_{\perp}^c})^m + (\frac{|\tau_{21}|}{\bar{R}_{\perp\|} + 0.5 \cdot \mu_{\perp\|} \cdot (-\sigma_2 + |\sigma_2|)})^m]^{1/m}$$

II b: 3D-SFCs of (quasi-)Brittle Porous UD Materials

This practically meets just IFF2. The table below shows the difference.

* IFF2 Failure Function for the dense UD material (for comparison)
$F^{SF} = [a_{\perp\perp} \cdot I_2 + b_{\perp\perp} \cdot \sqrt{I_4}] \,/\, \bar{R}_\perp^c = 1$ with $a_{\perp\perp} = b_{\perp\perp} - 1$ after inserting $\bar{R}_\perp{}^c$
$= [a_{\perp\perp} \cdot (\sigma_2 + \sigma_3) + b_{\perp\perp} \cdot \sqrt{(\sigma_2 - \sigma_3)^2 + 4\tau_{23}{}^2}] \,/\, \bar{R}_\perp^c = 1$
$= [a_{\perp\perp} \cdot (\sigma_2{}^{pr} + \sigma_3{}^{pr}) + b_{\perp\perp} \cdot \sqrt{(\sigma_2{}^{pr} - \sigma_3{}^{pr})^2 + 0^2}] \,/\, \bar{R}_\perp^c = 1 \leftarrow$ 2 structural stresses
* IFF2 Failure Function for the porous UD material (index por, *author's simple approach*)
$F^{SF}_{porosity} = \sqrt{a_{\perp\perp por}{}^2 \cdot I_2{}^2 + b_{\perp\perp por}{}^2 \cdot I_4} - a_{\perp\perp por} \cdot I_2 \,] \,/\, 2\bar{R}_\perp^c = 1$.
The two curve parameters are determined - as before performed - from insertion of the compressive strength point and from the bi-axial fracture stress point.

Mind: In contrast to an isotropic dense material the fracture body of a compressed dense UD-material has a closed bottom fracture surface, because the filaments may break under the tensile stress caused by biaxial compression due to the Poisson effect, when $\varepsilon^t_{axial} = \varepsilon_{||}^{fr}$.

III: 3D-SFCs of the Orthotropic Fabrics, (see [*Cun*24*b*])

9 modes → 9 SFCs. This is in line with Cuntze's 'generic' number 9 according to the FMC.
In this context, my thanks to Roman (Prof. Dr. Keppeler, UniBw; formerly Siemens AG).

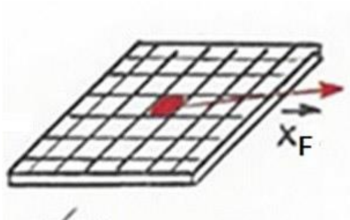

Fabrics lamina stresses:

$\{\sigma\}_{lamina} = (\sigma_W, \sigma_F, \sigma_3, \tau_{3F}, \tau_{3W}, \tau_{FW})^T$

Fabrics lamina strengths:

$\{\bar{R}\}$ = vector of mean strength values

x_W $\{\bar{R}\} = (\bar{R}^t_W, \bar{R}^c_W, \bar{R}^t_F, \bar{R}^c_F, \bar{R}_{WF}, \bar{R}^t_3, \bar{R}^c_3, \bar{R}_{3F}, \bar{R}_{3W})^T$

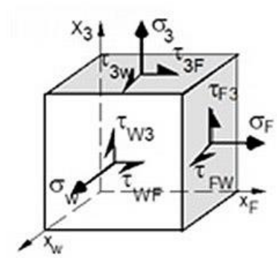

The following table includes the FMC-based SFCs for **porous orthotropic** (rhombic-anisotropic) **materials** composed for instance of 2D-woven fabrics**.** Three essential 2D-woven fabrics (Atlas or Satin) are depicted

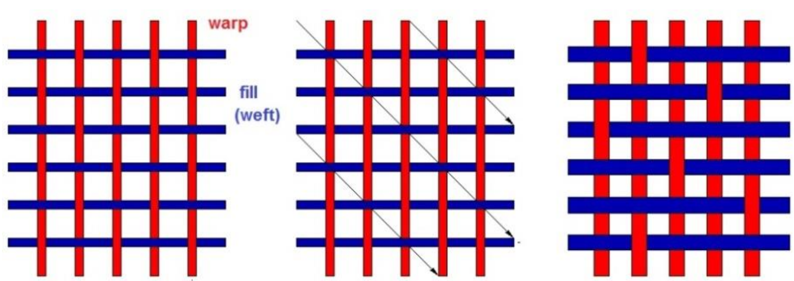

plain weave fabric *(Leinwandbindung)* ***twill fabric*** *(Köperbindung)* ***atlas fabric*** *(Atlasbindung)*

$$Eff = \left(\frac{\sigma_W + |\sigma_W|}{2 \cdot \bar{R}_W^t}\right)^m + \left(-\frac{\sigma_W + |\sigma_W|}{2 \cdot \bar{R}_W^c}\right)^m + \left(\frac{\sigma_F + |\sigma_F|}{2 \cdot \bar{R}_F^t}\right)^m + \left(\frac{-\sigma_F + |\sigma_F|}{2 \cdot \bar{R}_F^c}\right)^m + \left(\frac{|\tau_{WF}|}{\bar{R}_{WF} - \mu_{WF} \cdot (\sigma_W + \sigma_F)}\right)^m$$

$$+ \left(\frac{\sigma_3 + |\sigma_3|}{2 \cdot \bar{R}_3^t}\right)^m + \left(\frac{-\sigma_3 + |\sigma_3|}{2 \cdot \bar{R}_3^c}\right)^m + \left(\frac{|\tau_{3W}|}{\bar{R}_{3W} - \mu_{3W}\sigma_3^c}\right)^m + \left(\frac{|\tau_{3F}|}{\bar{R}_{3F} - \mu_{3F}\sigma_3^c}\right)^m = 1 = 100\% .$$

For a cross-ply fabric with Warp = Fill $\rightarrow$ $\bar{R}_W^t = \bar{R}_F^t$, $\bar{R}_W^c = \bar{R}_F^c$, the inter-laminar *Eff*s, suffix $_3$, vanish and just the in-plane (intra-laminar) *Eff*s remain.

The range of parameters is for the interaction-exponent $2.5 < m < 2.9$, and since the strong porosity-dependency is very different $\rightarrow$ recommendation: $\mu_{WF} < 0.2$, $\mu_3 < 0.2$.

If σ_F is also active, this double mode contributes via $\left(\frac{|\tau_{WF}|}{\bar{R}_{WF} - \mu_{WF} \cdot (\sigma_W^c + \sigma_F^c)}\right)^m$.

Modelling of laminates may be lamina-based (basic layers are UD layers), sub-laminate-based (semi-finished non-crimp orthotropic fabrics) or even laminate-based. Thereby, modelling complexity grows from UD, via non-crimp fabrics (NCF) through plain weave and finally to the spatial 3D-textile materials. Model parameters are just the measurable technical strengths *R* and the friction values *μ,* and on top the Weibull statistics-based interaction exponent *m*. The value of *μ* comes from mapping the compression stress-shear stress domain and of *m* by mapping the transition zone between the modes. A good guess is *m* = 2.6 for all mode transition domains and all material families. Model parameters are just the measurable technical strengths *R* and the friction values *μ,* and on top the Weibull statistics-based interaction exponent *m*. The value of *μ* comes from mapping the compression stress-shear stress domain and of *m* by mapping the transition zone between the modes. A good guess is *m* = 2.6 for all mode transition domains and all material families.

:

My experience and my present feeling considering the 3D-applications:

Much is reached with plenty of effort!
However, much more effort is required for the 3D-Validation. Test Data are missing.

Only when you get 'higher' the real 'peaks' do appear:

3D-applications are much more challenging.

8 Validity Limits of UD SFC Application → Finite Fracture Mechanics (FFM)

Aim: *Giving the SFC user a warning by information on the validity limits of the SFCs.*

There are three approaches available to deal with the occurring stress situations: Strength criteria (SFC), Continuum (micro-)Damage mechanics (CDM) criteria and Fracture Mechanics (FM) criteria which employ macro-crack growth models.

A SFC is a necessary condition but might not be a sufficient condition for the prediction of 'initiation of cracking' (Onset-of-Failure). This is known for a long time from the so-called 'thin layer effect' of UD-layer-composed laminate: *Due to being strain-controlled, the material flaws in a thin lamina cannot grow freely up to micro-crack size in the thickness direction, because the neighboring laminas act as micro-crack-stoppers*.

Considering fracture mechanics, the strain energy release rate, responsible for the development of damage energy in the 90° plies - from flaws into micro-cracks and larger -, increases with increasing ply thickness. Therefore, the actual absolute thickness of a lamina in a laminate is a driving parameter for initiation or onset of micro-cracks, i.e. [*Fla82*].

Further known is in the case of discontinuities such as notch singularities with steep stress decays: only a *toughness + characteristic length-based energy balance condition* may form a sufficient set of two fracture conditions.

When applying SFCs usually ideal solids are viewed which are assumed to be free of essential micro-voids or microcrack-like flaws, whereas applying Fracture Mechanics the solid is considered to contain macro-voids or macro-cracks.

Since about 20 years Finite Fracture Mechanics (FFM) fills a gap between the continuum mechanical strength criteria and the classical FM. FFM is an approach to offer a criterion to predict the crack initiation in brittle isotropic and UD materials. This is a bridge that had to be built from strength failure to fracture mechanics failure. Attempts to link SFC-described 'onset of fracture' prediction methods and FM prediction methods for structural components have been performed. Best known is the Hypothesis of Leguillon [*Leg02*]:

"*A crack is critical when and only when both the released energy and the local stress reach critical values along an assumed finite crack*".

Within the FFM Leguillon assumes cracks of finite length. Thus, using FFM one obtains one more unknown but also one eqation to solve together with the SFC the equation system.
This coupled criterion does not refer to microscopic mechanisms to predict crack nucleation.

[Leg02] Leguillon D: *Strength or Toughness? –A criterion for crack onset at a notch.* Europ. J. of Mechanics A/Solids 21 (2002), 61 – 72 end. Ist. D. sci. Lett., Cl. Mat. Nat.18, 705-714 (1885)

[Fla82] Flaggs D L and Kural M H*: Experimental Determination of the In Situ Transverse Lamina Strength in Graphite Epoxy Laminates*. J. Comp. Mat. Vol 16 (1982), S. 103-116

LL:

** In the case of plain structural parts crack initiation (according to FF, IFF of the ply and delamination of the laminate) in brittle and semi-brittle materials cannot be fully captured by the SFCs, because both a critical energy and a critical stress state must be fulfilled*

** SFCs are 'just' necessary but not sufficient for the prediction of strength failure. Basically, due to internal flaws, also an energy criterion is to apply. The novel approach 'Finite Fracture Mechanics (FFM)' offers a hybrid criterion to more realistically predict the stress-based crack initiation in brittle isotropic and UD materials.*

* *The coupled criterion SFC-FM can be used with some confidence to predict the crack initiation in brittle materials in new design situations as never could be done before.*
* *When applying test data from ‘isolated lamina’ test specimens (like tensile coupons) to an embedded lamina of a laminate one should consider that coupon test deliver tests results of ‘weakest link’ type. An embedded or even an only one-sided constrained lamina, however, possesses redundant behavior*
* *It is also to regard, when considering the formulations to be applied: Short cracks behave differently to Large Cracks*
* *For usual ‘strength problems’ FFM is not applicable.*
* *It is advantageous for the analysis of notched structural parts and captures applications usually performed by the well-known Neuber theory.*

Experience:

The caiman mother Maria observes the Limit “**No trespassing** (No pase!)”.
Maria stopped at the tape, marked with “No pase“!
That behavior was very good for the **personal** health of my friend Eddi
(*he unfortunately fell in front of her snout while running away*).

We learn:

Engineers should always observe the limits set by specifications etc.
*This is good for ‘**structural** health’ or Structural Integrity, respectively.*
And: This fully meets the SFC applications.

9 ‘Curiosities’ regarding Classical Material Mechanics

Aim*: Filling two rooms in the Material Mechanics Building by proving the assumed ’generic’ number.*

Regarding a material ‘generic’ number of 2 to be valid for isotropic materials there are two ‘empty rooms’ in the author-assumed ‘Mechanics Building’ of Isotropic Materials namely Normal Yielding NY and a counterpart of the tensile fracture toughness $K_{\mathrm{Icr}}^{(\mathrm{t})}$ in the compressive domain.

9.1 Normal Yielding NY: [*CUN22, §4*]

Glassy, amorphous polymers like polystyrene (PS), polycarbonate (PC) and PolyMethylMethacrylate (PMMA = plexiglass) are often used structural materials. They experience two different yield failure types, namely crazing under tension (*Fig.9-1*) and under compression a

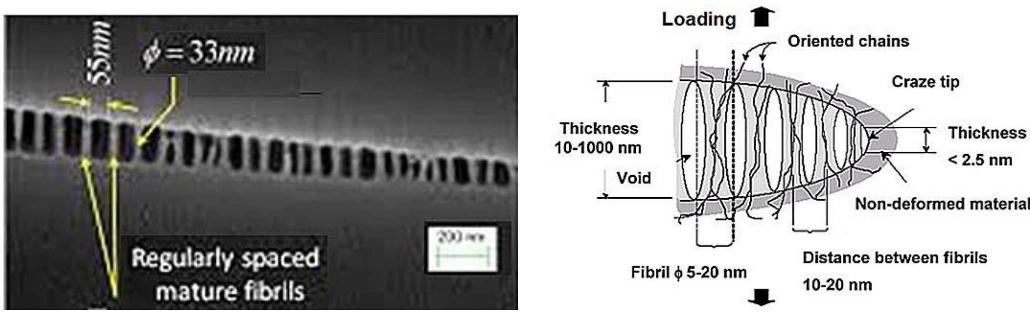

Fig. 9-1: PMMA, SEM image of a craze in Polystyrene Image (created by Y. Arunkumar)

shear stress yielding that is often termed by material specialist ‘shear-banding’.

Crazing can be linked to Normal Yielding (NY) which precedes the crazing-following tensile fracture. Crazing occurs with an increase in volume through the formation of fibrils bridging built

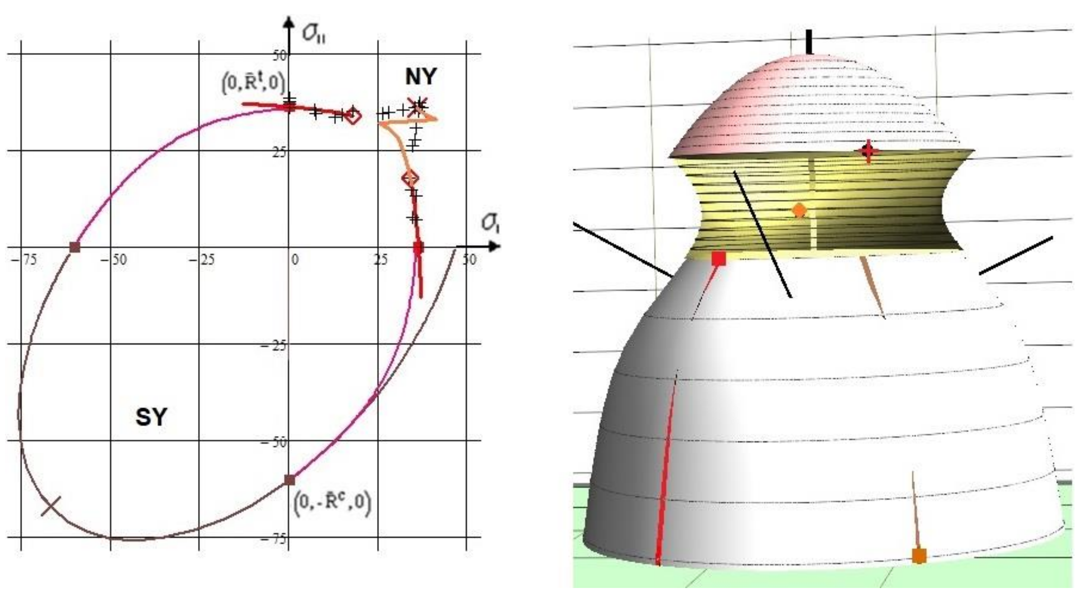

Fig. 9-2, PMMA: (left) Mapping of test data in tension and compression principal stress domain with and without interaction; (right) depiction of the fracture body shape with some representative points. For the validation of the FMC-based SFC for PMMA two data sets were available, one NY-2D-data set from Sternstein-Myers and a SY-3D-data set from Matsushige

[Ste73] Sternstein S S and Myers F A: *Yielding of glassy polymers in the second quadrant of principal stress space.* J. Macromol. Sci, Phys. B 8 (1973), 539-571

[Mat75] Matsushige K, Radcliffe S V and Baer E: *The mechanical behavior of polystyrene under pressure*. J. of Material Science 10 (1975), 833-845.

micro-cracks and shear banding keeps volume. Therefore, due to the FMC 'rules' the dilatational I_1^2 is to employ in the SFC-approach for tension $I_1 > 0$. Under compression, brittle amorphous polymers classically shear-band (SY) and experience friction. Therefore, I_1 must be employed in the approach for $I_1 < 0$ in order to consider material internal friction. 'Mises' means frictionless yielding and therefore it forms a cylinder.

For obtaining the complete yield failure body (Fig.9-2) its parts NY and SY are to interact in the transition zone. Doing this the used Mathcad 15 code had no problems to generate the **3D**-failure body, however the **2D**-visualization of the NY failure surface using Mathcad 15 code (*a 35 DIN A4-pages application*) was too challenging for the solver which had to face a concave 2D principal stress plane situation instead of a usual convex one.

> **LL:** *The failure type crazing shows a 'curiosity' under tensile stress states: A non-convex shape exists for Onset-of-Crazing ($\bar{R}_{NY}^{t}$). This violates the convexity stability postulate of Drucker, meaning "If the stress-strain curve has a negative slope then the material is not Drucker-stable". The inflection point of the hyperboloid results from the derivation dF/dI_1 of the NF criterion, neglecting 120°-symmetry (see later chapter)* $F^{NF} = \dfrac{\sqrt{4J_2 - I_1^2/3} + I_1}{2 \cdot \bar{R}^t} = 1.$

9.2 Compressive (shear) Fracture Toughness $K_{IIcr}^{(c)}$, *[CUN22,§4.2]*

Some reasons caused the author to search a compressive fracture toughness:

- An early citation of A. Carpinteri, that approximately reads: "*With homogeneous isotropic brittle materials there are 2 real energy release rates $\mathcal{G}_{Icr}$, $\mathcal{G}_{IIcr}$, one in tension and one in compression*"
- The number of the (basic) fracture toughness quantities may be *theoretically at least* also 2, namely $K_{Icr}^{t} \equiv K_{Ic}$ together with K_{IIcr}^{c} (Fig.9-3) and
- The novel approach Finite Fracture Mechanics (FFM) that offers a hybrid criterion to more realistically predict the crack initiation in brittle isotropic and UD materials.

A stringent postulate for the author was crack path stability which can be explained "*Only an angle-stable, self-similar crack growth plane-associated critical Stress Intensity Factor (fracture toughness) is a 'basic' property*". This requires as presumption an *ideally* homogeneous isotropic material in front of the crack-tip. Therefore, the investigation is only for an ideal structural mechanics building of importance, because in practice, there are usually no ideal homogeneous conditions at the crack-tip.

Practically, facture mechanics is presently only tensile driven performed using $K_{Ic} = K_{Icr}^{t}$ as a clear critical fracture intensity, where the crack plane does not change (the index cr is necessarily to be taken in this document in order to separate tension ^{t} from compression ^{c}). Why shouldn't there not be a quantity K_{IIcr}^{c} that fits as an opposite complement to K_{Icr}^{t} and where, in an ideal case of no flaws in front of the crack tip, the crack plane grows further along the generated shear fracture angle under a compressive fracture load?

The Fracture Mechanics Mode I delivers a real, 'basic' fracture resistance property generated under a tensile stress. Both the Modes II K_{IIc}, and III K_{IIIc} do not show a stable crack plane situation but are nevertheless essential FM model parameters to capture 'mixed mode loading' for performing a multi-axial assessment of the far-field stress state. $\rightarrow \bar{R}^{t}$ and $\bar{K}_{Icr}^{t}$ correspond! They are 'just' very helpful model parameters driving the crack plane in direction of a finally KIc-driven failure.

With the Mode-II compressive fracture toughness K_{IIcr}^{c} it is like with strength. One says compressive failure, but actually shear (stress) failure is meant, compressive stress is 'only' the descriptive term. Therefore the shear index $_{II}$ is to apply with K_{IIcr}^{c} .

One has to keep in mind: In mechanical engineering the structural tasks are usually lie in the tension domain (*index ^{t} is skipped*), whereas oppositely in civil engineering the compression domain is faced (*index ^{c} is skipped*):

*Tension domain: One knows from K_{Icr}^{t} (tension), that – viewing the fracture angle - it corresponds to R^t.

*Compression domain: Above not generally known second basic SIF K_{IIcr}^{c} seems to exist under ideal conditions. It corresponds to shear fracture SF happening under compressive stress R^c and leading to the angle Θ_{fp}^{c}. The crack surfaces are closed for K_{IIcr}^{c}, friction sliding occurs.

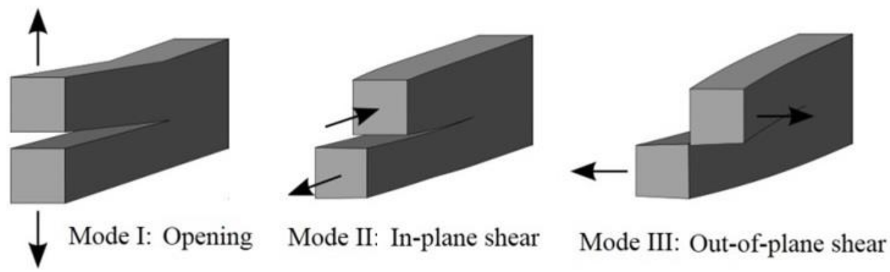

Fig.9-3: Classical Fracture Mechanics modes

Some proof of the author's postulate could be: There exists a minimum value of the compressive loading at a certain fracture angle. This means that the K_{IIcr}^{c} becomes a minimum, too. Liu et al performed in [*Liu14*] tests using a cement mortar material, (*Fig.9-4*). ► From his measured results, by now, it seems to - theoretically at least - that the 'generic' number 2 is met.

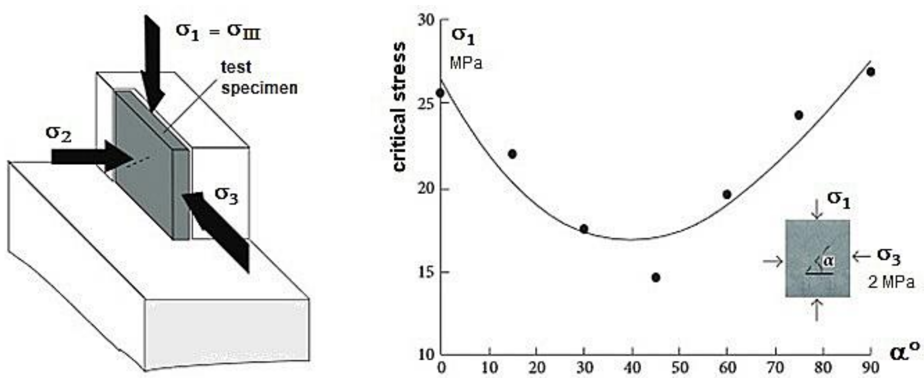

Fig.9-4: Scheme of the test set-up and of the test points obtained for cement mortar [Liu14], σ_1 represents the mathematical stress σ_{III} (largest compressive stress value).

[Liu J, Zhu Z and Wang B: *The fracture characteristic of three collinear cracks under true tri-axial compression.* The scientific World Journal, V 2014, article ID459025]

For the transversely-isotropic UD lamina materials it seems directly to match: ► 5 fracture toughness properties correspond to 5 strength properties, 'generic' number postulate is fulfilled.

LL: **Fracture Mechanics seems to follow material symmetry 'rules' and to possess a 'generic' number, too.*

** Note on K_{IIcr}^{c} as a design entity: Is of theoretical, but not of practical value due to the usually faced not ideal homogeneous situation of 'isotropic materials' at crack tips.*

10 Automated Generation of Constant Fatigue Life curves considering Mean Stress Effect

Aim: *Automated derivation of the Constant Life Curve with discussion of the Mean Stress Correction*

Generally, in Design Verification (DV) it is to demonstrate that “No relevant limit failure state is met considering all Dimensioning Load Cases (DLCs)”. This involves cyclic DLCs, focusing lifetime with non-cracked and cracked structural parts (*the latter would require Damage Tolerance tools*).
Methods for the prediction of durability, regarding the lifespan of the structural material and thereby of the structural part, involves long time static loading which is linked to ‘static fatigue‘ and in particular to ‘cyclic fatigue’. Fatigue failure requires a procedure for the Fatigue Life Estimation necessary to meet above cyclic DV.

Domains of Fatigue Scenarios and Analyses are:

LCF: high stressing and straining
HCF: intermediate stressing 10.000 < n < 2.000.000 cycles (*rotor tubes, bridges, towers, off-shore structures, planes, etc*.)
VHCF: low stress and low strain amplitudes (*see SPP1466 Very High Cycle Fatigue >* 10^7 *cycles (in centrifuges, wind energy rotor blades, etc*.).

Principally, in order to avoid either to be too conservative or too un-conservative, a separation of the always needed ‘analysis of the average structural behaviour’ in Design Dimensioning (*using average properties and average stress-strain curves*) in order to obtain the best structural information (= *50% expectation value*) is required from the mandatory single DV-analysis of the final design, where statistically minimum values for strength and minimum, or mean and maximum values for other task-demanded properties are applied as Design Values.

10.1 Fatigue Micro-Damage Drivers of Ductile and Brittle behaving Materials, see [*Cun23b*]

There are strain-life (*plastic deformation decisive, plastic strain-based* $\varepsilon_{pl}(N)$) and stress-life models (*SN*) used. For ductile materials, strain-life models are applied because a single yield mechanism dominates and the alternating stress amplitude counts. For brittle materials, the elastic strain amplitude becomes dominant and stress-life models are applied. With brittle materials inelastic micro-damage mechanisms drive fatigue failure and several fracture mechanisms may come to act. This asks for a modal approach that captures all failure modes which are now fracture modes.

Above two models can be depicted in a Goodman diagram and in a Haigh diagram. The Haigh diagram (σ_a, σ_m) will be applied here because the often used Goodman employs just one quantity σ_a or $\Delta\sigma = 2 \cdot \sigma_a$ or σ_{max} which is not sufficient. A Haigh Diagram represents all available SN curve information by its ‘Constant Fatigue Life (CFL) curves, being the focus here and using the two quantities σ_a, R .

Basic differences between ductile and brittle materials are the following ones:

- Ductile Material Behavior, isotropic materials: mild steel
  1 *micro-damage* mechanism acts ≡ *“slip band shear yielding“* and drives micro-damage under tensile, compressive, shear and torsional cyclic stresses: *This single mechanism is primarily described by* 1 *SFC, yield failure condition (HMH, ‘Mises‘)!*

- Brittle Material Behavior, isotropic materials: concrete, grey cast iron, etc.
  2 *micro-damage* driving mechanisms act ≡ 2 *fracture failure modes Normal Fracture failure (NF) and Shear Fracture failure (SF) under compression described by* 2 *fracture conditions, the 2 SFCs for NF and SF, where porosity is always to consider*
- Brittle Material Behavior, transversely-isotropic UD-materials:
  5 *micro-damage* driving fracture failure mechanisms act ≡ 5 fracture failure modes *described by 5 SFCs or strength fracture failure conditions*.

A very essential topic is the so-called 'Mean stress sensitivity': Within [*Cun23b*] the author attempts to redirect the *'Thinking, resulting from ductile material behavior using 'Mean stress influence correction factors', which in reality means 'Walking on crutches',* into a direct *'Thinking* with *fracture modes facing a realistic brittle material behavior*'.
Not fully ductile isotropic materials show an influence of the mean stress on the fatigue strength depending on the (static) strength ratio R^c/R^t and the material type. Mean stresses in the tensile range, $\sigma_m > 0$ MPa, lead to a lower permanently sustainable amplitude, whereas compressive mean stresses $\sigma_m < 0$ MPa increase the permanently sustainable amplitude or in other words.

LL:
** A tensile mean stress lowers the fatigue strength and a compressive mean stress increases the fatigue strength*
** If it is a pretty ductile material one has one mode 'yielding' and if the material is pretty brittle then many 'fracture modes' are to consider*
** Brittle materials like the transversely-isotropic UD material with its five fracture failure modes possess strong mean stress sensitivity, a brittle steel material just 2 modes*
** Whether a material has an endurance fatigue limit is usually open regarding the lack of VHCF tests. The strength at $2{\cdot}10^6$ cycles might be only termed apparent fatigue strength (scheinbare Dauerfestigkeit). However, e.g. CFRP could possess a high fatigue limit.*
** Whether the material's micro-damage driver remains the same from LCF until VHCF is questionable and must be verified in each given design case (continuum micro-damage mechanics is asked here)*
** The 'ductile material behavior thinking' in 'Mean stress influence' is to redirect for brittle materials into a thinking in fracture modes.*

10.2 Mapping Challenge of the decisive Transition Zone in the Haigh diagram [Cun23b]

The course of the test data in the transition zone determines the grade of the mean stress sensitivity. In *Fig.10-1,* at first all essential quantities are illustrated. Further, two Constant Fatigue Life (**CFL**)-curves of a brittle material are displayed, for the envelopes N = 1 and N = 10^7. The pure mode domains are colored and the so-called transition zone is separated by R_{trans} into two influence parts. The course of the R-value in the Haigh diagram is represented by the bold dark blue lines. The CFL curve N = 1 is curved at top because 2 modes act in the case of brittle materials! This is in contrast to uniaxial static loading, depicted by the straight static envelopes, $N \neq N_f$: One micro-damage cycle results from the sum of 2 micro-damage portions, one comes from uploading and one from unloading! For fully ductile materials practically no transition zone between 2 modes exists, because just one single mode reigns, namely 'shear yielding'. Therefore, it is no mean stress effect to correct in this case!

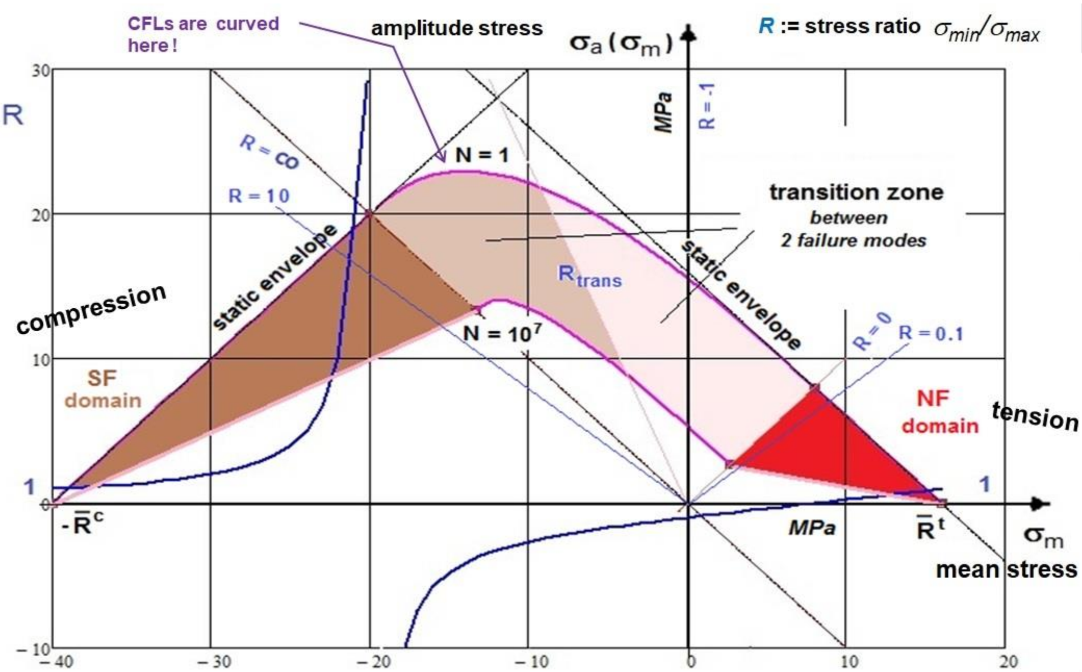

Fig.10-1, Haigh Diagrams: Scheme of pure mode domains, course of R *and transition zone parts .*
(a:= amplitude, m:= mean, N := number of fracture cycles, $\bar{R}$ *:= strength and* R *:=* $\sigma_{min}/\sigma_{max}$

The quality of mapping the course of data in the transition zone is practically checked by "How good is the more or less steep course along the stress ratio R_{trans}-line mapped?" This is performed by following the physical reality, that the pure SF-domain is fully decoupled from the NF-domain, and employing oppositely running decay functions $f_{d,}$ see *Fig. 10-2*.

$$Eff \;\; = [(Eff^{NF})^m + (Eff^{SF})^m]^{m^{-1}} = \; 100\% \quad \text{or}$$

$$\left(\frac{-(\sigma_{2m} - \sigma_{2a}) + |\sigma_{2m} - \sigma_{2a}|)}{2 \cdot \bar{R}_{\perp}^{\,c} \cdot f_d}\right)^m + \left(\frac{\sigma_{2m} + \sigma_{2a} + |\sigma_{2m} + \sigma_{2a}|)}{2 \cdot \bar{R}_{\perp}^{\,t} \cdot f_d}\right)^m = 1$$

$$\rightarrow \; f_d \; = \; 1/[1 + \exp(\frac{c_1 + \sigma_m}{c_2})] \, .$$

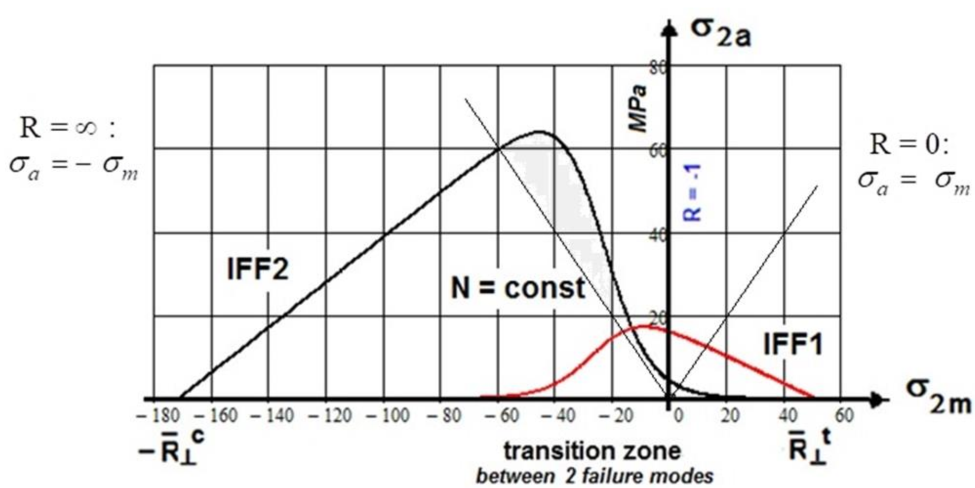

Fig.10-2, example UD material: Course of the decay functions in the transition zone $-\infty < R < 0$

Fig.10-2 illustrates the course of the mode decay functions f_d for the tension and the compression domain. The straight lines in the figure present the extreme SN curve beams, R = ∞ for the SF domain and R = 0 for the NF domain. In between, the envisaged slightly colored transition zone ($-\infty < R < 0$) is located. Mean stress sensitivity of brittle materials is demonstrated very impressively if the so-called 'strength ratio' = compressive strength / tensile strength R^c/R^t is high. The two plots in *Fig.10-3 will* clearly document this.

LL:

- *A large strength ratio R^c/R^t stands for a large mean stress sensitivity*
- *A steep decay cannot be captured by a 'mean stress correction factor' as can be still performed with not fully ductile materials*

10.3 Estimation of the cyclic Micro-damage Portions of Brittle Materials

A very essential question in the estimation of the lifetime of brittle materials is a means to assess the micro-damage portions occurring under cycling. Here, for brittle behavior the response from practice is: It is permitted to apply validated static SFCs due to the experienced fact:

"If the failure mechanism of a mode cyclically remains the same as in the static case, then the fatigue micro-damage-driving failure parameters are the same and the applicability of static SFCs is allowed for quantifying micro-damage portions". This is supported because FMC-based static SFCs apply equivalent stresses of a mode SF or NF. See again Fig.10-2 above.

10.4 Automatic Establishment of Constant Fatigue Life Curves (for details , see [Cun23b]

For a decade the author's intensive concern was to automatically generate Constant Fatigue Life curves on basis of just a few tested Master SN curves coupled to an appropriate physically based model. Such a model the author obtained when M. Kawai gave a presentation during the author's

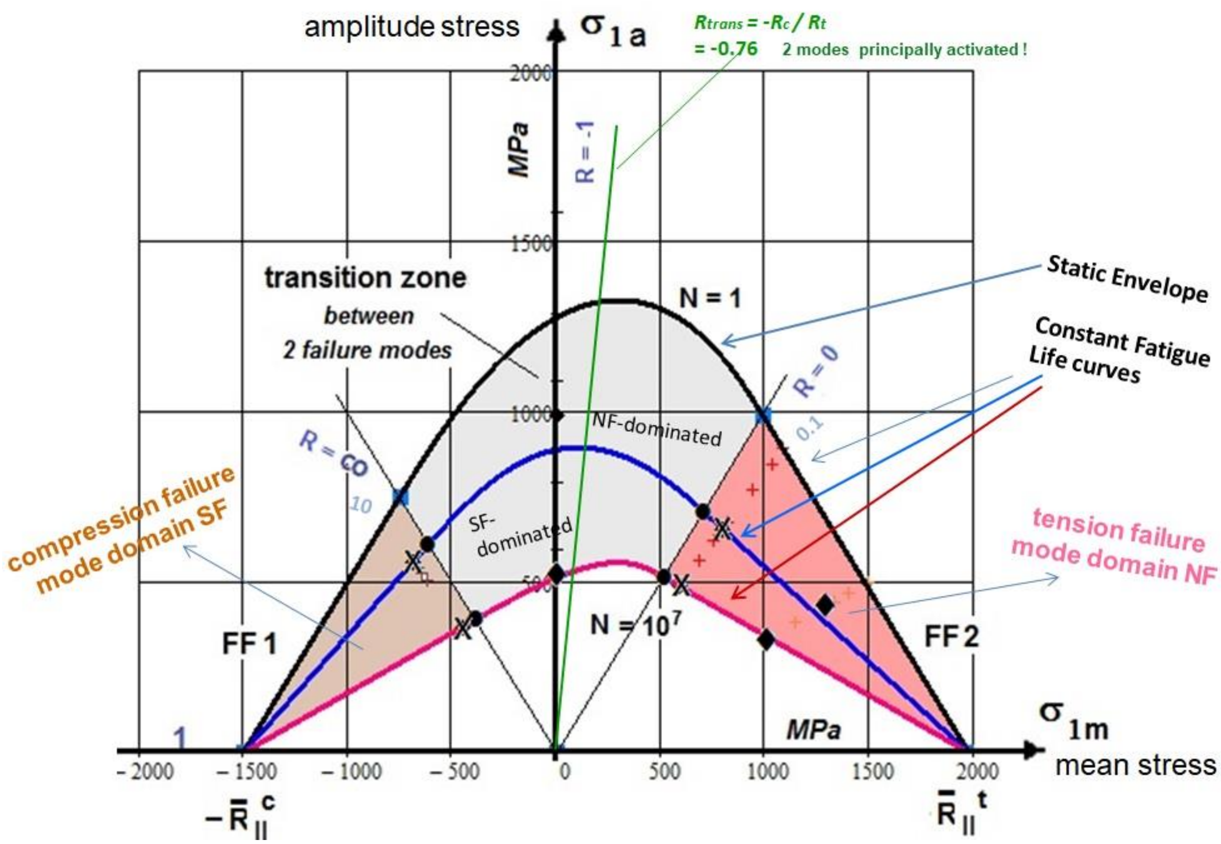

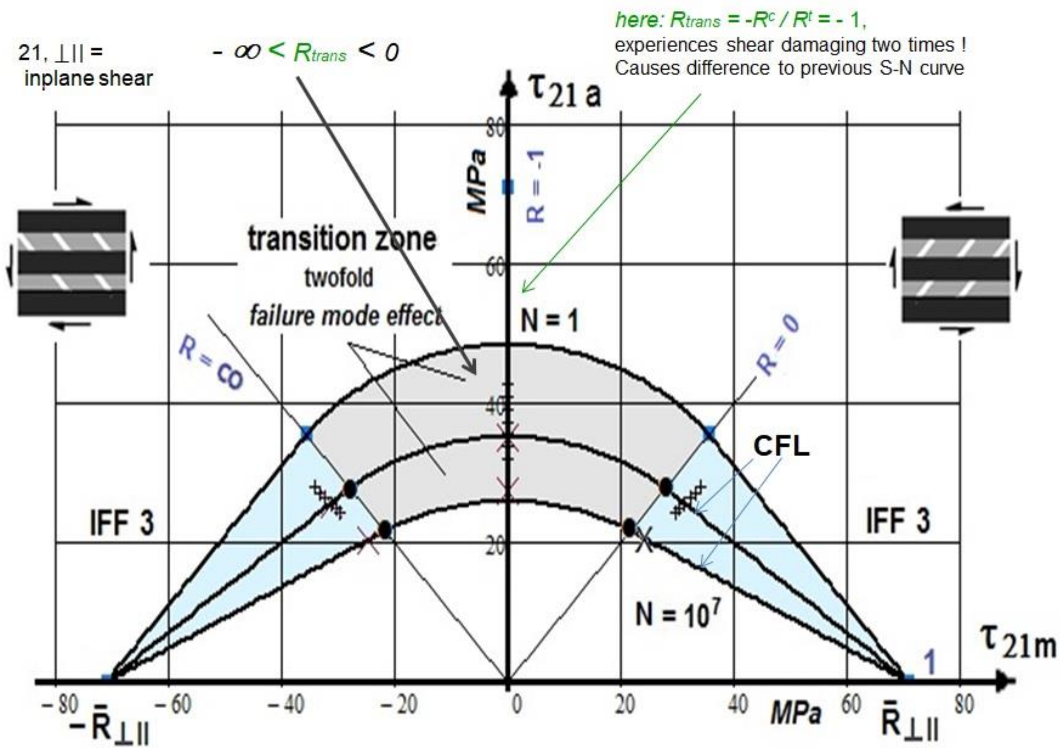

Fig.10-3, UD Haigh diagram: (up) FF with low strength ratio as with ductile materials. Rigorous Interpretation of the Haigh diagram for the UD-example FF1-FF2 displaying failure mode domains and transition zone [16], CFRP/EP, $\bar{R}_{\parallel}^{t} = 1980,\ \bar{R}_{\parallel}^{c} = 1500,\ \bar{R}_{\perp}^{t} = 51,\ \bar{R}_{\perp}^{c} = 172,\ \bar{R}_{\perp\parallel} = 71\ \text{[MPa]}.$

(down) IFF with high strength ratio as with brittle materials Display of a two-fold mode effect (a:= amplitude, m:= mean, N := number of fracture cycles, $\bar{R}$ *:= strength and* R *:=* $\sigma_{min}/\sigma_{max}$*). Test data CF/EP, courtesy Clemens Hahne, AUDI*

conference on composite fatigue in 2010 at CU Augsburg. Kawai's so-called '*Modified fatigue strength ratio'* Ψ - model was the fruitful tool found. Kawai's presented procedure was a novelty and is applicable to brittle materials such like UD plies (*depicted later in Fig.10-4*) and isotropic concrete material as well.

Fig.10-3 (left) displays the differently-colored failure mode domains FF1-FF2 in a UD FF Haigh diagram and (*right*) IFF1-IFF2 in a UD IFF Haigh diagram. The available test data set along R_{trans} in the transition zone is represented by the crosses.

The decay model quality in *Fig.10-3(right)* proves the efficiency of the decay functions in the transition zone. For proving this the author is very thankful because this was only possible because he got access to the test results of C. Hahne, AUDI.

In *Fig.10-4* the course of the cyclic failure test data can be well mapped by the 4-paramater Weibull formula $\text{R} = \text{constant}: \quad \sigma_{\max}(\text{R}, N) = c_1 + (c_2 - c_1) / \exp(\log N / c_3)^{c4}$.

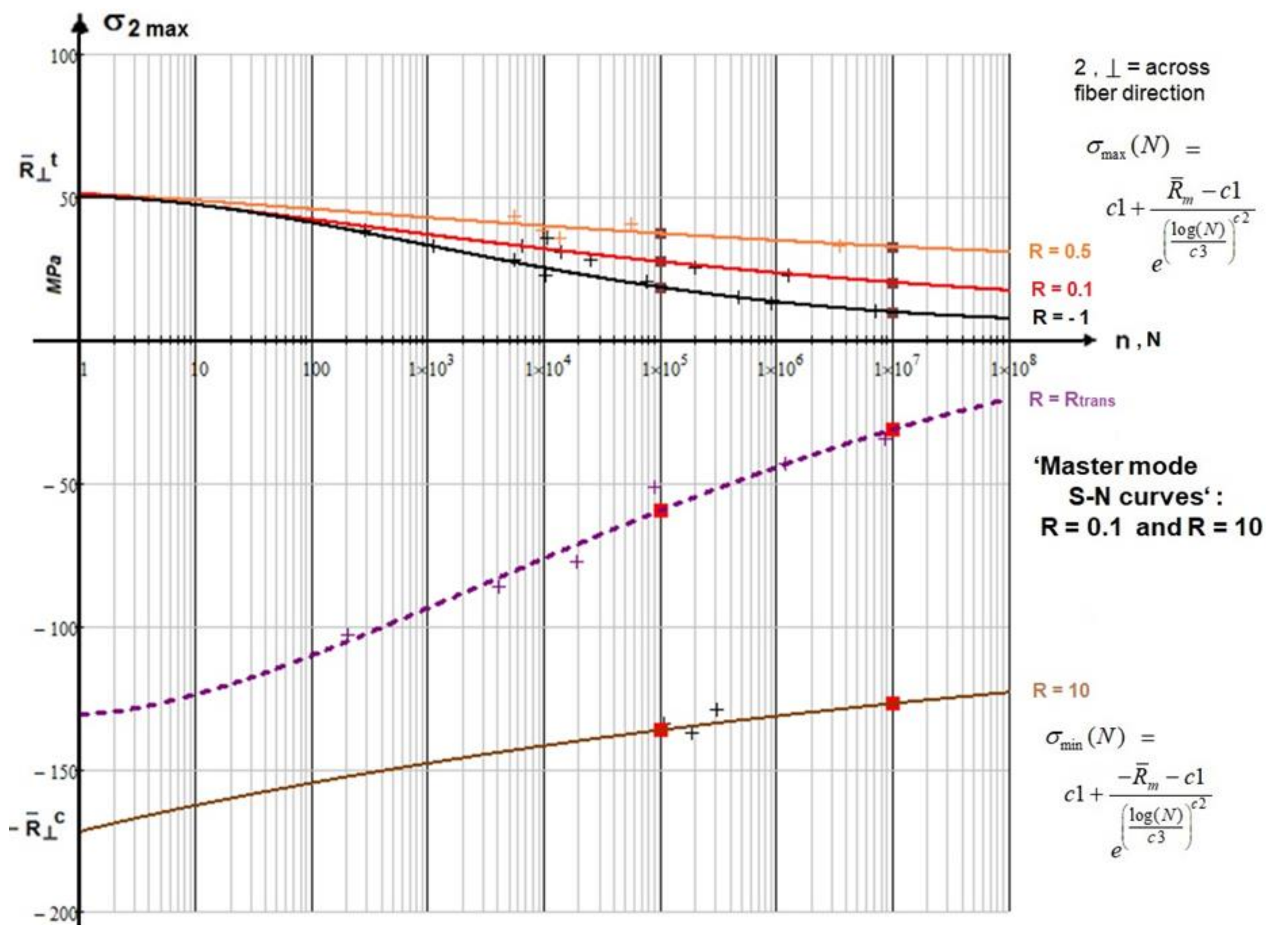

Fig.10-4: SN-curve, lin-log displayed IFF1-IFF2-linked SN curves [test data, courtesy C. Hahne, AUDI] [Kawai M: A phenomenological model for off-axis fatigue behavior of uni-directional polymer matrix composites under different stress ratios. Composites Part A 35 (2004), 955-963]

10.4 Lifetime Estimation

The so-called Palmgren-Miner rule is applied for summing up the cyclic micro-damage portions. Statistical analyses in the German aeronautical handbook HSB have shown that the fatigue life estimation using the linear accumulation method of Palmgren-Miner tends to be too optimistic. However a satisfactory reason with correction could not yet found:

- One explanation is the 'Right use of the right SFC: Mises is not anymore fully applicable?'
- A more severe second explanation is the loss of the loading sequence, an effect which is different for ductile and brittle materials. This inaccuracy is practically considered in design by the application of the so-called Relative Miner with defining a $D_{feasible}$ and which must be < 100 %.

In the case of variable amplitude loading several SN curves are needed. An example for the computation of the lifetime estimation is displayed by *Fig.10-5*.

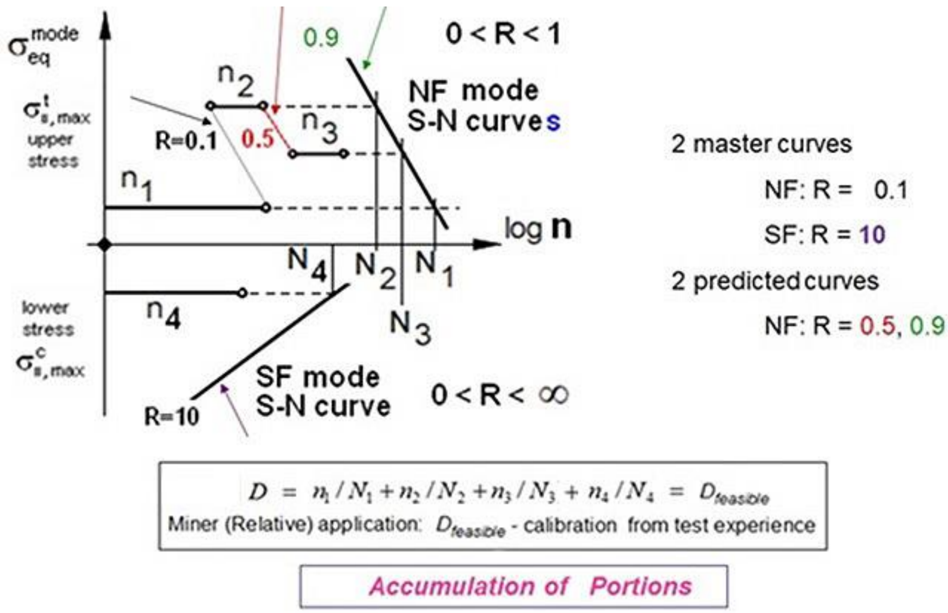

Fig.10-5: Lifetime Prediction (estimation) Method .Summing up of micro-damage portions by application of the Palmgren-Miner rule. Schematic application of a simple example, 4 blocks. D_{feasible} *from test experience*

LL:

* *A 'closed CFL-procedure' - as a coupled method - could be found to generate mandatory test data-based Constant Life Fatigue curves by using a Master SN curve plus the supporting model to determine other required SN-curves employing Kawai's Ψ-model*
* *The challenging decay along* $R_{trans} = -R^c / R^t$ *could be modelled (strength has a bias letter)*
* *Test data along* R_{trans} *are more helpful than for* $R = -1$*, which is standard with ductile behavior*
* *Right use of the right SFC. One cannot blame 'Mises' if yielding is not anymore decisive for the creation of the micro-damage portions*
* *The Palmgren-Miner rule cannot account for loading sequence effects, residual stresses, and for stresses below the fatigue limit (life → ∞ ?)*
* *Viewing brittle materials, all the SN curves have their physical origin in the strength points.*

► *The author would like to recommend: Redirect the traditional 'Thinking, resulting from ductile material behavior regarding Mean stress correction' into a 'Thinking with fracture modes' in the case of the usually not fully ductile structural materials.*

11 Evidencing 120°-symmetrical Failure Bodies of Brittle and Ductile Isotropic Materials

***Aim**: Structural Materials Building, Proof that 'All isotropic materials possess 120° rotational symmetry' with presentation of 3D-SFCs for isotropic, transversely isotropic UD-materials and orthotropic ones.*

11.1 General

From experiments is known, that brittle isotropic materials possess a so-called 120°-axially symmetric fracture failure body in the compressive domain. The question arises: Should ductile materials in the tensile domain not also possess a 120°-axially symmetric yield loci envelope instead of having just the rotationally symmetric 'Mises cylinder'?

According to the French saying " Les extrêmes se touchent" and based on his FMC-thinking the author assumed that there is a large similarity in the description of the behavior of very ductile and very brittle materials. Also with ductile materials a 120°-rotational symmetry should be found. In order to prove the 120°-rotational symmetry, test results from bi-axially measuring test specimens are necessary, such as a cruciform or a cylinder.

Searched is the description of a complete failure body. This requires that the SFC captures both the positive and the negative I_1-domain. Further, the 120°- rotational symmetry should be mapped by the SFC approach (*use of J_3*), too.

Thereby, brittle and ductile material behaviors are to discriminate:

Brittle: In order to show the difference of brittle to ductile materials *Fig. 11-1* outlines the brittle material with its features $\bar{R}^{tt} < \bar{R}^{t}$ and $\bar{R}^{cc} > \bar{R}^{c}$. (*Probably not considering the natural flaws in concrete, in [Lem08] was published $\bar{R}^{tt} > \bar{R}^{t}$ which is physically not explainable and might be the consequence of the difficult measurement*).

Ductile: Deformation measurements prove that for the same strain value of the growing yield surface it holds that equi-biaxial stress $\bar{\sigma}^{tt}(2D) > \bar{\sigma}^{t}(1D)$. This is similar to brittle concrete in the compressive domain where $\bar{R}^{cc} > \bar{R}^{c}$ and demonstrates the validity of the 120°-axial symmetry here, too.

Note*:*

Brittle: bi-axial tension = 'weakest link failure behavior (schwächstes Glied'-Versagen)
Brittle: bi-axial compression = redundant (benign) failure behavior (Stützwirkung)
Ductile: bi-axial compression = redundant (benign) failure behavior (Stützwirkung).

11.2 Brittle Isotropic Materials (Metals, Glass, Ceramics, Concrete, Soil, ..)

2 modes → 2 SFCs, which is in line with the 'generic' number 2 according to the FMC.

3D-SFCs of Isotropic Dense Materials

* Normal Fracture NF for $I_1 > 0$ ⇐ SFCs ⇒ Shear Fracture SF for $I_1 < 0$

$$F^{NF} = c_\Theta^{NF} \cdot \frac{\sqrt{4J_2 \cdot \Theta^{NF} - I_1^2/3} + I_1}{2 \cdot \bar{R}^t} = 1 \quad \leftrightarrow \quad F^{SF} = c_\Theta^{SF} \cdot \frac{\sqrt{4J_2 \cdot \Theta^{SF} - I_1^2/3} + I_1}{2 \cdot \bar{R}^c} = 1$$

after inserting $\sigma = R \cdot Eff$ and dissolving for Eff follows

$$Eff^{NF} = c_\Theta^{NF} \cdot \frac{\sqrt{4J_2 \cdot \Theta^{NF} - I_1^2/3} + I_1}{2 \cdot \bar{R}^t} = \frac{\sigma_{eq}^{NF}}{\bar{R}^t} \leftrightarrow Eff^{SF} = c_\Theta^{SF} \cdot \frac{\sqrt{4J_2 \cdot \Theta^{SF} - I_1^2/3} + I_1}{2 \cdot \bar{R}^c} = \frac{\sigma_{eq}^{SF}}{\bar{R}^c}.$$

The formulation of F^{NF} generates a straight line in the principal stress plane!

3D-SFCs of Isotropic Porous Materials with model parameter determination

* Normal Fracture NF for $\mathrm{I}_1 > 0$ $\Leftarrow$ SFCs $\Rightarrow$ Crushing Fracture CrF for $\mathrm{I}_1 < 0$

$$F^{NF} = c_{\Theta}^{NF} \cdot \frac{\sqrt{4J_2 \cdot \Theta^{NF} - I_1^2/3} + I_1}{2 \cdot \bar{R}^t} = 1 \quad \leftrightarrow \quad F^{CrF} = c_{\Theta}^{CrF} \cdot \frac{\sqrt{4J_2 \cdot \Theta^{CrF} - I_1^2/3} + I_1}{2 \cdot \bar{R}^c} = 1$$

after inserting $\sigma = R \cdot Eff$ and dissolving for Eff follows

$$Eff^{NF} = c_{\Theta}^{NF} \cdot \frac{\sqrt{4J_2 \cdot \Theta^{NF} - I_1^2/3} + I_1}{2 \cdot \bar{R}^t} = \frac{\sigma_{eq}^{NF}}{\bar{R}^t} \leftrightarrow Eff^{CrF} = c_{\Theta}^{CrF} \cdot \frac{\sqrt{4J_2 \cdot \Theta^{CrF} - I_1^2/3} + I_1}{2 \cdot \bar{R}^c} = \frac{\sigma_{eq}^{CrF}}{\bar{R}^c}.$$

with $I_1 = (\sigma_I + \sigma_{II} + \sigma_{III}) = f(\sigma)$, $6J_2 = (\sigma_I - \sigma_{II})^2 + (\sigma_{II} - \sigma_{III})^2 + (\sigma_{III} - \sigma_I)^2 = f(\tau)$

$$27J_3 = (2\sigma_I - \sigma_{II} - \sigma_{III}) \cdot (2\sigma_{II} - \sigma_I - \sigma_{III}) \cdot (2\sigma_{III} - \sigma_I - \sigma_{II}).$$

If a failure body is rotationally symmetric, then $\Theta = 1$ like for the neutral or shear meridian, respectively . A 2-fold acting mode makes the rotationally symmetric fracture body 120°-symmetric and is modelled by using the invariant J_3 and Θ as non-circularity function with d as non-circularity parameter

$$\Theta^{NF} = \sqrt[3]{1 + d^{NF} \cdot \sin(3\vartheta)} = \sqrt[3]{1 + d^{NF} \cdot 1.5 \cdot \sqrt{3} \cdot J_3 \cdot J_2^{-1.5}} \quad \leftrightarrow \quad \Theta^{CrF} = \sqrt[3]{1 + d^{CrF} \cdot 1.5 \cdot \sqrt{3} \cdot J_3 \cdot J_2^{-1.5}}$$

Lode angle ϑ , here set as $\sin(3 \cdot \vartheta)$ with 'neutral' (shear meridian) angle $\vartheta = 0°$ ($\rightarrow \Theta = 1, d = 0$) ;

tensile meridian angle 30° $\rightarrow \Theta^{NF} = \sqrt[3]{1 + d^{NF} \cdot (+1)}$; compr. mer. angle -30° $\rightarrow \Theta^{CrF} = \sqrt[3]{1 + d^{CrF} \cdot (-1)}$.

Mode interaction $\rightarrow$ Equation of the fracture body: $Eff = [(Eff^{NF})^m + (Eff^{CrF})^m]^{m^{-1}} = 1 = 100\%$

$$Eff = \sqrt[m]{(c_{1\Theta}^{NF} \cdot \frac{\sqrt{4J_2 \cdot \Theta^{NF} - I_1^2/3} + I_1}{2 \cdot \bar{R}^t})^m + (c_{\Theta}^{CrF} \cdot \frac{\sqrt{4J_2 \cdot \Theta^{CrF} - I_1^2/3} + I_1}{2 \cdot \bar{R}^c})^m} = 1.$$

* 120°-rotat. symmetric $\Theta \neq 1$:

$c_{\Theta}^{NF} \rightarrow c^{NF} = 1$ ($\Theta^{NF} = 1$ in practice chosen).

c_{Θ}^{NF}, d^{NF} from the 2 points $(\bar{R}^t, 0, 0) \rightarrow c_{\Theta}^{NF}$ and $(\bar{R}^{tt}, \bar{R}^{tt}, 0) \rightarrow d^{NF}$ or min.error fit of data course

$c_{\Theta}^{CrF}, d^{CrF}$ from the 2 points $(-\bar{R}^c, 0, 0) \rightarrow c_{\Theta}^{CrF}$ and $(-\bar{R}^{cc}, -\bar{R}^{cc}, 0) \rightarrow d^{CrF}$.

The failure surface is closed at both the ends! A paraboloid serves as closing cap and bottom

$$\frac{I_1}{\sqrt{3} \cdot \bar{R}^t} = s^{cap} \cdot (\frac{\sqrt{2J_2 \cdot \Theta^{NF}}}{\bar{R}^t})^2 + \frac{\max I_1}{\sqrt{3} \cdot \bar{R}^t} \quad , \quad \frac{I_1}{\sqrt{3} \cdot \bar{R}^t} = s^{bot} \cdot (\frac{\sqrt{2J_2 \cdot \Theta^{CrF}}}{\bar{R}^t})^2 + \frac{\min I_1}{\sqrt{3} \cdot \bar{R}^t}$$

Slope parameters s are determined connecting the respective hydrostatic strength point with the associated point on the tensile and compressive meridian, max I_1 must be assessed whereas min I_1 can be measured. $\bar{R}^t$ works as normalization strength. [*CUN*22,§5]).

[Lem08] Lemnitzer L, Eckfeld L, Lindorf A and Curbach M (IfM TU Dresden): *Bi-axial tensile strength of concrete – Answers from statistics*. In: Walraven, J. C.; Stoelhorst, D. (Hrsg.): Tailor made concrete structures. New solutions for our society. Amsterdam, The Netherlands: CRC Press / Balkema, 2008, S. 1101-1102

In order to illustrate the various SFCs a 3D-concrete Fracture Body is presented: (more pictures of such fracture bodies are found in [*CUN22*]).

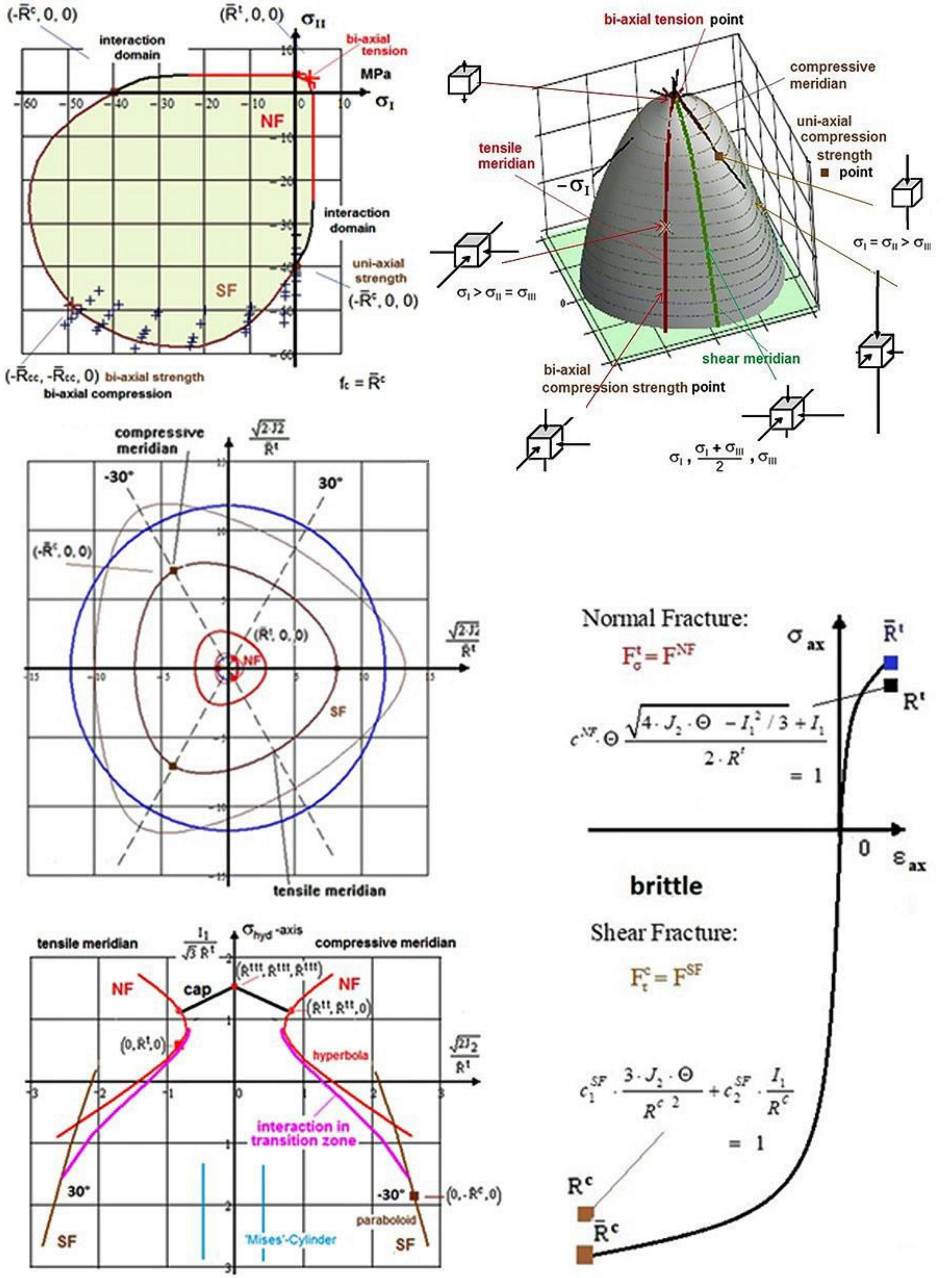

Fig.11-1: Visualization of the behavior of a brittle material (Normal Concrete) considering 1D stress-strain curve with 2D- and 3D-fracture failure curves and fracture body (surface). 120°-rotationally-symmetric

11.5 Ductile Materials, Metal

In *Fig.11-2(left)*, the failure body is presented with its meridians as axial lines. The center figure fully proves the general isotropic 120°-material rotational symmetry which is supported by the Mises ellipse being the *inclined cross-section of the Mises cylinder failure body* is added. The right octahedral figure shows the inner green curve with the Mises circle at the 'Onset-of-yielding' and the outer one at tensile strength R^t.

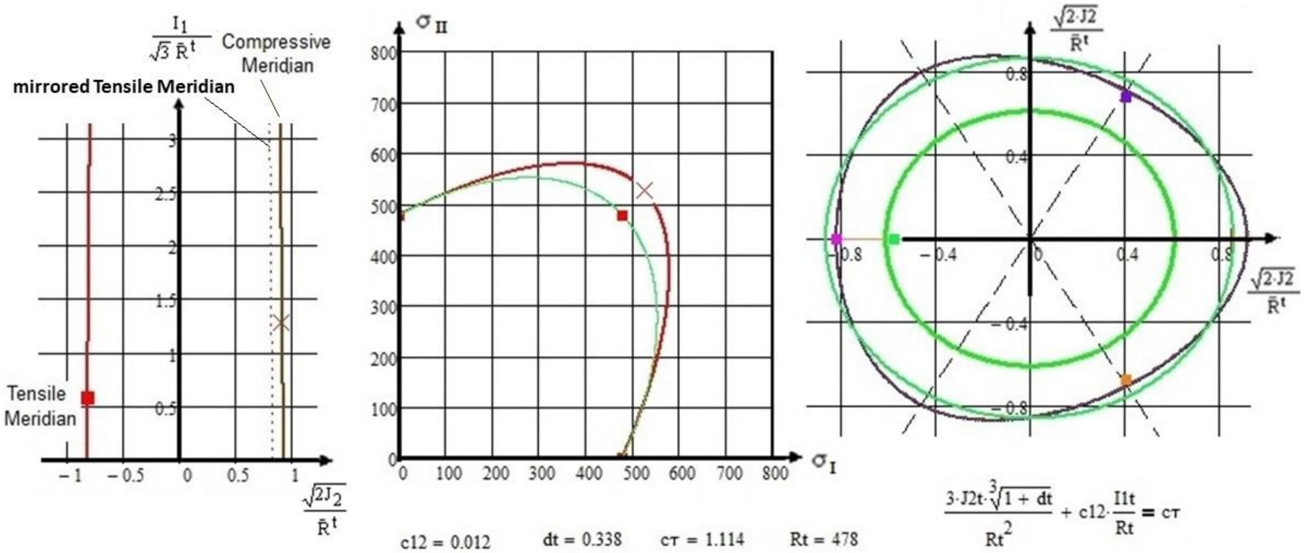

Fig.11-2, isotropic steel AA5182-0: Visualization of the behavior of a ductile material. (left) Yield body in Haigh-Lode-Wintergaard coordinates; (center) 120°-symmetry, visualized in the principal stress plane; (right) 120°-symmetry, visualized in the octahedral stress plane

The 120°-rotational symmetry can be best displayed in the octahedral stress plane which is a 'horizontal' cross-section of the failure body at a distinct I_1, *Fig.11-2(right)*. The points and curves on the spatial body (*left figure*) are projected onto the octahedral plane (*right figure*). Since they depend on I_1, they have different cross-section heights I_1, such as the uniaxial tensile strength point which is located higher than the equi-biaxial strength point x.

In the center figure, Mises is the green curve; red square: the tensile strength point; cross: the equi-biaxial tensile strength point ductile (trueR^{tt}, trueR^{tt}, 0), i. e. the cross x. In the case of ductile metals it can be assumed $R^{tt} \cong 1.1 \cdot R^t$.

An elaboration of four materials with the Mathcad calculation program leads to the *Fig.11-3* below: *Fig.11-3(left)* presents curves through the uniaxial tensile strength points and the equi-biaxial strength R^{tt}. The curves are inclined cross-sections of the failure body. *Fig.11-3(right),* for completion, displays the Beltrami potential surface (egg shaped), the 'Mises' cylinder and the three principal axes.

The figure shows extreme curve examples at *true*R^t level in the positive principal stress range. The red curve is occupied by the data of Kuwabara given below in the table, shown within *Fig.11-4*. The metal test data AA 5182-0 are from *[Kuw98] T. Kuwabara et al: Journal of Materials Processing Technology 80–81 (1998) 517–523. Gotoh's biquadratic yield criterion (not given here) was used to map the test data of the cold-rolled low-carbon steel AA 5182-0 sheets.*

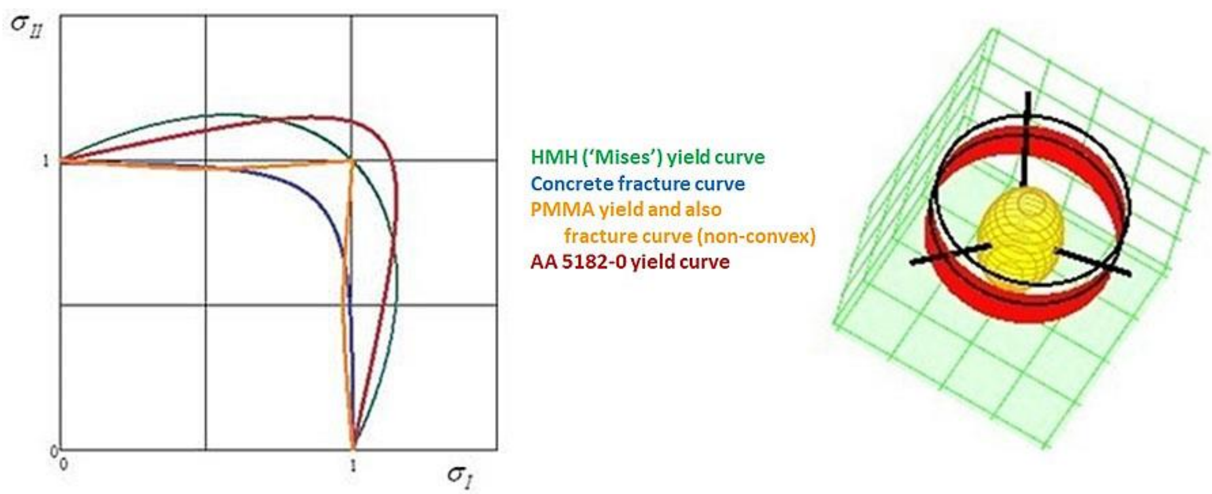

Fig.11-3: (left) Normalized principal stress plane failure curves of a set of fully different isotropic materials. (right) Failure body surface

Fig.11-4 depicts several failure cross-sections of an isotropic ductile steel demonstrating 120°-rotational symmetry like the brittle isotropic materials such as concrete in the compression domain and other ductile ones in the tensile domain.

For the generation of *Fig.11-4* biaxial tensile tests of cold-rolled low-carbon steel sheet were carried out using flat cruciform specimens with the biaxial loads maintained in fixed proportion. Contours of plastic work (of flow potential) were determined in stress space under the shown strain range.

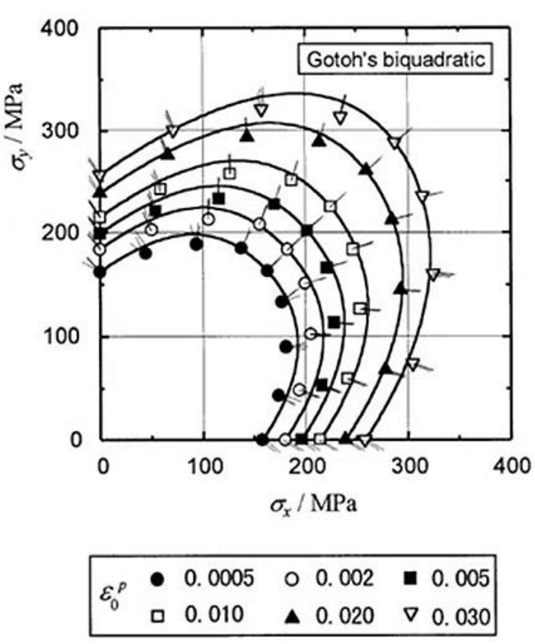

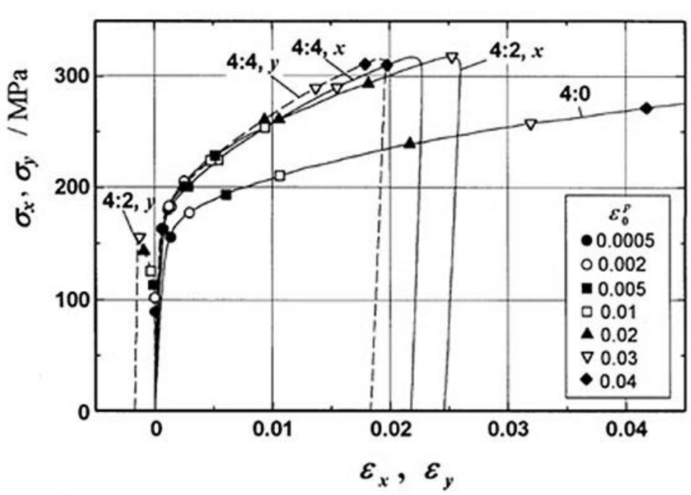

ε_0^p	0.0005	0.002	0.005	0.010	0.020	0.030	0.040
W (MPa)	0.07	0.33	0.89	1.92	4.19	6.68	9.33
σ_0 (MPa)	158	180	196	214	239	258	273
σ_{90} (MPa)	162	184	199	215	238	256	271
σ_{bi} (MPa)	163	184	202	225	260	288	310

Fig.11-4: (left) Test points as function of the experienced plastic straining ε_0^{pl} ; mapping by using Gotoh's bi-quadratic criterion. (right) True stress–true strain curves for different biaxial loadings= different stress ratios. Measured values using r_0, r_{45}, r_{90}. T = 1mm, flat cruciform

LL:

** The author was able to map the course of all the corresponding courses of test data points with his isotropic SFC models.*

** Also for the ductile materials, the 120°-rotational symmetry was demonstrated, see further [CUN22, §5.8].*

** The 120°-rotational symmetry of isotropic materials is nothing else than a 'double mode effect, a two-fold danger'.*

** This effect is faced with all isotropic materials independent whether they are ductile or brittle.*

Reminder to illustrate elastic and plastic behavior:

* Elastic deformation of crystalline structures occurs on the atomic scale: The bonds of the atoms in the crystal lattice are stretched. When de-loading, the energy stored within these bonds can be reversed. The material behaves elastic.
* Plastic deformation or sliding occurs along gliding planes inter-crystalline or intra-crystalline and is permanent (plastic). No volumetric change is faced. 'Mises' applied.

12 Completion of the Strength Mechanics Building

***Aim**: Completion of a material-'generic' number driven Strength Mechanics Building*

In the frame of his material symmetry-driven thoughts the author intended to test-proof some ideas that help to complete the Strength Mechanics Building by finding missing links and by providing engineering-practical strength criteria (SFCs), the parameters of which are directly measurable.

All this supports the assumption of a 'generic' number for the smeared-modelled materials.

The obtained Strength Mechanics Building matured, became clearer and more complete.

LL:

- ✓ *Beside the standard Shear (band) Yielding SY there also exists Normal Yielding NY analogous to the failure modes Shear Fracture SF and Normal Fracture NF* (author assumption proven)
- ✓ *120°-rotational symmetry is inherent to brittle and ductile isotropic materials* (author assumption proven)
- ✓ *Generic number 2, K_{Icr}^{t} with K_{IIcr}^{c} : K_{IIcr}^{c} was theoretically proven for the non-real, ideal case of no flaws in front of crack tip*
- ✓ *Also in consequence of above building: Different but similar behaving materials can be basically treated with the same SFC. Examples are: Concrete ↔ foam, different fabrics.*

Material Symmetry seems to tell:

"In the case of ideally homogeneous materials a generic number is inherent. This is valid for elastic entities, yield modes and fracture modes, for yield strengths R_{02} and fracture strengths R, fracture toughness entities K_{cr} and for the invariants used to generate strength criteria".

This **generic number** is
2 for isotropic and 5 for transversely–isotropic materials,

One might think:

"Mother Nature gives Strength Mechanics a mathematical order ! ?"

13 Safety Concept in Structural Engineering Disciplines

***Aim**: Providing basic knowledge for modeling, in order to pace the required finally necessary design verification of a component.*

Exemplarily, the *designer* of a structure (e.g. aerospace) has to demonstrate to the *operator* (airline) and the *regulator* (airworthiness authority) compliance with the design requirements concerning Structural Integrity of flight hardware components such as: Stiffness, strength, vibration, fracture behaviour as well as to material selection, manufacturing process, hardware tests, inspection methods, quality assurance and documentation. This procedure is principally valid for other disciplines like civil engineering, too.
Structural Integrity of Hardware shall be proved by analyses and verified by tests under mission environmental conditions considering the complete life history of each item.

13.1 General with Mentioning the Old safety Concept

A *Safety Concept* means to implement reliability into the structural component by 'capturing' the uncertainty of the design parameters! It can just provide an unknown safety distance between load ('stress' *S*) and load resistance ('strength' *R*). *FoS* capture uncertainties, small inaccuracies, and simplifications in analyses w.r.t. manufacturing process, tolerances, loadings, material properties (strength, elasticity etc.), structural analysis, geometry, strength failure conditions. *FoS* do not capture missing accuracies in modeling, analysis, test data generation and test data evaluation!

In the *deterministic concepts* or *formats*, respectively, the worst case scenario is usually applied for loadings considering temperature, moisture, undetected damage. Further, a load is to increase by a 'Design *FoS*' and the resistances are to decrease. For the decrease of the strength, statistical distributions are used. If the loading is also based on a statistical distribution, then one speaks about a *semi-probabilistic format*.

Design Development was the basic work of the author in industry. This is why at first the Flow Chart below shall remind of the structural analysis tasks. There are basically four blocks, where – after the material Model Validations - the fulfillment of the Design Requirements has to be demonstrated for obtaining Design Verification as precondition of the final Certification Procedure.

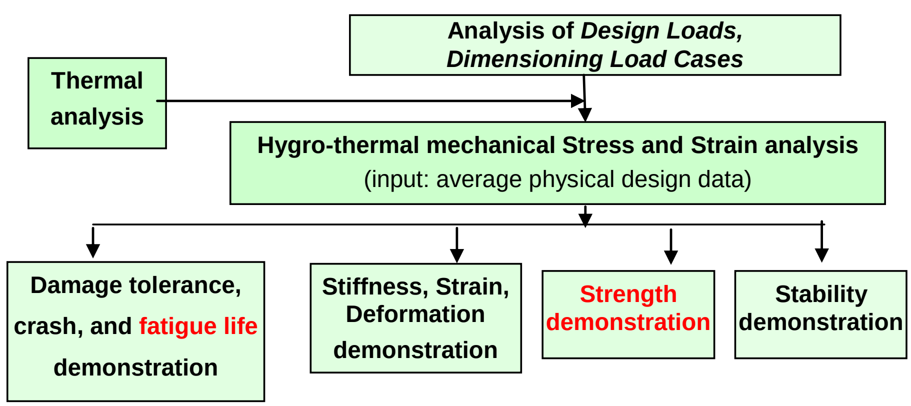

Fig13-1: Structural Design-Analysis Flow Chart

Essential question of engineers in mechanical and in civil engineering is: "*How much could one further increase the loading". Which is the reserve?*

Old Safety Concept of Allowable Stresses:

At least since 1926 the civil engineer M. Mayer questioned the old safety concept, which used allowable stresses, meaning: resistance was reduced by a design safety factor.
This gives no accurate results in the case of non-linear behavior. In construction this was replaced since some decades in DIN 1054 by the Partial Safety Factor concept, which applies design safety factors and combination factors for general service loads, live loads, snow, ice loads, and wind loads. Temperature effects are specified in DIN 1055-100.

Material resistance must be generally demonstrated by a positive Margin of Safety *MoS* or a Reserve Factor *RF* = *MoS* - 1 > 1 in order to achieve Structural Integrity for the envisaged Design Limit State! A *FoS* is given and not to calculate (***as it is too often to read even in FEA code manuals***) like the Margin of Safety *MoS* or the Reserve Factor *RF* = *MoS* + 1.

Fig.13-2 visualizes the stress-strength distribution which outlines that the crossing over will determine the probability of failure p_f. Its value is the area of the p_f-distribution within the overlapping (gusset) of the stress and the strength distribution tails, see for details [CUN22, §16]

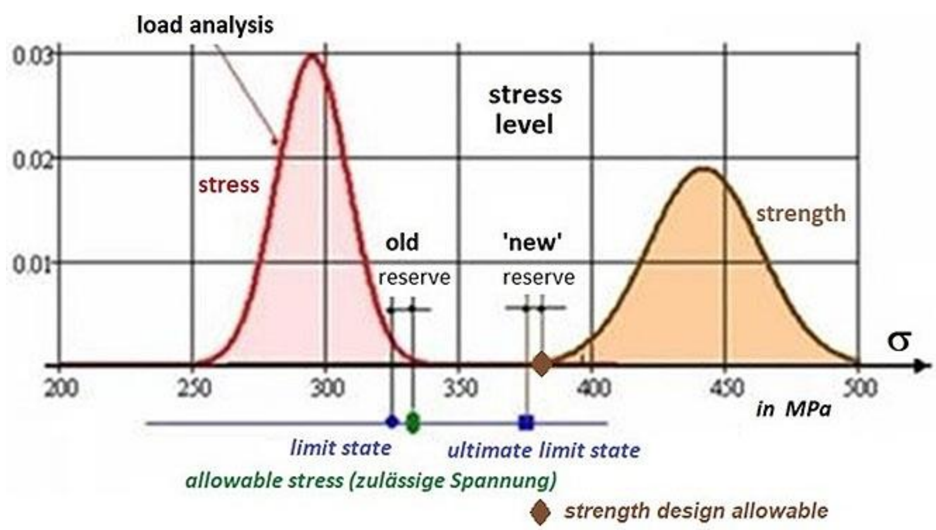

Fig.13-2: Visualization of the present ('new') and the old safety concept

LL:
The citation of the term 'allowable stress' is restricted to the former 'Concept of Allowable Stresses' and shall be not applied within present concepts anymore. Why? The usual application of the abbreviating term 'allowable' instead of 'strength design allowable' may not confuse, but 'allowable stress' is error-prone because the relation below is valid:

j · allowable stress = strength design allowable *!! (see again the figure above)* !

13.2 Global (lumped) Factor of Safety Concept ('deterministic format') on **Loading**

Concept, that deterministically accounts for design uncertainties in a lumped (global) manner by enlarging the 'design limit loads' through multiplication with a design Factor of Safety FoS j.

As still mentioned, FoS are applied to decrease the chance of failure by capturing the uncertainties of all the given variables outside the control of the designer. In the design process the scatter of individual values and parameters is usually treated by using fixed deterministic *FoS*, which act as load increasing multiplying factors *FoS* and should be called, more correctly, *Design FoS*.

Personal Experience:
A safety distance pays off ".

Comodo waran ≈ 80 kg

Presently, in mechanical engineering the loading is increased by one lumped (global) FoS *j*, and in civil engineering the procedure was improved by using several partial Design FoS *γ* for the uncertain stochastic design variables. These *FoS* are based on long term minimum risk experience with structural testing. Depending on the risk consequences different classes of *FoS* are applied, e.g. for manned space-crafts higher *FoS* are used than for unmanned space-crafts.
Present spacecraft safety concept is an *improved global deterministic format (intention: semi-probabilistic)* = 'Simplest' Partial Safety Factor concept: It discriminates load model uncertainties considering factors (K_{Model}, $\boldsymbol{K_{Project}}$) from design uncertainties which are considered by one global FoS *j* !

The to be applied values *j* for the *FoS* are risk or task driven. Facts to consider are:

- As mentioned exemplarily: Different application in cases of manned, un-manned spacecraft
- Design verification by 'Analysis only' (*by the way this is the usual case in construction*)
- Different risk acceptance attitude of the various industries.
  Example: $DUL = j_{ult} \cdot \text{design limit load } DLL$

Mind: The virtual design value must be written DUL, because is the real test fracture load.

<u>Different loading (action) FoS in aircraft and space engineering:</u>

The first task in aerospace industry is load analysis. In any load analysis there are to establish all load events the structure is likely to experience in later application. This includes as well the estimation of loadings induced by the hygro-thermal, the mechanical *(static, cyclic and impact)* and the acoustical environment of the structure as further the corresponding lifetime requirements (*duration*, *number of cycles*), specified by an authority or a standard.
Then, the so-called Design Limit Load values are determined, usually derived from mission simulations utilizing the so-called mathematical models of the full structure (*dynamical analyses, at first on basis of the preliminary design*).

When preparing the HSB sheet [*Cun12*] the author sorted out, that there practically is no different risk view between air-craft and space-craft:

* Spacecraft: using a *d*ynamic *L*imit *L*oad model obtaining a basic load prediction *dLL* considering a load model uncertainty considering factor j_{LM} =1.2. This delivers a Design Limit Load DLL= 1.2 ·*dLL*, and from this follows DUL = $dLL \cdot j_{LM} \cdot j_{ult}$, with 1.2 ·1.25 = **1.5** ! The DLL level is applied in spacecraft in fatigue life demonstration.

* Aircraft: Definition of a so-called (design) Limit Load LL delivering DUL = $LL \cdot$**1.5.**

***LL**: The author could conclude after comparing the ESA/ESTEC aerospace Standards* (the author had to work on)*, that the DUL-value is practically the same value in aircraft and in spacecraft !*

The resistance strength and the bearable loads (at joints etc ...):

Dependent on the design requirements the average, the upper or a lower value of the property is used for the various properties. In the case of strength a statistically reduced value R. To achieve a reliable design the so-called Design Allowable has to be applied. It is a value, beyond which at least 99% ("A"-value) or 90% ("B"-value) of the population of values is expected to fall, with a 95% confidence (*on test data achievement*) level, see MIL-HDBK 17. A "B"-value is permitted to use for multi-layered, redundant laminates.

Bearable loads require series tests of the distinctive structural component with statistical evaluation in order to determine the 'load-resistance design allowables'.

Measurement data sets are the result of a Test Agreement (norm or standard), that serve the desire to make a comparability of different test procedure results possible. The Test Agreement consists of test rig, test specification, test specimen and test data evaluation method and the Test Procedure. Therefore, one can only speak about *'exact test results in the frame of the obtained test quality'*. Hence, there are no exact property values.
Test specimens shall be manufactured like the structure ('as-built').

Considering property input: When applying test data from 'isolated lamina' test specimens (*like tensile coupons*) to an embedded lamina of a laminate one should consider that coupon test deliver tests results of 'weakest link' type. An embedded or even an only one-sided constrained lamina, however, possesses redundant behavior → "B"-values permitted.

Reserve Factor RF and Margin of Safety MoS**:** Formulas:

Linear analysis is sufficient (presumption): $\sigma \sim$ load $\Rightarrow RF \equiv f_{RF} = 1 / Eff$

Material Reserve Factor $$f_{\mathrm{RF},\,ult} = \frac{\text{Strength Design Allowable } R}{\text{Stress at } j_{ult} \cdot \text{Design Limit Load}} > 1,$$

Non-linear analysis required: σ not proportional to load

Reserve Factor (load-defined) $$RF_{ult} = \frac{\text{Predicted Failure Load at } Eff = 100\%}{j_{ult} \cdot \text{Design Limit Load}} > 1.$$

***LL**:*

* *A FoS is given and not to calculate such as a Margin of Safety MoS or the Reserve Factor RF = MoS + 1.*
* *A MoS is usually the result of worst case assumptions that does not take care of the joint actions of the stochastic design parameters and thereby cannot take care of their joint failure action and probability. This failure probability is a 'joint failure probability' because it considers the probability of joint acting*
* *A material with a high coefficient of variation CoV disqualifies itself, when computing the statistically-based strength design allowable values. Therefore, one must not penalize it further as performed in some standards in the past in the case of new materials.*
* *Both, an increasing mean value and a decreasing standard deviation will lower* p_f
* *The MoS value does not outline a failure probability. Failure probability* p_f *does not dramatically increase if MoS turns slightly negative*

* *A <u>local</u> safety measure of MoS = -1 % is <u>no</u> problem in design <u>development</u> if a 'Think (about) Uncertainties' attitude is developed in order to recognize the main driving design parameters and to reduce the scatter (uncertainty) of them*
* *Nowadays often non-linear analyses are performed, delivering true quantities, however Design Verification is executed with engineering strength values R. Why do we not use in such a case the true tensile strength, but calculate f_{RF} with four numbers accuracy?*
* *Fig.13-3 (left) visualizes strength distribution, Eff versus micro-damage growth and material reserve factor f_{RF}*
* *True-in requires True-out and an assessment by $true\bar{R}^t$. The <u>Fig.13-3 (</u>right) shows for an aluminum alloy a difference between the mean (material model) strength values $eng\bar{R}^t \rightarrow true\bar{R}^t$ of 8%.*

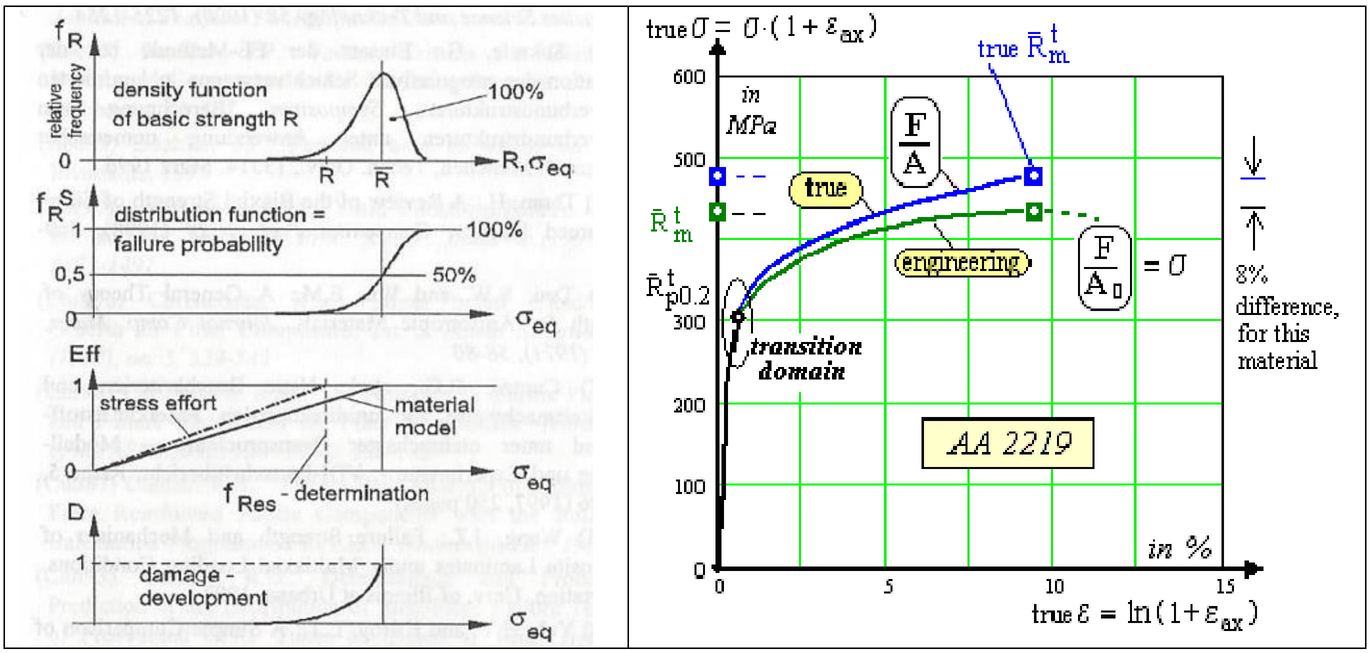

Fig.13-3: (left) Design quantities when approaching failure in Design Verification . (right) Difference engineering and true tensile strength of AA2219

<u>Robust Design Requirements:</u>

The goal of any design engineer should be to end up with a robust design. In order ta o achieve this, the main stochastic design parameters have to be used to outline the robustness of the design against the envisaged actual failure mode by firstly computing the sensitivity measures α and then investigating the reduction of the design's sensitivity to changes of *Xj while* keeping p_f at the prescribed level. This is important for the production tolerances. Probabilistic design may be used as an assessment of the deterministic design or is necessary as design method if a *reliability* target $\Re$ is assigned instead of a *FoS*. or its complement, the probability of failure p_f.

A structural reliability analysis in a Hot Spot reveals the influence of each stochastic design parameter on the distinct failure mode by means of the sensitivity measures. Robust designs (*robust to later changes of the design parameters*) are required with identification of the most sensitive design parameters!

For better illustration of the Safety Concepts from *[CUN22, §12]* the *Fig.13-4* is included. It clearly depicts the definition of the failure probability in this two-parameter case.

Design advantages found with the Ariane Booster design, when using a probabilistic tool:

Two advantageous applications of the probabilistic tool shall be shortly demonstrated where probabilistic modelling and computation were successfully applied:

* A reduced production tolerance width leads to a reduced mass which sequentially reduced further fuel mass savings. Improved production reduced the wall thickness tolerance from 8.2 +- 0.20 mm to 8.2 +- 0.05 mm. Keeping the same given reliability value $\Re = 1 - p_f = 1 - 5 \cdot 10^{-6}$ the nominal wall thickness could be set → 8.1 +- 0.05 mm leading to mass and fuel savings.
  (*As early as 1985 for our pre-design of the Ariane 5 launcher so-called target survival probabilities* $\Re$ *were fixed for the several structural parts*!)

* Probabilistic modelling of the geometrical tolerances of bore hole, pin, position (pitch) and strength minimum restrains with minimum residual stresses could be achieved, for the pin connection an optimum number of pins of 130 pins for a simpler assembly process and for reduced mounting stresses.

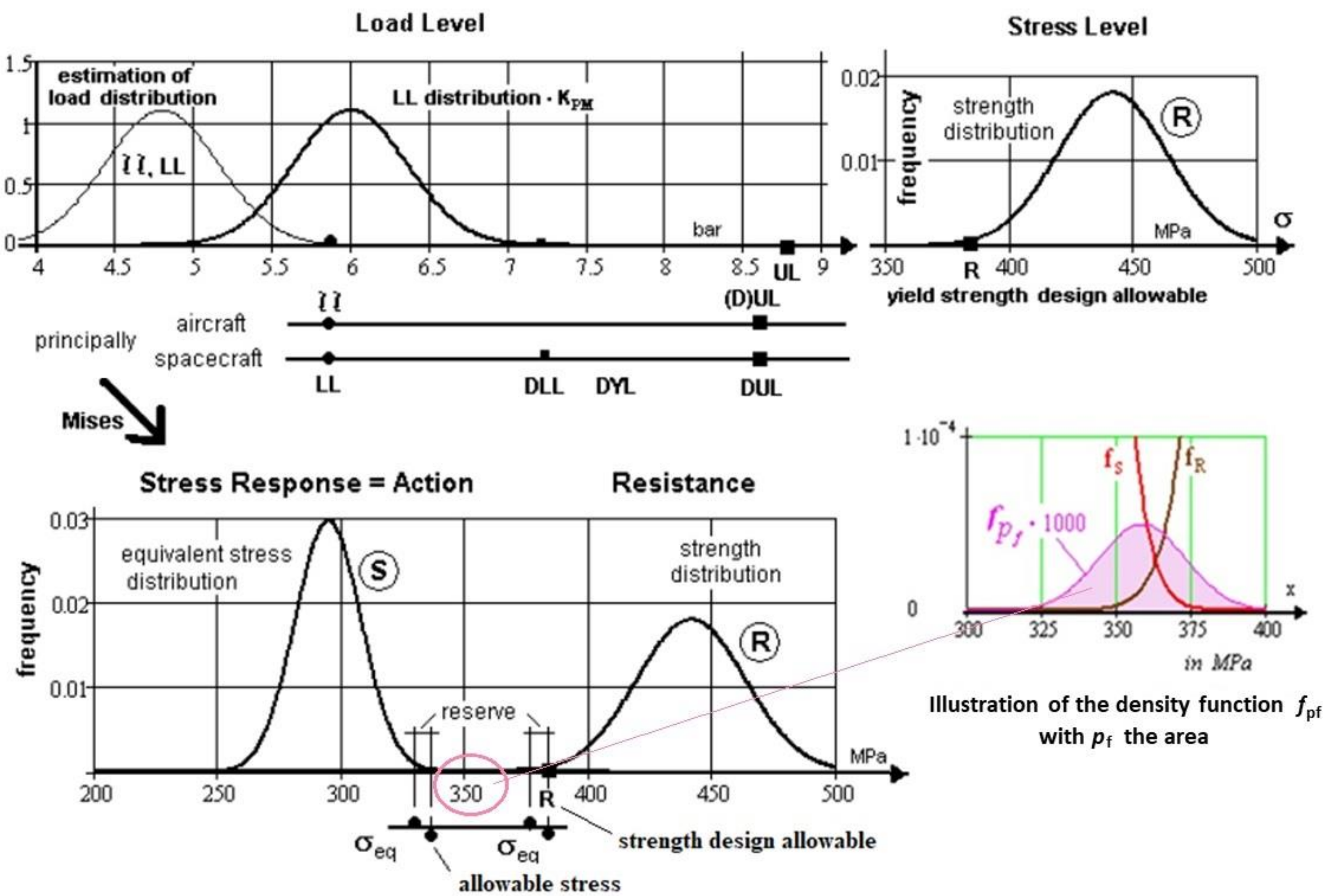

Fig.13-4: Visualization of the difference of the aerospace load terms used in the Strength Design Allowable Safety Concept and of the 'hopefully forgotten' Allowable Stress Safety Concept

Fig.13-5 presents a numerical example how the reserve factor *RF* is to compute.

Asssumption: Linear analysis permitted, design FoS $j_{\text{ult}} = 1.25$

* Design loading (action): $\{\sigma\}_{\text{design}} = \{\sigma\} \cdot j_{\text{ult}}$

* 2D-stress state: $\{\sigma\}_{\text{design}} = (\sigma_1, \sigma_2, \sigma_3, \tau_{23}, \tau_{31}, \tau_{21})^T \cdot j_{\text{ult}} = (0,\ -76,\ 0,\ 0,\ 0,\ 52)^T \text{MPa}$

* Residual stresses: $0\ \left(\textit{effect vanishes with increasing micro-cracking}\right)$

* Strengths (resistance) : $\{\bar{R}\} = (1378,\ 950,\ 40,\ 125,\ 97)^T \text{MPa}$ average from mesurement

statistically reduced $\{R\} = (R_{\parallel}^t, R_{\parallel}^c, R_{\perp}^t, R_{\perp}^c, R_{\perp\parallel})^T = (1050,\ 725,\ 32,\ 112,\ 79)^T \text{MPa}$

* Friction value(s) : $\mu_{\perp\parallel} = 0.3,\ (\mu_{\perp\perp} = 0.35)$, Mode interaction exponent: $m = 2.7$

$$\left\{Eff^{\text{mode}}\right\} = \left(Eff^{\parallel\sigma},\ Eff^{\parallel\tau},\ Eff^{\perp\sigma},\ Eff^{\perp\tau},\ Eff^{\perp\parallel}\right)^T = \left(0.88,\ 0,\ 0,\ 0.21,\ 0.20\right)^T$$

$$Eff^{m} = (Eff^{\parallel\sigma})^m + (Eff^{\parallel\tau})^m + (Eff^{\perp\sigma})^m + (Eff^{\perp\tau})^m + (Eff^{\perp\parallel})^m = 100\% \ .$$

The results above deliver the following material reserve factor $f_{\text{RF}} = 1/Eff$

* $Eff^{\perp\sigma} = \dfrac{\sigma_2 + |\sigma_2|}{2 \cdot \bar{R}_{\perp}^t} = 0, \quad Eff^{\perp\tau} = \dfrac{-\sigma_2 + |\sigma_2|}{2 \cdot \bar{R}_{\perp}^c} = 0.60, \quad Eff^{\perp\parallel} = \dfrac{|\tau_{21}|}{\bar{R}_{\perp\parallel} - \mu_{\perp\parallel} \cdot \sigma_2} = 0.55$

$$Eff = [(Eff^{\perp\sigma})^m + (Eff^{\perp\tau})^m + (Eff^{\perp\parallel})^m]^{1/m} = 0.80.$$

$\Rightarrow \quad f_{\text{RF}} = 1/Eff = 1.25 \rightarrow \text{RF} = f_{\text{RF}}$ (if linearity permitted) $\rightarrow \text{MoS} = RF - 1 = 0.25 > 0$!

Fig.13-5: Computation of a Reserve Factor RF

14 Nonlinear Stress-Strain relationships, Beltrami Theory with Change of Poisson's Ratio ν

Aim: *Provision of a Basis to generate an 'Extended Mises' model as a simplified 'Gurson' model.*

14.0 General on Stress-Strain curves σ(ε), Strengths R and Poisson's Ratio ν

There are two different stress-strain curves existing: the *monotonic* and the *cyclic stress-strain curve*. The first curve is derived by the static tests, whereas the second one is generated by fatigue tests. Strain-controlled cyclic hysteresis loops (*Fig.14-1, left down*) are performed on different strain levels with several test specimens. Dependent on hardening and softening behavior of the actual material these two curves may discriminate significantly. Monotonic stress-strain curves have long been used to obtain design parameters for limitation of the stresses in engineering structures subjected to static loading. Similarly, cyclic stress-strain curves are useful for assessing the durability of structures subjected to repeated loading.

Further, in the case of monotonic σ-ε-curves there are very different, material-specific stress-strain curves in the elastic-plastic transition domain, see *Fig.14-1, left up* and *right*. Some show an 'Onset-of-yield' at an upper yield stress level $\bar{R}_e^{upper}$ and others at a lower yield strength $\bar{R}_e^{upper}$. In this case usually the lower yield point is taken as the yield strength of the metal.

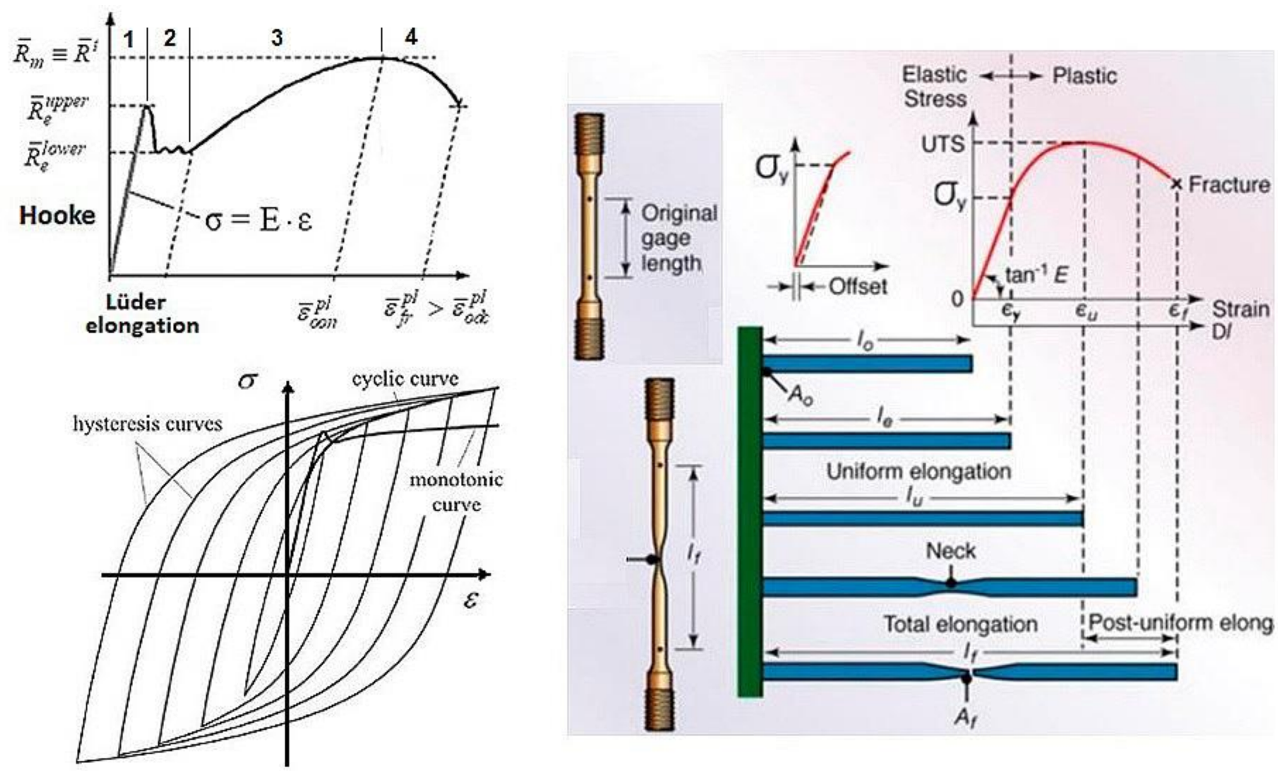

Fig.14-1, engineering quantities. modelling: (left,up) Discontinuous yielding, mean curve for mild steel showing the yield point phenomenon, termed Lüder's elongation effect. (left, down) Cyclic curves. (right) Tensile-test specimen with gage length, elongation before and after testing and finally after rupture (from Kalpakjian S and Schmid S: *Evaluation of the Possibility of Estimating Cyclic Stress-strain Para-meters and Curves from Monotonic Properties of Steels*. Manufacturing Engineering & Technology. 2013

For the 'left up'- metals in the paper of Hai Qiu and Tadanobu Inoue: *Evolution of Poisson's Ratio in the Tension Process of Low-Carbon Hot-Rolled Steel with Discontinuous Yielding*. *Metals* ***2023****, 13, 562.* https://doi.org/10.3390/met13030562 four different regimes are distinguished: Phase 1: Uniform elastic elongation, Phase 2: Discontinuous yielding, Phase 3 beyond R_{02} : Uniform elongation in the

hardening regime, Phase 4 beyond $\overline{R}^t$: Macroscopic plastic-strain localization experiencing radial deformation. Low-alloy iron usually has such an upper yield limit R_e^{upper} (R_{eH}, *Streckgrenze*). If it is stretched during the tensile test, a spontaneous yielding in the crystals-compound takes place under loading. This so-called Lüder's elongation effect of mild metals as a part of plastic stretching disappears until all crystals are finally commonly stretched. Austenitic steels do not have a pronounced yield strength.
Essential for an accurate analysis is a stress-strain curve which is derived from a set of test curves, delivering distributions for the *design parameters* $R_{p0.2}$, R_m, ε_{on}^{pl} *and* ε_{fr}^{pl}.

The yield strength is a material property defined as the stress at which a material begins to deform plastically. If it is not well-defined (*remind Lüder*) on the stress-strain curve, it is difficult to determine a precise onset-of-yield point. In general, discriminating the proportional tensile limit R_{prop} and $R_{p0.2}$ ($\equiv R_{0.2}^t$), the offset yield point is taken as the stress at which 0.2% plastic deformation remains (*in English literature $R_{p0.2}$ is termed proof stress).* The mean stress at Onset-of-Yielding, denoted $\bar{R}_{0.2}$ will be applied for ductile modeling. The stress $\sigma(\varepsilon_{pl})$, considering only the plastic deformation or plastic flow of the material, is termed Flow stress σ_F.

By the way, the actual 'Onset-of-yielding at $R_{prop} \equiv \sigma_{prop}$ can be determined by a temperature measurement. If a metallic material is subjected to tensile stress, it first cools down in the area of elastic elongation analogous to an ideal gas , thermo-elastic effect. With onset of plasticization heat is released, which leads to an increase in temperature. This temperature is measurable with glued thermocouples. In other words: The ***proportionality stress σ_{prop} can be allocated to that applied stress level, where the test specimen experiences a temperature increase due to internal dislocations.***

Regarding not only metals - for a conflict-free understanding – it will be denoted $R_{p0.2}$ ($\rightarrow R_{0.2}^t$) and $R_{c0.2}$ ($\rightarrow R_{0.2}^c$) in the body text from now on. At the maximum of the curve, characterized by the so-called 'End–of–uniform elongation' = 'Onset-of-(ductile) necking' in the ductile material case, the tensile strength R_m ($\rightarrow R^t$) is given. For very ductile materials is valid $R_{0.2}^c \cong R_{0.2}^t$.

Beyond the tensile strength R^t a multiaxial state of stress follows in the tensioned ductile behaving test specimen. Therefore, the index ax holds up to the 'End–of–uniform elongation' (Gleichmaßdehnung) at R^t (*index pl for plastic strain, oon for Onset-of-(ductile) necking, and odc for Onset-of-ductile cracking located before rupture = plastic collapse*).
In this respect, any formulations in this domain afford equivalent quantities in order to perform an accurate non-linear analysis with a correct $\sigma(\varepsilon)$-input.

14.2 Engineering and True Stress and Strain Quantities

The larger the strains the more the engineering quantities lose their applicability in structural dimensioning. Therefore, logarithmic (*usually termed true*) strains have to be used in an accurate dimensioning process. The derivation of these quantities is collected in *Table 14-1*.
Fig.14-2 contains a true and an engineering stress-strain curve. The figure presents a general view and uses classical Ramberg-Osgood mapping. Mapping of the course of stress-strain data in the non-linear domain is well performed by taking the usually applied Ramberg-Osgood equation for the true stress-true strain curve (*maps the true curve better than the engineering curve*)

$$\text{eng}\varepsilon = \varepsilon = \varepsilon^{\text{el}} + \varepsilon^{pl} = \frac{\sigma}{E_0} + 0.002 \cdot \left(\frac{\sigma}{\bar{R}_{0.2}}\right)^{\bar{n}} \quad \text{and} \quad \text{true}\varepsilon = \frac{\text{true}\sigma}{E_0} + 0.002 \cdot \left(\frac{\text{true}\sigma}{\text{true}\bar{R}_{0.2}}\right)^{\text{true}\bar{n}} .$$

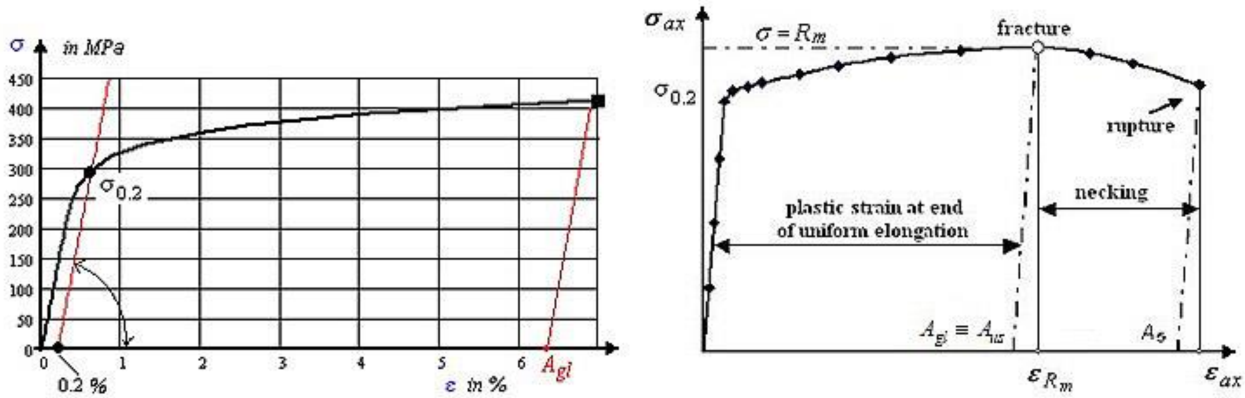

Fig.14-2: R-O mapping of a single engineering measurement test results, $A_{gl} = min\, \varepsilon_{oon}^{pl}$.
Typical (mean) engineering stress-strain curve of a distinct ductile metal material. End of uniform elongation (Gleichmassdehnung ε_{gl} *)*

Table 14-1 presents the derivation of true stresses and true strains in the 'Mises'-validity domain. In *Fig.13-4* the difference between the mean strength values $\text{eng}\bar{R}^t \rightarrow \text{true}\bar{R}^t$ was shown to be 8% for *AA2219! Fig.14-3(left)* depicts the linear elastic proportional domain and the hardening domain. *Fig.14-3(right)* presents stress-strain measurement with Ramberg-Osgood mapping. The course of the area reduction would show a slight kink beginning at 'Onset-of-ductile cracking $_{\text{odc}}$' (= o*nset-of-localized necking*) according to the deteriorating effect of the void coalescence.

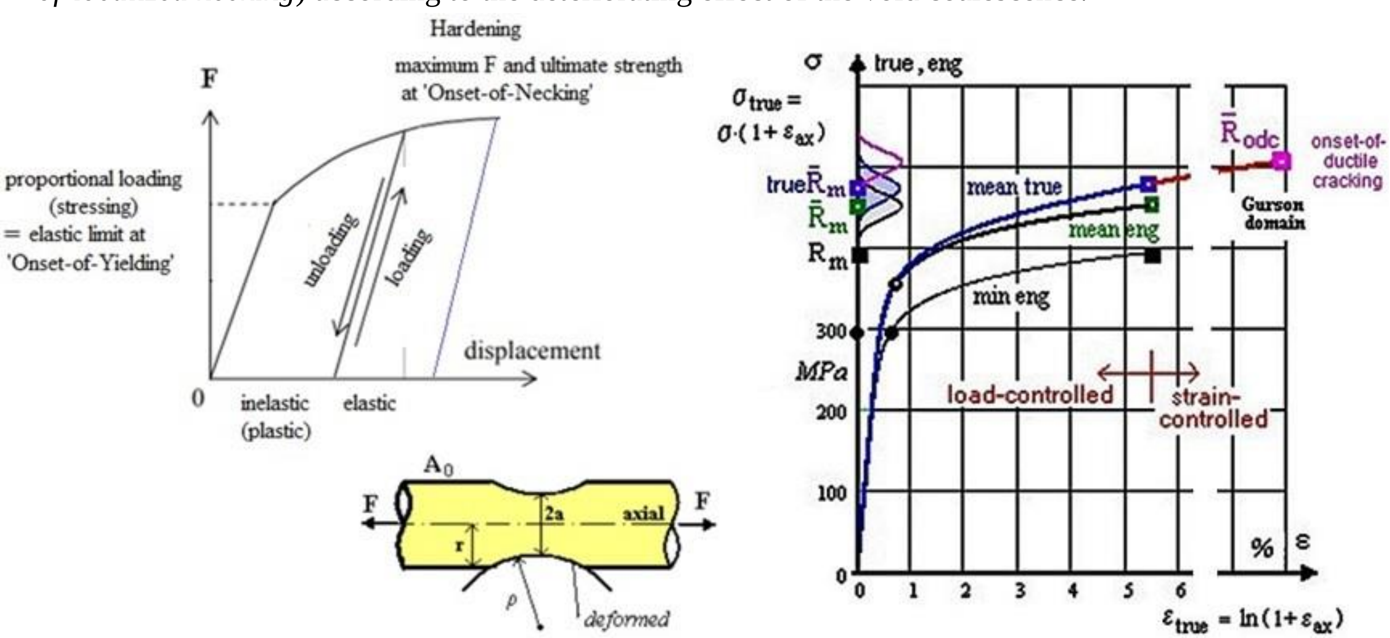

Fig. 14-3, modelling: (left) Display of proportional domain and hardening domain with the tensile rid test specimen. (right) Ramberg-Osgood-mapped true and engineering stress-strain curves of AA2219. F:= Force F_{ax}*,* A_0 *:= original cross-section, A:= actual cross section of the necked rod.* $\bar{R}^t = \max F / A_0$ *,* $\varepsilon \leq \bar{A}_{gl}$
(permanent strain linked to load-controlled fracture at $\bar{R}^t$ *). Necking radius is* ρ*. A bar over* $\bar{R}$ *indicates a mean (average) value of a sufficiently large test data set, and no bar over R will generally mean strength and later indicate a 'strength design allowable'.*

Table 14-1: Derivation of true stresses and true strains in the 'Mises'-validity domain

True Strains (logarithmic strains):

The application of engineering strain cannot be correct for larger strains, since it is based on the original gage length ℓ_0, whereas the length is continuously growing. Ludwik $[Lud09]$ therefore introduced the true strain (logarithmic strain), the increment of which for a given length is defined as $d(true\varepsilon) = d\ell / \ell$ and the total true strain, integrated from ℓ_0 to current length ℓ, is

$$true\varepsilon_{ax} = \int_{\ell_0}^{\ell} d\ell / \ell = ln(\ell / \ell_0) = ln(1 + eng\varepsilon_{ax}) .$$

Above equation delivers an accurate value up to 'onset-of-necking' or $\bar{R}^t$.

The replacement of the logarithmic function by a Taylor series

$$true\varepsilon_{ax} = eng\varepsilon_{ax} - eng\varepsilon_{ax}{}^2 / 2 + eng\varepsilon_{ax}{}^3 / 3 - .. +$$

clearly shows that identity is given for small strains, only. Applying the true strain has a physical and a numerical advantage: The incompressibility equation really becomes zero

$$\sum true\varepsilon_i = true\varepsilon_I + true\varepsilon_{II} + true\varepsilon_{III} = 0,$$

whereas in terms of engineering strains the correct equation from solid geometry reads

$$(1 + eng\varepsilon_I) \cdot (1 + eng\varepsilon_{II}) \cdot (1 + eng\varepsilon_{III}) - 1 = 0,$$

which reduces to 0 for negligible strains, only.

Once necking starts most of the deformation occurs in the smallest cross section. The longer the gage length used the smaller the percent elongation will be. Therefore, a better procedure is the measurement of the reduction of the cross-section. $\rightarrow$ Beyond $\bar{R}^t$, the true σ-ε curve can be more accurately obtained by measuring the radial strain

$$eng\varepsilon_{radial} = (r - r_0) / r_0 = r / r_0 - 1 \quad \text{and} \quad true\varepsilon_{radial} = -ln(1 + eng\varepsilon_{radial}) = -ln(r / r_0),$$

provided, the tensile test specimen has a circular cross-section, a rod. In this case $\varepsilon_{radial} = \varepsilon_{hoop}$

$$true\varepsilon_{ax} + true\varepsilon_{radial} + true\varepsilon_{hoop} = 0 \quad \text{and it holds} \quad true\varepsilon_{ax} = -2true\varepsilon_{radial} = 2\,ln(r / r_0),$$

which delivers an accurate value above 'onset-of-necking'. The equivalent strain in the center reads

$$true\varepsilon_{eq} = \frac{\sqrt{2}}{3} \cdot \sqrt{(true\ \varepsilon_{ax} - true\ \varepsilon_{hoop})^2 + 0 + (true\ \varepsilon_{hoop} - true\ \varepsilon_{ax})^2}$$

$$= \frac{\sqrt{2}}{3} \cdot \sqrt{2(2-(-1))^2} \cdot true\varepsilon_{radial} = \frac{2}{3} \cdot \sqrt{3^2} \cdot true\varepsilon_{radial} = 2\,ln(r / r_0)$$

$\Rightarrow$ Transferring strain data: $true\varepsilon = ln(1 + eng\varepsilon),\ eng\varepsilon = e^{true\ \varepsilon} - 1.$

True Stresses

Trueσ can be obtained from engσ, if the small changes in volume at the end of the transition domain are neglected. Then, incompressibility $\sum \varepsilon_i^{pl} = 0$ can be assumed and it follows:

$$eng\sigma = F / A_0,\ true\sigma = F/A \quad \text{with } A \cdot \ell = A_0 \cdot \ell_0,\ F := \text{load } F_{ax}$$

wherein ℓ_0 := original gage length, and A, ℓ current values of the necking cross-section.

Introducing the equation $\varepsilon_{ax} = (\ell - \ell_0) / \ell_0$ derived above, the true stress is linked by

$$true\sigma_{ax} = F / A = (F / A_0) \cdot (\ell / \ell_0) = eng\sigma \cdot (1 + eng\varepsilon_{ax}) = \sigma_{ax} \cdot (1 + \varepsilon_{ax}) \quad \text{usually written}$$

$\Rightarrow$ Transferring stress data: $true\sigma = eng\sigma \cdot (1 + eng\varepsilon)$ and $eng\sigma = true\sigma / exp(true\varepsilon)$.

Fig.14-4 (left) shows an experiment in the elastic-plastic transition region, carried out by O. Mahrenholtz /H. Ismar. The test was a flat compression test of a cube: One side constrained, one free, one compressed → Principal stress state ($\sigma_I = \sigma_{action}$, $\sigma_{II} = \sigma_{I\,(re\text{-}action)}$, $\sigma_{II} = 0$) → principal strain → ν . It turns out that R_{p01} is approximately ν = 0.4. The value at R_{p02} in Lode coordinates is 0.82 = $\sqrt{2/3} = \sqrt{2J_2}\,/\,R_{02}$, with $J_2 = 2R_{02}/6$ (left, down). Poisson's ratio, determined by a coupon measurement, reads $\nu = -\,\varepsilon_{lat}/\varepsilon_{ax}$ or $\nu = -\,(\Delta d/d)/(\Delta\ell/\ell$.

Concerning sheet test specimens the measurement problem increases because localized necking will occur at 'onset-of-ductile cracking and this depends on the thickness of the test specimen.

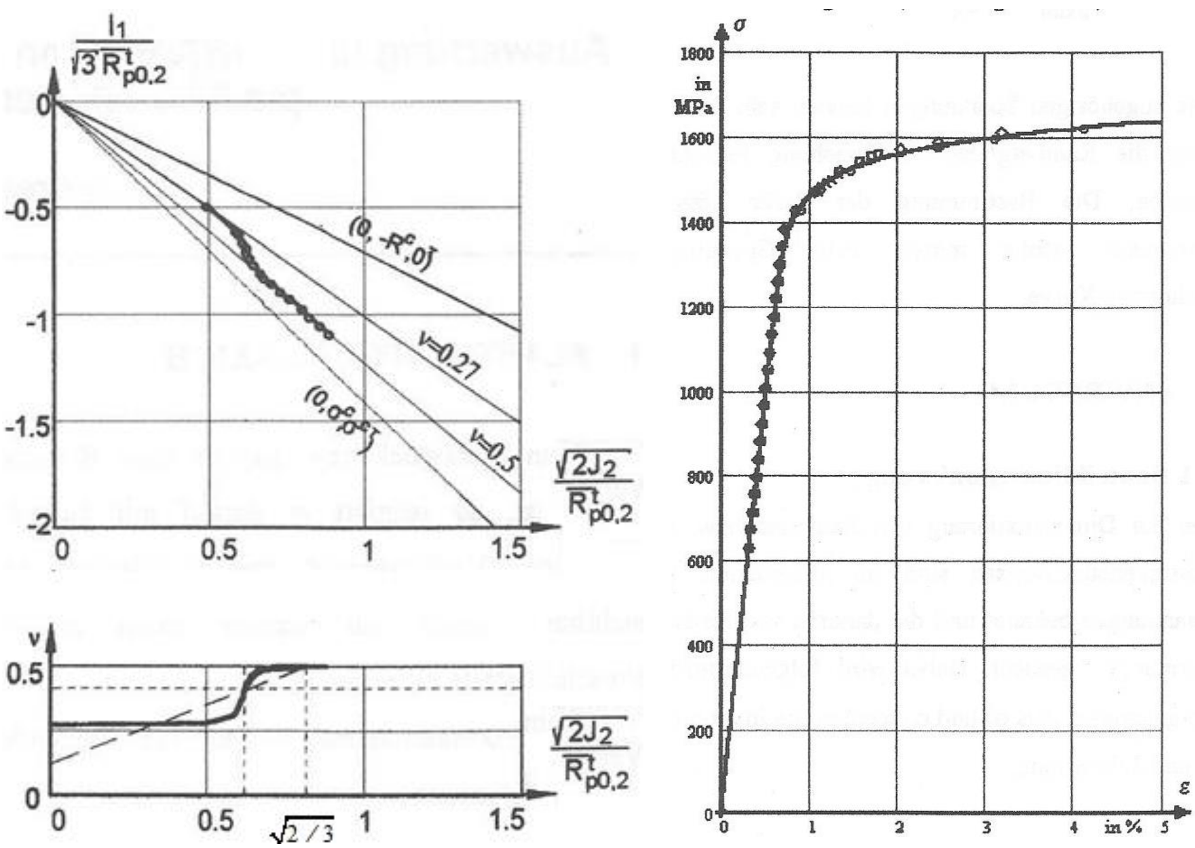

Fig. 14-4: (left) St37 Development of ν in Beltrami's elastic-plastic transition regime, a cube plane compression test. (right) D6AC, Ariane 5 Booster) Stress-strain measurement points with a Ramberg-Osgood engineering stress-strain data mapping curve under axial tension

14.4 Mapping of the measured stress-strain curve by the Ramberg-Osgood Model

In a contract of MAN-NT with the institute IWF at Freiburg all standard model-required properties have been determined. For completion, hopefully in a material-handbook given will be in addition the plastic strain A5 and also the final necking value Z, being usually minimum and not average values. $A_{fr} \equiv A_{rupture}$ comes from measurement of *A*5 (*type: $L_0 = 5 \cdot d_0$, original length L_0 and initial diameter d_0*) as plastic or permanent change in length, measured on the load-controlled broken test specimen and Z the radial plastic necking A-reduction ratio value, in % (Unfortunately, material mechanics also uses the letter A for this strain property).

Table 14-2 lists analysis-relevant quantities (in MPa and %) to be applied in a Ramberg-Osgood curve modelling.

Table 14-2: AA2219 material properties and Ramberg-Osgood parameters. Isotropic materials, in MPa and %), *d= 4.0 mm . Regarding* $\bar{R}_{odc}$ *, see the following Sub-chapter 14-6.*

$\bar{R}_{p0.2}$	$\bar{R}_m$	A_{gl}	true$\bar{R}_m$	trueA_{gl}	$\bar{R}_{odc}$	$A_{fr} = A_{rupt}$	trueA_{fr}	Z	$\bar{n}$	true$\bar{n}$	$R_{p0.2}$	R_m	R_{odc}
352	*453*	*4.9*	*478*	*4.8*	*535*	*7.7*	*7.5*	*20*	*12.7*	*10.6*	*297*	*417*	*492*
MPa	MPa	%	MPa	%	MPa	%	%	%	-	-	MPa	MPa	MPa
average *(mean, typical, characteristic)* values for best mapping											Design Allowables		

$$\text{true}\varepsilon = \frac{\text{true}\sigma}{E_0} + 0.002 \cdot \left(\frac{\text{true}\sigma}{\text{true}\bar{R}_{0.2}}\right)^{\text{true}\bar{n}} = true\varepsilon_{ax}^{el} + true\varepsilon_{ax}^{pl} ,$$

$$E_{\sec}^{\text{hard}} = \frac{\sigma}{\varepsilon} = \frac{\sigma}{\frac{\sigma}{E_0} + 0.002 \cdot (\frac{\sigma}{\bar{R}_{0.2}})^{\bar{n}}} = \frac{E_0}{1 + 0.002 \cdot \frac{E_0}{\bar{R}_{0.2}} \cdot (\frac{\sigma}{\bar{R}_{0.2}})^{\bar{n}-1}}, \quad E_{\tan}^{\text{hard}} = \frac{d\sigma}{d\varepsilon} = \frac{E_0}{1 + 0.002 \cdot \bar{n} \cdot \frac{E_0}{\bar{R}_{0.2}} \cdot (\frac{\sigma}{\bar{R}_{0.2}})^{\bar{n}-1}} .$$

14.5 Poisson's ratio

If analytically necessary the value of Poisson's ratio ν, which increases when stresses narrow the plastic regime, can be determined for stability analyses as a function of the stress. The formula, which uses quantities of the R-O-mapped true stress-true strain curve, is derived in *Table 14-3.*

Table 14-3: Derivation of a formula for Poisson's ratio

$$true\varepsilon = true\varepsilon^{el} + true\varepsilon^{pl} \text{ with } true\varepsilon_{ax} = true\varepsilon_{ax}^{el} + true\varepsilon_{ax}^{pl} , \quad true\varepsilon_{lat} = true\varepsilon_{lat}^{el} + true\varepsilon_{lat}^{pl} , \quad \nu_0 = \frac{-true\varepsilon_{lat}^{el}}{true\varepsilon_{ax}^{el}}$$

from incompressibilityin the plastic range (≡ volume conservation law) $\frac{V}{V_0} = \frac{\ell}{\ell_0} \cdot \frac{A}{A_0} = 1$

follows $true\varepsilon_{ax}^{pl} + 2 \cdot true\varepsilon_{lat}^{pl} = 0$ and $true\varepsilon_{lat}^{el} = -\nu_0 \cdot true\varepsilon_{ax}^{el}$, which gives after insertion of above relations

$$true\nu = -\frac{true\varepsilon_{lat}}{true\varepsilon_{ax}} = -\frac{true\varepsilon_{lat}^{el} + true\varepsilon_{lat}^{pl}}{true\varepsilon_{ax}} = -\frac{true\varepsilon_{lat}^{el} - 0.5 \cdot true\varepsilon_{ax}^{pl}}{true\varepsilon_{ax}} = -\frac{true\varepsilon_{ax}^{el}}{true\varepsilon_{ax}} \cdot \left(-\nu_0 - 0.5 \cdot \frac{true\varepsilon_{ax}^{pl}}{true\varepsilon_{ax}^{el}}\right)$$

$$= -\frac{true\varepsilon_{lat}^{el} - 0.5 \cdot true\varepsilon_{ax}^{pl}}{true\varepsilon_{ax}} = -\frac{-\nu_0 \cdot true\varepsilon_{ax}^{el} - 0.5 \cdot true\varepsilon_{ax}^{pl}}{true\varepsilon_{ax}} = -\frac{-\nu_0 \cdot true\varepsilon_{ax}^{el} - 0.5 \cdot (-true\varepsilon_{ax}^{el} + true\varepsilon_{ax})}{true\varepsilon_{ax}}$$

$$= -\frac{-\nu_0 \cdot true\varepsilon_{ax}^{el} - 0.5 \cdot (-true\varepsilon_{ax}^{el} + true\varepsilon_{ax})}{true\varepsilon_{ax}} = 0.5 + \frac{-\nu_0 \cdot true\varepsilon_{ax}^{el} - 0.5 \cdot (-true\varepsilon_{ax}^{el})}{-true\varepsilon_{ax}}$$

$$= 0.5 - \frac{true\varepsilon_{ax}^{el}}{true\varepsilon_{ax}} \cdot (0.5 - \nu_0) \text{, see. 14.5 .}$$

However, this formula does not fully lead to ν = 0.5 at R_{02} as can be seen in *Fig.14-5*. A better approximation $\nu = 0.5 - (E_{\tan}^{\text{hard}} / E_0) \cdot (0.5 - \nu_0) \equiv \text{true}\nu$ is usually applied in the elastic-plastic domain in stability analysis employing the tangent modulus function above in order to approximately consider the changing ν in analysis.

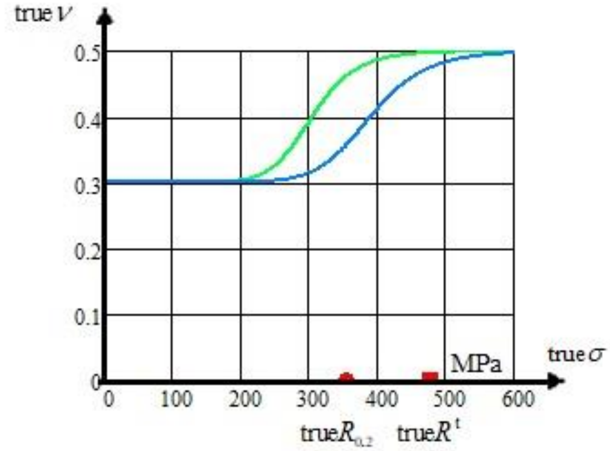

Fig.14-5: Course of Poisson's ratio in the elastic-plastic domain, determined with several formulas

__LL__:

* *The determination of the properties of a solid material requires a force-elongation curve which is then accurately to transfer into a stress-strain curve that is independent from the tested specimen type rod, sheet, coupon, cube.*
* *Before any performance of a non-linear analysis is executed it is to check whether true or engineering curve quantities are to provide for numerical input. This then fixes the output*
* *Beyond R^t necking occurs generating a hydrostatic stress σ_{hyd} in the tensile rod, which lowers the stress-strain curve (see Chapter 15) in the high plastic regime*
* *Poisson's ratio can only __approach__ the limiting points 0.5 > **ν** > (-1, principally.) So-called auxetic materials possess a negative ν. Being strained, the transverse strain in the material will also be positive*
* *UD-materials have different ν-values in the directions of anisotropy*
* *True strains can be added while engineering strains can not!*

In *__Fig.14-6__* the different growth of the engineering and the true stress-strain curve is displayed up to the tensile strength point at the 'End–of–uniform elongation'. Beyond R^t, in test data evaluation the axial stress has to be replaced by the equivalent stress because necking in the test specimen activates a hydrostatic residual stress state, dependent on the test specimen used.

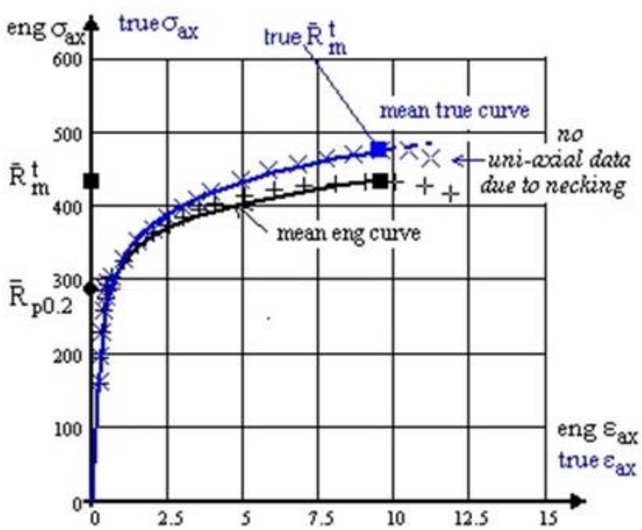

Fig.14-6, AA 2219:

Differences in R-O-mapping of engineering and true stress-strain curve, single measurement.. Bar over R indicates a mean value. F/A_0

at 'End of uniform elongation' = 'Onset-of-(diffuse) Necking'

In *Fig.14-7* the full stress-strain curve is presented and associated significant points including strength design allowables points are depicted. Additionally for 'Onset-of-yielding' the Margin of Safety is rendered in order to visualize the size of the fulfillment of the 'Design Yield' Limit State.

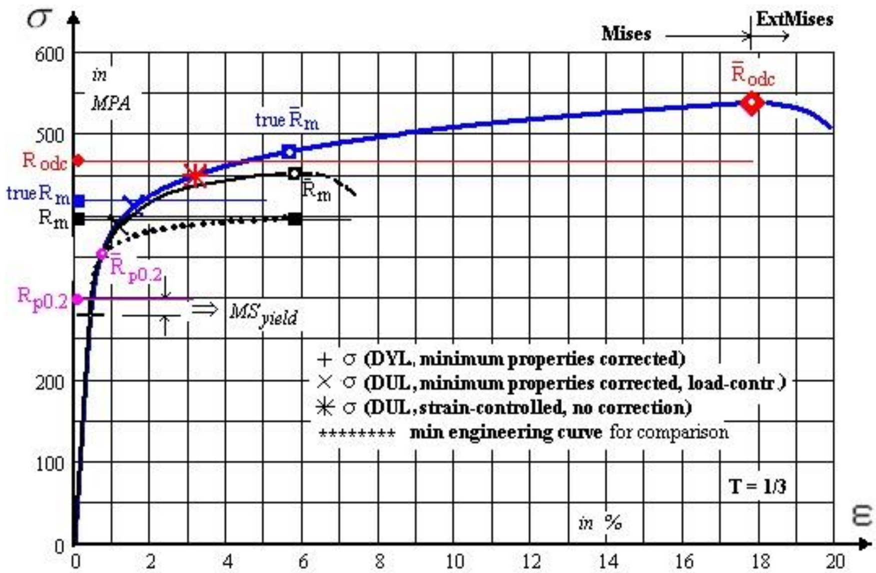

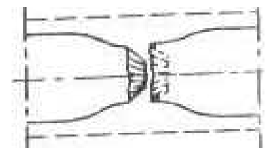

cup-cone picture
of the
failed rod

Fig. 14-7: Equivalent true stress-equivalent true strain curve. Proposed local strain-controlled extended stress-strain curve incl. mean fracture points and strength design allowables (no bar over)

The full curve ends with reaching the 'onset-of-ductile cracking' point at the associated strength R_{odc}.

LL:

* *Opposite to some regulations it is to note "In general, it can be not correct to use a minimum engineering curve in order to obtain the desired realistic structural behavior because structures are usually statically indeterminate".*
* *The elliptical shape of the 'Beltrami egg' and its surface potential description will be used in the 'Gurson domain' too, next chapter.*

14.6 Estimation of the Strength $\bar{R}_{odc}$

Beyond 'Onset-of-diffuse necking' the axial strain measurement becomes senseless, only representative is the rod radius-decrease measurement to investigate in this full plastic domain the influence of the hydrostatic stress. From the measured plastic cross-section reduction the plastic portion ε_{odc}^{pl} can be estimated and the 'plastic' curve point $\bar{R}_{odc}$ computed if the only counting associated plastic strain is known, fixed by the diameter reduction. Because the R/O-model excellently maps the true strength course of test data, its plastic part is employed to estimate a value for the *plastic point* $\bar{R}_{odc} \equiv$ 'Onset-of-ductile-cracking', which is of interest for plastic structural design.

This can be executed by using volume constancy applying the measured reduction of the initial radius $a = d/2$ of the tensile rod. With $Z\,(\bar{R}_{rup})$ taken as $Z\,(\bar{R}_{odc})$ the estimation of $\bar{R}_{odc}$ at trueε_{odc} from the Ramberg-Osgood curve is performed as shown in *Table 14-4*.

Ductile collapse or *rupture* $\bar{R}_{rupt}$, respectively, is just of theoretical interest.

Table 14-4: Derivation of an estimate value for the Strength $\bar{R}_{odc}$

At $\bar{R}^t$ 'Onset-of- (diffuse) necking' d_{oon} = 3.89 mm, at 'Onset-of-ductile cracking' d_{odc} = 3.78 mm.

$$\varepsilon^{pl} = 0.002\left(\frac{\sigma}{\bar{R}_{0.2}}\right)^n , \ \varepsilon_{rad}^{pl} = \ln(\frac{r}{a}) , \quad \frac{\Delta A}{A_0} = \frac{A_0 - A}{A_0} = 1 - \frac{A}{A_0} \ \rightarrow \ \frac{A_{rupt}}{A_0} = 1 - Z = \frac{r^2}{a^2}$$

$$\varepsilon_{ax,\,00n}^{pl} = -2\cdot\varepsilon_{rad}^{pl} \text{ at } \bar{R}^t \quad \text{and delivers} \quad \text{true}\bar{n} = \frac{\ln\left(\varepsilon_{ax,\,00n}^{pl} / 0{,}2\%\right)^n}{\ln\left(\bar{R}^t / \bar{R}_{p0.2}\right)} \ .$$

With known $\varepsilon_{rad}^{pl} = \ln(\frac{r}{a}) = \ln(\sqrt{1-Z}) = \ln(\sqrt{1-0.20}) = -11.2\ \%$ and $\varepsilon_{ax}^{pl} = -2\cdot\varepsilon_{rad}^{pl}$

follow for the non-corrected odc-point $\rightarrow true\varepsilon_{ax}^{pl} = 0.002\cdot\left(\frac{\bar{R}_{odc}}{\bar{R}_{0.2}}\right)^{\text{true}\bar{n}}$

$$\Rightarrow \ \bar{R}_{odc} \cong \bar{R}_{0.2}\cdot \sqrt[true\bar{n}]{\varepsilon_{ax}^{pl}} / 0.002 = 542 \text{ MPa} \quad \text{and}$$

$$\text{true}\varepsilon\text{odc} = true\varepsilon_{ax}^{el} + true\varepsilon_{ax}^{pl} = \frac{\bar{R}_{odc}}{E} + 0.002\left(\frac{\bar{R}_{odc}}{\bar{R}_{0.2}}\right)^{\text{true}\bar{n}} \ .$$

14.7 Beltrami's Potential Surfaces in the Elastic-plastic and as Idea for the Porous Regime

From previous investigations the author knows, that any volume change, due to the FMC 'rules', is to describe by the term I_1^2. If a shape change occurs then the invariant J_2 is required.

Elastic-plastic transition regime:

Beltrami cites: "*The deformation of a material consists of two parts, a shape* and *a volume change*". Based on this, one can formulate for the elastic-plastic transition regime

$$\frac{(2+2\nu)\cdot 3J_2}{\bar{R}^2} \text{ and } \frac{(1-2\nu)\cdot I_1^{\,2}}{\bar{R}^2} \ \rightarrow \ \frac{3J_2}{\bar{R}^2} + \kappa\cdot\frac{I_1^{\,2}}{\bar{R}^2} = c^{\text{Bel}} \text{ with } \kappa = \frac{1-2\nu}{2+2\nu} \ .$$

Into this formulation a normalizing strength is inserted: $I_1 = \bar{R},\ J_2 = 2\bar{R}/6 \ \rightarrow \ c^{\text{Bel}} = 1 + \kappa$ and

for the special yield potential surface (ν=0.5) yields $\frac{3J_2}{\bar{R}_{02}^{\,2}} + 0\cdot\frac{I_1^{\,2}}{\bar{R}_{02}^{\,2}} = 1 + 0$ ('Mises' cylinder).

Beltrami bridges the elastic domain with the plastic domain ($3\cdot J_2$ is Mises part). His formulation is not a failure function but a descriptive function to predict subsequent Beltrami surfaces $\nu(\bar{R})$, which are surfaces of equal potential. This means: A pair $(\nu, \bar{R})$ must be given for each desired ν-curve of the subsequent potential surfaces are obtained*, see* *Fig.14-8 left.* This part figure shows the change of the potential surface of the growing 'Yield' body with increasing ν in the elastic-plastic transition domain. The two center figures show the cross-section using the principal stresses and below the development of the yield body from the yellow egg ($\nu = \nu_0$) up to full yielding (ν = 0.5) rendered by the 'Mises cylinder' → *Poisson's ratio ν drives the elliptic shaping!*

Plastic porosity affected regime*:* an anticipation, considering Chapter 15

Porosity causes a volume increase. This works oppositely as in the elastic-plastic transition regime, which can be described by Beltrami, too. Increasing porosity *f* means a decreasing

Poisson's ratio ν and a more elliptic shape. In the outer figures of *Fig.14-7* both the regimes of the changing Poisson's ratio are displayed. The right part figure, modelled by Beltrami, pre-informs (see *§15*) how the surface of the yield body changes its shape with decreasing ν according to the increasing porosity *f*.

Fig.14-7(right) displays the development of the subsequent failure surfaces whereby an increasing true stress is considered. This is relevant for the critical material location. After achieving the tensile strength a small further radial increase of the surface is obvious together with the initiation of an increasing elliptic failure surface. With increasing degradation the subsequent surfaces become more and more elliptical. This is the opposite process regarding Beltrami in the elastic-plastic transition regime. A growing *f* means higher true stress but less cross-section or load-carrying material in the strain-controlled 'hot spot'.

The Beltrami formulation delivers an *Idea for the ductile porous regime* and is intended to replace the 'Gurson' formulation by Cuntze's so-called 'Extended Mises' one, reading

$$\frac{3J_2}{\bar{R}^t_{0.2}} + \frac{1-2\nu}{2+2\nu} \cdot \frac{I_1^{\,2}}{\bar{R}^t_{0.2}} = c^{\text{Bel}} \quad \Rightarrow \quad \frac{3J_2}{\bar{R}^t_{0.2}} + c_{12} \cdot \frac{I_1^{\,2}}{\bar{R}^t_{0.2}} = c^{\text{ExtMises}} \quad .$$

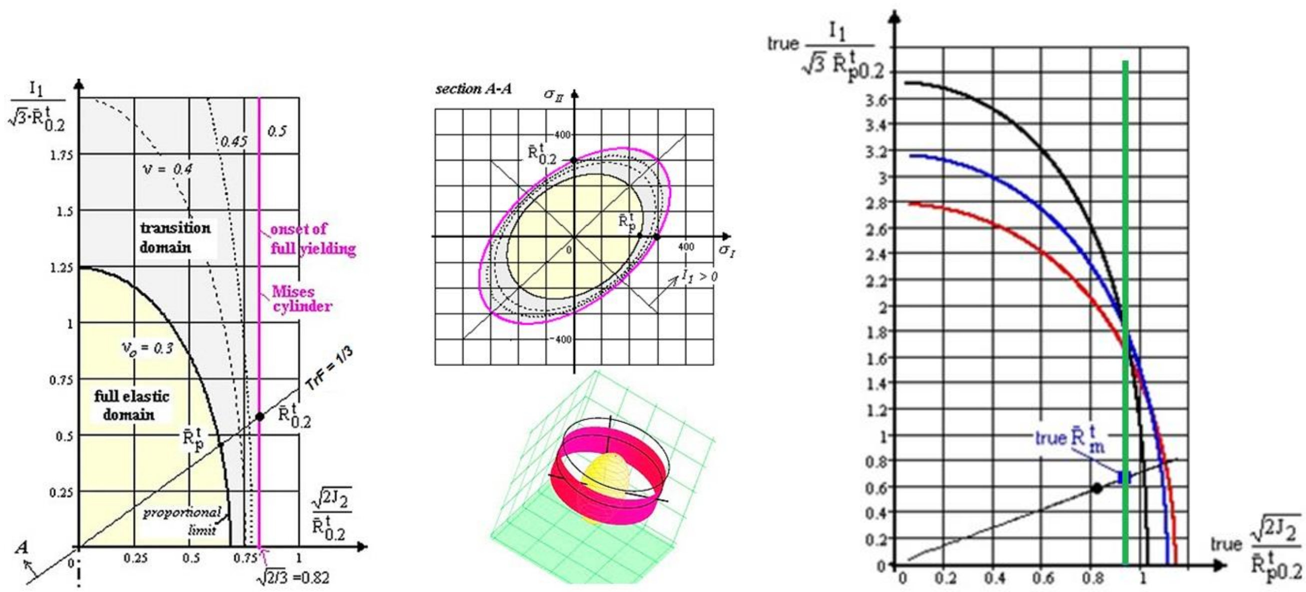

Fig.14-8: (left) Elastic-plastic transition domain, development of the Beltrami surfaces from egg shape (growing yield potential surface with ν_0 = 0.3 for metals (0 for foam = sphere) < ν < 0.5 ('Mises cylinder → J_2 = constant = incompressibility) depicted in Lode-Westergaard coordinates. (center) visualization of the Beltrami potential surfaces. (right) Change of potential surfaces in the porous domain computed with the Extended Mises formulation (see [CUN22, §17]), f = 0, 0.1, 0.2, 0.3

Also here, the yield strength can be used for normalization. The parameters c^{Bel}, c^{ExtMises} mark the size parameter of the changing potential surface (*see survey in Table 15-4*).

In order to understand the chosen Haigh-Lode-Westergaard coordinates *Fig.14-9* is provided below.

The vector $\{\sigma_{\text{prin}}\} = (\sigma_I, \sigma_{II}, \sigma_{III})^T$ is a vector-addition of the principal stresses. The cone angle between all principal axes and I_1 is 54.75°.

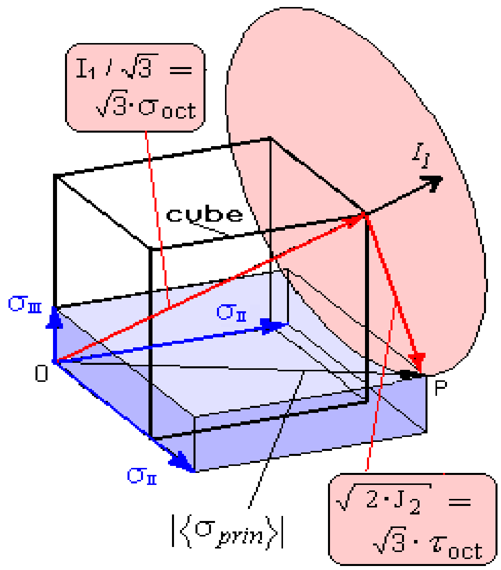

Fig.14-9:
Visualization of the used Lode-Westergaard coordinates by the principal stresses acting at a material cube.

Octahedral stresses:

$$\sigma_{oct} = I_I / 3 \quad \text{with } I_I = \sigma_I + \sigma_{II} + \sigma_{III}$$

$$\sigma_{eq}^{\text{Mises}} = \sqrt{3 \cdot J_2} = f(\tau), \text{ with}$$

$$6 \cdot J_2 = (\sigma_I - \sigma_{II})^2 + (\sigma_{II} - \sigma_{III})^2 + (\sigma_{III} - \sigma_I)^2$$

$$\tau_{oct} = \sqrt{6J_2}/3 \text{ -}$$

To make more familiar with potential surfaces *Fig.14-10* presents two potential surfaces dedicated to different *Effs*, for fracture *Eff* = 100% and for a loading that generates *Eff* = 50 %.

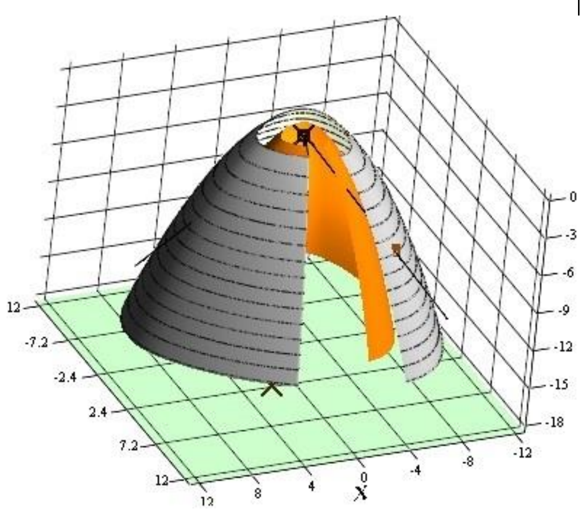

Fig.14-10: Two potential surfaces. Eff is the measure for he distinct potential surface with Eff=1=100% the fracture surface. The potential surfaces are Eff^{SF}=50% and Eff^{SF} =100%, fracture.

Indicated are the failure stress points

$\bar{R}^t = 4$ MPa, $\bar{R}^{tt} = 3$ MPa, $\bar{R}^c = 40$ MPa, $\bar{R}^{cc} = 49$ MPa

and the principle stress axes.

'Normal Concrete', 3D test data available

$$Eff^{SF} = c^{SF} \cdot \frac{\sqrt{4J_2 \cdot \Theta^{SF} - I_1^2 / 3} + I_1}{2 \cdot \bar{R}^c}$$

***LL**:*

* *The shape of the potential surfaces in the plastic porosity regime changes oppositely to the shape in the elastic-plastic regime. Both the surface shapes one can dedicate to the change of the Poisson ratio ν*
* *In structural analysis the stresses are most-often .determined in the elastic-plastic regime. This is performed very accurately, sometimes over-precise. However in this domain the Poisson's ratio changes significantly, which should be considered.*

15 A measurable parameters'-based 'Extended-Mises' Model instead of a 'Gurson' Model?

Aim: *De-complication of highly non-linear plastic analyses by generation of a simplified model to perform Design Verification in a Ductile Metal's high Porous Regime*

15.1 Introduction

There is stress- and strain-controlled behavior. Strain-controlled locations in a structure will not break, when the stress level reaches tensile strength R^t. A fuel-outlet hole in the upper tank of the Ariane 5 central stage was such a strain-controlled case at MAN, where the vicinity of the 'overstrained' critical material location takes over the reduced loading capability, no direct fracture is to face.

Such a (seldom) task caused MAN-Technologie to let perform an analysis together with IWM Freiburg applying a multi-parameter 'Gurson' yield model. Its model parameters cannot be measured directly, but are usually determined by a FE analysis which best models the deformation of the test specimen, a classical simulation process. An example for such a multi-parameter set, determined for the aluminum alloy AA2219 and by using the tensile rod test specimen, is given in the table below [*IWM Freiburg*]:

f_0	f_n	f_c	f_F	q_1	q_2	ε_n	s_n
0.00	0.05	0.04	0.15	1.5	1.0	0.20	0.01

.

The applied 'Gurson'-model (such a model is a model of the *Continuum (micro-)Damage Mechanics theory in the ductile materials regime)* of the IWM was a refined one. Refinement means that more parameters are to determine than for a simpler 'Gurson' model. Therefore, the optimal model parameter set *of a 'Gurson' model* depends on the mesh fineness and has to be inversely determined by an excellent simulation of the test specimen's behavior, see <u>*Fig.15-1 left*</u> for the tensioned rod

(Gurson A L: *Continuum Theory of Ductile Rupture by Void Nucleation and Growth. Part 1:Yield criteria and flow rules for porous ductile media*. J. Eng. Mater. Techn.99 (1977), 2-15)

Using 'Gurson' model results, the responsible design engineer must ask:

What about the scatter of the simulation-won parameters which are to insert in the analysis?

Without knowledge of the scatter there is not a generally accepted design verification possible. Might it be not better to apply a simpler model with 2 or 3 parameters at dispense of the little gain of the last load carrying portion after coalescence at 'onset-of-ductile cracking' marked by the corresponding strength value R_{odc}? This is the 'technically relevant point', where the coalescence of voids begins. Only a reduced procedure with directly measurable model parameters has the chance to capture the statistical Design Verification requirements.

In the context above the question comes up:

"*How much Gurson material modelling is necessary to achieve a reliable prediction of the <u>local</u> design-deciding ductile fracture level of the structure?"*

This failure mode 'ductile fracture' is defined here to be met at 'onset-of-ductile cracking' and it shall correspond to Design Ultimate Load. Such an application is a seldom case, where the deformation-controlled strength value $R_{odc} > R^t$ is used to *save the final design* not anymore possible via the load-controlled strength value R^t. A simpler model is required. Two challenging parts tasks are thereby faced:

(1) Creation of a model simpler than a multiple-parameter ‘Gurson’ model, and

(2) to capture the porosity *f* in the equivalent σ-ε-curve**,** to be provided, whereby *f* is an additional but measurable model parameter transferring the ‘Mises’ model to the ‘Extended Mises’ model. For its derivation, the various micromechanical mechanisms during ductile fracture are of basic interest:

* Void nucleation in the test rod at so-called second phase particles by debonding
* Void growth, controlled by stress Triaxiality Factor TrF and growing plastic strain ε_{eq}^{pl}, and
* Coalescence of voids by internal shear stress-driven rod necking with final ductile rupture.

For the evaluation of the usual rod test results, the widely used correction formula of P.W. Bridgman is employed. *Fig.15-1(left)* presents the dependency of the rod’s diameter reduction on the load *F* and further shows simulation curve and test curve. The measurement of the diameter reduction is mandatory beyond the ‘end of uniform elongation’ at the tensile strength point $\bar{R}^t = max\,F\,/\,A$, depicting the ‘onset-of-diffuse necking $_{oon}$ point and experiencing full plasticity. Beyond $\bar{R}^t$ only true values represent the reality.
Mind: $F(\Delta d)$ is not completely of the same shape like $true\sigma(true\varepsilon)$.

In the load-controlled regime axial strain measurements are performed whereas in the transversal, plastic strain-controlled necking regime diameter reduction measuremens are to execute. In the *Fig.15-1(right)* attention is drawn to the various stress-strain curves used and to the associated strengths. Displayed are the mean technical and mean true strengths together with the associated Design Allowables.

If materials do not fail when the tensile strength is reached, then this is accompanied by the fact (*Fig.15-1, left)* that max*F* does not essentially change over a certain range of the strain because hardening still works until a slight kink will occur due to void coalescence and destruction of piled–up dislocations. Degradation wins over hardening at the ‘onset of ductile cracking’ strength point R_{odc}. R_{odc} and marks the coalescence-linked kink and is defined here as the critical strength.

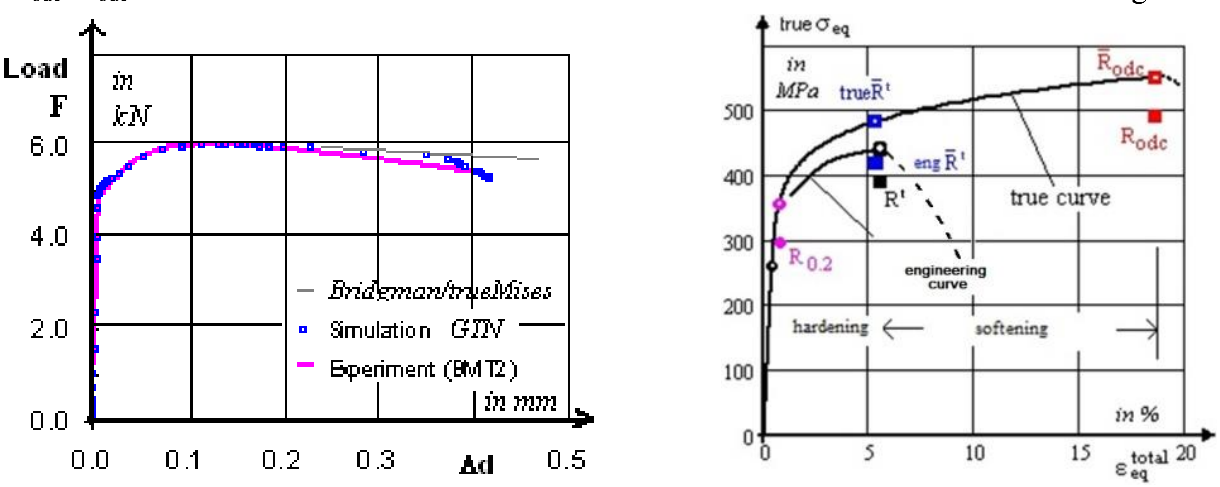

Fig.15-1: (left) Dependency of diameter reduction Δd on the applied load F. Comparison of global simulation and test results (IWM Freiburg, Dr. Sun). (right) Ramberg-Osgood-mapped true and engineering stress-strain curves of AA2219A bar over R indicates a mean value, no bar over R indicates a ‘design allowable’

15.2 Bridgman-3D Correction of the true σ-ε-Curve, employing ‘Mises’

Equivalent stress: true$\sigma_{ax} \rightarrow$ trueσ_{eq}

The validity of the uniaxial stress-strain curve measured in the smooth tensile rod test is terminated at the load-controlled strength point ${}_{max}\sigma_{true} = \bar{R}^t = max\,F / A$, which corresponds to the maximum load F and to the actual minimum cross section of the neck. However, beyond $\bar{R}^t$ ('end-of-uniform-elongation') at the 'onset-of-diffuse necking $_{od}$n' point the 1D-stress situation in the tensile rod becomes a 3D one and an equivalent stress σ_{eq}^{Mises} has to be considered in order to capture spatial stress tasks.

Under tensioning, in the plastic regime the lateral contraction of the material at the center of the neck is impeded by neighboring material leading to a 3D-stress state. Hence, a simple extrapolation of the F/A (σ-ε)-curve beyond $\bar{R}^t$ cannot provide a physically accurate curve, because the necking-generated 3D-residual stress state σ_{hyd} is to consider in the evaluation of the tensile rod test results in order to obtain a real σ_{eq}. The three stresses within σ_{eq} reach their maximum values at the center of the rod's cross-section with approximately equal values $\sigma_{radial} = \sigma_{hoop}$, except close to the surface, as depicted in <u>*Fig.15-2*</u>*(left)* below. The values of σ_{radial}, σ_{hoop} and of the created necking radius ρ raise with σ_{ax}. The former F/A-quantified capacity becomes continuously reduced with increasing necking. Hence, the true stress-strain F/A curve is to correct to obtain a realistic equivalent stress. In the center of the rod an increasing stress Triaxiality Factor *TrF* is faced. Assuming a constant σ over

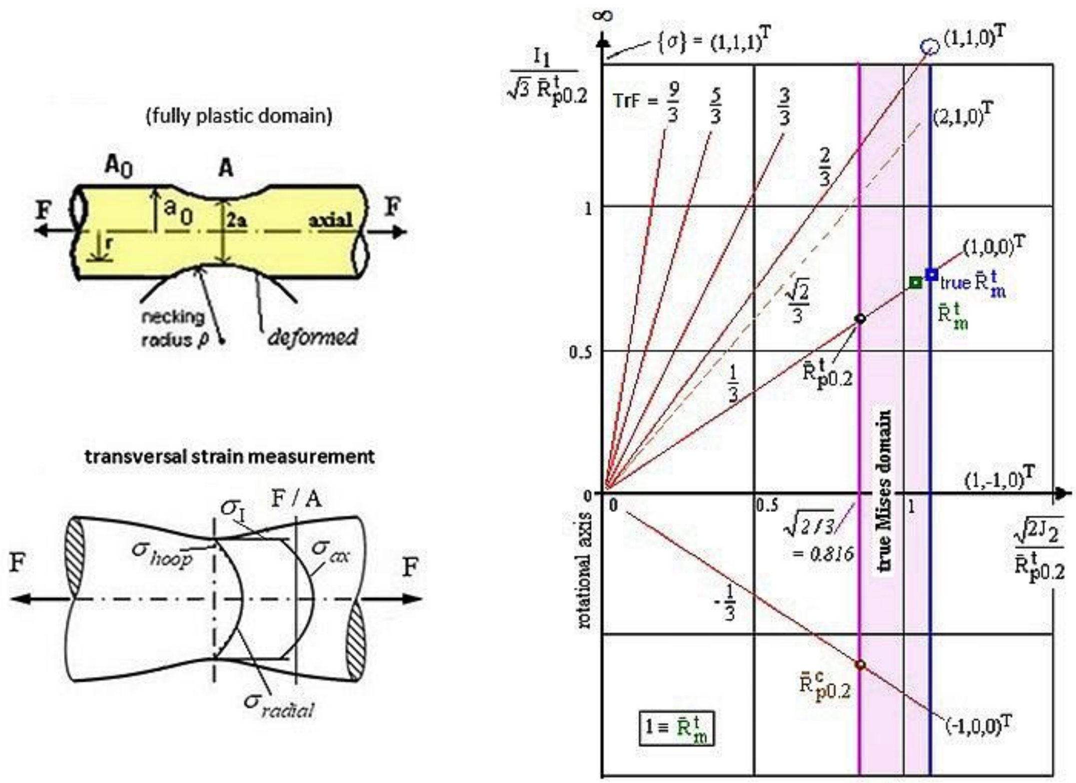

Fig.15-2: (left) Stresses and transversal (radial) strain measurement of the necked round tensile rod. F:=force, A:= minimum actual cross section of the neck. F:=Force F_{ax}, A_0 := original cross-section. $\bar{R}^t = \max F / A_0$, $\varepsilon \le \bar{A}_{gl}$ (permanent strain linked to load-controlled fracture at $\bar{R}^t$). Necking radius is ρ. (right) Schematic visualization of the Triaxiality Factor TrF, responsible for failure in the rod center

$$\{\sigma\} = \{\sigma_I, \sigma_{II}, \sigma_{III}\}^T,\ TrF\{\sigma_I, \sigma_{II} = \sigma_I, 0\}^T = 2/3.$$

the rod's cross-section, *Fig.15-2(right)* illustrates by a variety of *TrF*-beams that values higher than 2/3 (bi-axial stressing) are practically not possible. Assuming constancy is not anymore the case for a plastic rod neck, where the failure decisive location is the center of the cross-section with also there facing *maxTrF.* Notched test specimens are applied to capture higher multi-axial stress states, *TrF* = 1, values > 1/3.

Fig. 15-3 shows the void volume fraction in the necking region at failure. The highest values are reached in the center of the specimen (Element 20) as expected, *TrF* highest. From the central region micro-damage spreads out over the whole cross section.

Basic task now will be the necessary transfer from the uniaxial trueσ_{ax}(trueε_{ax}) → tri-axial trueσ_{eq} (trueε_{eq}) in the diffuse necking regime.
Bridgman provided a correction means how to adjust trueσ_{ax}, but had to make some essential assumptions:

(1) The cross section of the necked region remains angular *(like the 'Mises' cylinder, assuming a rotationally symmetric yield body*).
(2) The inner axial contour of the neck can be approximated by the arc of a circle with the radius ρ.
(3) 'Mises' can be applied (*effect of growing voids is therefore not considered*).

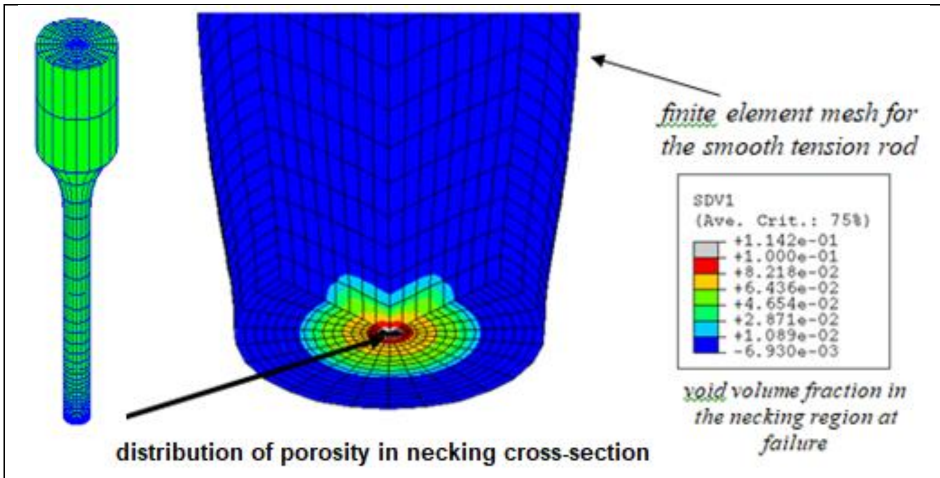

Fig.15.3: Tensile rod with porosity distribution in the 'Hot spot' center of the rod.). Finite element mesh of the rod. Void volume fraction f in the necking region at failure [Sun97, IWM 7] stresses in MPa, strains in %. Material source, AA2219 variant, T2: $\rho_{\text{initial}} = \infty$, 2 a = 4mm, Elasticity properties are E =70000MPa, ν = 0.3, t = 6 mm plate. Sample size n = 179, A5 = 7.4 %, Z = 20 %

Due to the diffuse necking, an axial load increase-caused internal hydrostatic *tensile* stress state σ_{hyd} is generated, representing a deformation-dependent residual stress state. Its radial distribution can be Mises-based estimated - under the axial loading $\{\sigma\} = (\sigma_{\mathrm{I}}, \sigma_{\mathrm{II}}, \sigma_{\mathrm{III}})^T = (F/A, 0, 0)^T$ - after Bridgman by $\sigma_{\text{hyd}}(r) \approx \sigma_{\mathrm{I}} \cdot ln\left(1 + \frac{a^2 - r^2}{2 \cdot a\rho}\right)$ with $\sigma_{\mathrm{I}} < \frac{F}{A} = \frac{F}{\pi \cdot a^2}$, *Fig.15-2*

with *F*:= load, *a*:= radius of actual cross section of neck, ρ := radius of neck curvature and F/A an integral quantity capturing the external loading F. The full set of relevant relations then reads:

$\sigma_{ax}^{t}(r) = \sigma_{I} + \sigma_{hyd}(r)$ and $\sigma_{radial}(r) \approx \sigma_{hoop}(r) = \sigma_{hyd}(r)$ and as equivalent stress follows

for a single stress $\rightarrow \sigma_{eq}^{Mises} = \sqrt{3 \cdot J_2} = \sqrt{\frac{1}{2}} \cdot \sqrt{\left[(\sigma_I)^2 + (0)^2 + (-\sigma_I)^2\right]} = \sigma_I$ and also

for a superimposed $\sigma_{hyd} \rightarrow \sigma_{eq}^{Mises} = \sqrt{3 \cdot J_2} = \sqrt{\frac{1}{2}} \cdot \sqrt{\left[(\sigma_I - \sigma_{hyd})^2 + (\sigma_{hyd} - \sigma_{hyd})^2 + (\sigma_{hyd} - \sigma_I)^2\right]} = \sigma_I$

$I_1 = max\,\sigma_{ax}^{t} + max\,\sigma_{radial} + max\,\sigma_{hoop} = \sqrt{3 \cdot J_2} + 3 \cdot \sigma_{hyd}$, $\sqrt{3 \cdot J_2} = \sigma_I$ ($\leftarrow$ no σ_{hyd} effect).

$TrF(r) = true\sigma_{mean} / true\sigma_{eq}^{Mises} = (I_1/3)/\sqrt{3J_2} = \left[\sqrt{2}/3\right] \cdot (I_1/\sqrt{3})/\sqrt{2J_2} = \frac{1}{3} + \frac{\sigma_{hyd}}{\sigma_I}$.

Decisive for failure in the rod is the still mentioned Triaxiality Factor *TrF*, which increases with the true axial loading. Its maximum is in the center, the 'hot spot' at $r = 0$. In this micro-damage critical cup-cone center the 3D-state of stresses reads

$$max\sigma_{hyd}\ (r=0) = \sigma_I \cdot ln\ (1 + \frac{a}{2 \cdot \rho}),\quad max\sigma_{ax}^{t}(r=0) = \sigma_I + max\sigma_{hyd}$$

with the stress state in the rod's center $\{\sigma\} = (\sigma_I + max\sigma_{hyd}, \max\sigma_{hyd}, \max\sigma_{hyd})^T$.

In the necessary adjusting process of the F/A-curve in the diffuse necking regime (Phase 3) the first step is to integrate the axial stress, which varies over the radius. From load balance the following relations are yielded in Table 15-1.

The last unknown is the neck radius ρ. It could be computed during testing by measuring the shape change of the neck via a real-time Digital Image Correlation (DIC) 3D full-field measurement optical technique of the surface strains and an associated surface geometry model.

Table 15-1: Bridgman-Derivation of the cross-section quantities of the tensioned rod

$$\frac{F}{A} = 2 \cdot \int_0^a \sigma_{ax}^{t} \cdot \pi \cdot r \cdot dr / (\pi \cdot a^2)$$
$$= 2 \cdot \int_0^a (\sigma_I + \sigma_I(r)) \cdot \pi \cdot r \cdot dr / (\pi \cdot a^2)$$
$$= 2 \cdot \int_0^a (\sigma_I + \sigma_I \cdot \ln(1 + \frac{a^2 - r^2}{2 \cdot a \cdot \rho})) \cdot \frac{\pi \cdot r \cdot dr}{\pi \cdot a^2}$$

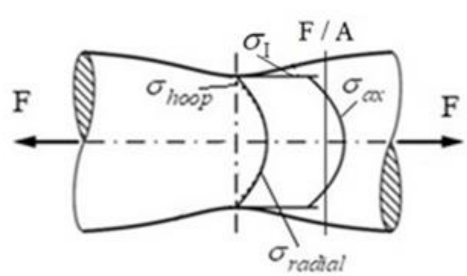

integrated follows $\frac{F}{A} = \sigma_I \cdot (1 + \frac{2\rho}{a}) \cdot \ln(1 + \frac{a}{2\rho})$ with $\sigma_{eq}^{Mises} = \sqrt{3 \cdot J_2} = \sigma_I$

$\sigma_I = \sqrt{3 \cdot J_2} = \sigma_{eq}^{MisBri} = \frac{F}{A} / (1 + 2 \cdot \rho/a) \cdot \ln(1 + a/2 \cdot \rho)$, valid $> \bar{R}^t$ or $A < Aoon$,

an equation, in which the ratio a/ρ is not known.

If no test result is available, then Lorrek-Hill's approach for rupture is applied at $\bar{R}_{rodc}$:

maximum $\frac{a}{\rho} = \sqrt{\ln(\frac{A_0}{A_{rupt}}) - \ln(\frac{A_0}{A_{oon}})}$, $\frac{A_{rupt}}{A_0} = 1 - Z$ with a

given cross section reduction Z in % at maximum necking at $\bar{R}_{rupt}$

and A_{oon} the cross section at $\bar{R}^t \equiv \bar{R}_m^t$, being 'Onset-of-(diffuse) necking'.

$$\frac{a}{\rho} = c_1 + c_2 + \text{true}\varepsilon_{ax}R_{odc}{}^2 + c_3 \cdot \text{true}\varepsilon_{ax}R_{odc}{}^3.$$

Equivalent strain: $\text{true}\varepsilon_{ax} \rightarrow \text{true}\varepsilon_{eq}$

For the Mises equivalent strain is valid in the plastic domain (elastic part is negligible):

$$\varepsilon_{eq}^{Mises} = \frac{\sqrt{2}}{3} \cdot \sqrt{(\varepsilon_{I}-\varepsilon_{II})^2+(\varepsilon_{II}-\varepsilon_{III})^2+(\varepsilon_{III}-\varepsilon_{I})^2} = \frac{\sqrt{2}}{3} \cdot \sqrt{(\varepsilon_{I}{}^{pl}-\varepsilon_{II}{}^{pl})^2+(\varepsilon_{II}{}^{pl}-\varepsilon_{III}{}^{pl})^2+(\varepsilon_{III}{}^{pl}-\varepsilon_{I}{}^{pl})^2}$$

considers plastic volume constancy (incompressibility) $\Sigma\varepsilon_i^{pl} = 0$ during plastic deformation it becomes

$$\varepsilon_{I}{}^{pl}/2 = -\varepsilon_{rad}{}^{pl} = -\varepsilon_{tan}{}^{pl} \text{ and } \varepsilon_{rad}{}^{pl} = ln(r/a) = \varepsilon_{tan}{}^{pl} \Rightarrow \varepsilon_{I}{}^{pl} = -2 \cdot ln(r/a) \text{ and it reads}$$

$$\text{true}\varepsilon_{eq}^{Mises} = \frac{\sqrt{2}}{3} \cdot \sqrt{((\varepsilon_{I}{}^{pl}+\varepsilon_{rad}{}^{pl}) - \varepsilon_{rad}{}^{pl})^2 + 0 + (\varepsilon_{rad}{}^{pl} - (\varepsilon_{I}{}^{pl}+\varepsilon_{rad}{}^{pl}))^2} = \frac{\sqrt{2}}{3} \cdot \sqrt{2\varepsilon_{I}{}^{pl\,2}} = \frac{2}{3} \cdot \varepsilon_{I}{}^{pl}.$$

LL: ** Bridgman correction = approach, which considers the varying stress over the rod's cross-section regarding that the center is the critical line*

** Lorrek-Hill = approach, which formulates a final value for the change of the curvature radius under loading. The increasing curvature triggers the increasing hydrostatic stress and this is to map*

** Measured ratio F/A = stress capacity smeared over the cross-section = load ability-quantity, which represents an effective (smeared) value, which decays with increasing axial strain*

** $\sigma_I \equiv \sqrt{3J_2}$ = constant basic stress quantity of the Bridgman approach, see Table 15-1*

** The applicability of axial measurement ends with 'End-of-uniform elongation' at $\bar{R}^t$*

** Bridgman model application is limited to about 30% cross-section reduction, due to not considering the coalescence of the voids*

** The Bridgman-correction is applied by using the 'Mises' yield function and not a 'Gurson'-type void growth-capturing (porosity f) yield function. This led the author 20 years ago to propose his so-called 'Extended Mises' yield condition at the end of a joint Research program MAN with IWF-Freiburg.*

Idea:

The replacement of a 'Mises'-based Bridgman correction by a porosity-considering one should lead to a more realistic stress-strain curve and should offer the advantage to escape in the analysis from the high number of non-measurable 'Gurson' model parameters except from *f*. In order to consider the void growth, the author proposes to replace the Bridgman-corrected Mises-model by the mentioned ***'Gurson' model-linked Extended Mises****-model*'.

15.3 Porosity-improved Bridgman 3D-Correction of true σ-ε-Curve employing 'Extended Mises'

Porosity means volume change due to void coalescence. Such a volume change can be transferred to a decaying Poisson's ratio as it is known from Beltrami. The author experienced, that the usual 'Gurson'-analyses base on a 'Mises'-linked equivalent stress-equivalent strain curve. This should be improved when considering the porosity *f*. The author's hypothesis from 2002 reads:

* Formulation of an egg-shaped yield model, termed Extended Mises, with
* Simplification to 1 measurable 'Gurson' parameter f, only
* Improvement of this simpler model idea by applying a porosity-capturing equivalent $\sigma - \varepsilon$ curve
* Taking a simple 'Gurson' yield model to obtain via a 'comparison of coefficients' a relation to the porosity f in the simple 'Gurson' -model from Gurson-Tvergaard-Needleman, index **GTN**
* Probable 120°-material symmetry in the high porosity regime is not documented and therefore not considered. It can be captured by replacing $\frac{3J_2}{\bar{R}^2}$ through $\frac{3J_2}{\bar{R}^2} \cdot \Theta$ (see *Chapter 11*).

***LL*:**

** The 'Mises' cylinder is a simplification* (remember: §11, 120°-symmetry, $\Theta = 1$)

** Increasing porosity also means decreasing Poisson's ratio ν and an increasing elliptic shape.*

From knowledge in *Chapter 13* is known: Values for the increasing porosity *f* are strain-controlled detectable. The effect of a probably initially not pore-free material is captured in the initial property values.

14.1 Measurement of rod failure stresses and estimation of the vertex of the failure body

Even for a porous plastic failure body its vertex should be known from theoretical reasons. A vertex represents the equi-triaxial tensile strength capacity of a load-controlled strength situation, remind *Fig.15-2*. Because the vertex stress state $\{\sigma\} = (\text{true}\bar{R}^{ttt}, \text{true}\bar{R}^{ttt}, \text{true}\bar{R}^{ttt})$ with $TrF = \infty$ practically cannot be measured as best substitute a 3D-stress state - closest possible to the vertex - must be employed. Realistic is a stress state $(\text{true}\sigma_{ax} + \sigma_{hyd}, \sigma_{hyd}, \sigma_{hyd})$ by investigating the center of an un-notched tension rod test specimen, being the 'hot spot' in this test specimen.

In such un-notched rods a neck radius builds up and increases with further increasing axial tensile stress. Due to the diameter reduction a hydrostatic stress state is generated and can be determined from the zero volume strain regime faced in the minimum neck cross-section. Hereby, difference due to rolling of the sheet material and how the test specimen is cut out are neglected and full isotropy assumed.

From the test rig loading comes the subsequently effective stress 'trueσ_{ax}', whereas the remaining neck cross-section experiences in the center the multi-axial stress state $(\text{true}\sigma_{ax} + \sigma_{hyd}, \sigma_{hyd}, \sigma_{hyd})$, estimated by the Bridgman model. In order to better understand the stress situation in the rod center the effect of increasing σ_{hyd} is of interest, depicted below. It is to conclude from mechanics, that a hydrostatic stress does not change Mises's representative invariant J_2 for shape deformation of the solid. However, σ_{hyd} affects the tri-axiality value *TrF* which might be interpreted to cause some quasi-embrittlement of the material:

$$I_1 = (\sigma_I + \sigma_{II} + \sigma_{III}) = \mathrm{f}(\sigma) \;,\; 6J_2 = (\sigma_I - \sigma_{II})^2 + (\sigma_{II} - \sigma_{III})^2 + (\sigma_{III} - \sigma_I)^2 = \mathrm{f}(\tau)$$

$$(\text{true}\sigma_{ax} + \sigma_{hyd},\; \sigma_{hyd},\; \sigma_{hyd}) \;,\; \sigma^t_{ax}(r) = \sigma_1 + \sigma_{hyd}(r)$$

$$\sigma_{eq}^{Mises} = \sqrt{3J_2} = \sqrt{3}\cdot\sqrt{(\sigma_1^{M.} - \sigma_{h.} - \sigma_{h.})^2 + 0 + (\sigma_{h.} - \sigma_1^{M.} - \sigma_{h.})^2} \;\rightarrow\; \sigma_{eq}^{Mises} = \sigma_1^{Mises}$$

$$TrF = \sigma_{mean} / \sigma_{eq}^{Mises} = (I_1/3)/\sqrt{3J_2} = \left[\sqrt{2}/3\right]\cdot(I_1/\sqrt{3})/\sqrt{2J_2}$$

$$I_1 = (\text{true}\sigma_{ax} + 3\sigma_{hyd}) = \mathrm{f}(\sigma) \;,\quad 6J_2 = (\sigma_I - \sigma_{II})^2 + (0)^2 + (\sigma_{III} - \sigma_I)^2 = \mathrm{f}(\tau)$$

uni-axial σ_{ax}, multi-axial $(\sigma_{ax} + \sigma_{hyd}, \sigma_{hyd}, \sigma_{hyd})$ in the rod's minimum neck section $\Rightarrow \sigma_{eq}^{Mises}$.

Again: The use of notched rods is principally also possible but considering that the original notch radius *ρ* increases. Thereby the critical rod surface stress concentration reduces a little and the originally surface-located critical material location moves to the center. *Fig.15-9(left)* shall display different stress states and the associated points on the respective *TrF*-beams. In the subpicture down left the indicated 2D stress-states and up left further the 3D stress states all collected in the table right down.

Of interest for the designing engineer is that the spatially formulated SFC $F^{NF} = 1$ dents the failure body at the pressure vesessel situation $\{\sigma\} = (2,1,0) \rightarrow TrF = \sqrt{2}/3$, *Fig.15-2* and *15-9*. Remember: In the 2D principal stress plane F^{NF} is a straight line and in the 3D failure body a hyperbolic curve!

Fig.15-9 (right) shall make the non-linear development of *TrF* more clear and further make familiar with the design failure surfaces in the very ductile regime. The figure schematically shows that the strain-controlled failure surface is outside and thereby larger than the load-controlled one.

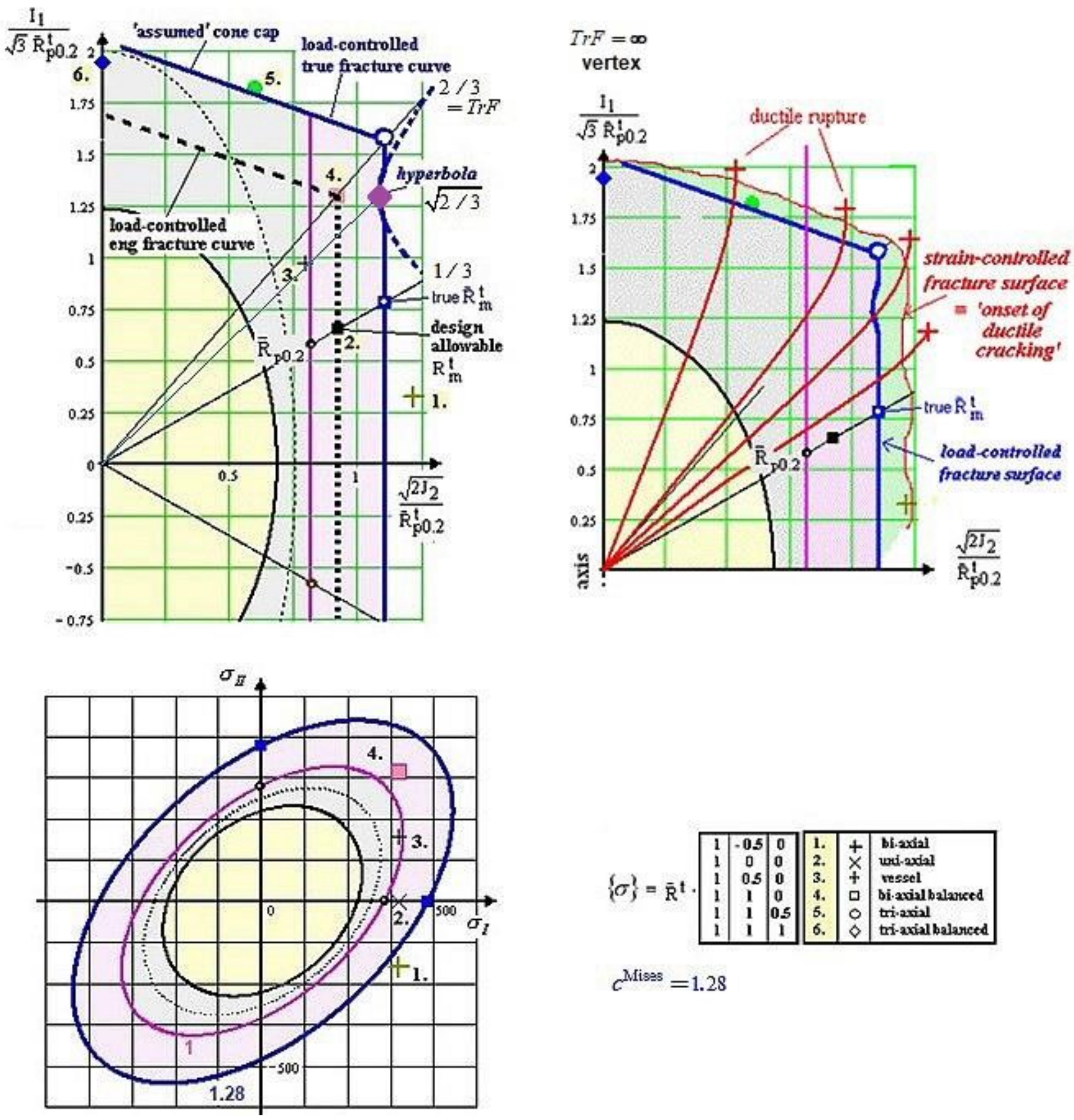

Fig. 15-9: Visualization of the effect of the TrF-beams and the related strengths, illustration of some stress state points and failure zones. 2D-potential surfaces on the inclined cross-section of the rotationally-symmetric failure body

15.4 Proposal of the Two Parameter 'Extended Mises' Yield function in the porosity domain

Extended Mises yield potential function

Originally, Gurson proposed for a metal, containing well distributed voids, a yield condition-based solution for a single spherical void. The model was modified later by Tvergaard and

Needleman, including the porosity f and the increasing Flow stress σ_F of the 'matrix' material: The porous body, called bulk material (*smeared material*), consists of the matrix material and the voids or pores. The voids are nucleated in tension, only. The dense matrix phase follows the HMH ('Mises') model, and f represents the mean void volume fraction or porosity (*average value of a porous matrix*) as the so-called internal damage variable. For $f = 0$, fully dense material, the model reduces to that of von Mises, whereas a ultimate value f_{ult} implies that the material is ultimately voided that it has lost its stress carrying capacity due to local ductile rupture. Here, f_{ult} shall be replaced by the smaller $f_{odc} = f_{crit}$. Values for the increasing porosity f are strain-controlled detectable and therefore, the ratio is fixed. <u>*Table 15-2*</u> describes the procedure how a relationship

Table 15-2: 'Comparison of Coefficients' of the models 'Gurson' ↔ 'Extended Mises' with σ_F as increasing true Flow stress as running stress variable

$$F^{\mathrm{GTN}} = \frac{3J_2}{\sigma_F{}^2} + 2 \cdot f \cdot q_1 \cdot cosh\left(\frac{I_1 \cdot q_2}{2 \cdot \sigma_F}\right) + q_3 \cdot f^2 = 1$$ ductile micro-damage failure function

simplified to $\frac{3J_2}{\sigma_F{}^2} + 2 \cdot f \cdot cosh\left(\frac{I_1 \cdot q_2}{2 \cdot \sigma_F}\right) + f^2 = 1$ appropriate for idea demonstration, $q_3 = q_3 = 1$

If the cosh-function is replaced by the first two terms of the associated Taylor row [*Cun*98,*Cun*01]

$$cosh\, x = \pm\,(1 + x^2 / 2 + ...) \rightarrow \cosh(I_1 \cdot q_2 / 2 \cdot \sigma_F) = \pm\,(1 + (I_1{}^2 \cdot q_2{}^2 / 8 \cdot \sigma_F{}^2) + ..) \,.$$

The negative sign is to chose because porosity reduces strength capacity

$$\frac{3J_2}{\sigma_F{}^2} - 2 \cdot f \cdot \left(1 + \frac{I_1{}^2 \cdot q_2^2}{8 \cdot \sigma_F{}^2}\right) + f^2 = 1 \quad \Rightarrow \frac{3J_2}{\sigma_F{}^2} - 1 \cdot f \cdot \left(\frac{I_1{}^2 \cdot q_2^2}{4 \cdot \sigma_F{}^2}\right) + 2f - f^2 = 1.$$

With $f^2 << f$ can be derived

$$\frac{3J_2}{\sigma_F{}^2} - f \cdot \frac{q_2^2}{4} \cdot \frac{I_1{}^2}{\sigma_F{}^2} - 2f = 1$$ with $q_2 = 1.5$ as guess for the plastic damage flow function

$$\frac{3J_2}{\sigma_F{}^2} - f^* \cdot \frac{I_1{}^2}{\sigma_F{}^2} - 2f = 1$$ with the elliptic shape parameter f^*

$$\kappa = \frac{1 - 2\nu}{2 + 2\nu} \equiv f \cdot \frac{q_2^2}{4} = f^* \quad \rightarrow \nu = (4 - f^*) / (8 + 2f^*).$$

$\Rightarrow$ Failure state, normalized again with the shear strength, to insert is $\sigma = \bar{R}_{odc}$

$$F = \frac{3J_2}{\bar{R}_{0.2}^2} + f_{ult}{}^* \cdot \frac{I_1{}^2}{\bar{R}_{0.2}^2} + 2 f_{ult} = 1 = Eff = 100\%$$ material stressing effort,

$F = 100\%$ = potential surface, which may be a fracture surface or a yield surface.

From 'Comparison of Coefficients' finally is obtained

ExtendedMises $F = \frac{3J_2}{\bar{R}_{0.2}^2} + c_{12} \cdot \frac{I_1{}^2}{\bar{R}_{0.2}^2} = c^{\mathrm{ExtMis}}$, generally

Analogous to 'Mises' $Eff^{\mathrm{Mises}} = \sigma_{\mathrm{eq}}^{\mathrm{Mises}} / \bar{R}_{0.2} = \sqrt{3J_2} / \bar{R}_{0.2} \Rightarrow Eff^{\mathrm{ExtMises}} = \sigma_{\mathrm{eq}}^{\mathrm{ExtMises}} / \bar{R}_{0.2}$

follows $\sigma_{\mathrm{eq}}^{\mathrm{ExtMises}} = \sqrt{\frac{3J_2 - f^* \cdot I_1{}^2}{1 + 2f}}.$

between the subsequent ‘Gurson’ type yield model and the ‘Extended Mises’ model was developed. A further equation is needed to determine the size parameter, such as with c^{Mises} of the ‘Mises cylinder’.

Void Porosity-linked reduction of Poisson’s ratio $0.5 > \nu$

Porosity means volume change due to void coalescence and volume change may be transferred to a decaying Poisson’s ratio, remind Beltrami. From the ExtM-model can be geometrically deduced $f^* = f \cdot q_2^2$ and $\nu = (4 - f^*) / (8 + 2 \cdot f^*)$.

Fig. 15-10 points out how the Poisson ratio is linked to the true strains (left), schematically to the true equivalent stress (center), and to the porosity f^*.

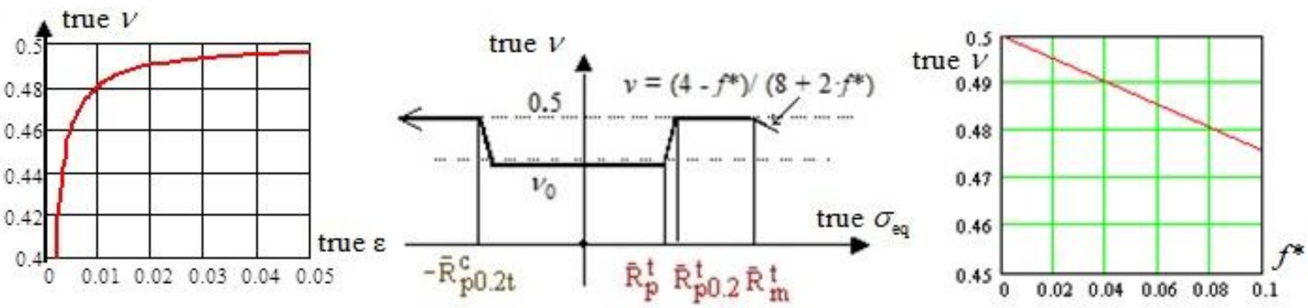

Fig. 15-10: Dependence of ν on the different parameters, the various regimes

Here, $f_{ult}(\bar{R}_{odc}) < f_{rup}$ is employed as that critical porosity which was dedicated by the author to ‘Onset of ductile cracking’, in order to ‘remain on the safe side’. The evolution function of f is assumed to follow an exponential course with practically $f = 0$ at the tensile strength point up to the defined ultimate value f_{ult} located at $\bar{R}_{odc}$.

15.3 Visualization of ’Gurson’-model versus ‘Extended Mises’-model

Failure conditions enable the designer to assess multi-axial states of stress $\{\sigma\}$ by an equivalent stress σ_{eq} and to map multi-axial stress-strain behavior $\sigma_{eq}(\varepsilon_{eq})$ via a measured, smeared stress F/A. For $f = 0$, fully dense material, the model reduces to that of HMH, whereas a maximum value f_{ult} implies that the material is ultimately voided that it loses its stress carrying capacity due to local ductile rupture.

The conventional visualization – as a parameter investigation - of the Gurson model is presented in *Fig.15-11 (left)* with f being the porosity parameter of the curves and q2 a Gurson parameter from the comparison. A growing f means higher true stress but less cross-section or load-carrying material in the strain-controlled ‘hot spot’. This is displayed in the figure by the change of the cylinder shape versus an egg shape.

Another visualization, usually practiced in structural mechanics, is given by using the Lode-Haigh-Westergaard parameters. This leads to a change in the shape, *Fig.15-11 (center)*. For $f = 0$ the Mises cylinder is obtained.

Fig.15-11 (right) depicts the various strength values such as $true\bar{R}^t, \bar{R}_{odc}$ as increasing true strength points to be inserted into the Extended Mises function size parameter, finally visualized as flow potential surfaces for four strength-linked porosity levels.

The parameter comparison with ‘Gurson’ let to take a reduced value $q_2 = 1.13$, however, due to missing test data the author sticks to 1.5. In this context, the respective ExtendedMises parameter

c_{12} can be determined, decoupled from the 'Gurson' Comparison of Coefficients, if having a reliable test data set available

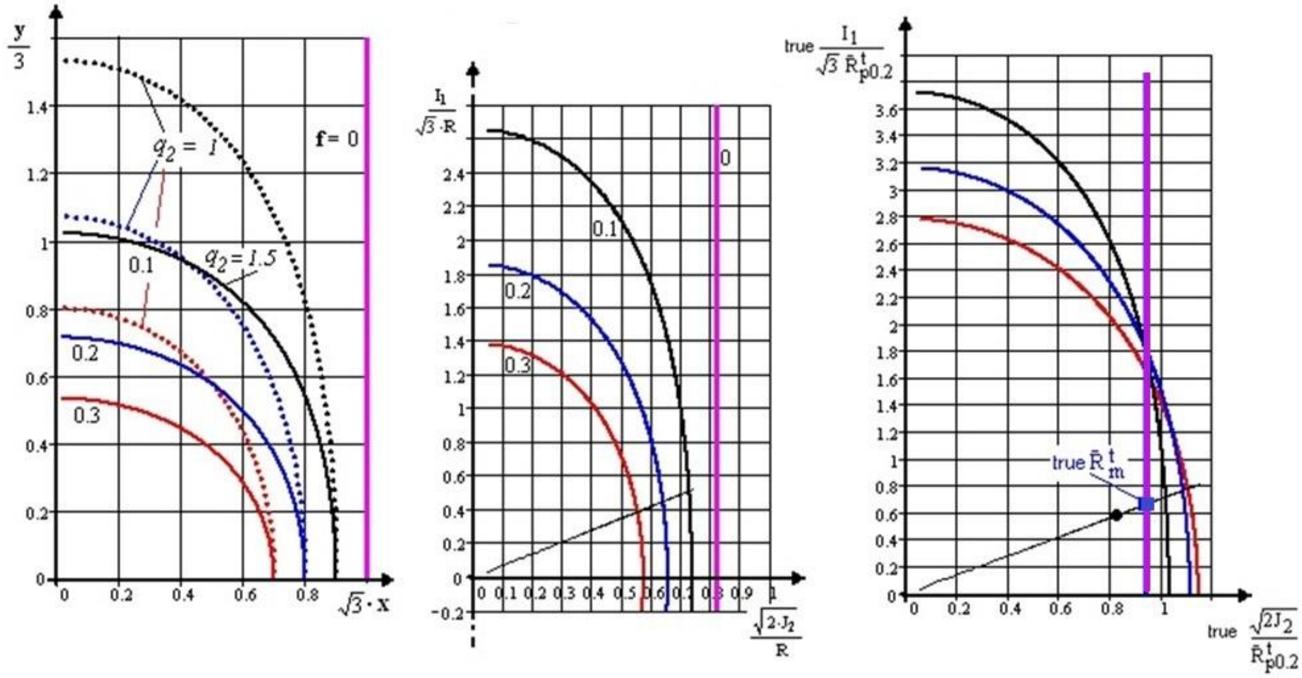

Fig. 15-11: Schematic comparison of the Gurson model (dots) and Extended Mises model Potential surfaces. (left) Display of curve parameter porosity f influence, using the 'Gurson' coordinates x =($\sqrt{J_2}/\sigma_F$), y= (I_1/σ_F), $\sigma_F = \bar{R}^t_{p0.2}$; (center) Display of the Gurson yield model in Lode-Haigh-Westergaard parameters $\bar{R}^t_{p0.2}$ = normalisation strength); (right) Ppotential surfaces of the ExtMises-model with four increasing true (graphs made about 2001) AA2219, (q2=1.5, $q2_{ExrM}$=1.13) true$\bar{R}^t$, $\bar{R}_{odc}$.

Table 15-3: Replacement of the Mises-based Bridgman curve $\sigma_{eq}(\varepsilon_{eq})$ by an ExtMises one

Table 25-1: $\sigma^t_{ax}(r) = \sigma_I + \sigma_{hyd}(r)$ and from Bridgman $\sigma_{hyd} \approx \sigma_I \cdot \boldsymbol{ln}\left(1+\frac{a^2-r^2}{2\cdot a\rho}\right)$
$\sigma^{MisBri}_{eq} = \sqrt{3\cdot J_2} = \sigma_I = \frac{F}{A} / (1+2\cdot\rho/a)\cdot\ln(1+0.5\cdot a/\rho)$, valid > $\bar{R}^t$ < ?**,**
$I_1 = \sigma_I + 3\sigma_{hyd} = \sigma_I\cdot(1+3\cdot\boldsymbol{ln}(1+0.5\cdot a/\rho))$ for the critical central 'fiber' at r = 0
considering Bridgman (above) and the notch-curvature change by Lorrek-Hill's approach,
giving a maximum value for the unknown $\rightarrow$ $\max\frac{a}{\rho} = \sqrt{\ln\left(\frac{1}{1-Z}\right) - \ln\left(\frac{A_0}{A_{oon}}\right)}$**,**
inserting $\sqrt{3\cdot J_2} = \sigma_I$ and $\frac{F}{A} = true\sigma_{ax}$ the equivalent stress reads:
$\sigma^{ExtMises}_{eq} = \sqrt{\frac{3J_2 - f^*\cdot I_1^2}{1+2f}} = \sigma_I\sqrt{\frac{1-f^*\cdot(1+3\cdot\boldsymbol{ln}(1+0.5\cdot a/\rho))^2}{1+2f}}$
valid $\bar{R}^t < \bar{R}_{odc}$, (shape parameter) $f\cdot\frac{q_2^2}{4} \equiv f^*$, set $q_2 \cong 1.5 \rightarrow 1.13$.
Porosity parameter f and curvature parameter a/ρ increase from about 0 to the maximum at $\bar{R}_{odc}$.

The author's full idea consisted of the two parts: Above ExtMises model plus porosity-improved

Bridgman evaluation, which was depicted in *Table 15-3*. The table displays all relations in order to establish the 'searched' equivalent stress $\sigma_{eq}^{ExtMises}$.

Reminder: to capture '120°-rotational symmetry' would require to replace J_2 by $J_2 \cdot \Theta$.

15.3 Visualization of the Bridgman–corrected true curve with consideration of porosity

In order to obtain a realistic equivalent stress curve it is physically mandatory to consider the increase of porosity *f* and the increase of the notch curvature by applying $a \;/\; \rho$. The mapping of the changing notch curvature and the changing porosity is shown below:

Mapping of the changing notch curvature: Data and determination procedure by Mathcad

$$\frac{a}{\rho} = \sqrt{\ln\left(\frac{A_0}{A_{rupt}}\right) - \ln\left(\frac{A_0}{A_{oon}}\right)} = 1.096 \text{ from } \frac{A_{rupt}}{A_0} = 1 - Z = 1 - 0.20 = 0.80,$$

$$\frac{A_0}{A_{rupt}} = \frac{1}{0.80} = 1.25, \quad \frac{A_0}{A_{oon}} = \left(\frac{4.0}{3.89}\right)^2 = 1.057 \to \max \frac{a}{\rho} = 0.409 \text{ at } R_{rup}.$$

Applying Lorrek-Hill's value Bridgman's approach delivers $\max\,(1+\frac{2\rho}{a}) \cdot \ln(1+\frac{a}{2\rho}) = 1.096.$

Then, for the previously proposed formulation the curve parameters can be computed:

$$\text{stressing} \qquad \frac{a}{\rho} = a\rho = c_1 + c_2 + \text{true}\varepsilon_{ax} R_{odc}{}^2 + c_3 \cdot \text{true}\varepsilon_{ax} R_{odc}{}^3.$$

$a\rho = 1.096 \quad \text{true}\varepsilon\,axR02 = 0.0071 \quad \text{true}\varepsilon\,axRt = 0.055 \quad \text{true}\varepsilon\,axRodc = 0.231$

Vorgabe $\quad c1 := 1 \quad c2 := 100 \quad c3 := 1$

$\boxed{1 = c1 + c2 \cdot \text{true}\varepsilon\,axR02^2 + c3 \cdot \text{true}\varepsilon\,axR02^3}$ $\quad \boxed{1.00005 = c1 + c2 \cdot \text{true}\varepsilon\,axRt^2 + c3 \cdot \text{true}\varepsilon\,axRt^3}$

$\boxed{a\rho = c1 + c2 \cdot \text{true}\varepsilon\,axRodc^2 + c3 \cdot \text{true}\varepsilon\,axRodc^3}$

$A\rho := \text{Suchen}(c1, c2, c3)$

$A\rho = \begin{pmatrix} 1 \\ -0.548 \\ 10.148 \end{pmatrix} \quad c1 := A\rho_0 \quad c1 = 1 \quad c2 := A\rho_1 \quad c2 = -0.5476 \quad c3 := A\rho_2 \quad c3 = 10.1478$

$$\boxed{A\rho_j := c1 + c2 \cdot \left(\text{true}\varepsilon\,ax_j\right)^2 + c3 \cdot \left(\text{true}\varepsilon\,ax_j\right)^3}$$

Mapping of the changing porosity *f*: Data set used and determination by Mathcad

The set points of the curve are the porosity values at the tensile strength point R^t and at R_{odc}.

Vorgabe $\quad e1 := 0 \quad e2 := 1$

$$0.0002 = \left(e1 \cdot \exp\left(\frac{\text{true}\varepsilon\,axRt}{\text{true}\varepsilon\,axRodc} - 1\right)\right)^{e2} \qquad fodc = (e1 \cdot \exp(1-1))^{e2}$$

$Af := \text{Suchen}(e1, e2)$

$Af = \begin{pmatrix} 0.6292 \\ 6.9469 \end{pmatrix} \quad e1 := Af_0 \quad e1 = 0.6292 \quad e2 := Af_1 \quad e2 = 6.947$

$$\boxed{fexp_j := \left(e1 \cdot \exp\left(\frac{\text{true}\varepsilon\,ax_j}{\text{true}\varepsilon\,axRodc} - 1\right)\right)^{e2}}$$

Fig.15-12 displays the author's design verification idea, about 2000. The influence of the practically starts at R_{odc}.

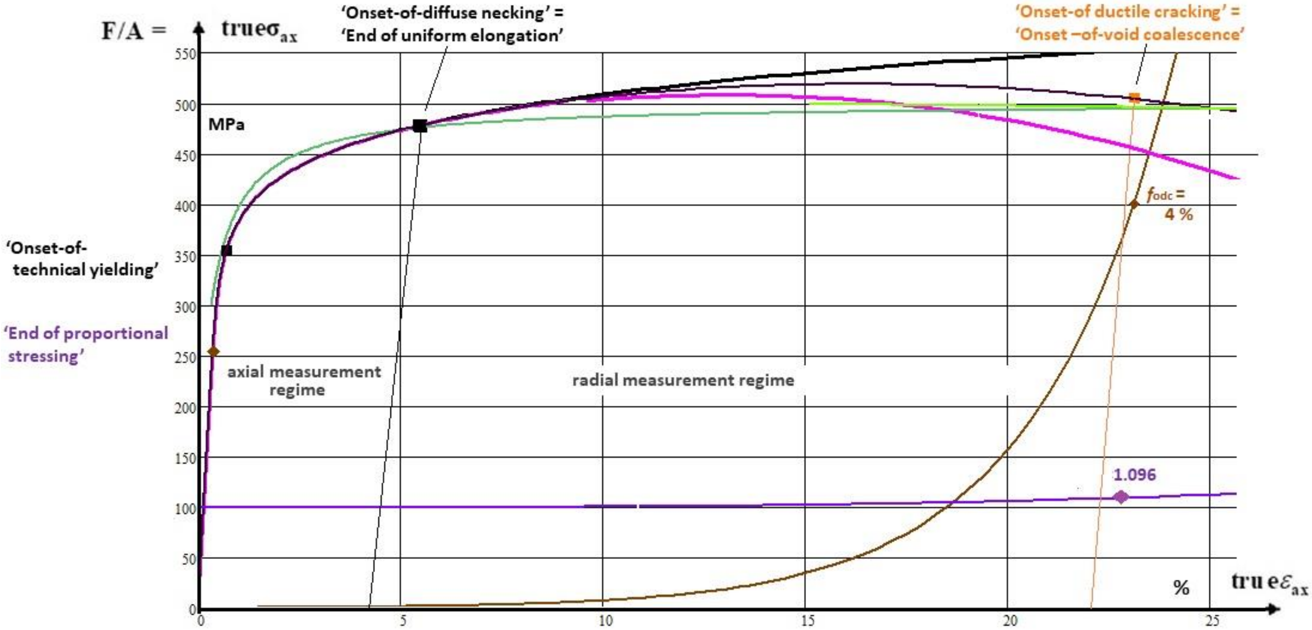

Fig. 15-12, AA2219, base material T2, 6 mm thick: Visualization of the equivalent stress curve $\sigma_{eq}^{ExtMises}$;

Ramberg-Osgood-mapped measured cross-section smeared axial stress F/A;

Increase of plastic porosity f with f_{odc} = 4% at R_{odc}; *Increase of the notch curvature* a / ρ *with*

$a / \rho = 0.409$ at R_{ult} (replacing the higher R_{odc}); *Increase of ν in the elastic-plastic transition domain approaching 0.5 and barely visible the decrease in the porous domain*

15.4 Specific Potential Surfaces being Strength Failure Criteria

Brittle 'porous' materials may still fracture in the elastic-plastic transition domain. For this fact, Ismar and Mahrenholtz [*Ism82*] developed a Beltrami-based SFC model describing the failure behavior of a material between the proportional limit and the 'onset of yielding'. In *Table 15-4* the SFC-formulations in all regimes shall be comparatively displayed. This includes potential surface descriptions and associate strength failure criteria SFCs.

LL:

- ✓ *Whereas with the elasticity formulation of Beltrami the Poisson ratio ν is growing this is opposite with the formulation of a porosity-linked plastic model due to the increasing porosity*
- ✓ *The hypotheses of Beltrami, Mises, Gurson describe an increase or decrease of surfaces of constant potential. The shape of the surface theoretically begins with $\nu = 0$ (sphere, found with foams) growing up from $0 < \nu$ to $\nu = 0.5$ via the growing Mises cylinder keeping $\nu = 0.5$ and ending with an ellipsoid, which shrinks into a spherical direction represented by 0.5 > ν.*
- ✓ *For two domain limits a clear value for the varying Poisson ratio is given:*

  proportional limit $\sigma \leq \bar{R}^t_{prop} \Rightarrow \nu = \nu_0$ *and yield limit* $\sigma = \bar{R}^t_{p0.2} \Rightarrow \nu = 0.5$
- ✓ *Designing requires to use limit state formulations, termed failure criteria (SFCs). These are fracture failure criteria for brittle materials namely for 'Onset-of-fracture' and yield failure criteria for ductile materials. In practice, for ductile materials these failures are 'Onset-of-yielding' and - for the author - 'Onset-of-void coagulation = Onset of ductile Cracking ' in the case where strain-softening applies*
- ✓ *A Strength Failure Criterion represents a defined Design Limit State and is therefore a special*
- ✓ *critical Potential Surface F.*

** The novel Extended Mises model just requires the determination of one more parameter, the porosity value f. All model parameters are measurable quantities.

** With the novel porosity-capturing σ-ε curve, being a ductile porosity-improved Bridgman correction, a simplified plastic analysis procedure could be achieved.

** For engineering reasons $true\bar{R}^t \Rightarrow \bar{R}_{\mathrm{odc}}$ will represent the load carrying capacity to be considered.

Table 15-4, Isotropic materials: Determination of model parameters,single mode view.

* Modelling Functions F describing a subsequent potential surface

elastic-plastic	plastic	plastic porous
Beltrami	Hencky-'Mises'-Huber	'Gurson' type

$$\bar{R}^t_{prop} < \sigma_{\mathrm{Bel}} < \bar{R}^t_{0.2} \quad \leftrightarrow \quad \bar{R}^t_{0.2} < \sigma_{\mathrm{Mis}} < \bar{R}^t_m \quad \leftrightarrow \quad \bar{R}^t_m < \sigma_{eq} < \bar{R}^t_{\mathrm{odc}}$$

stress - controlled *strain – controlled*

σ : = running variable of the subsequent potential surfaces

$$\bar{R}^{t\,2}_{prop} / \bar{R}^{t\,2}_{0.2} < c^{\mathrm{Bel}} < 1 \quad \leftrightarrow \quad 1 < c^{\mathrm{Mis}} < \bar{R}^{t\,2}_m \;/\; \bar{R}^{t\,2}_{0.2}$$

ellipsoid → cylinder → ellipsoid

$$I_1 = (\sigma_I + \sigma_{II} + \sigma_{III}) = \mathrm{f}(\sigma)\,, \quad 6J_2 = (\sigma_I - \sigma_{II})^2 + (\sigma_{II} - \sigma_{III})^2 + (\sigma_{III} - \sigma_I)^2 = \mathrm{f}(\tau)$$

$$\frac{3J_2}{\bar{R}^{t\,2}_{0.2}} + \kappa \cdot \frac{I_1^{\,2}}{\bar{R}^{t\,2}_{0.2}} = c^{\mathrm{Bel}} \leftrightarrow \quad F^{Mis} = \frac{3J_2}{\bar{R}^{t\,2}_{0.2}} = c^{\mathrm{Mis}}\,, \; \kappa = \frac{1-2\nu}{2+2\nu}$$

Insertion of a (measurable) normalizing strength, yield strength point with $\nu = 0.5 \rightarrow \kappa = 0$

$$\mathrm{F}^{Bel} = \frac{3\bar{R}^{t\,2}_{02} \;/\; 3}{\bar{R}^{t\,2}_{02}} + \kappa \cdot \frac{\bar{R}^{t\,2}_{02}}{\bar{R}^{t\,2}_{02}} = c^{\mathrm{Bel}}{*} \rightarrow c^{\mathrm{Bel}} = 1 + \kappa = 1, \text{ and } \kappa \text{ an elliptic shape parameter}$$

* Strength FailureCriteria (SFC), $\bar{R} \rightarrow R$, (with $\Theta = 1$ for full rotational symmetry)

R : = strength design allowable, marking a special potential surface ≡ design limit state

elastic, very brittle	ductile	very ductile

$$Eff = \frac{\sigma_1}{\bar{R}^t_m} = 1\,{*} \quad \leftrightarrow \quad Eff = \frac{3J_2}{\bar{R}^{t\,2}_m} = 1 \quad \leftrightarrow \quad Eff = \frac{3J_2}{\bar{R}^{\,2}_{\mathrm{odc}}} + c_{12} \cdot \frac{I_1^{\,2}}{\bar{R}^{\,2}_{\mathrm{odc}}} - 2\,f_{odc} = 100\%.$$

For similarity reasons: for the 2 modes Normal Fracture NF , Shear Fracture SF (brittle)

and after inserting $\sigma = R \cdot Eff$ and dissolving for Eff follows

$$\mathrm{I}_1 > 0: F^{NF} = 0.5 \cdot \frac{\sqrt{4J_2 - I_1^{\,2} / 3} + I_1}{2 \cdot \bar{R}^t} = 1\,; \quad Eff^{NF} = 0.5 \cdot \frac{\sqrt{4J_2 - I_1^{\,2} / 3} + I_1}{2 \cdot \bar{R}^t}$$

$$\mathrm{I}_1 < 0: F^{SF} = c_1^{SF} \cdot \frac{3J_2}{\bar{R}^{c2}} + c_2^{SF} \cdot \frac{I_1}{\bar{R}^c} = 1; \quad Eff^{SF} = \frac{c_2^{SF} \cdot I_1 + \sqrt{(c_2^{SF} \cdot I_1)^2 + 12 \cdot c_1^{SF} \cdot 3J_2}}{2 \cdot \bar{R}^c} = \frac{\sigma_{eq}^{SF}}{\bar{R}^c}$$

$c_1^{SF} = 1 + c_2^{SF}$ with direct consideration of the Poisson ratio $c_2^{SF} = (1 + 3 \cdot \mu) / (1 - 3 \cdot \mu)$

Last unknown to be searched is the elliptic shape linked parameters such as c_1^{SF} by insertation of a bi-axially compressive failure stress or a fracture angle $\mu = \cos(2 \cdot \theta^{c}_{fp}{}^{\circ} \cdot \pi / 180)$.

<u>Non-linear stress–strain analysis Note</u>:

Usually Co-axiality, Prandtl-Reuss equations and an Associated Flow Rule is employed in order to predict strain rate $\dot{\varepsilon}_{ij}$ and the Lagrange multiplication (*proportionality*) factor $\dot{\lambda}$.

16 Note on Continuum (micro-)Damage Mechanics (CDM)

***Aim**: Primarily checking CDM application whether it is mature for a reliable Static Design Verification.*

CDM is applied for ductile and brittle materials. The loading may be static and cyclic, with the latter requiring fatigue investigation. Regarding stress-strain curves, CDM principally captures the load-controlled hardening part and the deformation-controlled softening part. Softening part examples are the still mentioned embedded UD layer (*Fig.16-1*) and the ductile metal tensile rod described in the last Chapter by a porosity–capturing 'Gurson' model. Results of isotropic analyses, employing the softening curve branch, can be used to better design notches, openings in pressure vessels (fuel tank task in Ariane 5 upper stage) etc.

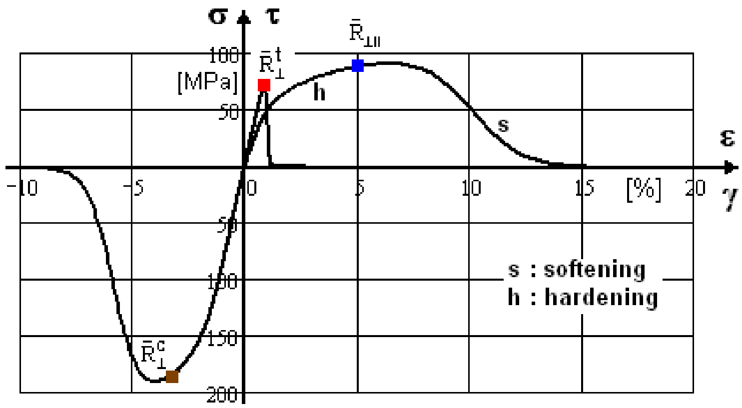

Fig.16-1, example UD ply: Full stress-strain curve with load-controlled hardening and deformation-controlled softening of the layer (ply) embedded in a laminate

CDM is pretty linked to multi-scale modelling, which will be looked at in the next Chapter.
All materials are generally composites. Applying CDM one goes down to the constituents of a composite to metallic grains or to fiber and matrix for instance.
Moving down on the scales it is helpful to use the physical formulations gained on the macro-scale such as Mises yielding with ductile metals in the tension and compression loading domain and Mohr-coulomb friction behavior of brittle materials in the compression domain.
Shear stress loading is composed of a tensile stress with a compressive stress. This activates two failure modes, which leads to normal fracture in the case of brittle materials. These physical effects stay valid at the lower scale and are to consider *adjusted*.

***LL**:*

It is always to check, whether a Mises yield criterion can be applied to quantify micro-damage portions or a fracture criterion in the case of very brittle behavior, i.e. Fiber Reinforced Plastics (FRP) experiencing matrix yielding:

16.1 Static Behavior

Micro-damage formulations:

CDM is basically used to capture the evolution of the micro-damage state from micro-damage $D = 0$ up to 'Onset-of-Failure' at *maxD*, which is for brittle materials at the end of hardening or at achieving the strength *R*.

In CDM, the formulation of the describing constitutive equation is based on one of the following two approaches (*Here the stress-strain curve is meant*):

(1) The strain equivalence principle approach or on

(2) The stress equivalence principle approach.

From engineering side, the latter is preferred because 3D stress states and residual stresses have to be considered in design dimensioning.

The constitutive relationships are formulated in the effective undamaged configuration $\sigma_{eff} = \sigma / (1 - D)$ with a stress-strain relation linked by the stiffness elasticity matrix [C], which reduces due to growing micro-damage. *Fig.16-2* exemplarily depicts the relationship for a 2D-loaded transversely-isotropic UD material. By inversion of the effective compliance matrix S_{eff} the decaying stiffness matrix C_{eff} is obtained.

$$\{\sigma\} = [C] \cdot \{\varepsilon\} \rightarrow \{\varepsilon\} = [S] \cdot \{\sigma\} \quad \text{as practical test-linked formulation}$$

$$S_{\text{eff}} = \begin{bmatrix} \dfrac{1}{E_1 \cdot (1 - D_{11})} & \dfrac{-\nu_{21}}{E_1} & 0 \\ \dfrac{-\nu_{12}}{E_2} & \dfrac{1}{E_2 \cdot (1 - D_{22})} & 0 \\ \text{(symm)} & 0 & \dfrac{1}{G_{12} \cdot (1 - D_{66})} \end{bmatrix} \quad \text{with } D = \begin{bmatrix} D_{11} & D_{21} & 0 \\ D_{21} & D_{22} & 0 \\ \text{(symm)} & 0 & D_{66} \end{bmatrix}$$

usually not considering the off-diagonal D_{21}.

Fig.16-2, 2D-example UD material: Compliance matrix [S] and micro-damage matrix [D].

The D_{ij} represent the accumulation of the micro-damage process portions and are theoretically terminated by max$D$ at the tensile strength point in the case of brittle materials and at the rupture point for very ductile isotropic materials. These portions may occur during a monotonically increasing static loading. For brittle materials micro-damage starts at the 'elastic end' being a level where *Eff* has still reached a value, see Fig.16-3. Unfortunately, max$D$ in static CDM cannot become 100% due to its usual modelling basis! The center figure outlines how a stress-man views the 'onset

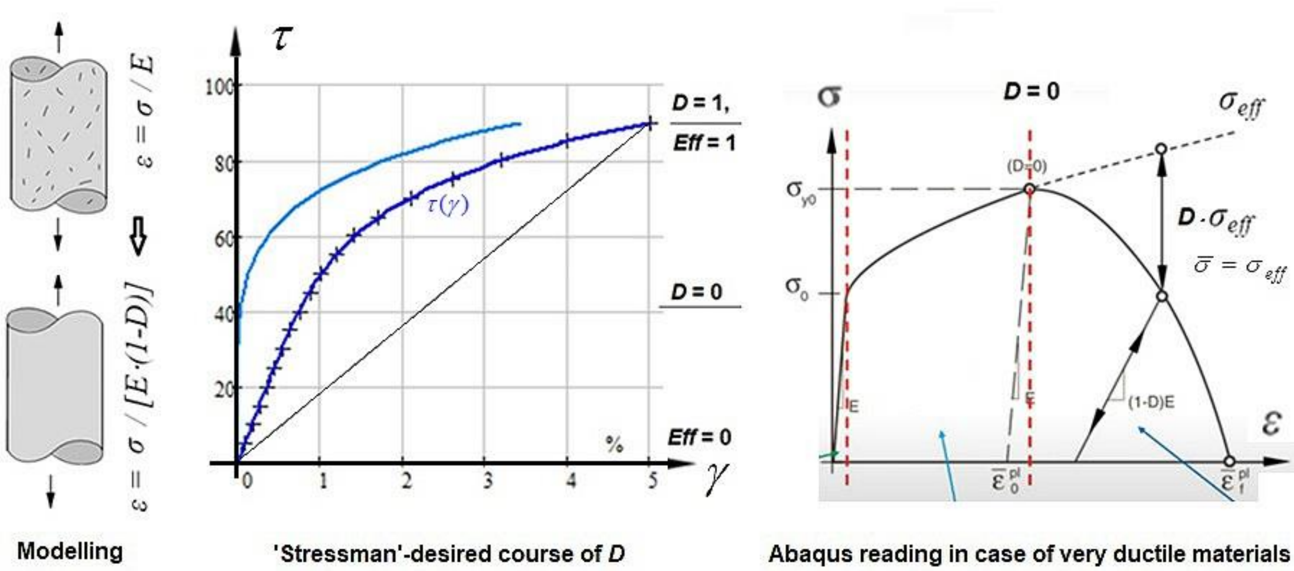

Fig.16-3: The various 'Onset- of- Failure' envelopes: (left) Smearing of the micro-damaged material, (center) shear of a slightly brittle material, (right) Ductile material (Ansys FEA code)

of micro-damage' of a slightly brittle material. In the elastic domain < $R_{prop} \equiv R_{e(lastic)}$ there is no D-contribution. The blue 'flow curve' then will contribute.
The right figure (from Abaqus) surprisingly outlines that there micro-damage first begins with void nucleation and coagulation which rises the Question:

Does really not any micro-damage happens below R^t ??

Micro-Damage-free (*in German schädigungsfrei, nicht schadensfrei*) and crack (= macro-damage, *in German Schaden*)-free does not mean free of flaws.

LL:
- *CDM is generally always good for understanding static & cyclic material behavior*
- *Confusing is faced regarding 'onset of counting micro-damage'portions in static case: once < R^t but also > R^t*

Material behavior-determined slip and failure angles:

The number of slip systems in ductile metals is usually high, and those that are active possess an orientation near to the planes with maximum shear stress. Under uniaxial loading the planes of micro-cracks are always inclined approximately 45° to the direction of the applied tensile stress, see (*Fig.16-4*). In single crystals, the lattice structure is spatially oriented in such a way that a sliding plane is obtained at an angle of 45°. In poly-crystalline metals with randomly distributed lattice sub-structures this will change a little.

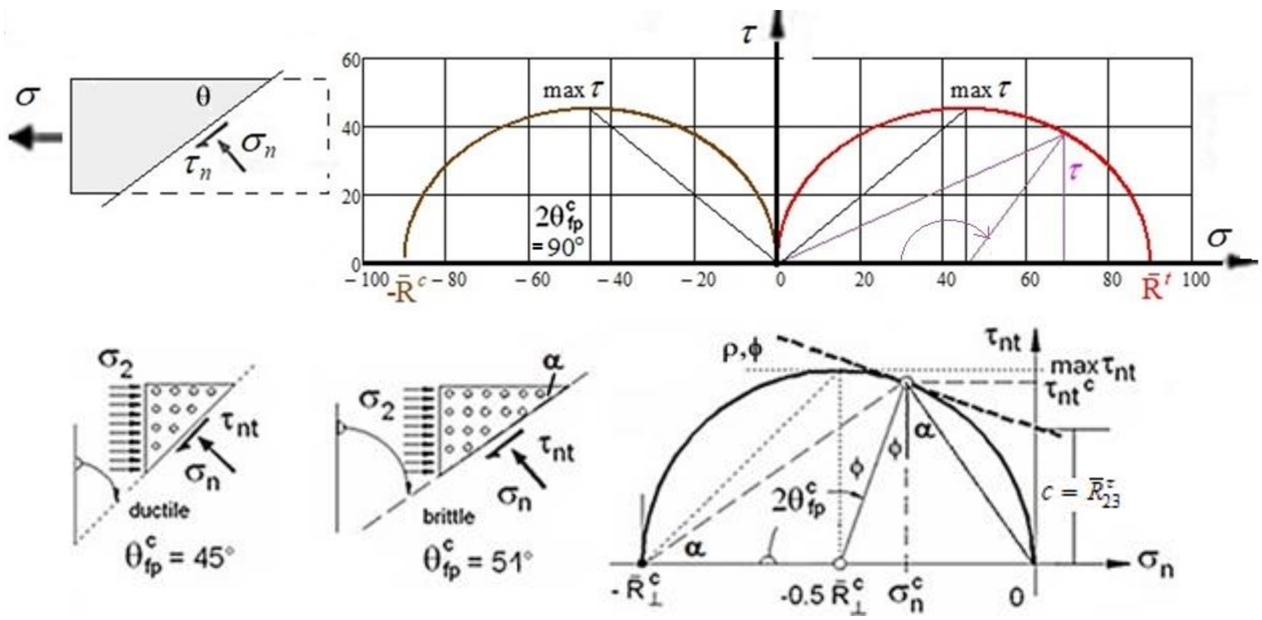

Fig. 16-4, very ductile metal material: (up) Mohr stresses and failure angles. (below) Mohr stress circle for a compressive and a tensile uniaxial external stress of a semi-brittle material

$\tau_n = \sigma \cdot \cos(\alpha) \cdot \sin(\alpha)$ with α the angle to σ direction, $2 \cdot \max\tau = \sigma$ for $\alpha = 45°$

Known from brittle material behavior under compression is: *The failure angle depends on the friction value* μ. After the formula, derived in [*Cun23c*], the computation of the failure angle with the Mohr-Coulomb model delivers exemplarily for a material friction value $\mu = 0$ (= *fully ductile)* the expected value of 45° and for a friction value $\mu = 0.2$ the angle 51°, see *Fig.16-5*. The author presents in this figure that the angle changes from the 51° at the compression strength point $\bar{R}_\perp^{\,c}$ up to 90° at the tensile strength point $\bar{R}_\perp^t$.

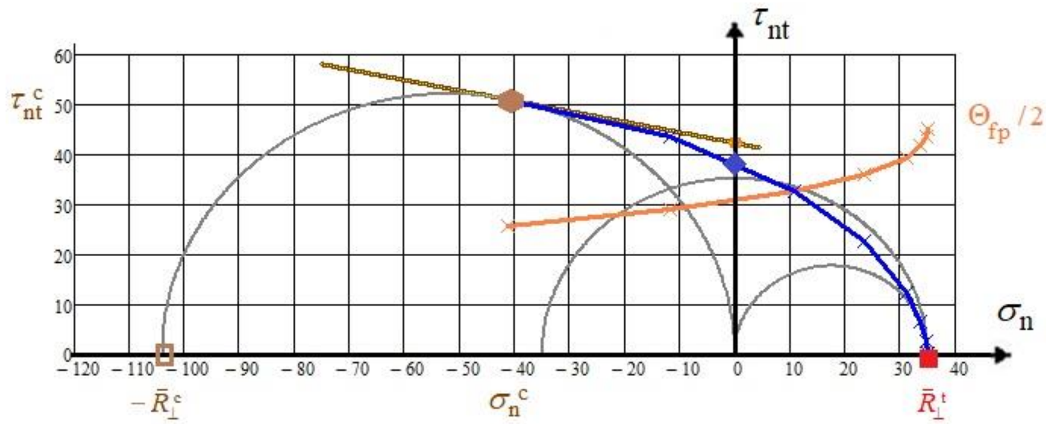

Fig.16-5, brittle UD-material: Joint display of the UD failure curve in Mohr stresses, indicating an fracture angle increase Θfp° when approaching $\bar{R}_\perp^t$. Shear fracture plane angle in the touch point 51° and linear Mohr-as well as a more realistic curved Mohr-Coulomb friction curve. Touch point is defined by $(\sigma_n^c, \tau_{nt}^c)$, linked to $\bar{R}_\perp^{\,c}$.

16.2 Cyclic Behavior of Ductile Metals applying Micro-scale Material Modelling

Once micro-cracks have nucleated due to strain accumulation from cyclic slipping, they grow in the early stage typically in the order of the material's grain size (text from M. Mlikota - S. Schmauder: *Thanks to Siegfried*). In the course of further cyclic loading, micro-cracks, formed along these slip bands, will grow and link together. In metals and alloys they grow predominantly along the crystallographic planes because they are highly affected by microstructural barriers such as grain boundaries or other micro-structural features. The coalescence of trans-granular micro-cracks, namely, if two micro-cracks meet each other at the same grain boundary, is performed in the numerical simulation of the crack initiation after Tanaka-Mura. It occurs if the average stress in between their tips surpasses the elastic limit *Re* of the material's new micro-crack, created on this grain boundary line, uniting the two trans-granular micro-cracks into a single one (*example pure iron Re = 260 MPa).*

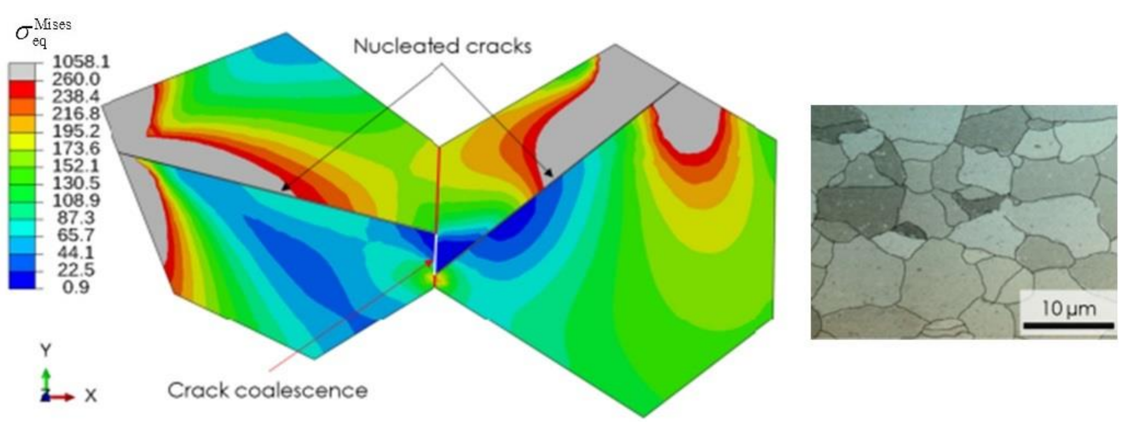

Fig.16-6: Simulation of AA micro-crack coalescence (Lorenzino, P., Navarro, A. & Krupp, U. (2013), 'Naked eye observations of microstructurally short fatigue cracks', Int. J. of Fatigue 56(0), 8-16.

Already nucleated crack segments tend to extend along the whole grain, causing local stress relaxation as well as concentrations at their tips and by that amplifying the likelihood for new crack

formation in the vicinity. In the course, micro-cracks form along the slip bands, grow and join.
The change of the crack plane from the crystallographic plane to a non-crystallographic plane perpendicular to the external stress axis is called the transition from Stage I (*crystallographic growth*) to Stage II (*non-crystallographic growth*) or transition from the micro-crack initiation to a micro-crack growth stage resulting in a short crack, as depicted in *Fig.16-6*.
However, the dominant short crack does not always continue propagating. Namely, in the case of a lower stress level, the short crack may stop growing. Such a situation is typically known as run-out, which indicates that at very low stress levels an infinite life may be obtained. Run-out below the endurance limit means crack-retardation, *Fig.16-7*. In the long-crack regime the fatigue crack growth rate da/dn can be characterized by the stress intensity factor range ΔK as a dominant driving parameter.

The CDM-driven Region I in the figure below is here of interest, but should be illustrated as part of the full crack failure picture: A typical fatigue crack growth rate curve da/dn (ΔK) for the long crack is illustrated in *Fig.16-7*, too. If in a double logarithmic scale the long crack propagation rate follows a straight line in Region II, in sufficient distance from the threshold ΔK_{th} , then the long crack growth rate domain can be well described for most engineering alloys by the so-called Paris law:

$$\text{Paris:} \quad da/dn = C_{Paris} \cdot \Delta K^{n_{Paris}} \;, \quad \text{Forman:} \quad da/dn = \frac{C_{Forman} \cdot \Delta K^{n_{Forman}}}{(1\text{-R}) \cdot \mathrm{K}_{Forman} - \Delta K} \quad [HSB\ 63205\text{-}01]$$

In the figure and in the formulas above *da/dn* is the crack growth increment per cycle, $\Delta K = maxK - minK$ is the range of stress intensity factor, and C (intercept with the y-axis) and n_{Forman} (slope) are material curve parameters that are deduced by fitting the course of experimental data. K_{Ic} is the so-called fracture toughness.

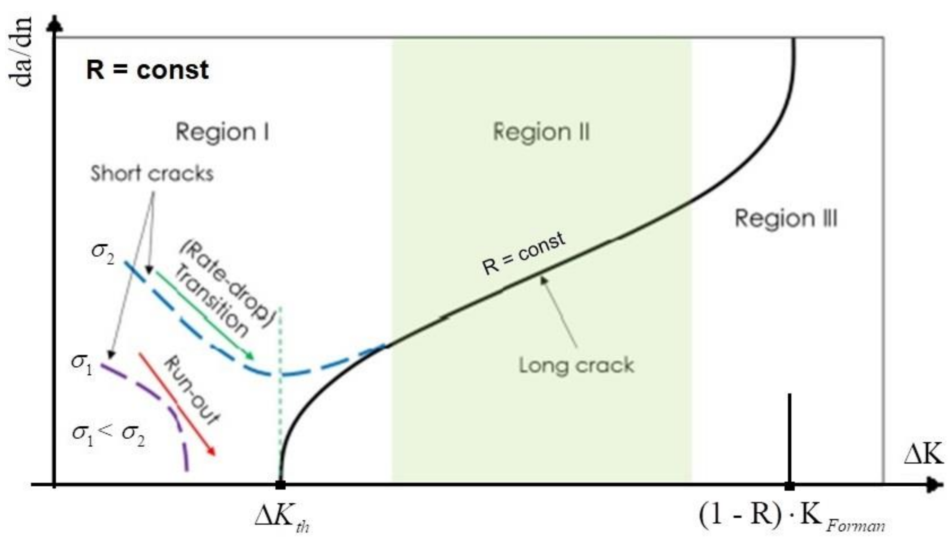

Fig.16-7: Fatigue growth rates of micro-cracks (short) and long cracks in dependence of Δ stress intensity factor. Schematic representation of the loading level- dependent transition from region I into region II.

n = number of cycles, a is crack size-

(Newman, J.; Phillips, E. & Swain, M. (1999), 'Fatigue-life prediction methodology using small-crack theory', Int. Journal of Fatigue 21(2), 109-119)

LL:
* *There is a hope, that in future for metals a basis will provided, that the estimation of an endurance limit will be possible.*
* *A grain is usually polycrystalline with crystal planes in various spatial orientations. Hence, a metallic 'composite' material can be only termed homogeneous and isotropic if these orientations are randomly distributed in order to become quasi-homogeneous. By the way, this is the same for an isotropic short fiber-reinforced polymeric material, otherwise the so-called orientation tensor has to take care of the non-isotropy.*

16.3 Note on Application of Continuum (micro)-Damage Mechanics (CDM) in Static Strength

Note on Stress effort *Eff* versus micro-damage development *D*:

For the designer of interest is how the material's stiffness decreases with increasing stress effort or load, respectively. Design allowable R and average strength $\bar{R}$ lead to different stress efforts in *design verification* and in *modelling of material damaging* (50% value = highest expectance probability), see *Fig.16-8.* The enlarging effect of the design FoS j on the value of *Eff*, when reaching failure, is considered in the design verification curve (*dashed line*) depicted below. The more reserve is, indicated by a positive Margin of Safety *MoS*, the lower *Eff* is. This has an effect on the actual strain in the non-linear analysis case. It becomes smaller and the strain is less plastic, which is of interest for the validity limit of an elastic analysis.

In the case of 3D modal SFCs (*for comparison*) the common micro-damage-caused degradation is considered by an interaction equation that reflects the micro-damage influence of all acting stress states and associated modes. The single mode efforts are interact via the experience-based interaction exponent m being about $m = 2.6$.

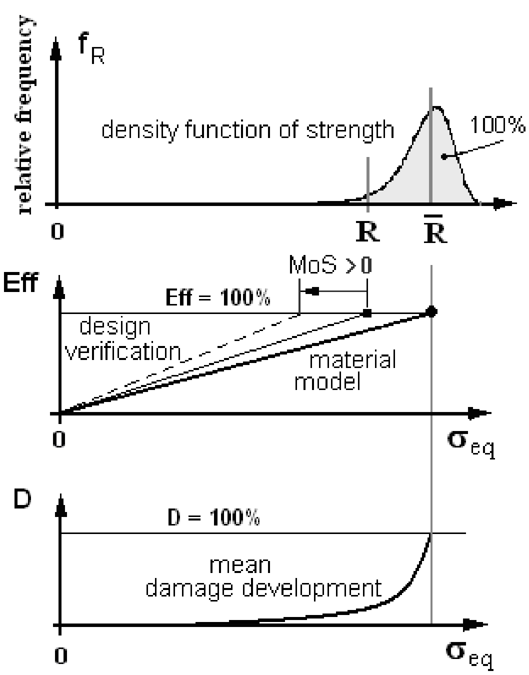

Fig.16-8:

Visualization of the development of stress effort, strength value, equivalent strength, and
Micro-damage understanding of a 'stressman'.

MoS = RF - 1

'Stressman's' Assessment of CDM applications:

During his engineering life CDM was often propagated to make in future a Design Verification possible. In literature, i.e. [*Jai20*], Continuum (micro-)Damage Mechanics (CDM) models are also used to determine a *RF*. However, this intention faces some obstacles.

Analogous to the standard procedure then statistically-based micro-damage model parameters would be required and a total maximum value *D* is to define according to $D < D_{admissible} < 100\%$ at failure and this must be statistically based. Defining such a *D*–value is a challenge for the application of (micro-)Damage Models in the Design Verification (DV) for serial production certification. This challenge is novel and higher than providing the classical strength design allowables *R,* necessary for computing *Eff*.

Further, in known standard procedures *Eff* runs 0 < *Eff* < 100%, whereas *D* begins at a distinct *Eff*-value but should principally also end at 100%, see [*CUN22, §15.3*]. Here, a very essential question comes up: "*How does the designer assess a stress level that is below the 'onset-of-micro-damage'?"* In this context another question arises: "*How are to consider low stresses in Low Cycle Fatigue*?"

The provision of a CDM-failure body would be mandatory for obtaining DV. Hence, up to now CDM seems not to meet the authority-demanded DV-requirements regarding the statistically reduced design strength *R* and regarding the relationship $\sigma \sim R \cdot Eff,$ which is valid in the linear elastic and in the non-linear regime.

LL:
* *Stiffness decay CDM model parameters are difficult to apply*
* *The 'stress-man' will not understand that at maximum load, which is at the strength point, the sum of micro-damage does not approach 100%.*
* *The author could not sort out a consistent procedure that might be used in design verification. A clear derivation of the maximum micro-damage values seems to be missing.*
* *How is the interaction of the damage portions in 3D-CDM solved?*
* *Stiffness decay CDM model parameters are difficult to apply*
* *Looking at 'well analyzing', which requires well-mapping of the stress-strain behavior in the hardening domain, one should always remember the scatter of the measured curves.*

Engineer's question, regarding above body text**:**

Is it possible to provide the engineer with similar design verification information when using micro-damage quantities D_i?

Fig.16.-9 left shows the scatter and distributions of some strain curves depicting strength and strain quantities.
Fig.16.-9 right up demonstrates that a compression test can, due to barreling, can just give a value for the yield strength $R^c_{0.2}$. This requires the determination of the increased hoop diameter, when aiming at realistic R_{02}- and *E*-values for tensile and compression. The figure also informs that for a static test specimen of a product the directions are marked by the subscripts L, LT and ST and that these are used for the description of sheet-type test specimens. These specimens are machined in the rolling direction (letter L), transversal direction (T) and thickness direction (S). In the case of thick structural parts smooth tension bar test specimens are cut out, in the case of thin plates flat test specimens are investigated, which better represent 2D-structural shapes.
This is similarly performed for the radial and axial direction of a cylindrical test specimen.

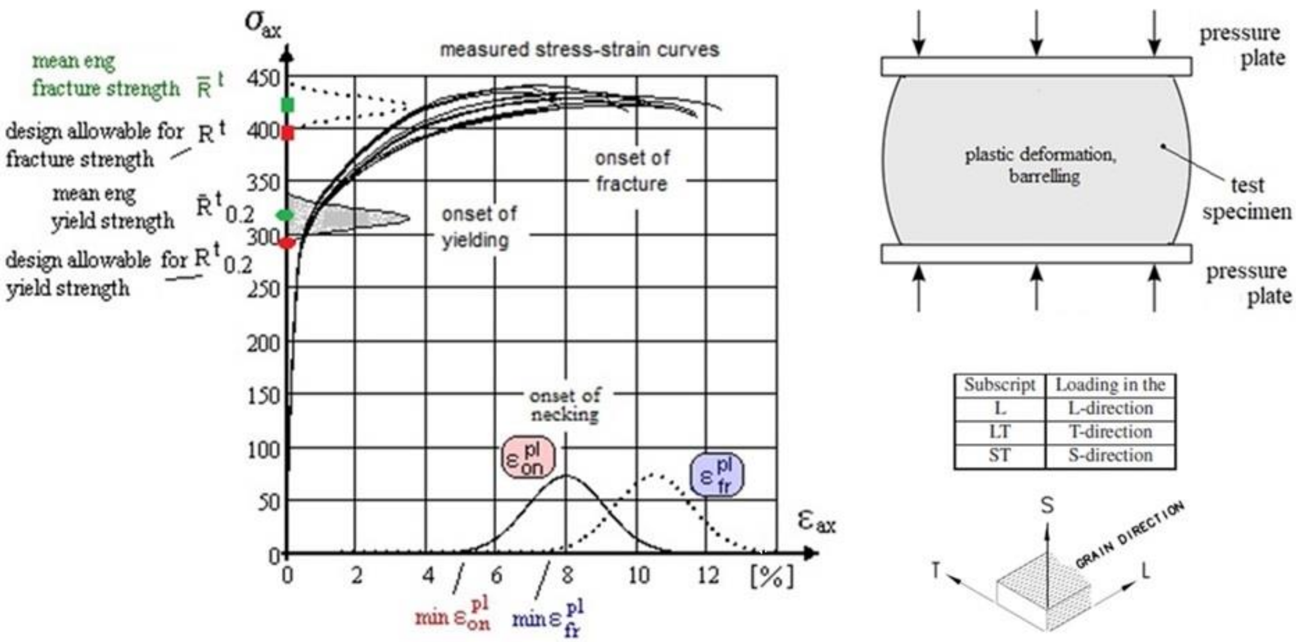

Fig.16-9: AA2219 engineering quantities and curves, deformation of a compressed ductile test specimen. (right down) Marking of sheet-type test specimens

Eventually *Fig.16.10* shall show the shape of the tensile rod test specimen and a picture of the porous fracture surface of the ductile material used

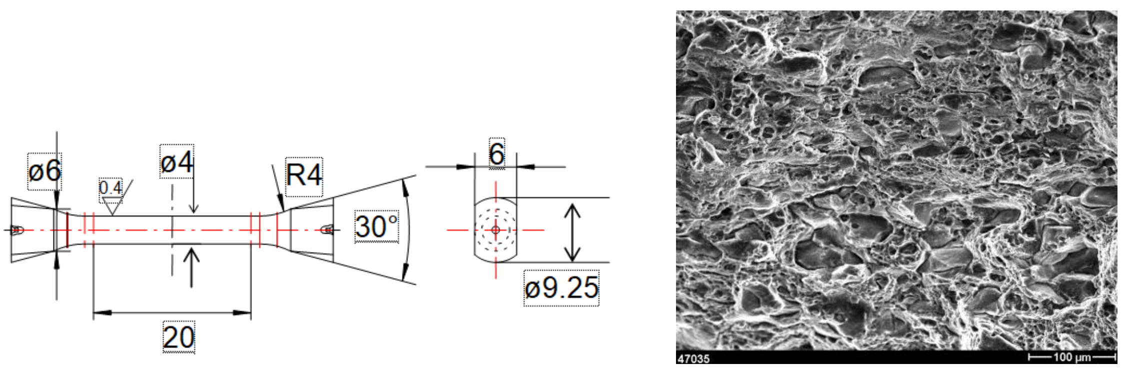

Fig.16-10: (left) Geometry of the tensile rod; (right) Voids on the fracture surface [IWM]

LL:

* *Before executing any analysis with a distinct code the designer has to check whether the actual stress-strain curve fits to the shape of the implemented curve*
* *For the best possible estimation of the component behavior, the average stress-strain curve $\overline{\sigma\varepsilon}$ must be taken*
* *The average stress-strain curve $\overline{\sigma\varepsilon}$ does not inescapably run through the means of yield $(\bar{\sigma} - \bar{\varepsilon})_{yield}$ and of fracture $(\bar{\sigma} - \bar{\varepsilon})_{fr.}$*

17 Multi-scale Structural modelling with Material Modelling and some Analysis

Aim: *Making aware of limits when applying validated macro-scale formulations at lower scales.*

17.1 Structural Analyses over the Scales

Structural modelling with associate analyses is performed at many scales, see *Fig.17-1*, from the macro-scale up to the Burj Khalifa building size.
Thereby, the challenging task is the input of the right material properties: Which values are to insert when analyzing at the lower scale? What about the stress-strain curve, and which for instance for the anisotropic UD material remains always bound to the macro-scale?

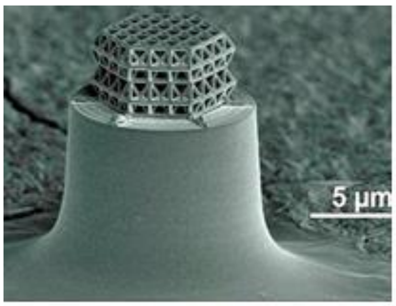

Fig.17-1: Size variety of structures.

(left) Truss structure, created by J. Bauer and O. Kraft with laser lithography. Glass-like carbon nano-framework $R^c = 3000$ MPa. Advanced Materials, Progress Report, 'Nanolattices: An Emerging Class of Mechanical Metamaterials'. JensBauer, Lucas R. Meza, Tobias A. Schaedler, Ruth Schwaiger, Xiaoyu Zheng, Lorenzo Valdevit. 2017,Wiley Online Library

Burj Khalifa, 828 m

All this requires investigating the applicability of the usual macro-scale formulations especially concerning static strength, fatigue and fracture mechanics. For the assessment of a stress state, when viewing Design Verification (DV), it is to know the 'Onset-of-micro-damage' and the later following 'Onset-of-micro-cracking'.

Multi-scale modelling is executed for static and cyclic problems. In the cyclic case, there are three key 'points' that separate the regions in *Fig.17-2*:

- Ultimate strength $R_m{}^t$: Stress level required to fail with one cycle, n = 1
- Onset of Yield, R_e: Stress value at onset of plastic behavior with being $R_e < R_{0.2}$
- Endurance limit $S_{e(ndurance)}$: Stress corresponding to the horizontal asymptote of the SN-curve.

The course of the cyclic failure test data, termed SN-curve, is again mapped by the 4-parameter Weibull formula R = constant : $\sigma_{max}(\mathrm{R}, N) = c_1 + (c_2 - c_1) / \exp(\log N / c_3)^{c4}$.

As the average SN-curve cannot be applied in fatigue life DV, a statistically reduced curve is to determine as design curve. This design curve defines a full D_{design} = 100% -SN-curve from the tensile strength as original point and ends in the running-out defining an endurance limit stress.

17-2 Macroscopic SN-curve with Relation Material Stressing Effort Eff ↔ Micro-damage D

There are practically two possibilities to present SN curves:

(1) Ductile: Applying the stress amplitude $\sigma_a(\mathrm{R}, N)$, also termed alternating stress

(2) Brittle: Applying the upper stress $\sigma_{max}(\mathrm{R}, N)$

The maximum stress is physically simpler to understand by the 'stress-man' than the amplitude, according to smooth transfer from the static to the cyclic behavior, *Fig.17-2*.

Namely, a decaying SN curve is interpretable like a decaying 'static' strength after a micro-damage process with *n* cycles.

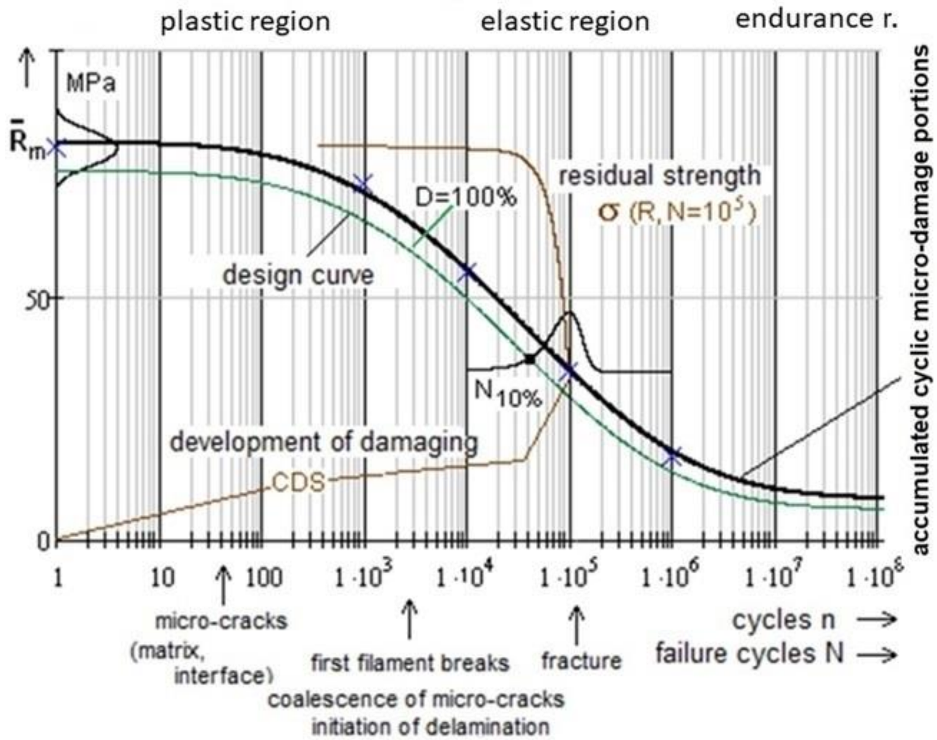

Fig.17-2, Design Verification: Fatigue average curve and **design curve R = 0.1.** *D = D_{design} for a survival probability P with a confidence level C. CDS is 'characteristic damage state' of a lamina*

[Hiatt, J. (2016), 'What is a SN-Curve?', Technical report, Siemens PLM Community). N_f = $N_{initial}$ + $N_{crackgrowth.}$ Run-out below the endurance limit means crack-retardation]

Thereby, the static material stressing effort *Eff* (Werkstoff-Anstrengung, $N_f = 1$) is replaced by the accumulated cyclic micro-damage sum *D*(*N*). Applied here is the classical 4-parameter Weibull curve with one parameter still fixed as strength point origin, because for brittle materials the strength value $\bar{R}^t = \sigma_{max}$ (n = N = 1) is preferably used as origin in the tension domain and anchor point of the SN curve and in the compression domain - $\bar{R}^c = \sigma_{min}$ (n = N = 1).

In detail, *Fig.17-3* visualizes the transfer from the static load-driven increase of the material stressing effort (n = N = 1) *Eff* = 100% (expectance value 50%) at the strength point to the cycle-driven micro-damage sum $D_{mapping}$ = 100% (expectance value 50%) of the SN curve. The evolution of *Eff* is not linked to the accumulation of the micro-damage. At onset-of-micro-cracking *Eff* is still > 0.

$$\text{If static failure} \rightarrow \max\sigma = \bar{R}_{static} \text{ at } Eff = 1 \quad \text{and} \quad \text{if cyclic failure } \max\sigma = \bar{R}_{cyclic}, \text{ at } D = 1.$$

LL:

* *It is always necessary to check whether the material at the lower level behaves in such a way that physically-based macro-mechanical formulations can be used*
* *The material data input should satisfy physical model demands, which includes measurable parameters*
* *DV demands for a statistically reduced SN-curve.*

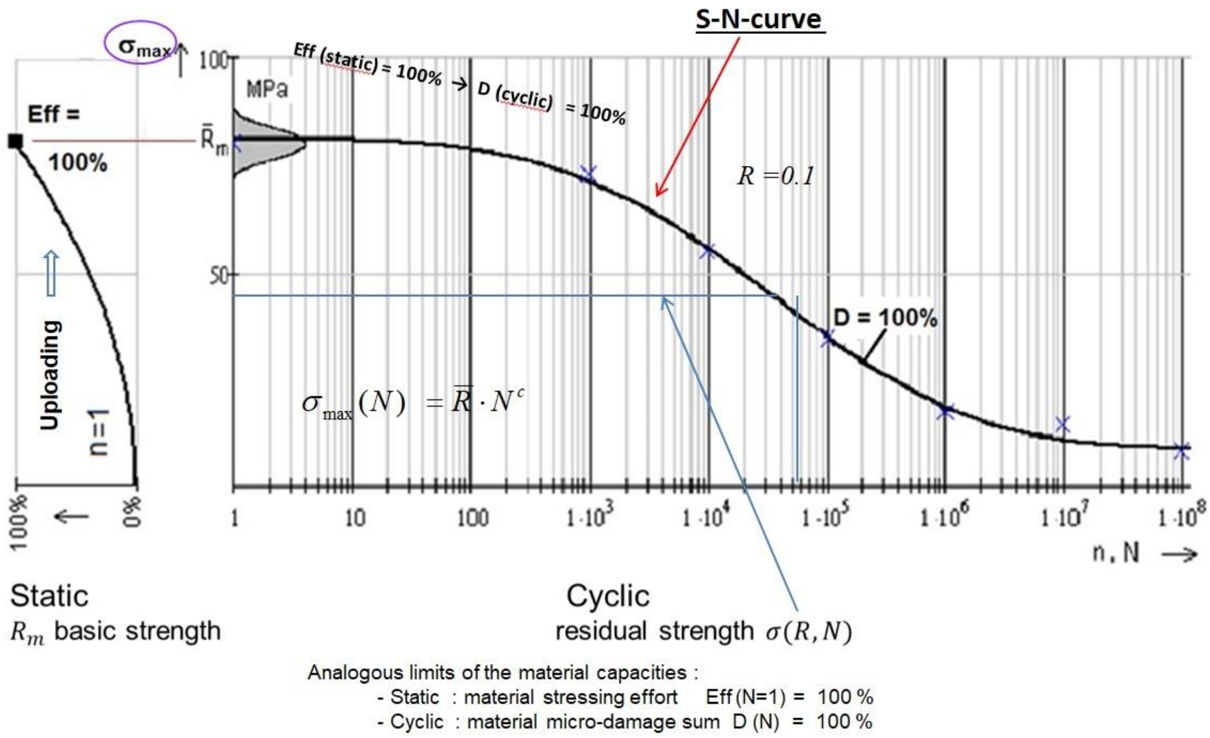

Fig.17-3, Mapping: Eff versus D. Mapping deals with averages ≡ 50% expectance value

17.3 Multi-scale Material Modelling regarding Infinite Life (endurance limit) of Metals

Infinite life or, in other words, the endurance limit is an ever-lasting topic of highest interest in structural design and concerns all materials.

Nowadays, valuable investigations on the micro-mechanics level seem to bring a significant progress for isotropic metals by using Continuum Damage Mechanics (CDM).

Mlikota and Schmauder found that the so-called Critical Resolved Shear Stress CRSS is the relevant fatigue-responsible quantity, (*Fig.17-4*), regarding the behavior of ductile metals in the micro-scale regime. Multi-scale Material modelling (MMM), based on enough computer power will probably allow in future 'Computational material mechanics' from < micro-scale models (*Molecular Dynamics-treated and test results-supported from statically and cyclically loaded 10 µm thick pillars for instance*) via micro-scale to bridge with the necessary properties (*hopefully statistically based)* to the classical macro-scale models in structural design.

Multiscale materials modelling could grow and become a significant tool for understanding complex material micro-damage processes for many homogeneous isotropic materials, a benefit for macroscale investigations.

The conclusions of Mlikota are:

- The CRSS is the resistance for the dislocations to move through the crystal. It is governed by the present strengthening mechanisms in the crystal. The CRSS is - according to critical stress strength - a micro-shear strength.
- The fatigue crack growth modeling procedure in the High Cycle Fatigue regime should include the following steps: Micro-crack nucleation within a grain → Coalescence of already existing flaws and/or arrest at grain boundaries → Short crack or Stage I growth → Transition from Stage I to Long crack or Stage II growth

- The discovered relation between endurance limit and the CRSS allows the virtual selection of those types of materials, which are more fatigue resistant! The physically-based MMM approach represents a breakthrough in the field of fatigue research
- The higher the CRSS magnitude of the metal of interest, the higher the loading stress level σ will be necessary to accomplish the transition from infinite to finite life
- The multiscale fatigue simulation approach is capable of properly taking into account the mean stress $\sigma_m = max\,\sigma \cdot (1+R)/2$ with the stress ratio R = minσ/maxσ and capturing the stress concentration factor K_t, which are influencing factors when designing structural components.
- Experimental tests demonstrate, that there is a drop in resistance to fatigue fracture with the increase of the grain size.

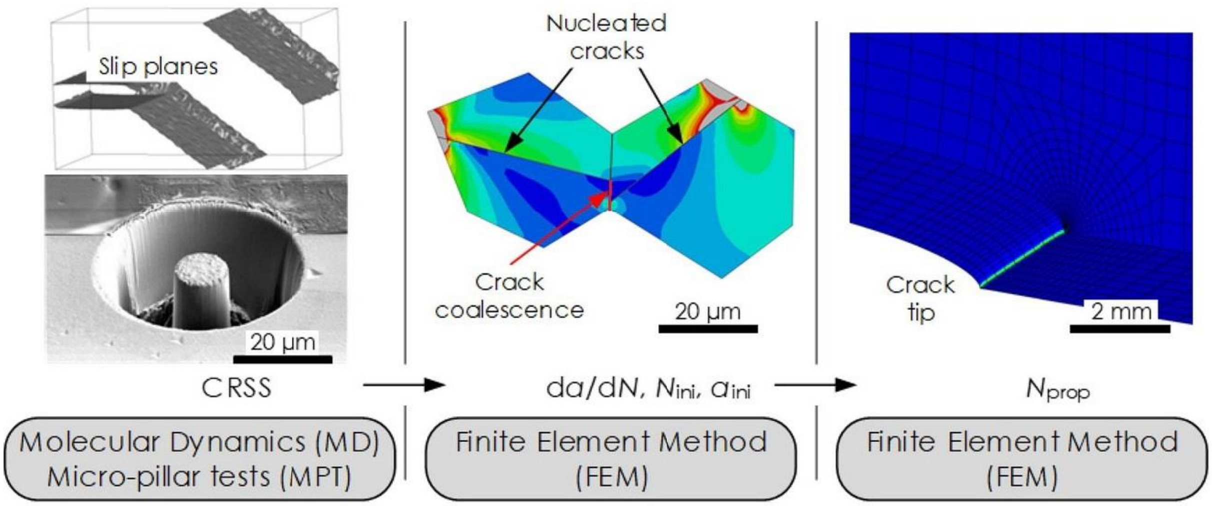

Fig.17-4: Full modelling approach. CRSS critical resolved shear stress, da/dn crack growth rate, N_{in} number of stress cycles until short-crack initiation, a_{ini} initiation short-crack length, N_{pro} number of stress cycles until short-crack propagation.

[Mlikota M. & Schmauder S. (2018), 'On the critical resolved shear stress and its importance in the fatigue performance of steels and other metals with different crystallographic structures', Metals 8(11), 883]

LL:

** There is a hope for some ductile materials in future to estimate the endurance limits of various metallic materials in the Ultra HCF regime just by knowing their CRSS values ! Available CDM models seem to be neither to be clear-defined nor classified to be used for Design Verification (DV). A DV-procedure is searched*

** A grain is usually polycrystalline with crystal planes in various spatial orientations. Hence, a metallic material can be only termed homogeneous and isotropic if these orientations are randomly distributed in order to become quasi-homogeneous. (*By the way, this is the same for an isotropic short fiber-reinforced polymeric material. Otherwise, the so-called orientation tensor has to take care of the non-isotropy*).*

** For the analysis the Mises SFC was employed in order to localize the peaks of shear banding (yielding) of the investigated steel material*

$$\sigma_{eq}^{Mises} = \sqrt{3 \cdot J_2} \quad \text{with} \quad 6J_2 = (\sigma_I - \sigma_{II})^2 + (\sigma_{II} - \sigma_{III})^2 + (\sigma_{III} - \sigma_I)^2 = f(\tau), \quad \tau_{oct} = \sqrt{J_2/3}$$

** Clearly to be defined is the quantification of the D-portions for ductile and brittle behavior with a maximum value of total D = 100%:*

- static case: the achieved micro-damage value at a distinct (equivalent) stress level

- cyclic case: the cycle-associated micro-damage portions with its derivation formula.

17.4 ‘Meso’ –Modelling of the Example UD material

Fig.17-5 gives a look at the present multi-scale modelling performed with Fiber-Reinforced-Polymers (FRP). Two scales are linked together, the micro-scale with the macro-scale by a meso-model. What is meso? Meso is no scale, per definitionem!

* Micro-scale > μm, macro-scale > *mm*.
* The author experienced (1999) in a BMFT R&D discussion round on three MaTech Competence centers of institutes working from the polymer-scale to the structural macro-scale - after one day - that the term meso-scale is used in polymer mechanics by the research colleagues at the nano-level. This level is one thousand times smaller than the solid mechanics people apply meso.
* A further classification is available for porous materials, according to pore size: ‘microporous’ pores < 2 nm, ‘mesoporous’ pores between 2 nm and 50 nm, ‘macro-porous’ pores > 50 nm. [*International Union of Pure and Applied Chemistry*].

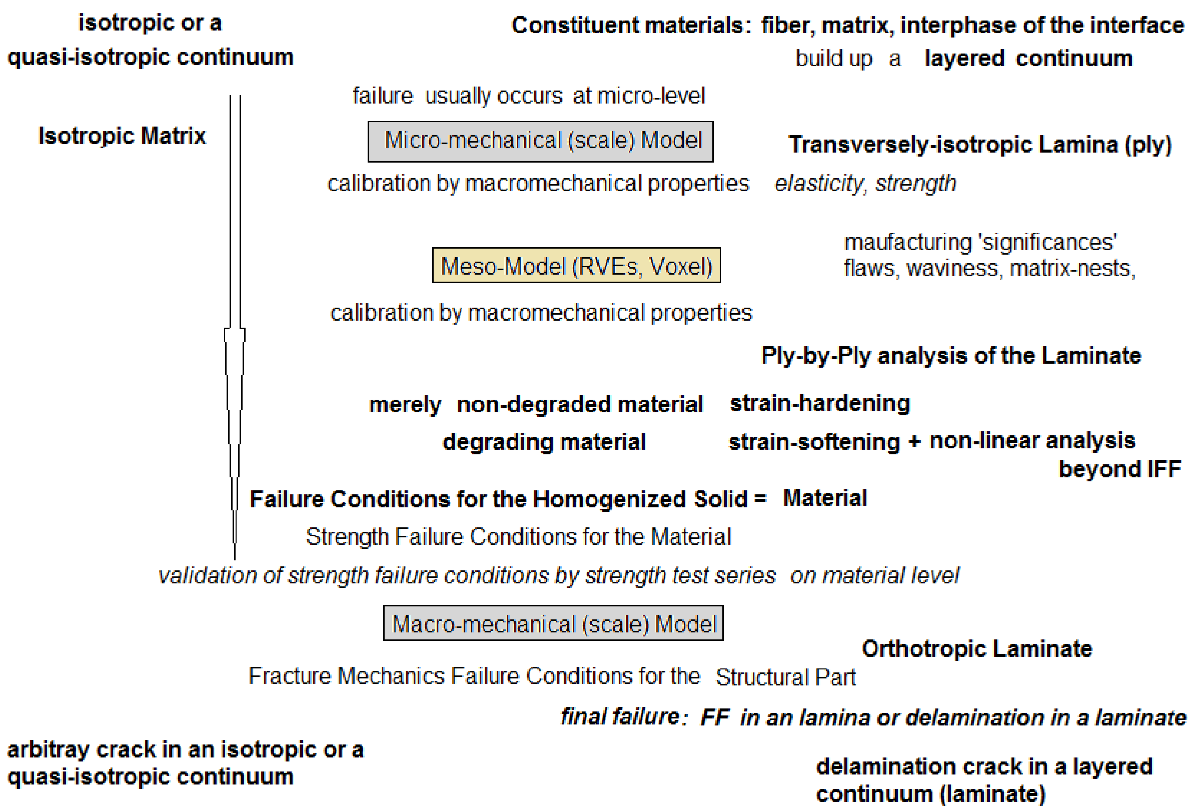

Fig.17-5:Multi-scale modelling, example FRP, brittle. 2 scales. RVE: Representative Volume Element, Voxel: volumetric pixel

LL: The term meso is a task-linked chosen size level. Apply the term meso-model, not meso-scale, and define it. In structural engineering meso is used at about 0.1 mm.

17.5 Note on Micro-mechanical Formulas (mixture rules) for Example UD lamina (ply)

***Aim**: Guideline how to use micro-mechanical models and properties with giving some warning.*

Mixture rules are employed in many technical disciplines (polymer and mineral composites like concrete). Exemplarily, here at the so-called micro-mechanical formulas of UD-materials will be looked at, only.

Creep investigations and pressure-related effects on the matrix and in consequence on the UD material of composite materials i.e. usually require a micro-mechanical input.

Examples of the author, a centrifuge and a WWFE Test Case: The non-creeping constituent fiber is to separate from the creeping/relaxing constituent matrix. In order to capture these features the use of 'micro-mechanical mixture rules' in structural engineering is common practice. It requires properties of the constituents and the so-called mixture rule, how these constituent properties are linked, to be able to predict properties of the envisaged ('smeared') material on the macro-scale.
Not all micro-mechanical properties applied can be measured. A solution will be obtained by setting up mixture rules and calibrate them via macro-mechanical test results on the lamina macro-level. This makes an inverse parameter-identification necessary.

Hence, the application of a micro-mechanical formula underlies the constraint that the given micro-mechanical properties can be only used together with the formulas they are based on. Otherwise the results might be pretty wrong. For example within the WWFE, Test Case 1, the organizer QinetiQ just provided micro-mechanical material properties but not the associated micro-mechanical formula. Therefore, the author had to apply micro-mechanical UD formulas from [VDI 2014, sheet 3] and found a discrepancy of a factor 2 for the data to be predicted! This is not acceptable for the WWFE-task model validation.

LL: Micro-mechanical properties can be used only together with the formulas they have been determined with! ⇐ *Warning!!*

18 Some Lessons Learned from Testing and from Evaluation of Test Results

***Aim**: Forwarding lessons learned.*

In structural design one basically faces 3 types of testing**:**

- Structural Testing (destructive, non-destructive)
- Materials Testing (destructive, non-destructive) and
- Non-Destructive Testing of structure and material (NDT, NDI, NDE).
  Other tasks here are: Failure detection, localization, size + shape, Failure assessment (risk-based).

All structural tests to be performed aim to uncover a deficiency: Workmanship, design mistake, oversight of a failure mode, tightness, shock resistance etc.

Fig.18-1 presents the test strategy of the MIL handbook 17, a forerunner guideline for the development of composite structures which are more challenging than developing isotropic structures.

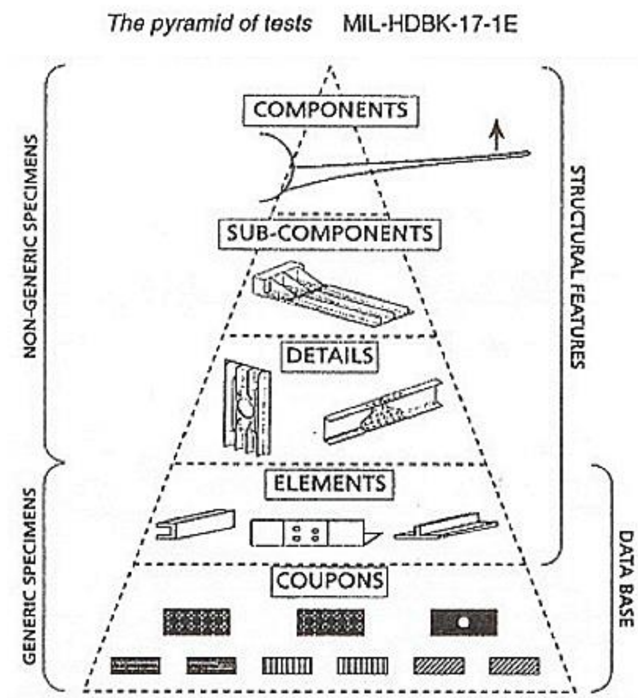

Fig18-1: Test strategy of MIL-HDBK 17 (original edition about 1970). MIL-HDBK-17/1F (VOL. 1 OF 5), DEPARTMENT OF DEFENSE HANDBOOK: COMPOSITE MATERIALS HANDBOOK - POLYMER MATRIX COMPOSITES GUIDELINES FOR CHARACTERIZATION

In this Chapter some personal experience is presented, beginning with structural testing.

18.1 Structural Testing primarily based on the Ariane launcher development

At first, a Test Agreement is to provide. It consists of test rig, test specification, test specimen and test data evaluation method and the Test Procedure. Therefore, one can only speak about ’exact’ test results in the frame of the obtained test quality.

Fig.18-2 presents the so-called sub-structuring (*affecting shares between the participating Ariane partners)* an example for violating mechanics: MAN was not permitted to include the neighboring structural part despite of the fact that it was also a MAN contract part. We could not implement the FE model of this neighboring part in order to optimally represent the real boundary stiffness conditions in the model of the 'studied structural part' but had to implement the given boundary conditions of the contract. This caused a wrong behavior of the 'studied structure' and was a real mess regarding the evaluation of the test results and comparison with analysis results. The first test article has been allegedly strengthened, which was senseless.

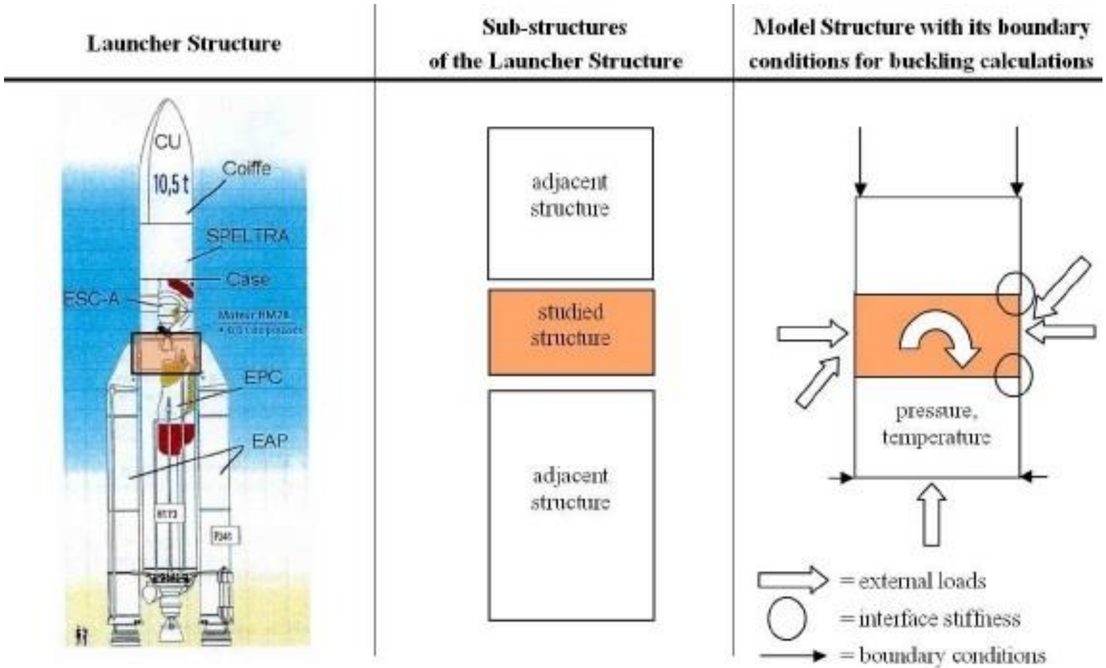

Fig.18-2: Sub-structuring of the Ariane 5 launcher, Front Skirt test

LL

* *Test article analysis is mandatory to interpret the test results and simulation-based improve the design. Only well-understood experiments can verify the design assumptions made!*
* *Splitting of a large structure (Ariane experience) is dangerous: The first buckling mode can appear on an adjacent structure and not on the studied one*
* *Mandatory for a realistic qualification of a sub-structure is a realistic set of cross-section loadings and pressure loading with an accurate structural designing of the interface stiffness of the adjacent structural parts. If the interface is too stiff in the test assembly this will attract loading and lead to a non- realistic failure site (experience from Ariane 5 tests)*
* *Not all critical locations of a structural component can be tested, because an 'over-testing' of some parts may happen to be. 'Verification By-Analysis-Only' is to be considered if the structure is too big or if the test model shall e.g. be applied later as flight model*
* *Put strain gauges there where a clear stress situation is in order to avoid useless discussions about the interpretation. Check locally by strain measurements and then rely globally on FEA-test result comparison*
* *Specific design requirements drive testing*
* *Requiring different so-called system margins MoS_{sys}* (suffered nonsense in a Ariane Technical Specification) *for the various structural parts, then not all critical locations can be tested without overloading other integrated parts. Components of such a structural assembly cannot be verified by a qualification test, because system margins cannot be used locally like a 'fitting factor'. They should have been considered directly in the Ariane 5 as a usual design FoS, applying $j_{sys} = (MoS_{sys} +1)\cdot j$. Otherwise, the design process is obscured and is prevented from applying the most economic measure in order to take risk out of the structure*
* *Requirement to put a design FoS j on a design temperature violates physics and structure behavior*

** So-called test correction factors are applied to adjust the design verifications by accurately evaluated structural test results linked to the test article analysis results.*

*18.2 **Material Testing** primarily based on the World-Wide-Failure-Exercises-I and -II*

The author succeeded with test-validation of 3D-strength criteria models for isotropic concrete, transversely-isotropic UD-material, orthotropic ceramic (fabrics) with visualization of the derived 3D failure surfaces if reliable test data sets were given.

This was only partly given in the *the World-Wide-Failure-Exercises-I, concerning2D-mapping, and –II, concerning 3D-mapping of UD materials.*The author's WWFE-I and -II contributions had to be based on an intensive assessment of provided test results. In this sub-chapter the Lessons Learned during the examination of several WWFE-Test Cases (TC) will be collected.

Validation of the lamina-material SFCs models can be only achieved by 2D- together with 3D-lamina test results. Since SFC-model validation is focused just lamina-TCs are now investigated in detail. The normal user is just interested to well map his course of failure test data by a UD-SFC and not on the laminate analysis tools.

The laminate test cases serve for the verification of the laminate design. There the full WWFE failure theory is required. This makes a comparison between the contributions very challenging because different FE codes were applied by the contributing competing institutes. These better tools further had to be equally compared to the retired author's tools. He could just use his handmade non-linear CLT-code upgraded by experience and using his sensibleness for the problem and the delivered input.

***LL**, more general ones*

** Measurement data is the result of a Test Agreement (norm or standard), that serves the desire to make a comparability of different test procedure results possible. Hence, there are no exact property values. Material properties are the result of the material model applied inclusively mapping process.*

** Stresses, strength, strains, elasticity properties cannot be directly measured*

** Check of assumptions is necessary before designing (example: WWFE on UD-material). Pore-free material, specimen surfaces polished, well-sealed, fiber volume is constant, tube specimens show no warping and do not bulge, perfect bonding, no layer waviness, edge effects do not exist*

** Sometimes one must live with a substitute test situation in order to get some approximate properties (Example: UD-Tension/Compression-Torsion test device → Arcan test device)*

** Before thinking about test data evaluation the associated underlying micro-damage processes must be sorted out in order to get a better understanding of failure*

** Test specimens shall be manufactured like the structure ('as-built')*

** Comparisons between theoretical predictions and test data help to identify the major discrepancies, limitations, and areas which require further theoretical and experimental work. There is always a lot to be done and following Moslik Saadi **"All is difficult prior to becoming simple**"! This begins with the provision of appropriate test specimens for the various material families being extreme ductile or brittle and ends with appropriate test procedures and an appropriate test data evaluation*

** Considering FE-results: We must more and more 3D-design! However the situation of properties, especially for composites is: „3D-property data test sets are seldom sufficiently available".*

Of high interest for future scientists and engineers might be the following assessment results of the provided properties during the author's many WWFE-designated years. They are results which stem from a very careful and effortful test data evaluation of about one man year. Otherwise, a successful WWFE-contribution could not have been made possible.

Thereby, some essential WWFE TestCase-examples for lamina-input shortcomings were found:

* WWFE-I, TC1: the provided strengths have been changed from Part A to B and two test points are doubtful regarding own test results (*Reason is known: non-accurate raw test data evaluation of the test engineer at DLR Stuttgart. Organizers did not question the test data but required mapping of the false ones*!).

* WWFE-I TC2: the author informed the organizers that apples and oranges have been put here together in a diagram. One cannot fill into the same diagram 90°-wound tube test specimen data together with 0°-wound tube data. The 0°-stresses have to be transformed in the 2D-plane due to the fact that shearing under torsion loading turns the fiber direction (see *Fig.17-3*) and the lamina coordinate system CoS is not anymore identical with the structure coordinate system of the tube. In order to also use these test data the author exemplarily transformed magenta-colored two fracture test points by the occurring twisting angle γ using a non-linear CLT-analysis. Then he could achieve a good mapping showing, that the two transformed fracture points accurately lie in the lamina CoS on the 90°-curve.

* WWFE-II, TC3: the same mistake happened again! However, here the much more complicated 3D-stress situation was to face, so that the 3D-transformation of the 0°-data set could be simply performed.

* WWFE-II, TC2 an average stress-strain curve should have been provided because otherwise no realistic treatment is possible. Therefore the Part A results could be only inaccurate. From the Part B information the author could derive an average curve and then all 3 TC test data courses could be mapped and the mutual check points in the fully connected TC2-TC3-TC4 matched. Incomprehensively, there was no response of the organizers to the author's idea, which made 3 TCs to successful test cases.

* Viewing the final papers of the WWFE-organizers "*A comparison of the predictive capabilities of current failure theories for composite (UD-composed) laminates, judged against experimental evidence*" and "*Maturity of 3D failure criteria for fiber-reinforced composites, comparison between theories and experiments*", there is not any doubt to find concerning the quality of the only available, provided test data sets. One third of the provided TC test data was at least questionable till not applicable for model validation.

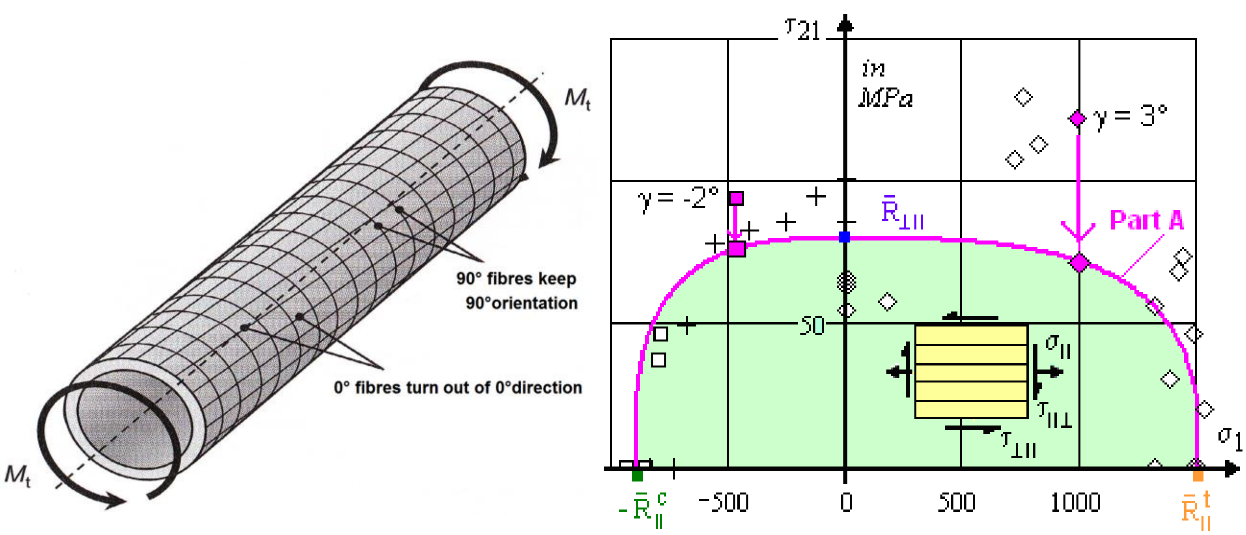

Fig.18-3, $\tau_{21}^{fr}(\sigma_2)$ *basic cross-section of the fracture failure body: (right) WWFE-I, TC2, UD lamina, CFRP, T300/BSL914C Ep ; (left) Tube test specimen picture: [Courtesy IKV Aachen] The normal user is just interested to well map his course of failure test data by a SFC*

**** Test results can be far away from the reality like an inaccurate theoretical model.***

**** Theory creates a model of the reality, one experiment shows one realization of the reality.***

19 2D-Laminate Design: Direct Determination of Tsai's 'Omni principal FPF strain failure envelopes

Aim: *Replacing the ply-by-ply proof of multiple-ply laminates by a much simpler method*

Steve Tsai's idea was to by-pass the effortful ply-by-ply analysis of multiple-ply laminates by using a so-called 'Omni-(principal FPF strain) failure envelope'. This envelope surrounds an intact Non-FPF area whereby FirstPlyFailure (FPF) includes Fiber Failure FF and Inter-Fiber-Failure (IFF).

Such an 'Omni failure envelope' is to determine for each composite material, applying a FPF-Strength Failure Criterion (SFC), and will capture all possible laminate stacks. Naturally, the used SFC significantly determines the shape of the envelope, see *Fig.19-1*.

Dimensioning is performed by showing that the design loading-caused principal strains are lying within the Non-FPF area. The idea can serve as a very practical Pre-design tool.

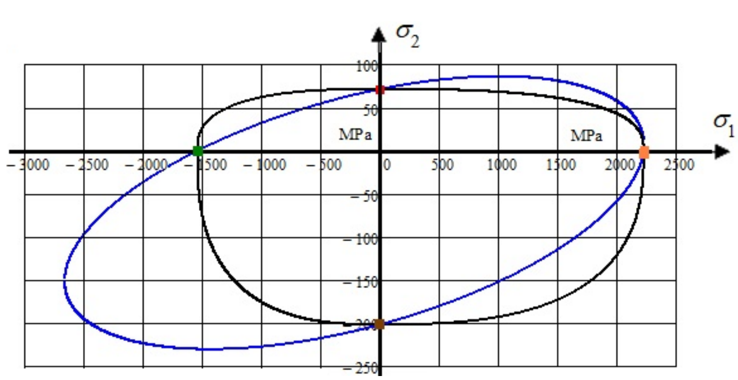

Fig.19-1: Cross-section $\sigma_2(\sigma_1)$ of the failure body, Tsai-Wu versus Cuntze

19.1 Tsai's indirect Determination of the 2D 'Omni envelope'

Fig.19-2 displays different 'butterflies' (*name, how the author Cuntze termed the bundle of **i** FPF-curves),* derived using the SFCs of Tsai-Wu and Cuntze). These numerical results of the FPF-linked

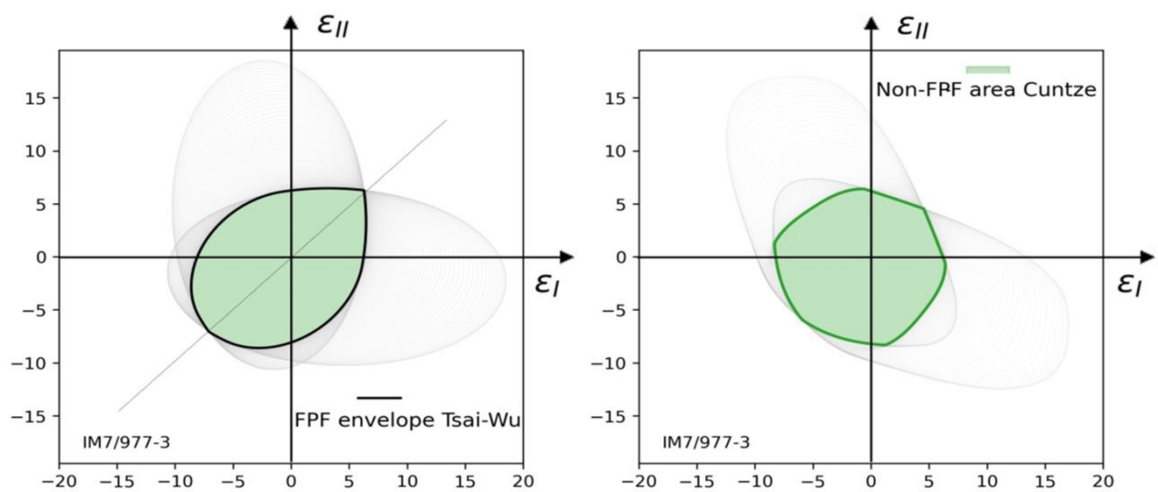

Fig.19-2, bundle of all FPF envelopes = 'butterflies': All ply FPF-envelopes enclosing a non-FPF failure area; 0°< α < 90° (91 ply angles). Principal strain in ‰, suffix FPF is skipped. CFRP IM7/977-3. In all pictures: (left) Tsai-Wu with $\mu_{\perp\parallel} = 0$, $F_{12} = -0.5$ and (right) Cuntze with $\mu_{\perp\parallel} = 0.2$, $m = 2.7$

principal strain curves clearly depict the significant effect of the chosen SFC, see above figure. The different lateral properties determine the shape (wing edge) of the obtained symmetric 'butterfly' with its single, grey-marked principal strain curves provided by E. Kappel.

19.2 Cuntze's Determination of the 2D 'Omni Envelope'

The derivation of such an 'Omni failure envelope' is pretty effortful and no direct formulation could be found in the past. Recently, this bottleneck could be by-passed by an idea of the author, who examined various horizontal cross–sections τ_{21} = constant of the UD-FPF fracture body in *Fig.19-3* below. He found that $\tau_{21}=0$ delivers the smallest Non-FPF area.

► Pre-Dimensioning can now be performed by showing that the design loading-caused principal strains are located within the Non-FPF area, a simpler pre-design of arbitrary laminates is possible.

.

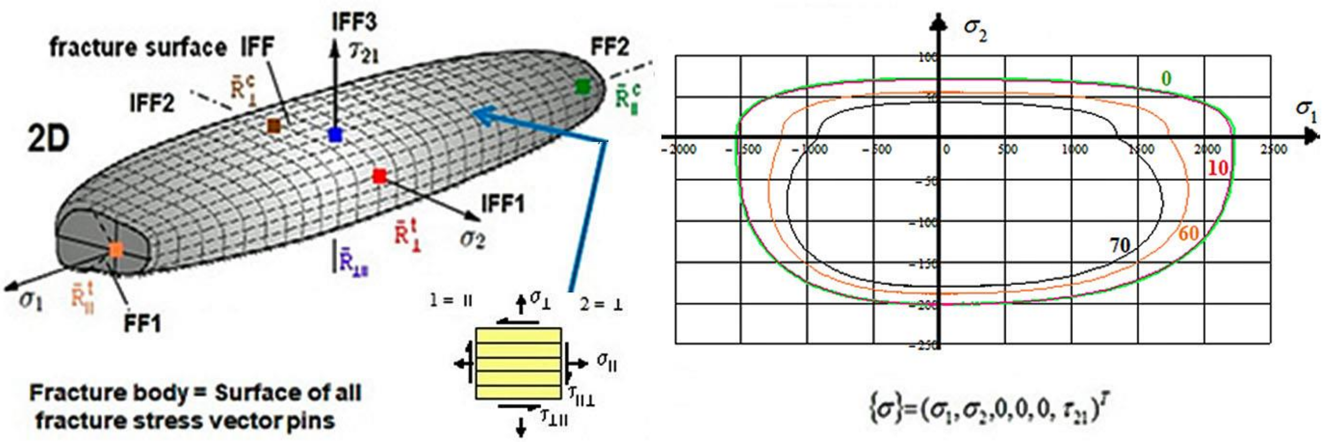

Fig.19-3: (left) 3D UD Failure body. (right) FPF-envelopes for 3 planes τ_{21}= const. CFRP IM7/977-3

Fig.19-4 (left) presents the resulting Omni principal strain FPF curves $\varepsilon_{II}(\varepsilon_I)$ with a not unambiguously solution $\varepsilon_{II}(\varepsilon_I)$ for each parameter level τ_{21} = const. → The failure curve $\sigma_2(\sigma_1, \tau_{21} = 0)$ describes the 'Omni envelope'.

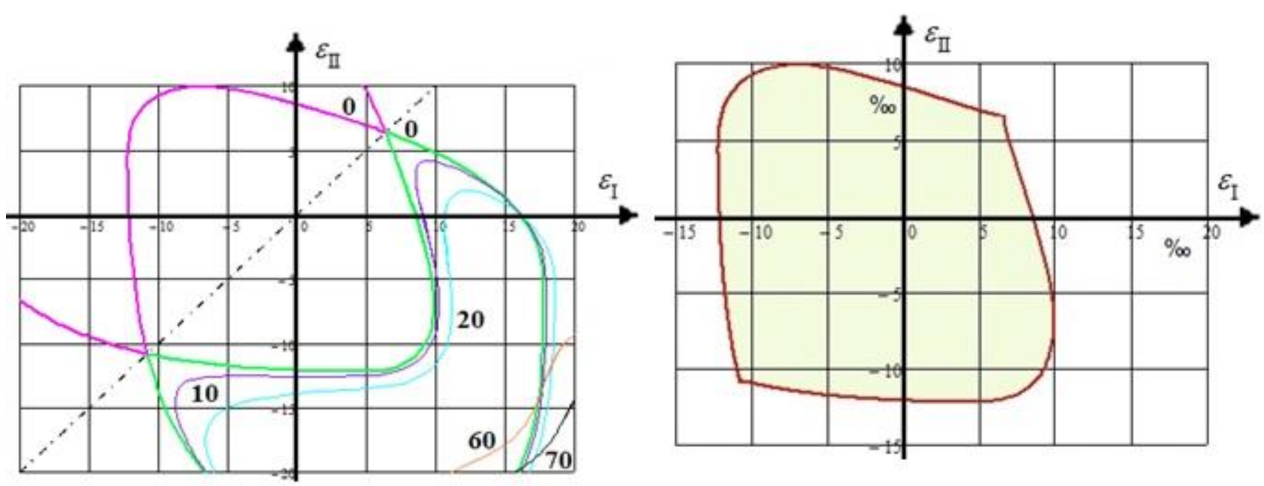

Fig.19-4: Mirrored envelope of the Non-FPF area (Cuntze procedure), CFRP IM7/977-3

Originally, the 'second' solution-linked additional outer curve parts were excluded in the graph and the right figure eventually shows the 'cleaned-up' envelope, representing the limit *Eff* = 100%,

enveloping the Non-FPF area. The cleaned-up graph is identical to the Non-FPF area obtained by the standard Tsai 'butterfly'-determination procedure.
Domains of the envelope could be dedicated to the locally faced failure mode types FF and IFF.

In a novel investigation, detailed in *Table 19-1*, Cuntze could give a complete look of the different envelopes in *Fig.19-4* (*left*). Depicted are the 'butterfly' wings (outside) and internally the green shadowed Non-FPF area. For optical comparison reasons E. Kappel 'traditionally' provided the 'butterfly' procedure plots for *Fig.19-4* (*right*) and *Fig.19-5*.

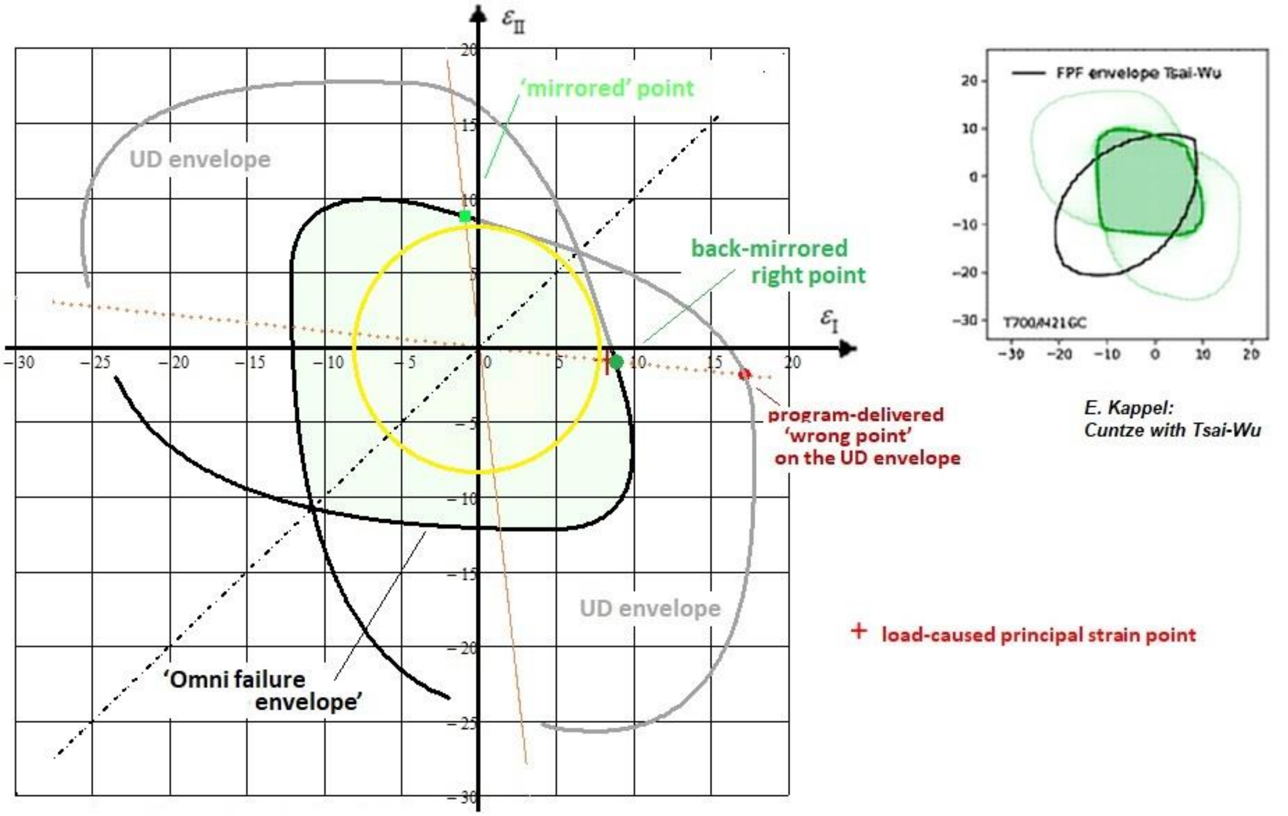

Fig.19-5: (left) Various envelopes of the Non-FPF area (Cuntze procedure following Principal Strain Procedure Cuntze in Table 19-1)..(right) 'Butterfly' and Non-FPF area applying the SFCs of Tsai-Wu and Cuntze

19.3 Pre-design Example using the 'Omni Non-FPF area' and Determination of Reserve Factor

Of highest interest is the reserve factor which must be smaller for a simplified design method than obtained by the classical 'Ply-by-ply procedure', thus remaining on the Safe Side. Laminate Design Verification is traditionally performed by above 'ply-by-ply' analysis, assessing the obtained ply (lamina) stresses $\{\sigma\}$ in the critical location of the most critical plies. Now, a simpler more global assessment is possible (*Table 19-2*) by using the in-plane principal strains of the laminate, strains

Table19-2: Procedure of checking a probably critical design stress state

A Non-FPF area within an 'Omni failure envelope' is given for the chosen laminate material
➢ FEA delivers the maximum state of the 3 strains of the laminate stack
➢ Transformation into the 2 principal strains as coordinates of the Non-FPF area
➢ Check, whether the strain point $(\varepsilon_I, \varepsilon_{II})$ lies within the envelope or Non-FPF area
➢ Determine material reserve factor f_{RF} = vector length ratio of *failure strain/design strain.*

which represent the loading. Such principal strains are a standard output of modern FE software. They are mathematical and not material symmetry-linked quantities.

Remember, please: The execution of the Design Check runs under the Presumption
"*Linear Analysis, proportional stressing* $\sigma \sim \varepsilon$ *is permitted*".

Table 19-1: Procedures, how to obtain the material reserve factor f_{RF}

SFC Cuntze: Failure Function $\mathrm{F}\left(\{\sigma\},\{\bar{R}\},\mu \text{ directly}\right) = 1$

$$Eff_{\mathrm{FPF}} = [(Eff^{\|\sigma})^m + (Eff^{\|\tau})^m + (Eff^{\perp\sigma})^m + (Eff^{\perp\|})^m + (0)^m]^{m^{-1}} = 1, \ m = 2.7$$

Input

$$\{\sigma\} = (\sigma_1, \sigma_2, \sigma_3, \tau_{23}, \tau_{31}, \tau_{21})^T \rightarrow (\sigma_1 = 900, \sigma_2 = 20, 0, 0, 0, \tau_{21} = 25)^{\mathrm{T}} \mathrm{MPa},$$

$$\{\bar{R}\} = (\bar{R}_{\|}^t, \bar{R}_{\|}^c, \bar{R}_{\perp}^t, \bar{R}_{\perp}^c, \bar{R}_{\perp\|})^{\mathrm{T}} \rightarrow (2230, 537, 71, 202, 78)^{\mathrm{T}} \ \mathrm{MPa}, \ \mu_{\perp\|} = 0.2.$$

$\{\sigma\}$-loading-caused ply strains and loading-reperesenting principal strains

$$\varepsilon_1 = s_{11} \cdot \sigma_1 + s_{21} \cdot \sigma_2, \ \varepsilon_2 = s_{21} \cdot \sigma_1 + s_{22} \cdot \sigma_2, \ \gamma_{21} = s_{66} \cdot \tau_{21}$$

$$\varepsilon_I = 0.5 \cdot \left[(\varepsilon_1 + \varepsilon_2) + \sqrt{(\varepsilon_1 - \varepsilon_2)^2 + \gamma_{21}^2} \right], \ \varepsilon_I = 0.5 \cdot \left[(\varepsilon_1 + \varepsilon_2) - \sqrt{(\varepsilon_1 - \varepsilon_2)^2 + \gamma_{21}^2} \right]$$

$$\varepsilon_I = 0.0083 \equiv \mathrm{UD}\varepsilon\mathrm{I}, \ \varepsilon_{II} = f_\varepsilon \cdot \varepsilon_I = 0.0009, \ f_\varepsilon = \varepsilon_{II} / \varepsilon_I = -0.109.$$

*Stress Procedure Cuntze: Lamina task, solved by ply-by-ply failure analysis

$$Eff^m = [(Eff^{\|\sigma})^m + (Eff^{\|\tau})^m + (Eff^{\perp\sigma})^m + (Eff^{\perp\tau})^m + (Eff^{\perp\|})^m] \text{ with the mode portions inserted,}$$

$$Eff = [(\frac{(\sigma_1 + |\sigma_1|)}{2 \cdot \bar{R}_{\|}^t})^m + (\frac{(-\sigma_1 + |\sigma_1|)}{2 \cdot \bar{R}_{\|}^c})^m + (\frac{\sigma_2 + |\sigma_2|}{2 \cdot \bar{R}_{\perp}^t})^m + (\frac{-\sigma_2 + |\sigma_2|}{2 \cdot \bar{R}_{\perp}^c})^m + (\frac{|\tau_{21}|}{\bar{R}_{\perp\|} + 0.5 \cdot \mu_{\perp\|} \cdot (-\sigma_2 + |\sigma_2|)})^m]^{1/m}$$

$$\rightarrow Eff = 0.513 \Rightarrow \text{material reserve factor } f_{\mathrm{RF}} = 1 / Eff = 1.95.$$

*Principal Strain Procedure Cuntze: classical laminate task, solved by a laminate failure analysis; $\tau_{12} = 0$

Due to $\varepsilon_1 = \varepsilon_I$, $\varepsilon_2 = \varepsilon_{II}$ for the 2 failure determining stresses follows, $\gamma_{21} = 0$

$\sigma_1 = (s_{21} \cdot \varepsilon_2 - s_{22} \cdot \varepsilon_1) / (s_{21}^2 - s_{11} \cdot s_{22})$ and $\sigma_2 = (\varepsilon_2 - s_{21} \cdot \sigma_1) / s_{22}$ which is to insert into the FPF-criterion-based 'Omni principal strain failure envelope' formula

$$(\frac{(\sigma_1 + |\sigma_1|)}{2\bar{R}_{\|}^t})^{\mathrm{m}} + (\frac{(-\sigma_1 + |\sigma_1|)}{2\bar{R}_{\|}^c})^{\mathrm{m}} + (\frac{\sigma_2 + |\sigma_2|}{2\bar{R}_{\perp}^t})^{\mathrm{m}} + (\frac{-\sigma_2 + |\sigma_2|}{2\bar{R}_{\perp}^c})^{\mathrm{m}} + (0)^m = 1 = 100\% .$$

With the chosen SFC the $\rightarrow$ Non-FPF area $\varepsilon(\sigma_{FPF})$ is to derive .

On the strain beam $f_\varepsilon = \dfrac{\varepsilon_{II}}{\varepsilon_I} = \dfrac{\varepsilon_{II,\mathrm{FPF}}}{\varepsilon_{I,\mathrm{FPF}}}$ it will be finally obtained

$$f_{\mathrm{RF}} = \sqrt{(\varepsilon_{I,\mathrm{FPF}}^2 + \varepsilon_{II,\mathrm{FPF}}^2)} / \sqrt{(\varepsilon_I^2 + \varepsilon_{II}^2)} = \varepsilon_{I,\mathrm{FPF}} / \varepsilon_I = 1.06 .$$

Cuntze's direct determination of the 'Omni failure envelope' enables to determine the reserve factor straightforward instead of using the *Non-FPF smaller* internal circle in *Fig.19-5,* how it was usually performed up to now, see [*Cun 24*].

However, there was a computational problem: Mathcad unfortunately delivers a principal failure strain value ε_{FPF} outside of the Non-FPF area as result of its solution process. The other solution seems to be received, if a shear strength is involved. This wrong point value can be localized on the UD 'butterfly wing' edge in *Fig 19-4* and this enabled to successfully use the symmetry of the envelope as it is executed in *Fig-19-5*.

Now, Design Verification can be performed as described below:

$$f\varepsilon = \frac{\varepsilon II}{\varepsilon I} \quad f\varepsilon = -0.109 \qquad UD\varepsilon I = 0.0083$$

Vorgabe $\quad \varepsilon IFPF := 0.01 \quad \sigma 1 := 100 \quad \sigma 2 := 10$

$$\boxed{\varepsilon IFPF = s11\cdot\sigma 1 + s21\cdot\sigma 2} \qquad \boxed{f\varepsilon\cdot\varepsilon IFPF = s21\cdot\sigma 1 + s22\cdot\sigma 2}$$

$$\left(\frac{\sigma 1 + |\sigma 1|}{2R1t}\right)^{mint} + \left(\frac{\sigma 2 + |\sigma 2|}{2R2t}\right)^{mint} + \left(\frac{-\sigma 1 + |\sigma 1|}{2R1c}\right)^{mint} + \left(\frac{-\sigma 2 + |\sigma 2|}{2R2c}\right)^{mint} = 1$$

$$A\varepsilon := \text{Suchen}(\varepsilon IFPF, \sigma 1, \sigma 2) \quad \varepsilon IFPF := A\varepsilon_0 \quad \varepsilon IFPF = 0.01712$$

$$f\varepsilon = -0.109 \quad fRF\varepsilon := \frac{\varepsilon IFPF}{UD\varepsilon I} \quad \boxed{fRF\varepsilon = 2.07}$$

This result of the Mathcad program leads to a value which belongs to another solution brunch (see the figure). Using the plot's symmetry the real value can be found after the replacement of fε by fεr = 1/ fε

$$f\varepsilon r := \frac{1}{f\varepsilon} \quad f\varepsilon r = -9.214 \quad fRF\varepsilon r := \frac{\varepsilon IIFPFr}{UD\varepsilon I} \quad \boxed{fRF\varepsilon r = 1.06}$$

$$< \boxed{fRF\sigma = 1.95}$$

Fig.19-6 Successful computation of f_{RF} after utilizing the plot's symmetry (code Mathcad 15). $\varepsilon_I \equiv UD\varepsilon_I$

LL:

** The method is more or less a linear method.*

** The investigation of various cross–sections τ_{21}=constant proved, that τ_{21}=0 delivers the smallest Non-FPF area, thus making a simpler pre-design of arbitrary laminates possible*

** Basic result:*

*The principal strain approach delivers the required smaller reserve factor compared to the conventional ply-by-ply stress-based procedure. → The approach is 'on the safe side' **!***

Note, once again please:

Tsai's 'Omni principal strain envelope' principally surrounds a Non-FPF or even a Non-LPF area.

*FPF is required if the design requirement asks to fulfill a First-Ply-Failure in the critical locations of the plies of the laminate.

*LPF, if to apply, is required to fulfill a Last-Ply-Failure limit. However, this usually involves a non-linear analysis up to the ultimate failure load of the structural part.

In order to cope with the reserve factor definition these shall be sketched again below:

$$\text{About 'linear' FPF: tress-defined } f_{RF} = \frac{\text{Strength Design Allowable } R}{\text{Stress at } j \cdot \text{Design Limit Load}} > 1$$

20 Note on Criticality of Fiber Micro-Fragments and Dusts of CFR-Plastic/CFR-Concrete

Matter of my heart:

Supporting the application of sustainable carbon concrete with low-risk PAN-CFs in Production and my concern regarding Recycling.

Carbon Fibers (CFs) usually are produced using the precursors Polyacrylonitrile (PAN) and Pitch. Problem and question: Machined Pitch CFs generated many toxic split-up fiber fragments. What about the PAN-based CFs? They can be classified into the types: intermediate-modulus (IM), high-modulus (HM) and ultrahigh-modulus (UHM), whereby UHM-CFs seem to show some and the lower modulus Standard PAN no hazard. These facts ask for an investigation of the UHM-CF with the objective to finally sort out that the use of the less '*risky*' Standard PAN CF causes no threat.

Inhaled particles with its size, geometric shape and contaminants adhering to the surface are relevant for a health effect. Of course, targeted workplace prescriptions always have to counteract the occurrence of excessive stress on the lungs from inhaling too large amounts. Respirable bio-persistant particles accumulate in the alveoli of the lungs. These so-called 'WHO fibres' pierce the macrophages in the lungs and can migrate into the abdomen and pleural tissues and cause cancer.

CF application in Construction

As structural engineer, who has founded and led two working groups in the carbon concrete sector for 10 years: "*It is my deep wish to use more fatigue-resistant [VDI2014] PAN-CF in the construction industry in order to increase the life of bridges and to save concrete, a composite material, which has a negative CO_2 footprint due to the necessary clinker (cement constituent) production*."

The next figure displays a CFRP application by a fiber grid (*mat*) as a slack reinforcement (*no pretension*) of a bridge.

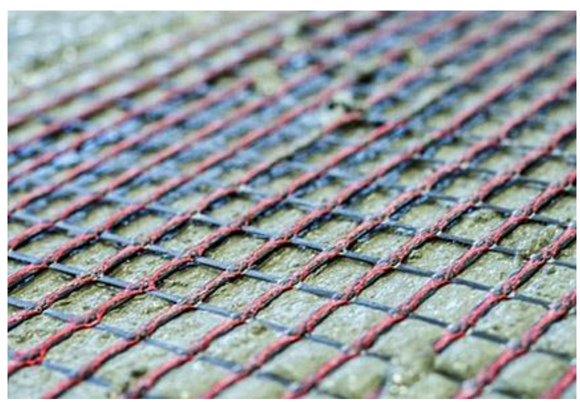

Fig.20-1: Bridge Wurschen, 2022: (left) Superstructure made exclusively of carbon concrete, shell construction. (right) Textile FRP mats in the super-structure) (Foto: Stefan Gröschel, IMB,TU Dresden)

Note: Full exploitation of the Carbon Fiber (CF) is only to achieve by pre-tensioning, which will advantageously compress the usual low tensile strength of the matrices concrete and plastic. Just pre-tensioning of plates is still series production.

Carbon Fiber Production

CF-properties strongly depend on the production process and above precursors which need different conditions but the essential processes are similar. A CF requires a heating and stretching treatment to get the high strength products. A thermoset treatment is first applied in the temperature range from 200 to 400 °C in air under stretching to get the stabilized fiber, followed by a carbonization process in the temperature range from 800 to 1500 °C in oxygen-free condition to remove impurities and to improve the crystallinity of carbon. To further improve the performance of CFs, a graphitization process is required to graphitize carbonized fibers with temperature up to 3000 °C. During these processes, stretching is required to get preferred orientated carbon crystals, because the crystal alignment makes the fiber incredibly strong and stiff. The graphitization process leads to differences between PAN and Pitch and within the PAN-CFs. This will be later of interest.

The very expensive Pitch CF is mainly used in spacecraft and antennas. The market is dominated by the PAN-CF. With regard to possible toxic fragments, PAN-CF (Ø 7 µm, usually) is therefore of interest, especially the 'highly' graphitized UHM-PANCF such as Torayca's M60J, which comes next to the Pitch-CF considering the tensile modulus (stiffness). CF tensile modulus and fracture toughness naturally depend on the fabrication regarding precursor, on carbonization and graphitization. Furthermore, Pitch-CFs are more layer-like in their crystal structure in contrast to the more granular PAN-CF. This probably further explains the higher tensile modulus compared to the PAN-CF. Knowing the different crystal structure is therefore important for explaining the splintering process, originator of possible toxic fragments.

<u>‘WHO-Fiber’ criticality</u>

WHO criterion for respirable fibers: ‘WHO-<u>Fiber</u>‘ ≡ tiny fragment of a filament with a diameter Ø of less than 3 µm, a length L of greater than 5 µm and a length-to-diameter ratio of L/Ø > 3:1.

Naming <u>Fiber</u>: (1) Does not address a long CF, which of course never meets the WHO criterion. (2) Asbestos fiber, for example, is just a fiber-like looking particle, which may break into above tiny WHO-size fragments).

Too many dust-related particles, smaller than the WHO 'fiber' size, can also cause a hazard. A so-called Particulate Matter of the µm-size PM2.5 can penetrate into the alveoli and ultrafine particles with a diameter of less than 0.1 µm (*Corona virus size level*) can even penetrate into the lung tissue. Aerosol particles from the environment have diameters ranging from about 1 nanometer (nm) to several 100 micrometers (µm). Larger particles quickly sink to the ground, particles smaller than 10 µm can remain in the air for days.

The figure below summarizes the topics faced when considering the criticality.
The macrophage lifespan of a few weeks is one of the decisive factors for the success of disposal or 'cleaning'. ‘WHO-fiber’-pierced macrophages usually die.

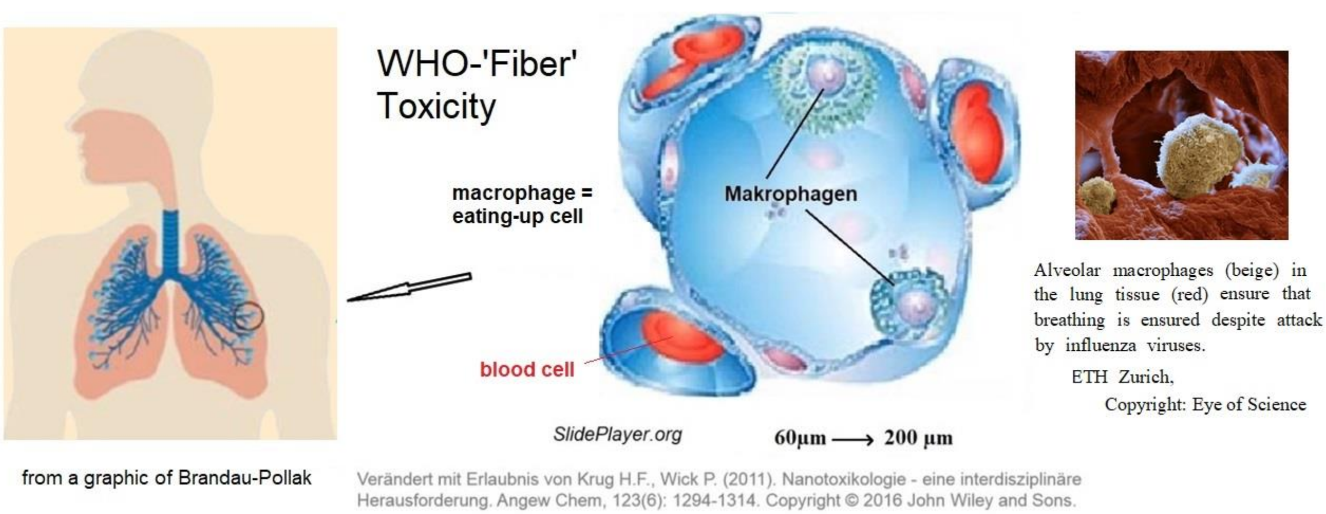

Fig.20-2: Effect of WHO-‘Fibers'

A distinction must be made between long fibers, micro-fragments of fibers such as the ‘WHO-fiber' size, as well as the micro-fragments of composite constituents, i.e. fiber-reinforced polymers FRP or fiber-reinforced concrete FRC. In addition to the fiber, the matrix with the interphase material in the fiber-matrix interface must be considered, too.

Criticality-relevant variables are geometry and bio-resistance:

Geometry: Critical are the already defined ‘WHO-'fiber', as well as dusts and fiber fragments with Ø < 3µm, which penetrate directly into the alveoli and the lung tissue. Since the ‘WHO-fiber’ size is smaller than the diameter of common CFs, the fiber fragment must experience a reduction of the diameter. This can happen by splintering or by burning. CF is not toxic per se!

Bio-persistance: High bio-persistance causes high toxicity, a low bio-solubility in living organisms already speaks as an indication of possible carcinogenicity. Fragments with short residence times that are quickly dissolved or removed are less risky.

Only if a sufficiently high amount of CF-‘WHO-'fibers' is produced and inhaled there is a potential for danger, whereby the following applies:

Risk = hazard potential (severity) • *probability of occurrence*.

Hazard potential = exposure to CF-WHO (size) particles combined with toxicity.
The duration of the exposure in terms of quantity and the possible frequency of occurrence of the event per unit of time are therefore decisive.

Generation and Counting of WHO ’fibers’

A quantity for the risk assessment delivers the counting of the fragments which are generated in machining processes. Question: *Which machining processes seems to be the worst for the generation of ‘WHO-fiber' shaped CF particles, faced in production and recycling*?

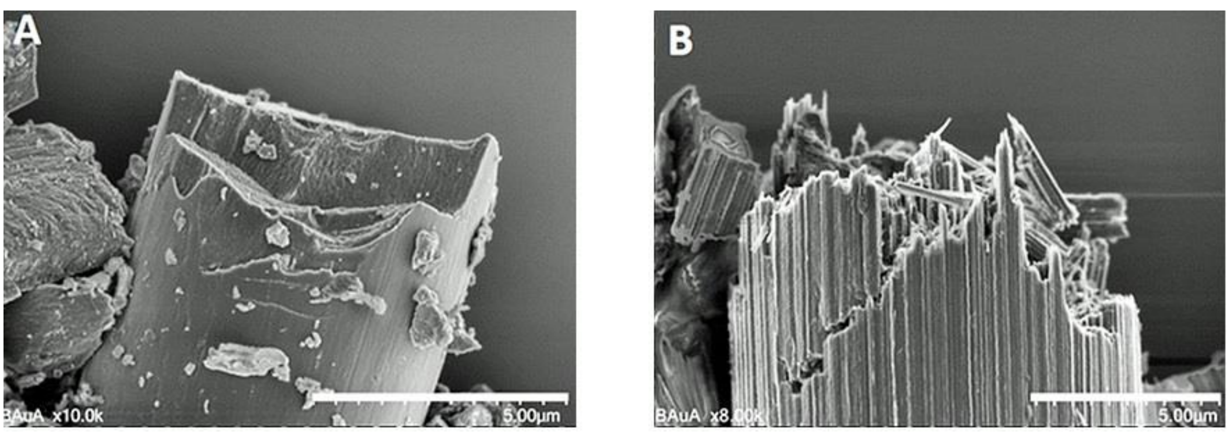

Fig. 20-3:(left) PAN-based, (right) Pitch-based. (Courtesy BAuA, Berlin)

Some answer is given in the BMBF research project *CarboBreak* (*headed by BAuA: the Federal Institute for Occupational Safety and Health conducts research for a safe, healthy and humane working environment*): Investigation of the release behaviour of respirable fragments made of pure fibres and fibre composites (*consisting of CF, sizing, matrix etc.*) under mechanical stress. Basically here, rovings were subjected to an extreme mechanical stress in a so-called ball vibrating mill (*an assumed 'worst case' machining process*), the resulting CF fragments were evaluated with regard to their morphology and then the WHO 'fibers' counted, namely the ‘WHO-Fiber’ quantity / unit volume. The CF portion is considered to be the critical part of the full composite. One significant finding was the different splintering process between PAN (left) and Pitch CF (right).

Fact & Idea:

(1) Pitch fibers are obviously more dangerous because they do extremely splinter. Since the UHM-CF comes closest to the pitch fiber in terms of stiffness of all PAN-CFs, the PAN-UHM represents the more critical PAN CF in terms of risk of splintering.
(2) A CF-parameter is being sought that could be a parameter for explaining the fiber splintering hazard and finding a characteristic.

The sought-after, splinter hazard-descriptive parameter could be the fracture toughness. This property is likely to show some difference in relatively similarly stiff (Young's modulus) brittle materials. *The author lectured fracture mechanics, which he also had to apply at MAN*.
His test proposal was a micro-fracture mechanics investigation of a laser-notched single fiber to determine the different brittleness based on the fracture toughness values of K_{Ic} to be measured. In fracture mechanics, fracture toughness describes the resistance of a material to unstable crack progression An ultra-high graphitized UHM PAN CF such as Torayca's M60J is to be basically investigated, because it is to place narrowest to the behavior of the critical Pitch-Fiber.

Asssumption: *Different fracture toughness values indicate different risk of splintering*.

*The proposed test specimens, together with the difficult notching of a single CF by a laser beam, have already been realized in Kaiserslautern by the institutes IVW with PZKL!

*The search for a fracture mechanics model that allows us to estimate the fracture toughness of a CF is essential for the qualitative differentiation of the envisaged fibers. A formula will provide a not realistic ‘exact’, but a quantified relationship which is fully sufficient.

The searched characteristic for the tensioned notched test specimen is the so-called critical stress intensity factor (SIF) K_{Icr} (= fracture toughness), at which unstable crack progression begins. Its formula reads $K_{\text{Icr}} = \sigma_{\text{fracture}} \cdot \sqrt{\pi \cdot a_{cr}} \cdot Y$, with the so-called geometry factor Y taking the fact into account that the SIF value is theoretically independent of the dimensions of the test specimen only for infinitely large plates. Therefore, the corresponding function Y must be sought for the intended test specimen 'Notched Single Fiber'. This was made possible by the author-available Manual "*NASGRO Reference Manual Version 9.01 Final; December 2018. Fracture Mechanics and Fatigue Crack Growth Analysis Software*".

The application of the full model requires several assumptions:

- CF is a very brittle material
- The crack instability, expressed by the formula, can be applied at the µm-level (micromechanics) for these brittle materials!
- The cross-section, cut by the laser beam, is just a circle section but can be transferred to the elliptical shape of a typical crack
- The 'model for a full cylinder' given as SC07 in the NASGRO document is applicable. Experience has shown that the impact is small, the model can be used also in the µm range
- The crack depth a is given by the laser notch depth.
- Diameter D = Ø = 0.007 mm, UHM 60J.
- The applied stress σ_{fracture} at the fiber ends = breaking tensile force F / area A
- The cross-section cut by the laser beam can be transferred to the elliptical shape of a typical SC07 crack. The difference in surface area is neglected because it is the same for all tested fibers. In the SC07 associated Table C15: For R/t = 0, i.e. a solid cylinder with R = 0 (*t* =

wall thickness = R), approximately to be expected a/t = 0.3, gives c/t = 0.35 and thus Y = 1.6.

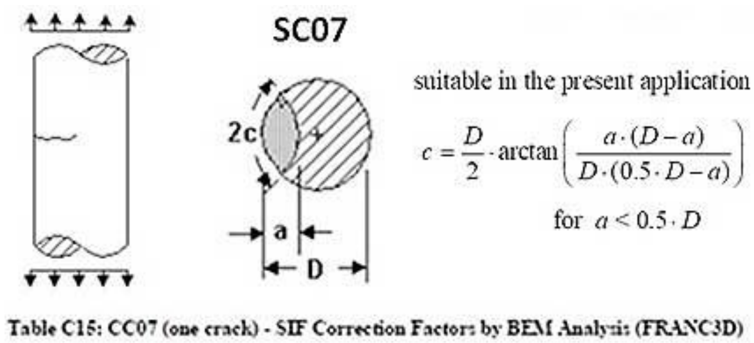

Fig. 20-4: Thumbnail crack in a solid cylinder. Surface crack case SC07
*Manual NASGRO Reference Manual Version 9.01 Final; December 2018***.**
Fracture Mechanics and Fatigue Crack Growth Analysis Software

The author's great wish, driven as a GROWIAN wind turbine co-responsible (*about 1980*), in view of future fear-spreading media about a wind turbine fractures with blades made of standard CFs, i.e. not UHM-CFs:

Submission of an 'official recommendation' by the BAuA, together with Composites United (CU), including adapted recycling safety requirements. on working with CFRP in general and specially on PAN-CF carbon reinforced concrete.

.

LL:

*** The test idea could be fully realized, which is a seldom experienced luck when testing. Unfortunately there is no deeper research ongoing, which would give the basis for the realization of the author's wish.*

Read in Sikkim, about 2011 !

Personal Note on Oil consumption in CF-production and Carbon Concrete Recycling

Fig.20-5 shall give a survey about the portions of the structural materials in the market, dated 2016. It shows how insignificant the carbon fiber content presently is in relation to its origin oil and to the material competitor steel. A yearly CF output of 50000 t equals 4 min steel production (2018). The yearly concrete production equals oil production. This is of basic interest and helpful for many discussions. CF is not yet a real market in construction, basically due to the present regulations of the authorities which does not permit a faster gain of knowledge which is always the result of widespread application, only. Of course, if the concrete mass saving Carbon Concrete market will become significant (*presently about 100.000 t / year*), then CF-production has to be multiplied.

In the context of this chapter's focus and considering recycling: (1)*Why is this marginal crude oil consumption very often considered to be very harmful to the environment. (2) Why must Carbon Concrete be recycled by separating the CF and thereby downgrading it to rCF! T*he author does not consider it reasonable for ecological and economic reasons to extract CF – as required by the current regulations – from shredded carbon concrete parts instead of bringing the recycled CF material parts together with the multifold concrete content into the superstructure of a bridge or street. For safety reasons one can provide measurements of the traffic-generated abraded dust if no further cover is foreseen and the official recommendation above is not yet available.

If basalt fibers BsF will reach a general approval from sustainability reasons they would be much better ecologically and economically due to the fact that enough base material is available. Added ZrO_2 is foreseen to provide alkali resistance. Unfortunately, the available reliable property knowledge is not made public. Of course, the production of carbon fibers still requires energy. However, this will also be the case if carbon fibers are produced from natural fibers in the future.

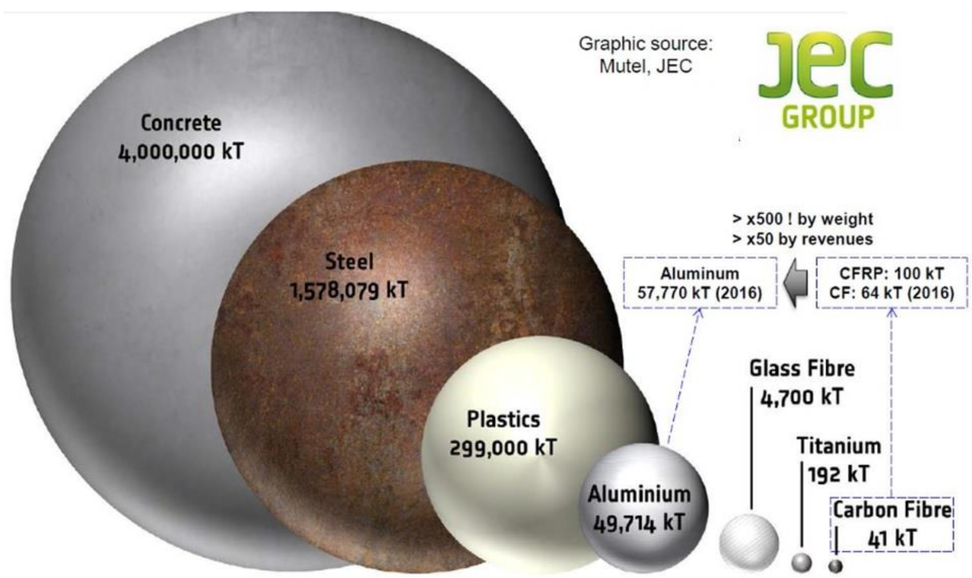

Fig.20-5: Weight ratios of structural materials, year 2016

Please keep in mind:
40000 tons carbon fibers would require just about 40 /4,000,000 = 0.001 % crude oil.

CF total / Steel = 1/10000.
In Germany it is CF total / concrete reinforcing steel ≈ 0.1%.
Concrete / crude oil = 1, GF / CF = 100.
Single car consumes about *1 t oil / year.*

21 A novel Determination of the Residual Strength *R*res, non-cracked, Fatigue Phase 2

Aim: *Derivation of a procedure to determine and rendering the residual strength value R*res

21.1 General for a Proof of Structural Integrity in Projects

Residual strength *Rres* is the fracture stress after pre-damage and re-loading. Not only in mechanical engineering design but also in civil engineering residual strength values are required such as in soil mechanics or for UD-hangers of a railway bridge at Stuttgart, below a hanger or for tension rods of cranes.

Fig.21-2 Stuttgart Stadtbahn bridge.
World's first network arch railway bridge (127 m) that hangs entirely on tension elements made of carbon fiber-reinforced plastic (CFRP). The 72 hangers are produced by Carbo-Link AG

The value is of basic interest, because – due to authority demands - Design Ultimate Load is to sustain even after a distinct fatigue life. The residual strength task is one task to demonstrate structural integrity.

This subject is linked to cyclically micro-damaged structural components (*Phase 2 of fatigue life, strength tools applied*) and macro-damaged ones (*Phase 3 of fatigue life, fracture mechanics problem, damage tolerance mechanics tools applied*), as displayed in *Fig.21-2*. The cyclic loading may range from constant amplitude-loading up to spectrum-loading and has to capture proportional and non-proportional loading scenarios.

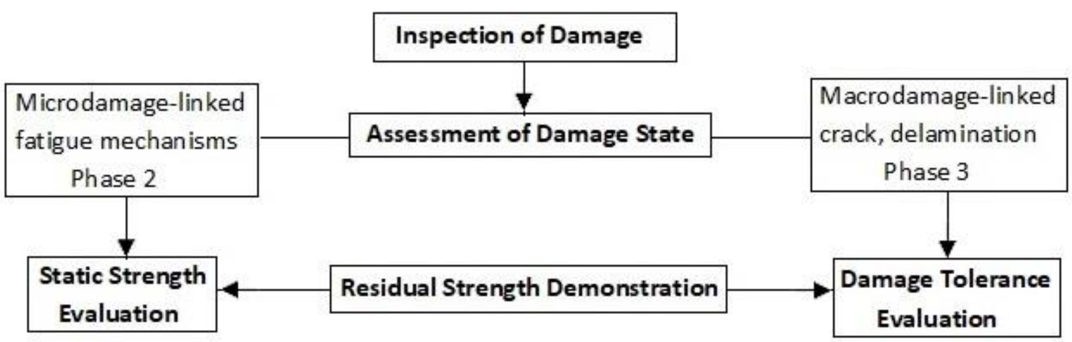

Fig.21-2: Ways of residual strength determination

This task especially comes up in cases such as: A multiple site damage phenomenon is faced with aerospace components such as fabrication-induced flaw clouds (fatigue strength problem, Ariane 5 Booster wall) or real short-crack 'clouds' from e.g. multiple rivet holes in stringer-stiffened panels of aging aircraft components (fracture mechanics problem). Here, the focus is on the Phase 2 residual strength *Rres*. Mind: R_{res} should not be confused with *residual stress* σ_{res}).

In some projects a number for the residual strength at a certain operation cycle value is required. This is well known from impact cases of laminated panels. There, a Compression-After-Impact

(CAI) test is to execute after the impact event because the impact may result in a barely visible external damage and it may generate a dramatic reduction of compressive strength due to separation of layers resulting in a large bending stiffness loss. Regarding crack-linked fatigue life Phase 3 residual strength problems the reader is referred to fracture mechanics.
Residual strength tests are long-lasting and expensive. Therefore, procedures are searched that help to reduce the test effort if enough physical knowledge is available.

First step is to map the relevant SN-curve (Wöhlerkurve) by taking the widely used 4-parameter Weibull function

$$\text{stress ratio R} = \sigma_{\min} / \sigma_{\max} = \text{constant}: \quad \sigma_{\max}(\mathrm{R}, N) = c1 + (c2 - c1) / \exp(\log N / c3)^{c4} .$$

(stress ratio → straight letter R, strength→ bias letter *R*).

An SN-curve describes the relation between the cyclic loading and the number of cycles to failure *N*. On the horizontal axis in *Fig.21-3* the number of cycles to failure is given on logarithmic scale. On the vertical axis (*either linear or logarithmic*) the stress amplitude $\sigma_{amplitude}$ of the cycle is often given. In the case of brittle materials *sometimes the maximum stress* σ_{max}.. The provided mean SN-curves, R = constant, base on the fatigue test measurement types 'pearl-chain testing' or 'horizontal load level testing'. Fatigue curves are given for un-notched test specimens ($K_t = 1$) and for notched ones, the loading can be uniaxial or multi-axial. Considering residual strengths, measurements on the vertical axis at n = constant are required.

In design verification very often as fractile (quantile) numbers, representing the failure probability p_f, 5% or 10% are taken in order to capture some uncertainty compared to the average of 50%. For the loading side the design FoS *j,* in construction *γ,* capture the uncertainty of the loading. The residual strength design verification has to meet Design Ultimate Load. Following HSB 62200-01 the determination of the static residual strength for single load paths must be made with statistically significant A-values; for possible multiple load path structural parts B-values may be used.
Moving to the required statistical properties some notions are to depict. Capturing the uncertainty of the resistance quantities, the following is performed: Denoting P the survival probability and C the confidence level applied, when estimating a basic population value from test samples, partly enriched by some knowledge of the basic population. Regarding C a one-sided tolerance level it reads:

Static → Statistical reduction of average strength from (P= 50%, C= 50%) to e.g. (B-value: P = 90%, C = **95**%).
Cyclic→ Statistical reduction of average SN curve from (P=50%, C= 50%) to e.g. (P= 90%, C= **50**%).

All this is executed to keep a generally accepted survival reliability of about $\Re = 1 - p_f > 1 - 10^{-7}$.

21.2 Classical way to determine Rres

Determination via the interpretation "*The course of the residual strength is the difference of the static strength* and *the maximum strength* $\sigma_{max}(N)$ *of an SN curve* R", see *Fig.21-3*. This leads to the formulation $\quad R_{res} = \sigma_{max}(N) + [R^t - \sigma_{max}(N)] \cdot \rho(n)$ with $\rho(\mathrm{n}) = 1 - (\mathrm{n/N})^p \equiv 1 - D^p$,

where the exponent p describes the decay of the residual strength capacity and D the micro-damage quantity, (see Hahne C: *Zur Festigkeitsbewertung von Strukturbauteilen aus Kohlenstofffaser-Kunststoff-Verbunden unter PKW-Betriebslasten*. Shaker Verlag, Dissertation 2015, TU-Darmstadt).

Fig.21-3 depicts for R = 0.1 the mean (average) 50% SN-curve and the 90% SN-curve. The residual strength curve *Rres* is given for the point (10^5 cycles, σ = 34 MPa). The stress σ belongs to a so-called 'one stage test' or constant amplitude test. Regarding the residual strength value at the 90% SN-curve the question arises: "*Where does the necessary statistical basis for a reduced SN-curve come from, if not sufficient test series on vertical and horizontal levels were run*"?
Due to missing test data a test data-based work case cannot be presented. Therefore, the author tried to figure out a procedure which gives an understanding of the subject.

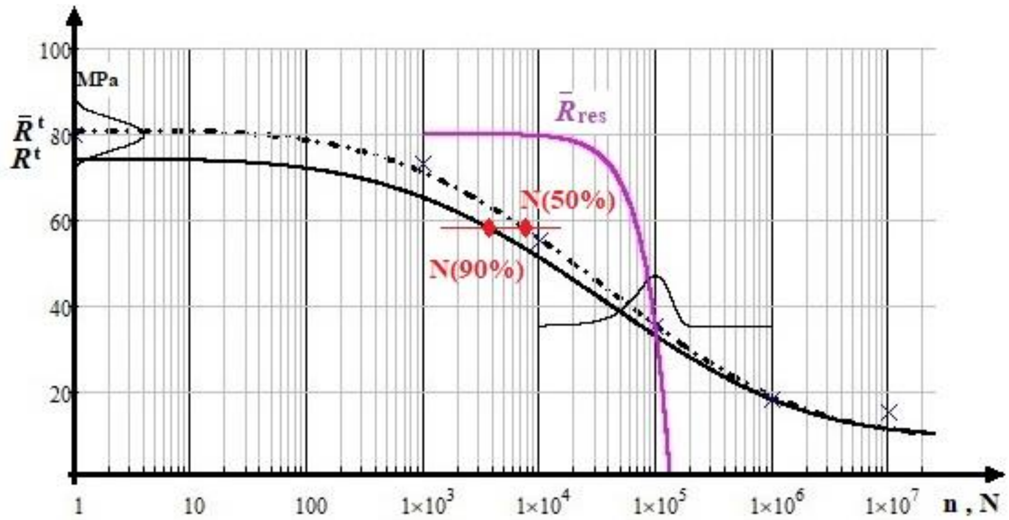

Fig.21-3, Schematic example, uniaxial loading: R= 0.1. $\bar{R}_{res}$ *is mean tensile residual strength*

21.3 Idea Cuntze, probabilistic way to determine a 90% value by the convolution integral

A possibility to determine a 90%-value is given by the application of the so-called convolution integral, using density distributions of R_{res} and of N with just a little hope to find the distribution measured, Fig.21-3. The output of the mathematical expression convolution integral represents the probability of failure p_f. The numerical analysis is based here on the assumption: 'The density distributions on x- (f_N) and y-axis (f_{Res}) are approximately basic populations and of Normal Distribution-type' f_{ND} (for the density distributions also a logarithmic, a Weibull density function or a truncated function could be employed). The convolution integral, solved by Mathcad 15, reads

$$(1-p_f) = \Re = p_{ü} = \int_{-\infty}^{\infty} \left(\int_{Rres}^{\infty} f_{Res}(R) \cdot dR \cdot f_N(N)\, dN \right) = 90\% \text{ fractile} \quad \text{for ND density distributions}$$

$$\text{with} \quad f_{ND}(x) = \frac{1}{\sigma \cdot \sqrt{2 \cdot \pi}} \cdot exp\left[-\frac{1}{2}\left(\frac{x-\mu}{\sigma}\right)^2\right] \quad \text{for abscissa } N \text{ and ordinate } R^t .$$

Data base of the numerical probabilistic example (statistical: μ = mean, σ = standard deviation) is:

* Static strength distribution μ = 80 MPa, σ = 3.2 MPa
* R_{res} distribution in computation point, y-axis, μ = 43.5 MPa, σ = 2.9 MPa
* Cycle distribution in computation point, x-axis, μ = 3431 cycles, σ = 446 cycles and the Coordinates of the chosen computation point * (38 MPa, n = 2000 cycles in *Fig.21-4*).

(Note, please: The presented application outlines a limit of the Mathcad 15 code application. Mathcad has

(Note, please: The presented application outlines a limit of the Mathcad 15 code application. Mathcad has no computation problem with the computation of the required so-called convolution integral. However, when visualizing the probability hill in Fig.21-5, it was only partly able to manage the 'big data' problem and runs into endless loops. Therefore the author had to sort out a work case with reduced stress and cycle regimes. The original SN data set was for fiber fracture (FF) of CFRP considering the hanger. This reduction to a relatively simple numerical example does not matter because the procedure is of interest and will explain the posed task.)

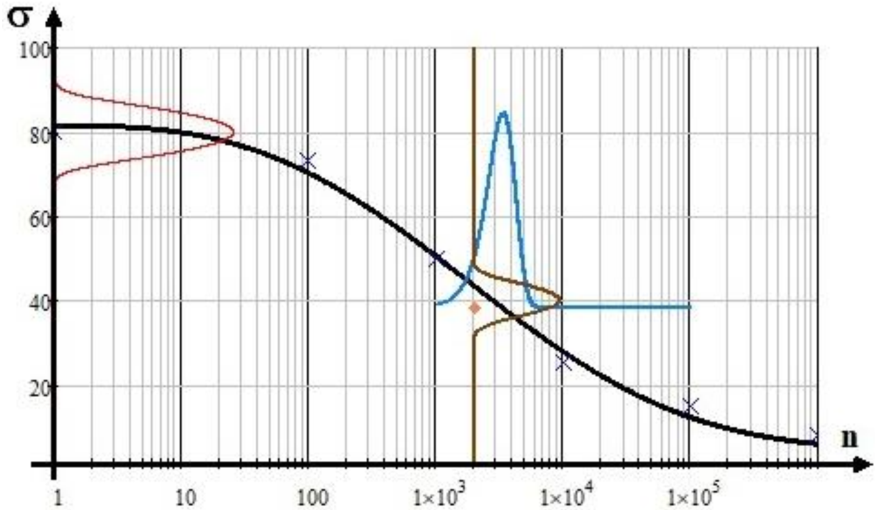

Fig.21-4, Simplified Mathcad calculable example: Assumed distributions of residual strength and cycles linked to R_{res} *(38 MPa, 2000 cycles). SN-curve,* R = 0.1: *c1= 20 MPa, c2= 80 MPa , c3= 3.77, c4= 2.92*

Fig.21-4 depicts the SN-curve, the chosen computation point, static strength distribution with an assumed residual strength distribution and cycle distribution, all through the computation point *. It is a semi-logarithmic graph. As it is a brittle example material, the use of σ_{max} (*involves* R^t *as origin*!) as ordinate is of advantage for the 'strength-oriented' design engineer compared to using a stress amplitude σ_a .

The probabilistic treatment delivers the 'joint' probability hill of both the distribution functions in *Fig.21-5*, (right). The hill's average center coordinates are 43.5 MPa, 3430 cycles. The figure further depicts the density distributions of the residual strength $R_{res}(\sigma)$ and of the fracture cycle N .

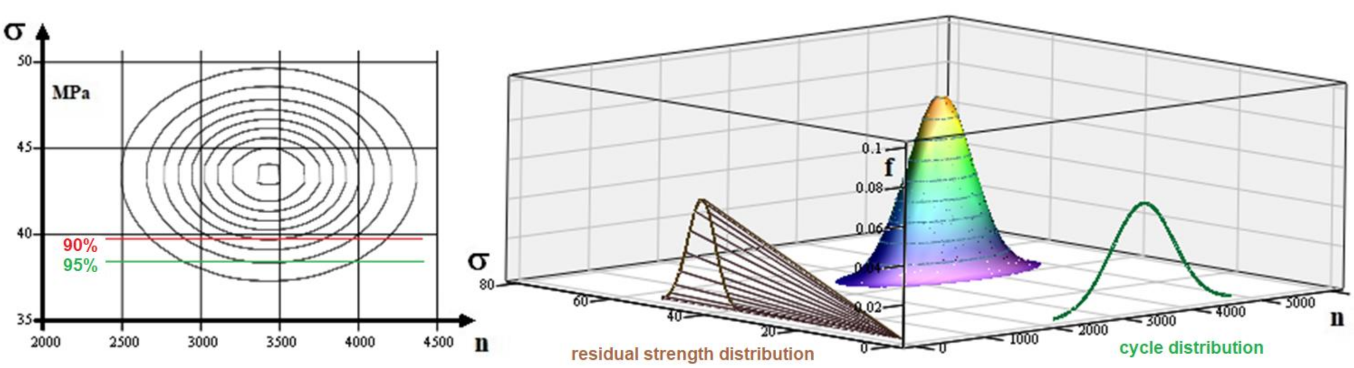

Fig.21-5: (right) Cyclic distributions and assumed residual strength distribution with survival probability hill applying the convolution integral. (left) Projection of lines of equal probability with two chosen residual strength cut-offs , M is the hill designation

In the right part figure, the residual strength distribution is not clearly visible due to additional Mathcad-drawn beams running out from the origin, which are to neglect. The task seems to be an

overloading of the Mathcad code which could not anymore handle the numerically effortful task for too large cycle numbers. The left figure shows the projection of the probability hill with lines of equal probability belonging to the chosen computation point *. Below, the computation parameter input set is depicted:.
Design Safety considering the scatter of the design parameters is tackled as follows:
The scatter of loading is considered in the residual strength design verification because DUL with its design safety factor j_{ult} has to be verified. The scatter of the residual strength R_{res} and of the fracture cycle N is captured by a joint probability calculation indicated below. This procedure is effortful, however of high fidelity if test data is available.

Under above assumptions an estimation of a required 90%-linked residual (tensile) strength value can be determined according to the formula below representing the probability hill volume truncated by R_{res}

$$\mu NR = 3431 \quad \sigma NR = 446 \quad \mu\sigma R = 43.5 \quad \sigma\sigma R = 2.9 \qquad n := 2000..6000 \quad \sigma := 0..80$$

$$x_n := \mathrm{dnorm}(n, \mu NR, \sigma NR) \qquad y_\sigma := \mathrm{dnorm}(\sigma, \mu\sigma R, \sigma\sigma R) \qquad F(x,y) := x \cdot y \qquad M_{n,\sigma} := F(x_n, y_\sigma) \cdot 750$$

$$p\ddot{u} := \int_{\sigma res}^{Rt+\sigma Rt} \int_{2500}^{5500} \frac{1}{\sigma\sigma R \cdot \sqrt{2\pi}} \cdot e^{\left[\frac{-1}{2} \cdot \left(\frac{y-\mu\sigma R}{\sigma\sigma R}\right)^2\right]} \cdot \left[\frac{1}{\sigma NR \cdot \sqrt{2\pi}} \cdot e^{\left[\frac{-1}{2} \cdot \left(\frac{x-\mu NR}{\sigma NR}\right)^2\right]}\right] dx\, dy$$

The computation delivers for the point ($\sigma_{res} \equiv R_{res}$ = 38.0 MPa, 2000 cycles) the value pü = P = 95% = $\Re$.
Setting the value 39.5 MPa, the demanded survival probability pü = 90% = (1- p_f) is obtained for R_{res} .

LL:

- *The proposed procedure clearly shows how to statistically understand a residual strength value*
- *It could be proven that the proposed model leads to an acceptable value for the residual strength of fatigued, non-cracked structural parts.*

21.4 Residual Strength R_{res}, pre-cracked, Fatigue phase 3, Fracture Mechanics (for completion)

To estimate the residual strength of a pre-cracked structural part or the critical length of an initial macro-crack is essential regarding the questions:

(1) Is the crack-length at the end of static loading critical?

(2) Is the crack-length at the end of cyclic loading critical for further static loading, considering a SN-curve? Here, the certification of cracked components in aircraft structures requires a damage tolerance assessment.

22 Full Mohr UD Envelope $\tau_{nt}(\sigma_n)$, Derivation of $\Theta_{fp}(\sigma_n)$ and of Cohesive shear Strength

Aim: *Unlocking the 'mystery' behind the shear quantities* R_{23}, R_{23}^{τ} and R_{23}^{A} *faced in UD analysis.*

22.1 Shear Strength Quantities in Analysis, Survey

Fig.22-1 collects all figures which are necessary to understand the difference of applied shear quantities (*upper part figure*): Shear fracture stress (Tsai-Wu, Hashin) and so-called cohesive strength R_{23}^{τ} (construction, rock mechanics) and the Action plane shear strength R_{23}^{A} (Puck).

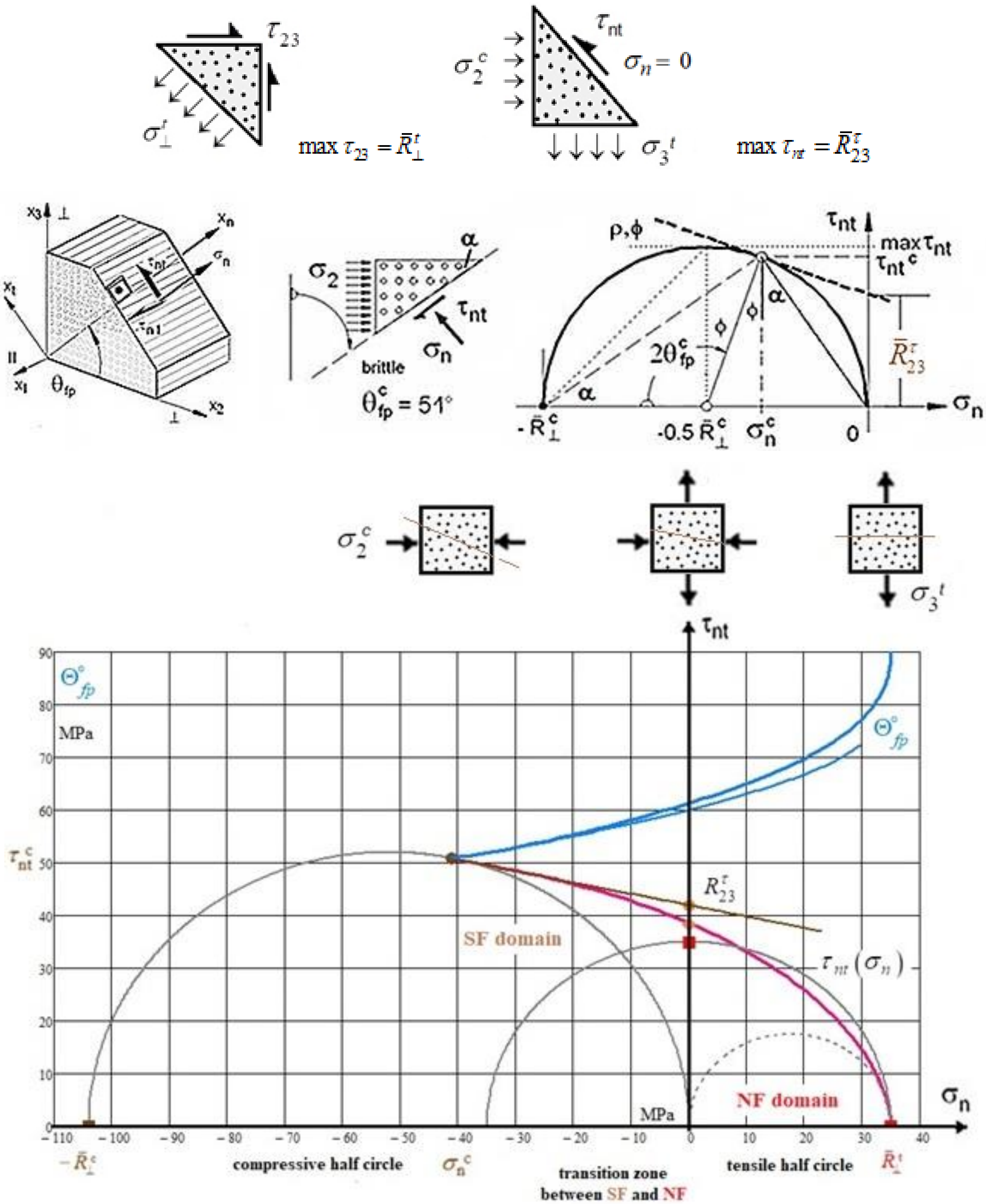

Fig. 22-1: (up) Difference of transversal shear fracture stress and cohesive strength. (below) Mohr-Coulomb curve characteristics, Mohr shear curves τ_{nt} (σ_n) with its special points and three Mohr half-circles

The brown curve in *Fig.22-1* is the Linear Mohr-Coulomb (M-C) curve. This approach is a simple IFF2-extrapolation from the compressive strength point, keeping the fracture angle measure $C = C_{fp}^{c}$ constant, when estimating the so-called cohesive strength by $R_{23}^{\tau} = \tau_{nt}{}^{c} + \mu \cdot \sigma_{n}{}^{c}$ at $\sigma_n = 0$. The letters ρ = ϕ address the so-called friction angle. The 3 sketches above the bottom figure demonstrate that the cohesive strength point $\bar{R}_{23}^{\tau}$ is located in the mode's transition zone and cannot be reliably estimated just by an IFF2-Extrapolation, employing just SF! The parallel acting normal fracture part NF, namely IFF1, was neglected. But IFF1 usually causes much more failure danger than the compression-linked shear mode IFF2 from the transition zone beginning on.

The analytical determination of the M-C failure curve and of a value for the cohesive strength depends on the quality of the used IFF2-model and the interaction of both in the transition zone.
Therefore, in order to accurately determine $\tau_{nt}(\sigma_n)$ both the modes are to include in the derivation process of a realistic M-C curve, the determination of the fracture angle $\Theta_{fp}°$ and of the cohesive strength $\bar{R}_{23}^{\tau}$ at $(\tau_{\mathrm{nt}}^{\mathrm{fracture}}, \sigma_{\mathrm{n}} = 0)$.
An improved treatment by a correction f_{corr} of the M-C curve has been effortful executed by the author in [*Cun23b*]. This became necessary because any SFC has to be as simple as possible. Of course, this means that all presently applied SFCs have a deficiency in the mode transition zones. The author has compensated for this with a correction, for details of this elaboration see [*Cun*]. The bottom figure in *Fig.22-1* displays, how the fracture angle increases, when approaching $\bar{R}_{\perp}^{t}$. Thereby the **bold** curve represents the optimum corrected mapping of the M-C curve in the transition zone around $\sigma_n = 0$.
Now the steps of the tedious way obtain *Fig.22-1* shall be presenred.

22.2 Relations for a Transformation from a Test Fracture Curve $\sigma_3(\sigma_2)$ to Mohr's $\tau_{nt}(\sigma_n)$

The general stress state $\{\sigma\}$ in the material point of the lamina has to be transformed around the 1-axis to the arbitrary Mohr stress state $\{\sigma^{\theta}\} = [T_{\sigma}(\theta)] \cdot \{\sigma\}$, a fibre-parallel plane, by applying *Fig.22-1*, wherein $c := \cos\theta$, $s = \sin\theta$ and n is normal to the 'action plane' [*Cun22*]. Values of the parameters depend on the approach, whether it is a linear or a parabolic one.

$$\begin{array}{c} \\ \rightarrow \\ \\ \rightarrow \\ \\ \rightarrow \end{array}\begin{bmatrix} \sigma_1 \\ \sigma_n \\ \sigma_t \\ \tau_{nt} \\ \tau_{t1} \\ \tau_{n1} \end{bmatrix} = \{\sigma^{\theta}\} = [T_{\sigma}(\theta)]\{\sigma\} = \begin{bmatrix} 1 & 0 & 0 & 0 & 0 & 0 \\ 0 & c^2 & s^2 & 2sc & 0 & 0 \\ 0 & s^2 & c^2 & -2sc & 0 & 0 \\ 0 & -sc & +sc & c^2 - s^2 & 0 & 0 \\ 0 & 0 & 0 & 0 & c & -s \\ 0 & 0 & 0 & 0 & +s & c \end{bmatrix} \begin{bmatrix} \sigma_1 \\ \sigma_2 \\ \sigma_3 \\ \tau_{23} \\ \tau_{31} \\ \tau_{21} \end{bmatrix}$$

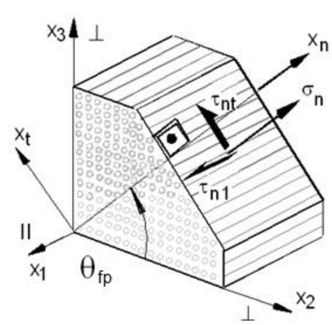

Fig. 22-2: Visualization of the transformation of lamina stresses into associated Mohr stresses. $\theta = \Theta_{\mathrm{fp}}$ denotes the angle of the anti-clockwise transformation from the (1, 2, 3)-CoS to the (1, n, t)-CoS

According to

$$\sigma_n^A(\theta) = c^2 \cdot \sigma_2 + s^2 \cdot \sigma_3 + 2 \cdot s \cdot c \cdot \tau_{23}, \; \tau_{n1}^A(\theta) = c \cdot \tau_{21} + s \cdot \tau_{31}, \; \tau_{nt}^A(\theta) = -s \cdot c \cdot (\sigma_2 - \sigma_3) + (c^2 - s^2) \cdot \tau_{23}$$

the transformed stresses $\sigma_n(\theta)$, $\sigma_t(\theta)$, $\tau_{nt}(\theta)$, which Puck termed 'Action Plane' Stresses, *Fig.22-1*, right, in the turned CoS depend on $(\sigma_2, \sigma_3, \tau_{23})$ only, whereas τ_{t1}, τ_{n1} is linked to (τ_{31}, τ_{21}). They

are acting in the potentially physical (fracture) failure 'plane' and are decisive for fracture. In case of normal stress- induced fracture (NF) σ_n will be responsible for fracture and in case of shear stress-induced fracture τ_{nt} will be the fracture dominating Mohr stress. The Mohr stress τ_{t1} has no impact but has to be considered in the derivations of the *Eff*-functions until it vanishes during the later transformation process.
Fracture plane will become that 'action plane' where the material stressing effort *Eff*($\sigma(\theta)$) will reach the value 1 = 100% at (maximum) failure loading and by that, where the theoretical material reserve factor f_{RF} will become a minimum.

*22.2 Accuracy Problem of the IFF2-model in the transition zone IFF2 (*SF*) - IFF1 (*NF*)*

In this subchapter the cohesion strength R_{23}^{τ}, activated by τ_{nt} in the quasi-isotropic plane of the UD material is envisaged. This quantity is located in the transition zone of the two modes IFF1 and IFF2. With isotropic materials the author learned that a transformation from UD lamina stresses into the desired Mohr stresses τ_{nt}, σ_n must be also possible. Thereby a closer look at R_{23}^{τ} and at the Mohr envelope $\tau_{nt}(\sigma_n)$ or M-C curve will be possible.

Here addressed is the quasi-isotropic UD plane (*works similar to isotropic concrete materials, using* ***available*** *multi-axially compression test-based data [Cun**22**]*). The compromise is on the 'safe Reserve Factor side'. This means: The engineering approach of above $Eff^{\perp\tau}$ (SF) is not problematic for Design Verification, because *Eff* = 1 delivers conservative *RF*-values in the transition zone, since the curve runs more internally due to the generally *minimum value choice* of the interaction exponent *m*.

Focus here is the derivation of $\tau_{nt}(\sigma_n)$, $\Theta_{fp}(\sigma_n)$ and R_{23}^{τ} from a well mapped measured fracture curve $\sigma_3(\sigma_2)$ and its course in the 2nd quadrant of $\sigma_3(\sigma_2)$. In *Table 22-1* all relations necessary for the transformation are compiled and formulas for the searched entities τ_{nt} , σ_n , Θ_{fp}° are presented. After transformation of the UD lamina (layer) stresses σ_2, σ_3, τ_{23} in the quasi-isotropic plane into the principal stresses σ^{pr} (*index* ^{pr} *means principal*), the shear stress τ_{23} vanishes. Therefore, with no loss of generality σ^{pr} can be simpler written in the further text, back again as plain letter σ, but thinking they might be principal stresses acting in the quasi-isotropic plane. In the addressed quasi-isotropic plane this transformation of the lamina stresses into Mohr stresses practically works via addition theorems and using $C(\Theta_{fp}°) = cos\Theta^2 - sin\Theta^2$, which might be termed 'fracture angle measure'.

As the author still found with isotropic materials, the interaction considering curve (thinly-marked) in *Fig.22-3* cannot accurately map the course of test data. The improved **bold-**marked curve is physically more accurate and this local mapping shortcoming is to model more detailed as follows. *Fig 22-1* shows that with the IFF2-function the shear effort $Eff^{\perp\tau}$ cannot become zero in the M-C domain at $\sigma_2 = 0$. This numerical behavior is a shortcoming in the transition zone of the 'simple' engineering FMC-based IFF2 approach. An accurate alteration of the fracture angle Θ_{fp}° and of the associated Mohr stresses τ_{nt}, σ_n is not to achieve with the mathematical course of the given 'engineering' IFF2 function. The mapping quality of the given IFF2 is not fully sufficient if the alteration of the fracture angle Θ_{fp} in the transition zone is to determine. This bi-axially stressed transition zone between the normal fracture mode domain NF and the shear fracture mode domain SF is ruled by interaction and therefore requires both the Eff-modes to be inserted into the interaction equation *Eff* = 1. Specific points of the investigated M-C domain are: $(\sigma_2 = -\bar{R}_\perp^{\,c}, 0) \rightarrow (\sigma_2, \sigma_3 = -\sigma_2) \rightarrow (0, \sigma_3 = \bar{R}_\perp^{\,t})$. In order to sort out a better mapping description it is essential to know how the pure mode efforts of the activated modes IFF1 and IFF2 change its influence along the σ_2-axis, which is depicted in *Fig.22-2*. $Eff^{\perp\tau}$ firstly becomes zero at the equi-biaxial tensile 'strength' point $(\bar{R}_\perp^{\,tt}, \bar{R}_\perp^{\,tt}) < \bar{R}_\perp^{\,t}$. This zero point lies physically 'too late' for a more accurate revised local mode description. An improvement is to achieve.

22.3 Improvement of the IFF2 Criterion in the Transition Zone

The required entities τ_{nt} , σ_n , $\Theta_{fp}°$ and $\bar{R}_{23}^{\tau}$ only become accurate if a physically necessary correction of $Eff^{\perp\tau}$ is considered by using a correctively acting decay function f_{corr} . In order to implement f_{corr} one just has to replace $a_{\perp\perp}$ by $f_{corr} \cdot a_{\perp\perp}$ and $b_{\perp\perp}$ by $f_{corr} \cdot b_{\perp\perp}$. For a realistic transformation of the test curve, formulated in lamina stresses into a Mohr stress formulation, it is considered that $Eff^{\perp\tau}$ (SF) physically must become zero when reaching the pure NF domain at the point $(\sigma_3 = \bar{R}_\perp^t, \sigma_3 = 0)$, (see the course in *Fig.22-3*):

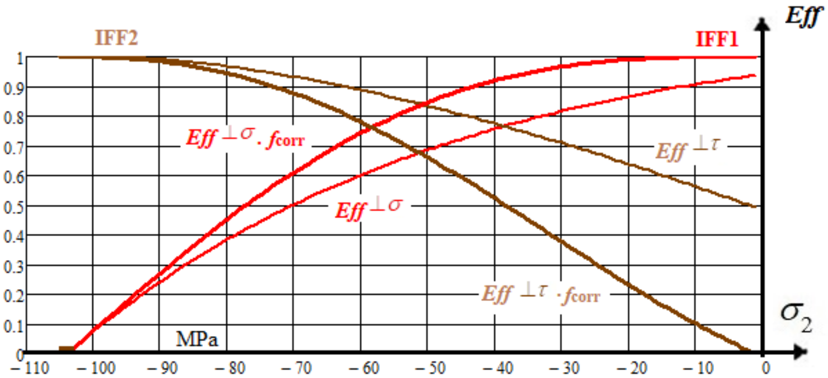

Fig.22.3: Course of the two efforts $Eff^{\perp\sigma}$, $Eff^{\perp\tau}$ *composing the fracture stress curve Eff =1= 100%.*

$\bar{R}_\perp^c = 104 MPa$, $\bar{R}_\perp^t = 35$ MPa, $\Theta_{fp}° = 51°, C^c = -0.21 \leftrightarrow$ $a_{\perp\perp} = 0.26$, $\mu_{\perp\perp} = 0.21$.

$f_{corr} = 1 + c_0 \cdot (\bar{R}_\perp^c + \sigma_2)^2$ with c_0 from inserting $(\sigma_2 = 0,\ \sigma_3 = \bar{R}_\perp^t)$, $c_0 = 8.9 \cdot 10^{-5}$.

IFF1: $Eff^{\perp\sigma} = [(\sigma_2 + \sigma_3) + \sqrt{\sigma_2^{\,2} - 2\sigma_2 \cdot \sigma_3 + \sigma_3^{\,2}}\,] / 2\bar{R}_\perp^t$,

IFF2: $Eff^{\perp\tau} = [a_{\perp\perp} \cdot f_{corr} \cdot (\sigma_2 + \sigma_3) + b_{\perp\perp} \cdot f_{corr} \sqrt{\sigma_2^{\,2} - 2\sigma_2\sigma_3 + \sigma_3^{\,2}}\,] / \bar{R}_\perp^c$.

Similar to the isotropic case the bi-axial stress-ruled quasi-isotropic M-C curve, located in the quasi-isotropic plane, is oppositely dominated by two modes, IFF2 (SF) with IFF1 (NF). Therefore, attention was paid to the interaction of both these modes in the transition zone in order to finally obtain an 'accurate' fracture angle $\Theta_{fp}°$, being the pre-condition to determine the envisaged two Mohr stresses τ_{nt}, σ_n. the shear material stressing effort $Eff^{\tau} = Eff^{SF}$ must physically become zero at the tensile strength point (0, R^t). This specific shortcoming is brought about by a correction function that defines the decay of Eff^{τ} and is practically performed by setting $Eff^{\tau} = 0$ at $\sigma_{II} = 0$. As decay function was taken an exponential one, namely:

$$f_d = 1/(1 + \exp(\frac{c_{1d} + \sigma_{II}}{c_{2d}})), \text{ with } c_{1d}, c_{2d} \text{ fixed at } (-\bar{R}^c, 0.995), (-0.01, +0.01).$$

The correction changes the formula for the determination of the fracture angle measure *C* in *Table 22-1.*

Table 22-1: IFF2-IFF1-interacted Derivation of $\tau_{nt}(\sigma_n), R^{\tau}_{23}, \Theta_{fp}$ from a measured curve $\sigma_3^{fr}(\sigma_2)$

$SF: Eff^{\perp\tau} = [a_{\perp\perp}\cdot(I_2) + b_{\perp\perp}\cdot\sqrt{I_4}] / \bar{R}^c_{\perp} = 1$

$= [a_{\perp\perp}\cdot(\sigma_2^{pr}+\sigma_3^{pr}) + b_{\perp\perp}\cdot\sqrt{(\sigma_2^{pr}-\sigma_3^{pr})^2+0^2}] / \bar{R}^c_{\perp} = 1$ (lamina stresses)

$\equiv [a_{\perp\perp}\cdot(\sigma_n+\sigma_t) + b_{\perp\perp}\cdot\sqrt{(\sigma_n-\sigma_t)^2+4\tau_{nt}^2}] / \bar{R}^c_{\perp} = 1$ (in Mohr stresses)

$NF: Eff^{\perp\sigma} = (\sigma_2^{pr}+\sigma_3^{pr}) + \sqrt{(\sigma_2^{pr}-\sigma_3^{pr})^2+0^2}] / 2\cdot\bar{R}^t_{\perp} = 1$

$\equiv [(\sigma_n+\sigma_t) + \sqrt{(\sigma_n-\sigma_t)^2+4\tau_{nt}^2}] / 2\cdot\bar{R}^t_{\perp} = 1.$

Known: $\sigma_2^{pr}, \sigma_3^{pr}$. Searched is: $\sigma_n, \tau_{nt}, \Theta_{fp}$ with $C = \cos(2\cdot\Theta_{fp}{}^{\circ}\cdot\pi/180^{\circ})$.

Use of addition theorems, $\sigma_{\lambda} = 0$. For lamina stresses ^{pr} now dropped for simplification

$\sigma_n - \sigma_t = c^2\cdot(\sigma_2-\sigma_3) - s^2\cdot(\sigma_2-\sigma_3) = C\cdot(\sigma_2-\sigma_3)$, $S = \sqrt{1-C^2}$

$\sigma_t = \sigma_n - C\cdot(\sigma_2-\sigma_3)$, $C = c^2 - s^2 = 2c^2 - 1 = 1 - 2s^2$, $\sigma_n + \sigma_t = \sigma_2 + \sigma_3$,

$\tau_{nt} = -0.5\cdot S\cdot(\sigma_2-\sigma_3) = -0.5\cdot\sqrt{1-C^2}\cdot(\sigma_2-\sigma_3)$, $\sigma_n = (C+1)\cdot 0.5\cdot\sigma_2 + (1-C)\cdot 0.5\cdot\sigma_3$.

Differentiation of structural stresses-linked Mohr stresses delivers (minus due to implicit derivation)

$\frac{d\tau_{nt}}{d\sigma_n} = \frac{(s^2-c^2)\cdot(\sigma_2-\sigma_3)}{-2\cdot s\cdot c\cdot(\sigma_2-\sigma_3)} = \frac{C}{S}$, valid *uni-* and *bi-axial* (like isotropic!).

Fracture (interaction) equation $\equiv$ mathematical equation of the fracture body

$Eff = [(Eff^{NF})^m + (Eff^{SF})^m]^{m^{-1}}$ *or* computationally simpler

$(Eff^{NF})^m + (Eff^{SF})^m = 1 = 100\%$ total effort fracture curve

From differentiation of the interaction equation (σ_t goes away)

$\{[(\sigma_n + \sigma_n - C\cdot(\sigma_2-\sigma_3)) + \sqrt{(\sigma_n-\sigma_n-C\cdot(\sigma_2-\sigma_3))^2+4\tau_{nt}^2}] / 2\cdot\bar{R}^t_{\perp}\}^m +$

$+\{[a_{\perp\perp}\cdot(\sigma_n+\sigma_n-C\cdot(\sigma_2-\sigma_3)) +$

$+ b_{\perp\perp}\cdot\sqrt{(\sigma_n-\sigma_n-C\cdot(\sigma_2-\sigma_3))^2+4\tau_{nt}^2}] / \bar{R}^c_{\perp}\}^m = 1.$

are obtained the two equations

$d[(Eff^{NF})^m + (Eff^{SF})^m]/d\sigma_n =$

$m\cdot\{2\sigma_n - C\cdot(\sigma_2-\sigma_3) + \sqrt{(C\cdot(\sigma_2-\sigma_3))^2+4\tau_{nt}^2}]/2\bar{R}_{\perp}^{t}\}^{m-1}/\bar{R}_{\perp}^{t} +$

$+2a_{\perp\perp}\cdot\mathrm{m}\cdot\{a_{\perp\perp}(2\sigma_n - C\cdot(\sigma_2-\sigma_3)) + b_{\perp\perp}\sqrt{(C\cdot(\sigma_2-\sigma_3))^2+4\tau_{nt}^2}] / \bar{R}_{\perp}^{c}\}^{m-1}/\bar{R}_{\perp}^{c}$,

$d[(Eff^{NF})^m + (Eff^{SF})^m]/d\tau_{nt} =$

$\frac{2m\cdot\tau_{nt}\cdot\{2\sigma_n - C\cdot(\sigma_2-\sigma_3) + \sqrt{(C\cdot(\sigma_2-\sigma_3))^2+4\tau_{nt}^2}]/2\bar{R}_{\perp}^{t}\}^{m-1}}{\bar{R}_{\perp}^{t}\cdot\sqrt{(C\cdot(\sigma_2-\sigma_3))^2+4\tau_{nt}^2}} +$

$+4b_{\perp\perp}\cdot\mathrm{m}\cdot\{a_{\perp\perp}(2\sigma_n - C\cdot(\sigma_2-\sigma_3)) + b_{\perp\perp}\sqrt{(C\cdot(\sigma_2-\sigma_3))^2+4\tau_{nt}^2}] / \bar{R}_{\perp}^{c}\}^{m-1}/\bar{R}_{\perp}^{c}$.

Equating above two equations and replacing Mohr stresses by ply stresses

via $\sigma_n = (C+1)\cdot 0.5\cdot\sigma_2 + (1-C)\cdot 0.5\cdot\sigma_3$, $\tau_{nt} = -0.5\cdot\sqrt{1-C^2}\cdot(\sigma_2-\sigma_3)$

yields an implicitely to solve equation for the fracture angle measure C

$$\frac{C(\sigma_2,\sigma_3)}{\sqrt{1-C^2}} = -[\frac{A}{\bar{R}_{\perp}^{t}} + \frac{2\cdot a_{\perp\perp}\cdot B}{\bar{R}_{\perp}^{c}}]/[\frac{2\cdot A}{\bar{R}_{\perp}^{t}\sqrt{(\cdot\sigma_2-\sigma_3)^2}} + \frac{4\cdot b_{\perp\perp}\cdot\tau_{nt}(C)}{\bar{R}_{\perp}^{c}\sqrt{(\cdot\sigma_2-\sigma_3)^2}}] \quad \text{with}$$

$$\mathrm{A} = [\frac{\sigma_2+\sigma_3+\sqrt{(\sigma_2-\sigma_3)^2}}{2\cdot\bar{R}^t_{\perp}}]^{m-1}, \quad \mathrm{B} = [\frac{a_{\perp\perp}\cdot(\sigma_2+\sigma_3)+b_{\perp\perp}\cdot\sqrt{(\sigma_2-\sigma_3)^2}}{\bar{R}^c_{\perp}}]^{m-1}$$

and finally via $C = \cos(2\cdot\Theta_{fp}) \rightarrow \Theta_{fp} = 0.5\cdot\mathrm{arcos}\,C$, $\Theta_{fp}{}^{\circ} = \Theta_{fp}\cdot 180^{\circ}/\pi$.

By insertion of any stress state the associated 'running' C can be computed.

Cohesion strength $\bar{R}^{\tau}_{23}$ is determinable for $\tau_{nt}^{fail}(\sigma_n) = 0$

Therewith, after effortful MathCad programming and implicit numerical computations the desired accurate bi-axial fracture stress M-C-curve τ_{nt} (σ_n) could be derived by the refined IFF2 model and also the results formulated in ply stresses. The fracture angle becomes now the realistic 90° instead 71°.

$$\frac{C}{\sqrt{1-C^2}} = -m \cdot \left[\frac{A}{\bar{R}_\perp^{\,t}} + \frac{2 \cdot a_{\perp\perp} \cdot f_{\mathrm{corr}} \cdot B}{\bar{R}_\perp^{\,c}}\right] / \left[\frac{2 \cdot A}{\bar{R}_\perp^{\,t}\sqrt{(\sigma_2-\sigma_3)^2}} + \frac{4 \cdot b_{\perp\perp} \cdot f_{\mathrm{corr}} \cdot B \cdot \tau_{nt}}{\bar{R}_\perp^{\,c}\sqrt{(\sigma_2-\sigma_3)^2}}\right],$$

$$B_{\mathrm{corr}} = \left[\frac{a_{\perp\perp} \cdot (\sigma_2+\sigma_3) + b_{\perp\perp} \cdot \sqrt{(\sigma_2-\sigma_3)^2}}{\bar{R}_\perp^{c}} \cdot f_{\mathrm{corr}}\right]^{m-1} \quad \text{with} \quad f_{\mathrm{corr}} = 1 + c_0 \cdot (\bar{R}_\perp^{c} + \sigma_2)^2 .$$

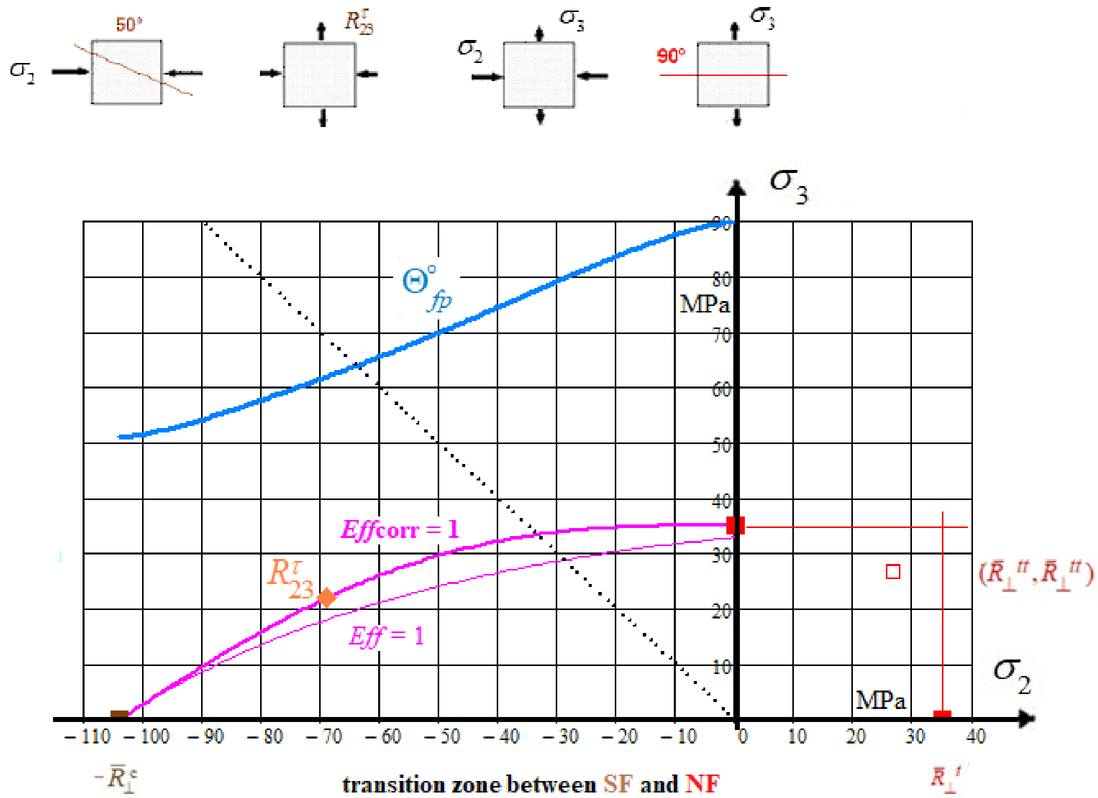

Fig. 22-4: Interaction curve $\sigma_3^{\mathrm{fracture}}(\sigma_2)$ with Eff = 1Failure stress curve $\sigma_2(\sigma_3)$ with alteration of fracture angle Θ_{fp}° in the transition zone. (Numerical example stems from a measurement of the fracture plane angle Θ_{fp}° in [VDI97, bi-axial failure stress $\bar{R}_\perp^{tt}$). Marking of R_{23}^{τ}.

- ▶ IFF2-IFF1- interacted fracture curve (*thin, original IFF2. With this 'simple' approach, the curve cannot run through* $\bar{R}_\perp^{t}$ = 35 MPa)
- ▶ IFF2-IFF1- interacted fracture curve *(bold, IFF2 decay function corrected, which better maps the course of measured fracture stress data)* and
- ▶ Course of the fracture plane angle Θ_{fp}° (*bold, corrected*)

22.4: Determination of Cohesive shear *Strength* R_{23}^{τ}

The interaction curve can be dedicated to the basic Mohr-Coulomb curve which runs from the compression strength point till the tensile strength point $\sigma_3 = \bar{R}_\perp^{t}$. In order to find all relationships in one diagram the Mohr stresses are also inserted as functions of the lamina stresses σ_2 (σ_3) and not of σ_n alone, which is the usual diagram form. *Fig.22-4* includes the development of the fracture plane angle as function of the lamina stress σ_2 . *Fig.22-1* still presented all MathCad-computed Mohr entities providing:

* Extrapolation from compressive strength point (IFF2-determined Mohr-Coulomb fracture curve)
  - A straight Linear Mohr-Coulomb curve, considering σ_2 (*linear Mohr*), *Cohesive Strength*
  - A straight Linear Mohr-Coulomb curve, considering σ_2 and σ_3 ; *Cohesive Strength* $\bar{R}_{23}^{\tau}$
* Full IFF2-IFF1-interacted Mohr-Coulomb fracture curve *(bold, decay function- corrected)*
* Course of the fracture plane angle Θfp°/2 (thin, not decay function corrected) and (bold).

The definition of the cohesive (shear) strength is $(\tau_{nt}^{fail} = \bar{R}_{23}^{\tau},\ \sigma_n = 0)$. Searching $\bar{R}_{23}^{\tau}$ (C), the derived formulation permits to continuously MathCad-compute the alternating fracture plane measure C with the associate fracture angle $\Theta_{fp}{}^\circ$. The interpretation of the figures leads to the following conclusions:

- The general macro-mechanical IFF2 approach cannot offer a full accuracy of the realistically predicted Mohr-Coulomb curve. Just the *physically-based* decay function correction delivers the desired fidelity
- A SFC in lamina stresses can be transferred into a Mohr-Coulomb version
- The course of the fracture plane angle $\Theta_{fp}{}^\circ$ can be determined, too
- The idea of the FMC that IFF1 and IFF2 commonly add its *Eff* portions, which leads to the result that $\Theta_{fp}{}^\circ$ is in the sixty degrees ° at the cohesive strength point $\bar{R}_{23}^{\tau}$, with a degree value being the higher the higher the strength ratio $\bar{R}_{\perp}^{c} / \bar{R}_{\perp}^{t}$ is.

LL:

- ➢ *Failure stress under pure shear* $\tau_{23}^{\text{fracture}} = max\,\tau_{23} \leq R_{\perp}^{t}$ *, an approach-formalistic introduced quantity*
- ➢ *Mohr-based approach linked so-called cohesive strength* $R_{23}^{\tau} = \tau_{nt}(\sigma_n = 0)$
- ➢ *Puck's Action plane shear resistance* R_{23}^{A} *: Puck formulated a full IFF-SFC and could model-associated dedicate his action plane resistance a relation with the inclination model parameters p and the other strengths reading* $\bar{R}_{23}^{A} = \left[\bar{R}_{\perp||} \cdot \sqrt{1 + 2 \cdot p_{\perp||}^{c} \cdot \bar{R}_{\perp}^{c} / \bar{R}_{\perp||}} - 1\right] / 2 \cdot p_{\perp||}^{c}$.

  Above quantities are not measurable ones
- ➢ *Generally, assuming a transverse shear failure stress , which would be a sixth strength, will contradict material symmetry demands, which seem to require for UD materials a 'generic' number of 5, meaning 5 measurable strengths and 5 elasticity properties*
- ➢ *The ability for mobilizing friction processes depends on active compression stresses that cause via the friction value μ the necessary shear stress.*

Analogous to the saying " *If something becomes a fact it is no science anymore*".
Here transferred: ***The three shear strength quantities should be no mystery anymore*".**

On the history of the Mohr-Coulomb (M-C) curve = Mohr Envelope: Otto Mohr did not commit himself to the intersection of the envelope with the σ_n-axis. A. Leon was probably the first to use an envelope, taking a parabolic one.

23 Replacing fictitious UD Model Parameters $a_{\perp\perp}, a_{\perp||}$ by measurable Friction Values μ

Aim: *Engineers prefer measurable friction values instead of fictitious friction parameters.*

23.1: Relation of Friction parameter $a_{\perp\perp}$ to Fracture angle $\Theta_{fp}{}^c$ and Friction value $\mu_{\perp\perp}$

The measurement of a realistic fracture angle is practically not possible, just the determination of the friction curve parameter $a_{\perp\perp}(\mu_{\perp\perp})$ by mapping the course of test data points is a practical approach. Then, from the mapped test curve the relation of the curve parameter $a_{\perp\perp}$ to the friction value $\mu_{\perp\perp}$ and to the fracture angle $\Theta_{fp}{}^\circ$ can be derived according to the formulas in *Table 23-1*. This is to perform in the compressive strength point $\bar{R}_\perp^c$, see also the chapter before.

Basic assumption is the *brittle-fracture hypothesis* which goes back to O. Mohr's "*The strength of a material is determined by the Mohr stresses on the fracture plane"*. This means for the Linear Mohr-Coulomb (M-C) formulation $\tau_{nt} = \bar{R}_{23}^\tau - \mu_{\perp\perp} \cdot \sigma_n$ including the friction value $\mu_{\perp\perp}$ being an intrinsic property of the UD material.

Table 23-1: Determination of the friction curve parameter $a_{\perp\perp}(\mu_{\perp\perp})$

IFF2: $F_\perp^\tau = [a_{\perp\perp} \cdot (\sigma_2 + \sigma_3) \; + \; b_{\perp\perp} \cdot \sqrt{(\sigma_2 - \sigma_3)^2 + 4\tau_{23}{}^2}\,] \;/\; \bar{R}_\perp^c = 1$, in Mohr stresses, after inserting $\bar{R}_\perp^c$

$= [a_{\perp\perp} \cdot (\sigma_n + \sigma_t) \; + \; b_{\perp\perp} \cdot \sqrt{(\sigma_n - \sigma_t)^2 + 4\tau_{nt}{}^2}\,] \;/\; \bar{R}_\perp^c = 1$ and $a_{\perp\perp} = b_{\perp\perp} - 1$ is friction parameter

$$\frac{dF}{d\sigma_n} \cdot \bar{R}_\perp^c = a_{\perp\perp} \; + \; b_{\perp\perp} \cdot (\sigma_n - \sigma_t) / \sqrt{(\sigma_n - \sigma_t)^2 + 4\tau_{nt}{}^2}, \quad \frac{dF}{d\tau_{nt}} \cdot \bar{R}_\perp^c = 4 \cdot b_{\perp\perp} \cdot \tau_{nt} / \sqrt{(\sigma_n - \sigma_t)^2 + 4\tau_{nt}{}^2}$$

$$\frac{d\tau_{nt}}{d\sigma_n} = -\frac{dF}{d\sigma_n} / \frac{dF}{d\tau_{nt}} = -[\frac{b_{\perp\perp} \cdot (\sigma_n - \sigma_t) \; + \; (b_{\perp\perp} - 1) \cdot \sqrt{(\sigma_n - \sigma_t)^2 + 4\tau_{nt}{}^2}}{4 \cdot b_{\perp\perp} \cdot \tau_{nt}}],$$ minus due to implicit derivation

Use of addition theorems ($\sigma_\lambda = 0$), gives the relationships $c = \cos(\Theta_{fp}{}^\circ \cdot \pi / 180°)$

$$\sigma_n - \sigma_t = c^2 \cdot (\sigma_2 - \sigma_3) - s^2 \cdot (\sigma_2 - \sigma_3) = C \cdot (\sigma_2 - \sigma_3), \quad S = \sqrt{1 - C^2}, \; C = \cos(2 \cdot \Theta_{fp}{}^\circ \cdot \pi / 180°)$$

$$\sigma_t = \sigma_n - C \cdot (\sigma_2 - \sigma_3), \; C = c^2 - s^2 = 2c^2 - 1 = 1 - 2s^2, \quad \sigma_n + \sigma_t = \sigma_2 + \sigma_3 \quad \text{and}$$

$$\tau_{nt} = -0.5 \cdot S \cdot (\sigma_2 - \sigma_3) = -0.5 \cdot \sqrt{1 - C^2} \cdot (\sigma_2 - \sigma_3), \; \sigma_n = (C+1) \cdot 0.5 \cdot \sigma_2 + (1 - C) \cdot 0.5 \cdot \sigma_3.$$

Stress σ_t has no influence, as Mohr assumed! Failure responsible due to Mohr are just τ_{nt} with σ_n !

$$\frac{d\tau_{nt}}{d\sigma_n} = -\,\mu_{\perp\perp} = \frac{C}{S} = -[\frac{b_{\perp\perp} \cdot (\sigma_n - \sigma_t) \; + \; (b_{\perp\perp} - 1) \cdot \sqrt{(\sigma_n - \sigma_t)^2 + 4\tau_{nt}{}^2}}{4 \cdot b_{\perp\perp} \cdot \tau_{nt}}] =$$

$$= -[\frac{b_{\perp\perp} \cdot (C \cdot \sigma_2) \; + \; (b_{\perp\perp} - 1) \cdot \sqrt{(C \cdot \sigma_2)^2 + 4 \cdot (-0.5 \cdot S \cdot \sigma_2)^2}}{4 \cdot b_{\perp\perp} \cdot (-0.5 \cdot S \cdot \sigma_2)}]$$

$$C = -[\frac{b_{\perp\perp} \cdot (C \cdot \sigma_2) \; + \; (b_{\perp\perp} - 1) \cdot \sqrt{(C \cdot \sigma_2)^2 + 4 \cdot (-0.5 \cdot \sigma_2)^2 \cdot (1 - C^2)}}{4 \cdot b_{\perp\perp} \cdot (-0.5 \cdot \sigma_2)}]$$; $C \to C_{fp}{}^c$ inserting strength $\bar{R}_\perp^c$

$$\to \; C_{fp}{}^c = \; -[\frac{b_{\perp\perp} \cdot C_{fp}{}^c \cdot (-\bar{R}_\perp^c) \; + \; (b_{\perp\perp} - 1) \cdot \sqrt{C_{fp}{}^{c2} \cdot (-\bar{R}_\perp^c)^2 + 4 \cdot (-0.5 \cdot (-\bar{R}_\perp^c))^2 \cdot (1 - C_{fp}{}^{c2})}}{4 \cdot b_{\perp\perp} \cdot (-0.5 \cdot (-\bar{R}_\perp^c))}]$$

Resolving : $b_{\perp\perp} = \dfrac{1}{C_{fp}{}^c + 1} \cong \dfrac{1}{1 - \mu_{\perp\perp}}$, $a_{\perp\perp} \cong \dfrac{\mu_{\perp\perp}}{1 - \mu_{\perp\perp}}$, $\mu_{\perp\perp} = -\dfrac{C}{S} = -\dfrac{C_{fp}{}^c}{S_{fp}{}^c} \cong -\,C_{fp}{}^c$ (being a small value).

Assuming $\Theta_{fp}^c{}^\circ = 51°$: Example $C_{fp}^c = \cos(\dfrac{2 \cdot \Theta_{fp}^c{}^\circ}{180°} \cdot \pi) = -0.21$, $\mu_{\perp\perp} = 0.21 \cong -C_{fp}^c$, $a_{\perp\perp} = 0.26$.

If IFF occurs in a parallel-to-fiber plane of the UD lamina, the components of the failure stress vector are the normal Mohr stress σ_n and the two Mohr shear stresses σ_{nt} and σ_{n1}. The shear stress σ_{tl} and the normal stress σ_t will have no influence and this was proven in the derivation. Further, the Mohr stress σ_{n1} belongs to IFF3 and is not of interest, here.

The transformation of the IFF2 SFC in lamina stresses into Mohr stresses-based formulation works via above addition theorems.

During this transformation procedure there are a lot of lessons to learn**:**

- *The Linear Mohr-Coulomb model can be employed to obtain a sufficiently good relationship for the determination of the friction value μ in the compressive strength point $\sigma_2 = -\bar{R}_{\perp}^{c}$.*
- *Establishing the relationship $a_{\perp\perp}(\mu_{\perp\perp})$ it is assumed that the tangent of the FMC-curve has the same value as that of the straight Linear Mohr envelope curve $\tau_{nt}(\sigma_n)$ in the touch point of Mohr's circle, see Fig.23-1*
- *σ_1 is not relevant. The shear stress τ_{23} can be assumed zero because it would anyway vanish after a principal stress transformation. No reduction of generality is caused*
- *The stress σ_t has no influence! It is not representative such as Mohr supposes. Failure responsible are τ_{nt} and σ_n, only. But mind in the differentiation process: the Mohr stress σ_t cannot be simply set zero at the beginning of the derivations, it must be considered due to its relation to σ_n,*
- *Above derivation demonstrates that, if really desired, the fracture plane angle Θ_{fp}^{c} of an UD-material could be also determined from an invariant-based SFC and not only from Mohr-based formulations*
- *Viewing Fig.23-1, it is obvious that the cohesive strength $\bar{R}_{23}^{\tau}$* (Civil engineers take the letter c) *belongs to the transition zone of the normal fracture mode domain IFF1 and therefore not alone to the shear fracture mode domain IFF2. Hence, one cannot simply extrapolate from the compressive strength point.*
-

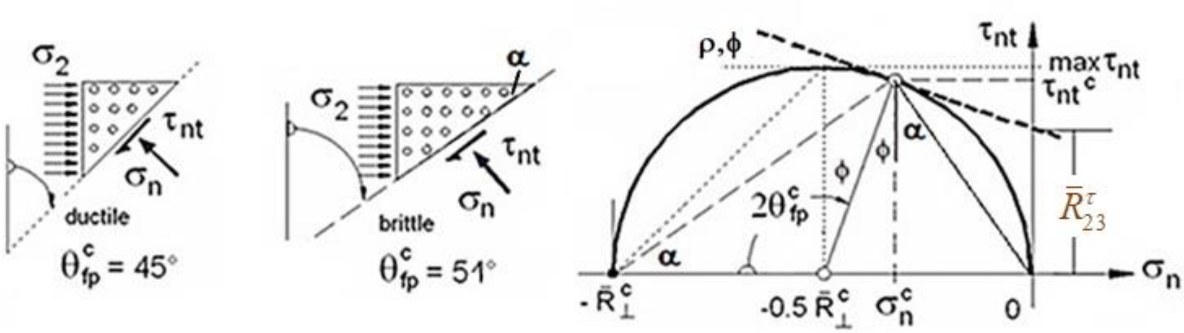

Fig.23-1, Shear stressing situation: Shear fracture plane angle in the touch point and 'linear' Mohr-Coulomb friction curve. The touch point is defined by $(\sigma_n^c, \tau_{nt}^c)$ and linked to $\bar{R}_{\perp}^{c}$

23.2: *Relation of Friction parameter* $a_{\perp\|}$ to *Friction value* $\mu_{\perp\|}$

The same procedure is analogously to perform for the mode IFF3, see Table 23-2.

Table 23-2: Relationships for the determination of friction curve parameter $a_{\perp||}(\mu_{\perp||})$

$$F_{\perp||} = \frac{I_3^2}{\bar{R}_{\perp||}^{\ 4}} + b_{\perp||} \cdot \frac{I_2 \cdot I_3 - I_5}{\bar{R}_{\perp||}^{\ 3}} = 1 \quad \text{with} \quad I_{23-5} = 2 \cdot \sigma_2 \cdot \tau_{21}^2 + 2 \cdot \sigma_3 \cdot \tau_{31}^2 + 4 \cdot \tau_{23}\tau_{31}\tau_{21} \ \text{ from}$$

$$I_2 = \sigma_2 + \sigma_3 \ , \ I_3 = \tau_{21}^2 + \tau_{31}^2 , \ I_5 = (\sigma_2 - \sigma_3) \cdot (\tau_{31}^2 - \tau_{21}^2) - 4 \cdot \tau_{23} \cdot \tau_{31} \cdot \tau_{21} .$$

The transfer to a Mohr-shaped SFC is directly possible, because the fracture plane is already known (parallel to the fibre direction), via $(\tau_{n1}, \ \sigma_n) \equiv (\tau_{21}, \ \sigma_2)$, $|\tau_{21}| = \bar{R}_{\perp||} - \mu_{\perp||} \cdot \sigma_2$

* FMC: $\frac{\tau_{21}^4}{\bar{R}_{\perp||}^{\ 4}} + a_{\perp||} \cdot \frac{2 \cdot \sigma_2 \cdot \tau_{21}^2}{\bar{R}_{\perp||}^{\ 3}} = \frac{\tau_{nt}^2}{\bar{R}_{\perp||}^{\ 4}} + a_{\perp||} \cdot \frac{2 \cdot \sigma_n \cdot \tau_{nt}^2}{\bar{R}_{\perp||}^{\ 3}} = 1 \ \rightarrow \sigma_n = \frac{\bar{R}_{\perp||}^{\ 3} \cdot (\tau_{21}^4 / \bar{R}_{\perp||}^{\ 4} - 1)}{2 \cdot \tau_{nt}^2 \cdot a_{\perp||}}$

$\frac{d\tau_{n1}}{d\sigma_n} \rightarrow$ simpler to perform is $\frac{d\sigma_n}{d\tau_{n1}} = \frac{2 \cdot \tau_{21}}{\bar{R}_{\perp||} \cdot a_{\perp||}} - \frac{\bar{R}_{\perp||}^{\ 3} \cdot (\tau_{21}^4 / \bar{R}_{\perp||}^{\ 4} - 1)}{\tau_{21}^3 \cdot a_{\perp||}}$

* Simple linear Mohr: $\tau_{n1} = \bar{R}_{\perp||} - \mu_{\perp||} \cdot \sigma_n \ \rightarrow \ \sigma_n = \frac{\bar{R}_{\perp||} - \tau_{21}}{\mu_{\perp||}}$ and $\frac{d\sigma_n}{d\tau_{nt}} = \frac{-1}{\mu_{\perp||}}$.

In the strength point $\tau_{n1} = \bar{R}_{\perp||}$ an equal slope exists, then equating delivers

$$\frac{2 \cdot \tau_{21}}{\bar{R}_{\perp||} \cdot b_{\perp||}} - \frac{\bar{R}_{\perp||}^{\ 3} \cdot (\tau_{21}^4 / \bar{R}_{\perp||}^{\ 4} - 1)}{\tau_{21}^3 \cdot a_{\perp||}} = \frac{-1}{\mu_{\perp||}} \ \rightarrow \ a_{\perp||} = \frac{\mu_{\perp||} \cdot (\bar{R}_{\perp||}^{\ 4} + \tau_{21}^4)}{\tau_{21}^3 \cdot a_{\perp||}} \ \Rightarrow a_{\perp||} = 2 \cdot \mu_{\perp||} .$$

A good guess for $\mu_{\perp||}$ and sufficient for application.

23.3: Evaluation of friction values $\mu_{\perp\perp}$, $\mu_{\perp||}$ from test results

The determination of curve parameters *a(μ)* and thereby also of *μ* can be performed differently:

1. One strength value with one multi-axial failure stress point on the respective pure mode curves, usually applying a linear Mohr friction envelope (*sufficient*, *see Figs. 23-2 and -3 below, it requires some fitting to optimally map the course*)
2. A more sophisticated fitting optimization process of the test data course in the respective pure domain (*min error square*) in 'pure' failure mode domains
3. The so-called Tension/Compression-Torsion test machine delivered the test points in *Fig.23-2 left*. If such a test rig is not available, then, one point on the pure mode Iff2-curve plus one in the transition zone IFF2-IFF1, see Fig.23-3, become an approximation basis, see *Fig. 23-3 right*
4. For $\mu_{\perp\perp}$, in addition: Derivation from fracture angle measurements Θ_{fp}^{c} °, see experience in the associate figure in [*VDI 97, p. 138*], facing a pretty high scatter.

The formulas for the friction values read:

- Linear Mohr envelope: $\mu_{\perp||} \cong (\tau_{21}^{\ fr} - \bar{R}_{\perp||}) / \sigma_2^{\ fr}$ from tension-compression/torsion test machine with tube test specimens, evaluating at least two curve points or if sufficient tests from curve fitting .
- From bi-axial compression test in order to compute the friction value from evaluating $\mu_{\perp\perp} = (\bar{R}_{\perp}^{c} + \sigma_3^{fr}) / \sigma_2^{fr}$. However, the danger to buckle is to face

- If the test machine only allows a $\mu_{\perp\perp}$-test in the transition zone of the modes, *Fig.23-3*, then, the estimation from strength point $(\sigma_3^{c\,fr}, \sigma_2^{t\,fr})$ demands for a qualified stress interaction-mapping SFC. For the evaluation the interaction equation has to be employed, shown by the following MathCad procedure below:

Mathcad implicite calculation: *Vorgabe* $\mu_{\perp\perp} := 0.1$ (estimation)

$$([(\sigma_2+\sigma_3) + \sqrt{(\sigma_2-\sigma_3)^2+0}\,]/2\bar{R}_\perp^t\ )^m + ([(\frac{\mu_{\perp\perp}}{1-\mu_{\perp\perp}})\cdot(\sigma_2+\sigma_3) + \frac{1}{1-\mu_{\perp\perp}}\sqrt{(\sigma_2-\sigma_3)^2+4\tau_{23}^2}\,]\ /\ \bar{R}_\perp^c\ )^m = 1 = Eff = 100\%\ .$$

Search *Suchen* $(\mu_{\perp\perp})$.

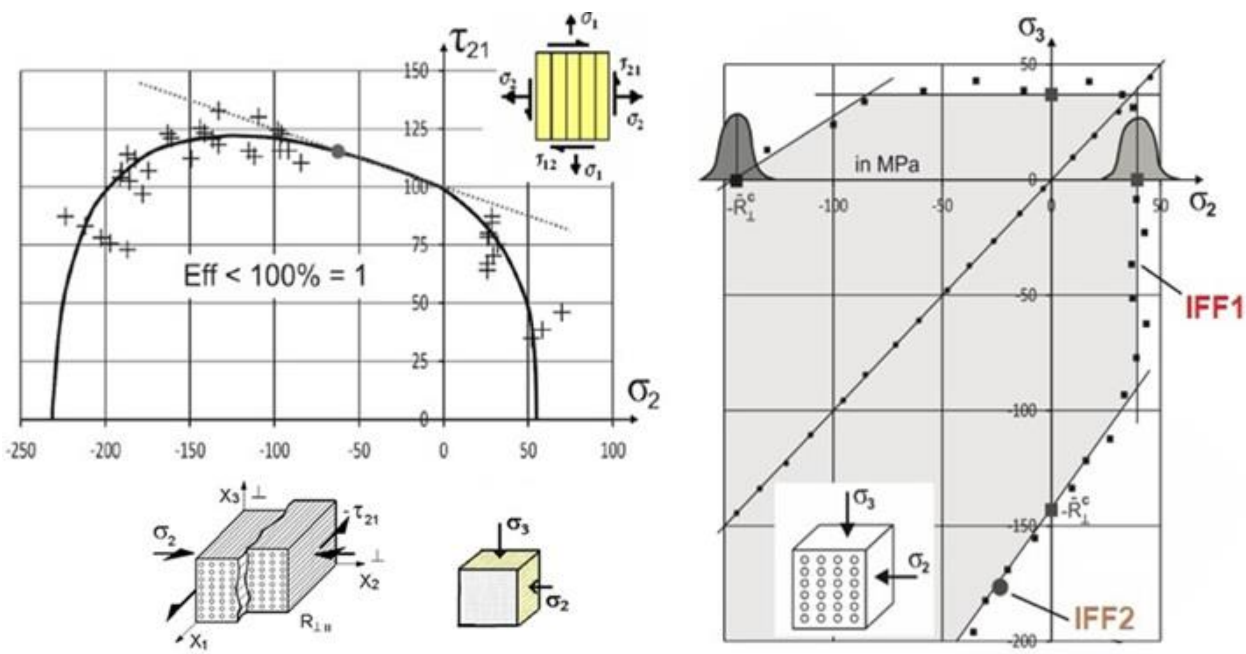

Fig.23-2: Determination of the friction values $\mu_{\perp\perp}$, $\mu_{\perp||}$ (own results)

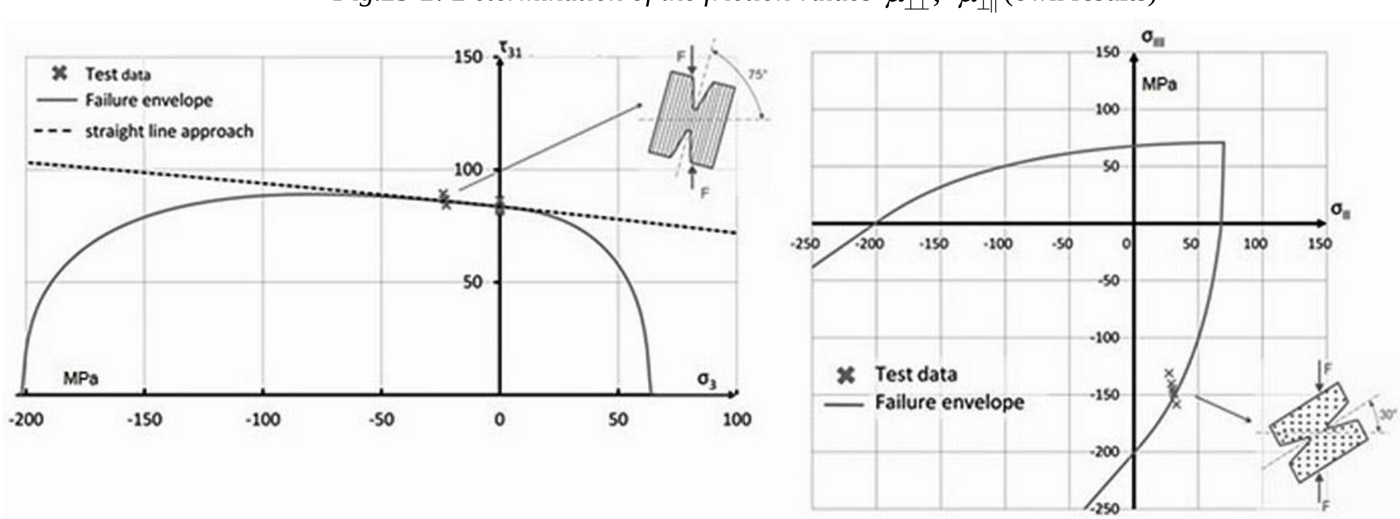

Fig.23-3: ARCAN tests performed on distinct stress paths. UD prepreg [Pet15]

LL:

- *A relationship of the measurable friction value and the fictitious friction parameter could be derived*
- *The application of the tension-compression-torsion test machine is recommended.*

24 Fracture Bodies of Normal Concrete, UHPC and Foam

Aim: *Optical clarification of the multiaxial fracture stresses.*

24.1 Isotropic Fracture Body

Used Stresses and Invariants

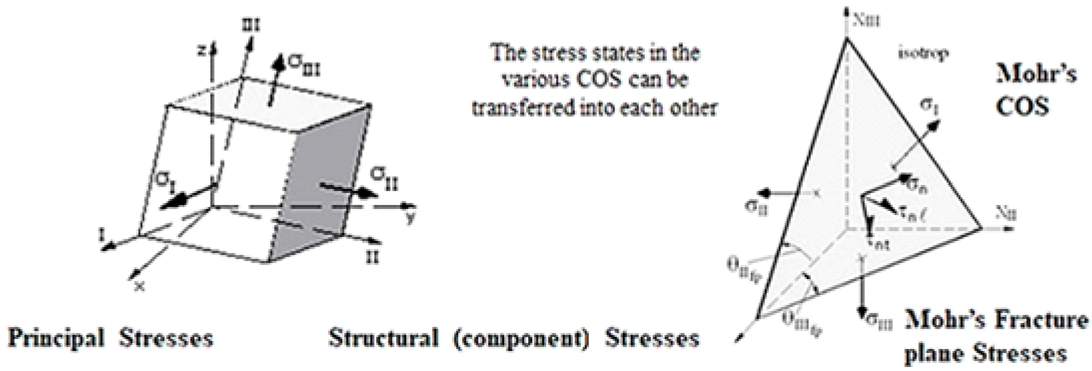

$$\{\sigma_{\text{principal}}\} = (\sigma_I, \sigma_{II}, \sigma_{III})^T, \quad \{\sigma_{\text{struct}}\} = (\sigma_x, \sigma_y, \sigma_z, \tau_{yz}, \tau_{xz}, \tau_{xy})^T, \quad \{\sigma_{\text{Mohr}}\} = (\sigma_\lambda, \sigma_n, \sigma_t, \tau_{nt}, \tau_{\lambda t}, \tau_{n\lambda})^T$$

In the transformation of structural stresses into Mohr stresses the advantage of invariants fully comes out: *They do not depend on the coordinate system, one can simply switch between the systems.*

Structural Stresses and Invariants, 3D and 2D:

$$I_1 = (\sigma_I + \sigma_{II} + \sigma_{III}) = f(\sigma), \quad 6J_2 = (\sigma_I - \sigma_{II})^2 + (\sigma_{II} - \sigma_{III})^2 + (\sigma_{III} - \sigma_I)^2 = f(\tau) \text{ 'Mises invariant'}$$

$$27J_3 = (2\sigma_I - \sigma_{II} - \sigma_{III}) \cdot (2\sigma_{II} - \sigma_I - \sigma_{III}) \cdot (2\sigma_{III} - \sigma_I - \sigma_{II}),$$

$$3 \cdot \sigma_{oct} = \sigma_I + \sigma_{II} + \sigma_{III} = \sigma_\ell + \sigma_n + \sigma_t \;; \quad 9 \cdot \tau_{oct}^2 = 6J_2 = 4 \cdot (\tau_{III}^2 + \tau_I^2 + \tau_{II}^2), \quad \tau_{II} = \max \tau (mathem.)$$

$\sigma_I, \sigma_{II}, \sigma_{III}$ are principal stresses, $\sigma_I > \sigma_{II} > \sigma_{III}$ are mathematical stresses (> *means more positive*)

Mohr Stresses and Invariants, 3D and 2D

$$I_1 = (\sigma_n + \sigma_t + \sigma_\lambda), \quad 6J_2 = (\sigma_n - \sigma_t)^2 + (\sigma_t - \sigma_\lambda)^2 + (\sigma_\lambda - \sigma_n)^2 + 6 \cdot \left(\tau_{nt}^2 + \tau_{n\lambda}^2 + \tau_{t\lambda}^2\right), \text{isotropic}\, \tau_{nt} \to \tau_n$$

Strength Failure Criteria (SFC), *Eff*-linked

At first the 'basic' formulations are displayed. Then, according to the 'proportional (stressing) concept' the relationships *Eff* (*F*) are performed. And finally, how the two shear mode parameters depend on another after having inserted R^c into F^τ .
If mode-interaction occurs the SFC *F* is to be replaced by the associated *Eff* in order to enable the interaction of modes in the mode transition zone. Mind: The cohesive strength is located in the transition zone between the two modes.

Table 24-1 summarizes the Eff^{mode} formulations for the usually as rotationally-symmetric *assumed* fracture failure body, and further the realistic isotropic 120°-rotational symmetry relations.

$$FNF = F\sigma = \frac{\sqrt{4 \cdot J2 - \frac{I1^2}{3}} + I1}{2 \cdot Rt} = Eff\sigma = 1 \qquad FSF = F\tau = c2 \cdot \frac{I1}{Rc} + \frac{c1 \cdot 6J2}{2 \cdot Rc^2} = 1$$

$$Eff\sigma = \frac{\sqrt{4 \cdot J2 - \frac{I1^2}{3}} + I1}{2 \cdot Rt} \qquad c2 \cdot \frac{I1}{Rc \cdot Eff\tau} + \frac{c1 \cdot 6J2}{2 \cdot Rc^2 \cdot Eff\tau^2} = 1 \qquad Eff\tau = \frac{\sqrt{I1^2 \cdot c2^2 + 12 \cdot J2 \cdot c1} + I1 \cdot c2}{2 \cdot Rc}$$

due to homogeneous F

Insertion of the compressive strength delivers delivers a parameter -relation : $c2 \cdot \frac{-Rc}{Rc} + \frac{c1 \cdot 2 \cdot Rc^2}{2 \cdot Rc^2} = 1$ $\quad \boxed{c1 = c2 + 1}$

Monotonic stressing of all stresses

Interaction requires to go from F to Eff, linked due to the 'proportional stressing concept'

for instance $\quad c_2^{SF} \cdot \frac{I_1 / Eff}{\bar{R}^c} + c_1^{SF} \cdot \frac{6 \cdot J_2 / Eff^2}{2 \cdot \bar{R}^{c2}} = 1.$

Fig.24-0: Some basic relationships

Procedure how to determine the Fracture Body

(1) Fracture failure body is rotationally symmetric (like the Mises yield body)

* Normal Fracture NF, $I_1 > 0$ $\quad \leftrightarrow \quad$ * Shear Fracture SF, $I_1 < 0$

$$F^{NF} = F^{\sigma} = \frac{\sqrt{4J_2 - I_1^2/3} + I_1}{2 \cdot \bar{R}^t} \qquad F^{SF} = F^{\tau} = c_2^{SF} \cdot \frac{I_1}{\bar{R}^c} + c_1^{SF} \cdot \frac{6 \cdot J_2}{2 \cdot \bar{R}^{c2}}$$

with σ and τ as failure driving stresses. Resistances $\bar{R}$ are average values (We model !).

Strength Failure Criterion (SFC), mode interaction exponent m, friction μ

$$Eff^{NF} = \frac{\sqrt{4J_2 - I_1^2/3} + I_1}{2 \cdot R^t} = \frac{\sigma_{eq}^{NF}}{\bar{R}^t} \leftrightarrow Eff^{SF} = \frac{c_2^{SF} \cdot I_1 + \sqrt{(c_2^{SF} \cdot I_1)^2 + 12 \cdot c_1^{SF} \cdot 3J_2}}{2 \cdot R^c} = \frac{\sigma_{eq}^{SF}}{\bar{R}^c}.$$

with $c_1^{SF} = 1 + c_2^{SF}$, $c_2^{SF} = (1 + 3 \cdot \mu)/(1 - 3 \cdot \mu)$ from $\mu = \cos\ (2 \cdot \theta_{fp}^{c}{}^{\circ} \cdot \pi / 180\ )$

or from fitting of the test data course.

(2) Fracture failure body is 120°-rotationally symmetric = Reality !

In a chapter before we had to learn: Each isotropic material is "120° – rot. symmetric",

which leads to the little more complicate *Effs* below

$$Eff_{\Theta}^{NF} = c^{NF} \cdot \frac{\sqrt{4J_2 \cdot \Theta^{NF} - I_1^2/3} + I_1}{2 \cdot R^t} \leftrightarrow Eff_{\Theta}^{SF} = \frac{c_2^{SF} \cdot I_1 + \sqrt{(c_2^{SF} \cdot I_1)^2 \cdot \Theta^{SF} + 12 \cdot c_1^{SF} \cdot 3J_2}}{2 \cdot R^c}$$

$c_{1\Theta}^{SF} \cdot \Theta^{SF} = 1 + c_2^{SF}$, and above friction parameter c_2^{SF}

Modelling of the cap is performed by the function $y_{cap} = \frac{I_1}{\sqrt{3} \cdot \bar{R}^t} = s^{cap} \cdot \left(\frac{\sqrt{2J_2 \cdot \Theta^{NF}}}{\bar{R}^t}\right)^2 + \frac{max\, I_1}{\sqrt{3} \cdot \bar{R}^t}.$

For $R^c >> R^t$ can be set : $\Theta^{NF} \rightarrow \Theta^{TM} = \sqrt[3]{1 + d^{NF} \cdot (+1)}$, $c^{NF} = \Theta^{NF} = 1.$

Θ as non-circularity function with d as non-circularity parameter , $(d^{SF} = d\tau)$

$\Theta^{SF} = \sqrt[3]{1 + d^{SF} \cdot \sin(3\vartheta)} = \sqrt[3]{1 + d^{SF} \cdot 1.5 \cdot \sqrt{3} \cdot J_3 \cdot J_2^{-1.5}}$, compr. angle -30° $\rightarrow \Theta^{SF} = \sqrt[3]{1 + d^{SF} \cdot (-1)}$.

The tests are performed by adding an axial load, generating a stress σ_{ax}, upon a hydrostatic loading p_{hyd} . The test data sets have been forwarded by Dr.-Ing. Silke Scheerer and Dr.-Ing. Kerstin Speck (*IfM, TU-Dresden, Prof. Dr. M. Curbach)*. From their provided raw data sets as sub-sets the meridian data sets, the constant Lode angles for the envisaged meridians had to be extracted by the author. The usual tests are run along the tensile meridian (TM) and the compressive meridian (CM). This situation causes to apply the realistic isotropic 120°-rotationally-symmetric model in order to account for the Lode angle ϑ.

Determination of the model parameters in the mode domain of F_τ : The measurement of Θ_{fp} – based on the usually small-scale test level - is practically not possible. The determination of the curve parameters c_i by mapping the course of test data points is the better and practical procedure. Then, the relationship of the curve parameter c_2 to the friction value μ and to the fracture angle Θ_{fp} can be derived. These relations are obtained in the *touch point,* pointed out in *Fig.22-1*.

I Visualization of 3D compression test data: Normal Concrete

In *Fig. 24-1, left*, the course of test data is mapped. As coordinates, the Lode-Haigh-Westergaard coordinates are used which equally count in all directions of the 3D stress space (*for understanding see Fig.14-9*). The tensile strength is used for normalization in the case of brittle materials.

The right part figure displays the fracture failure body, on which the 3 main meridians are depicted. For the tensile meridian a Lode angle ϑ = +30° is valid and for the compressive meridian ϑ = -30°. The shear meridian was chosen by the author as neutral meridian with the Lode angle ϑ = 0. For each mode, the SFC model parameters must be determined in each associated 'pure' failure mode domain. In this context physics of slightly porous isotropic materials is to remember: **bi-axial tension = weakest link failure behavior ($R^{tt}<R^t$, which partly seems to be not accepted in civil engineering) and * bi-axial compression = redundant (benign) failure behavior ($R^{cc}>R^c$).*

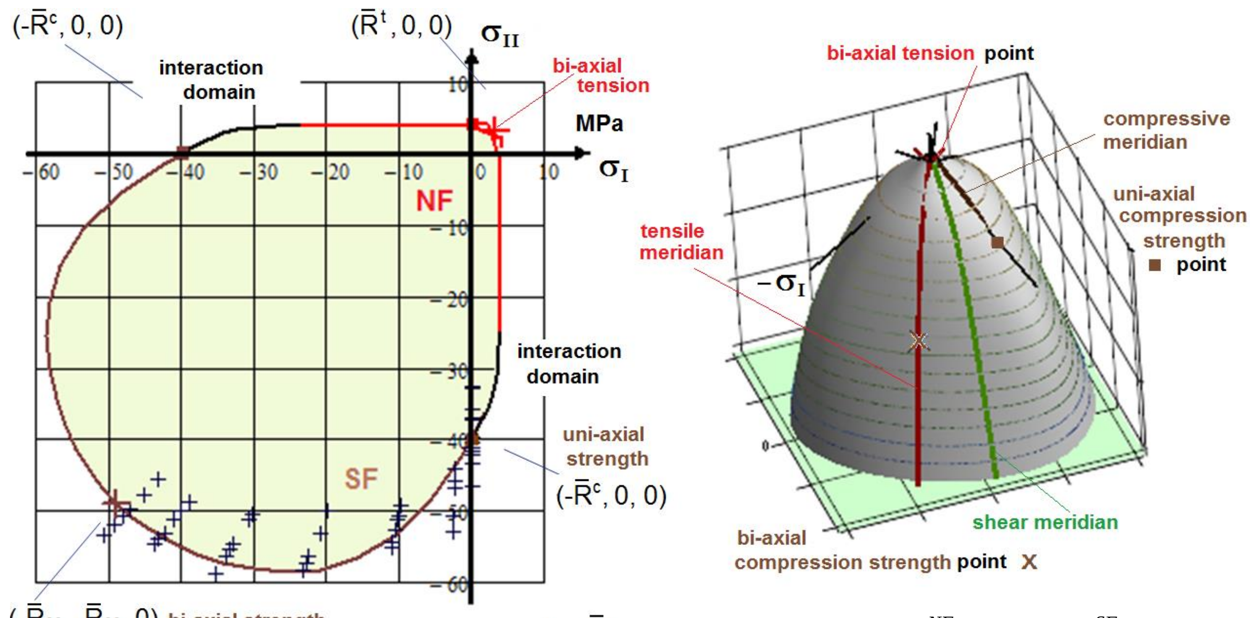

$$Eff = (Eff^{NF})^m + (Eff^{SF})^m = 1$$

Fig.24-1, Normal Concrete: mapping of 2D-test data in the Principal Stress Plane as the bias cross-section of the fracture body. R= strength, t=tensile, c=compressive; bar over means average (mean) value. μ = 0.2. (test data, courtesy: IfM Dresden,)R^{cc}

Table 24-2, Normal Concrete: Data set

$$F^{NF} = F^{\sigma} = c^{NF}\cdot\frac{\sqrt{4J_2 - I_1^{\,2}/3}+I_1}{2\cdot\bar{R}^t}\ ,\quad F^{SF} = F^{\tau} = c^{SF}_{1\Theta}\cdot\frac{6J_2\cdot\Theta^{SF}}{2\cdot\bar{R}^{c2}} + c_2(\mu)\cdot\frac{I_1}{\bar{R}^c} = 1$$

Normalizing here with $\bar{R}^t$ and $\bar{R}^c$. Dent too small to be practically of interest $\rightarrow c^{NF} = 1$.

3 remaining unknowns at least require 3 fix stress state failure points on the failure surface

$$\{\sigma_{fr}\} = (\ ,\ ,\ )^T : (-\bar{R}^c, 0, 0),\ (-\bar{R}^{cc}, -\bar{R}^{cc}\, 0, 0),\ (\sigma_I^{frict}, \sigma_I^{frict}, 0),\ m = 2.9,$$

with the values in MPa = N/mm^2: $\bar{R}^t = 4$, $\bar{R}^c = 44$, $\bar{R}^{cc} = 49$, $\sigma_I^{frict} = -20$, $\sigma_{II}^{frict} = -56$

$c^{SF}_{1\Theta}\cdot\Theta^{CM} = 1 + c_2$ with $c_2 = 1.07$ as friction parameter ($\Theta_{fp}^{\ c} = 51°$), $\vartheta = +-30°$

$c^{SF}_{1\Theta} = 2.45$, $d^{SF} = 0.39$, $\Theta^{SF} = \sqrt[3]{1 + d^{SF}\cdot\sin(3\vartheta)} \rightarrow \Theta^{TM} = 0.49$, $\Theta^{CM} = -0.49$.

For the determination of the closing cap and the open bottom:

$\bar{R}^{ttt} = 3.6 \rightarrow$ closing cap point $\max I_1 = 3\cdot\ \bar{R}^{tt}$, $\bar{R}^{ccc} = 1000$ MPa (set for computation).

With Awaji-Sato the non measurable $\bar{R}^{ttt}$ is estimated: $\bar{R}^{tt} = \bar{R}^t / 3^{1/M}$, $M = \ln(2)/\ln(\bar{R}^t / \bar{R}^{tt})$.

$\bar{R}^{tt} = 0.9\cdot\bar{R}^t$ (assumed) , $s^{cap} = -0.57$.

Fig.24-2 through *24-4* present a hoop cross–section (*octahedral stress plane or so-called π-plane*), two axial cross-sections, the meridians of the failure body, and two views of the failure body.

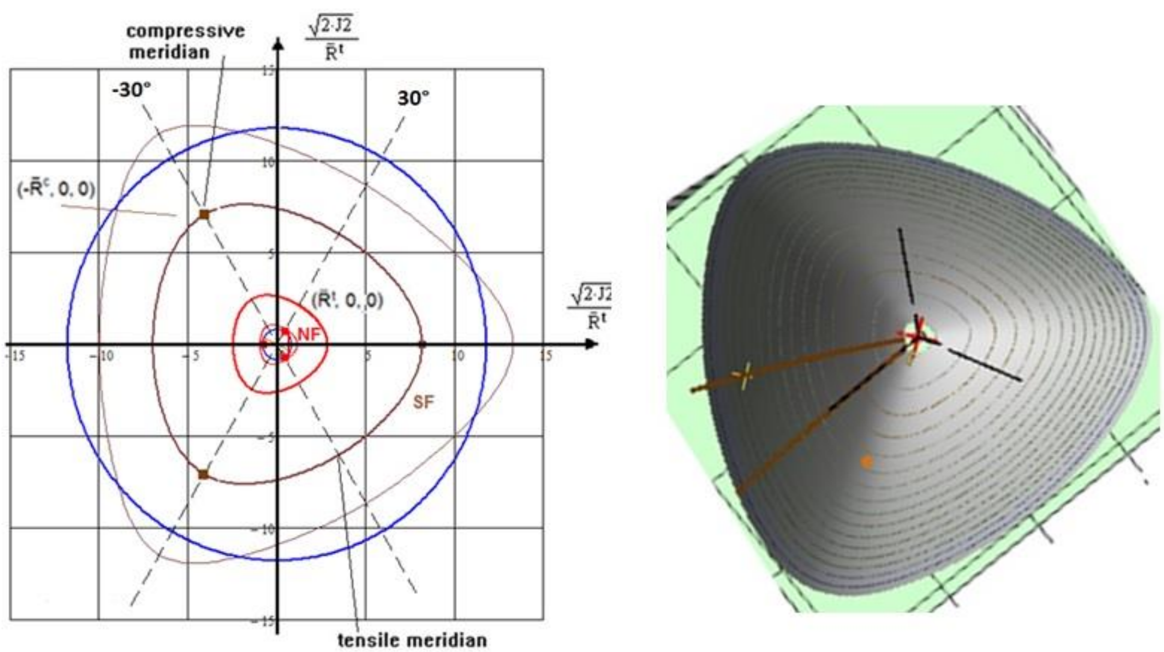

Fig.24-2, Normal Concrete: Top view: Octahedral stress plane (π-plane) exhibiting the constant Eff- lines on the body (the ***blue*** *line refers to $I_1 = 0$). Right:* X R^{cc}, ● R^c .

One recognizes that with increasing negative I_1 the hoop shape becomes more and more circular.
In *Fig.24-3* the modeling of cap, NF domain (marginal) and of the SF fracture domain is depicted.

Fig.24-4 shows the three basic meridians and two strength points, compressive strength (dot) and bi-axial compressive strength (cross).

Fig.24-5 informs about the test data scatter of the 3D fracture states experienced under hydrostatic pressure when running test on the tensile meridian and on the compressive meridian (-30°), selection of test data performed.
The Neutral Meridian is dashed.

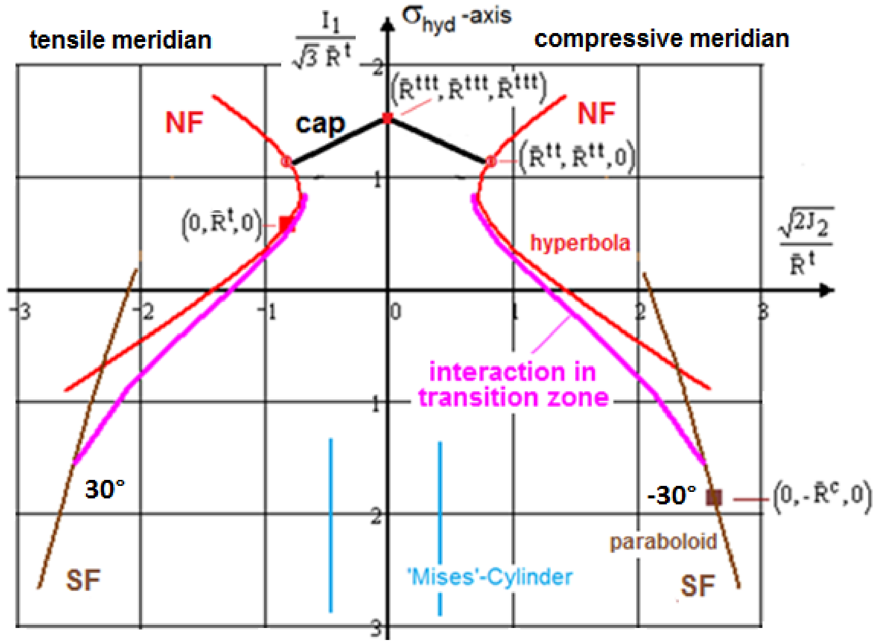

Fig. 24-3, axial cut: Visualization of the courses of the 2 mode mapping functions for NF and SF along the meridian cross sections of the fracture body (180° cut of the120°-body) and after ***interaction***

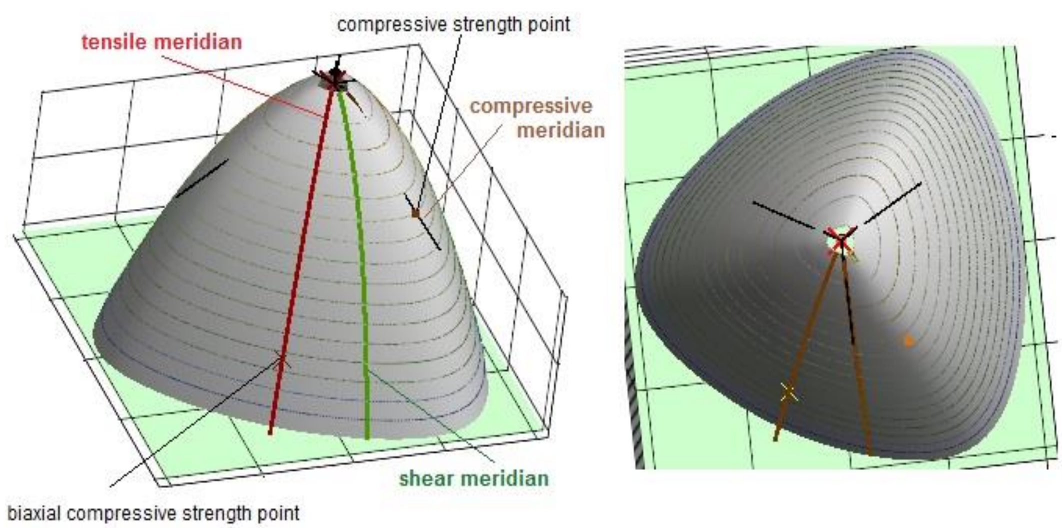

Fig.24-4: Two views of the 120°-rotationally-symmetric fracture body (hoop cross-section) of Normal Concrete with the basic three meridians and the strength points [Cun17]

In *Fig.24-6* the meridian failure curves are depicted and CM test points are inserted indicating where the determination of the Mohr quantities τ_n , σ_n , Θ_{fp} has been performed. As coordinates, the Haigh-Lode-Westergaard coordinates are used which equally count in all directions of the space.

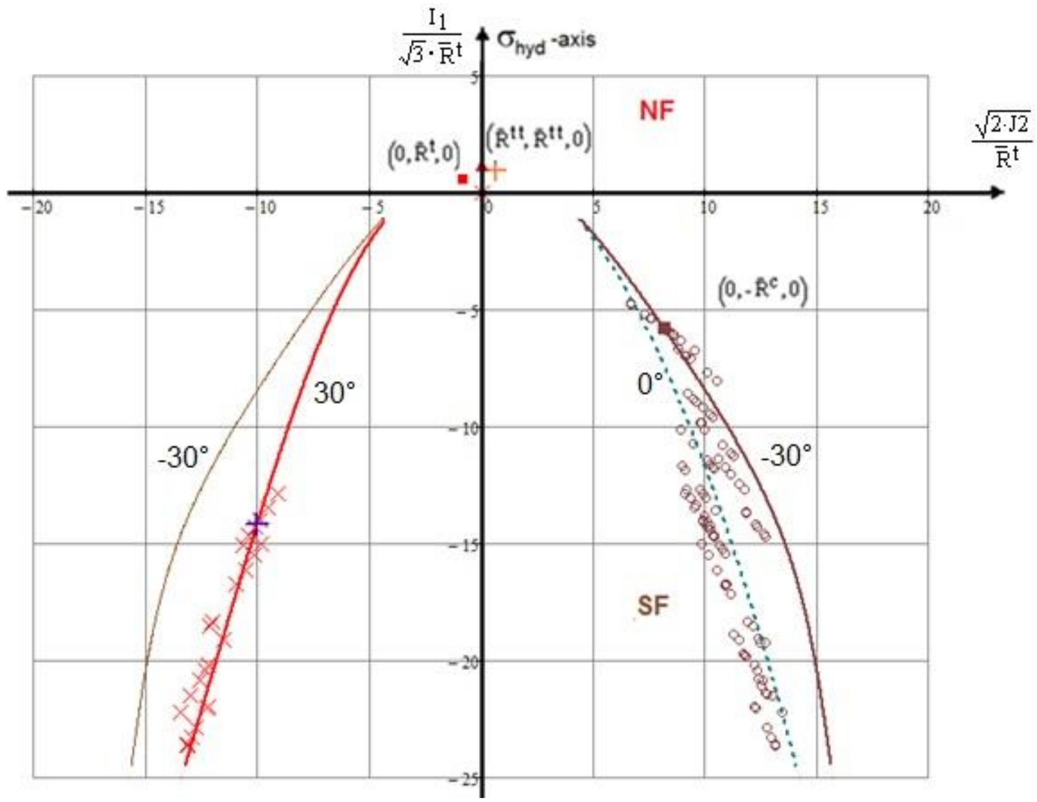

Fig.24-5: (left) Tensile meridian curve (TM) and associated test data (x, 30°), (right) compressive meridian (-30°) curve (CM) and test data on the respective hoop ring o (these circles o are located at different meridian angles ϑ), courtesy IfM Dresden. $\alpha_\tau =$, $\beta_\tau =$

Extrapolated guess of the CM-curve on basis of mapped TM test data and vice versa:

Just replace the Lode angle part for 30°, sin (3ϑ) = 1, by that for -30°, sin (3ϑ) = -1.

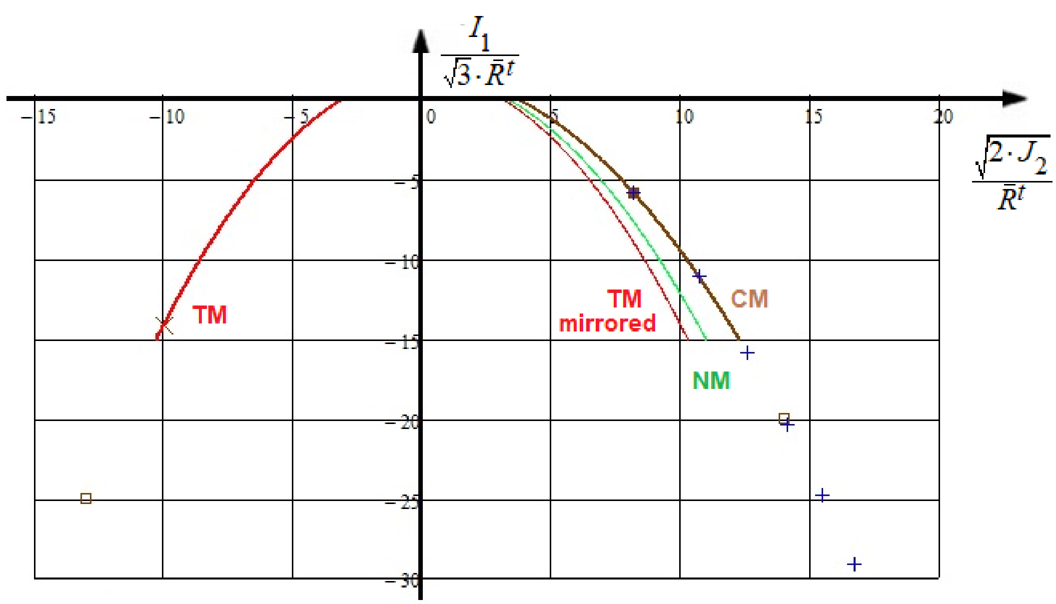

Fig.24-6: Display of all basic meridians of Normal Concrete. The + are the points where the evaluation of τ_{nt}, σ_n, Θ_{fp} was performed. p = p_{hyd}. TM Tensile Meridian, CM Compressive Meridian, NM Normal Meridian.
(Mathcad unfortunately did not draw below -15, an often faced Mathcad problem)

The above depicted basic three meridians are: Tensile Meridian TM (ϑ = +30°) inside, Neutral Meridian NM (0°) and Compressive Meridian CM (ϑ = -30°), outside. Test points lie on the respective meridian, determined by ϑ, which means on different distances from the axis for a specific $I_1 / \sqrt{3 \cdot \bar{R}^t}$. For Normal Concrete, *Fig.24-6* significantly supports the existence of the 120°-rotational symmetry of brittle (and ductile) isotropic materials.

III Visualization of 3D compression test data: UltraHighPerformanceConcrete (UHPC)

Fig.24-7, left depicts the separated and later intensively investigated TM and CM test data points.

Fig.24-7, right presents all 3D test points located at different Lode angles.

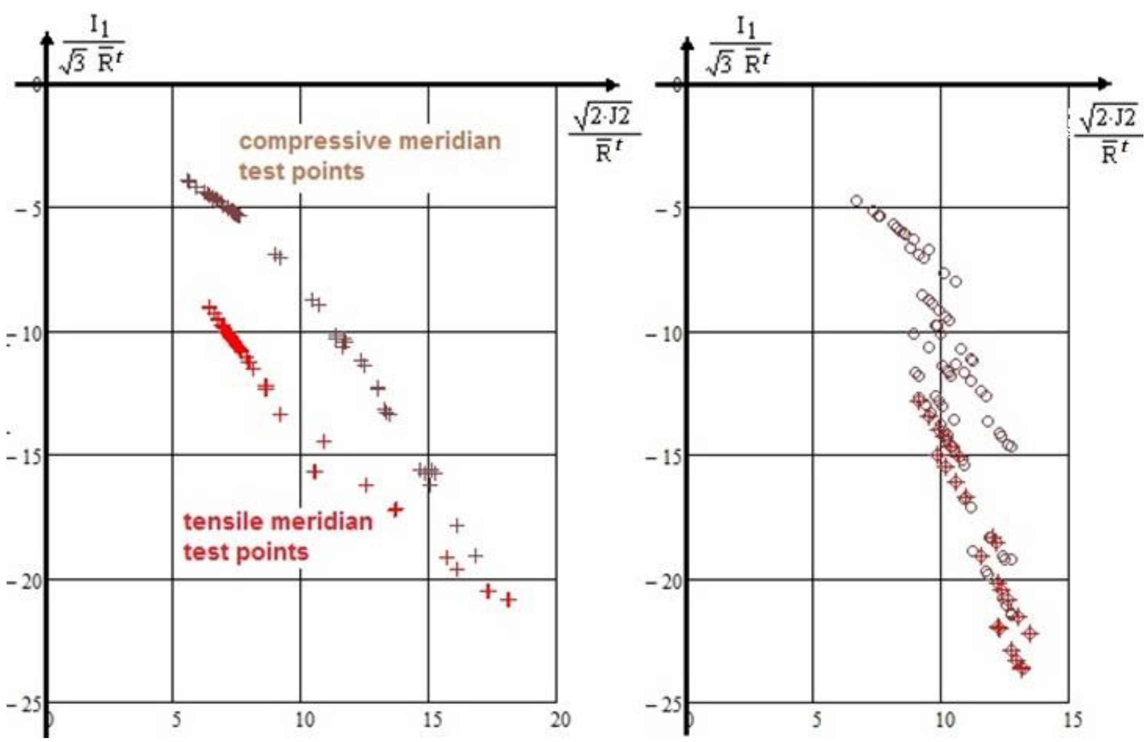

Fig.24-7 UHPC: Compressive and tensile meridian points
UHPC, separated test points: (left) tensile meridian + (ϑ = +30°) *and compressive meridian* + (ϑ = -30°) *;*
(right) all 3D test points are marked by **o** *(hoop ring,* ($\vartheta \neq$,+, - 30°)*), visualizing to be located at different meridians*

Fig.24-8 outlines modelling ideas for UHPC.

As could be still recognized for Normal Concrete, the failure body possesses inward dents for $I_1 > 0$ and outward dents for $I_1 < 0$ in contrast to porous concrete stone, where it is also inward, see *Fig.24-9.* These dents become smaller with increasing $|I_1|$.

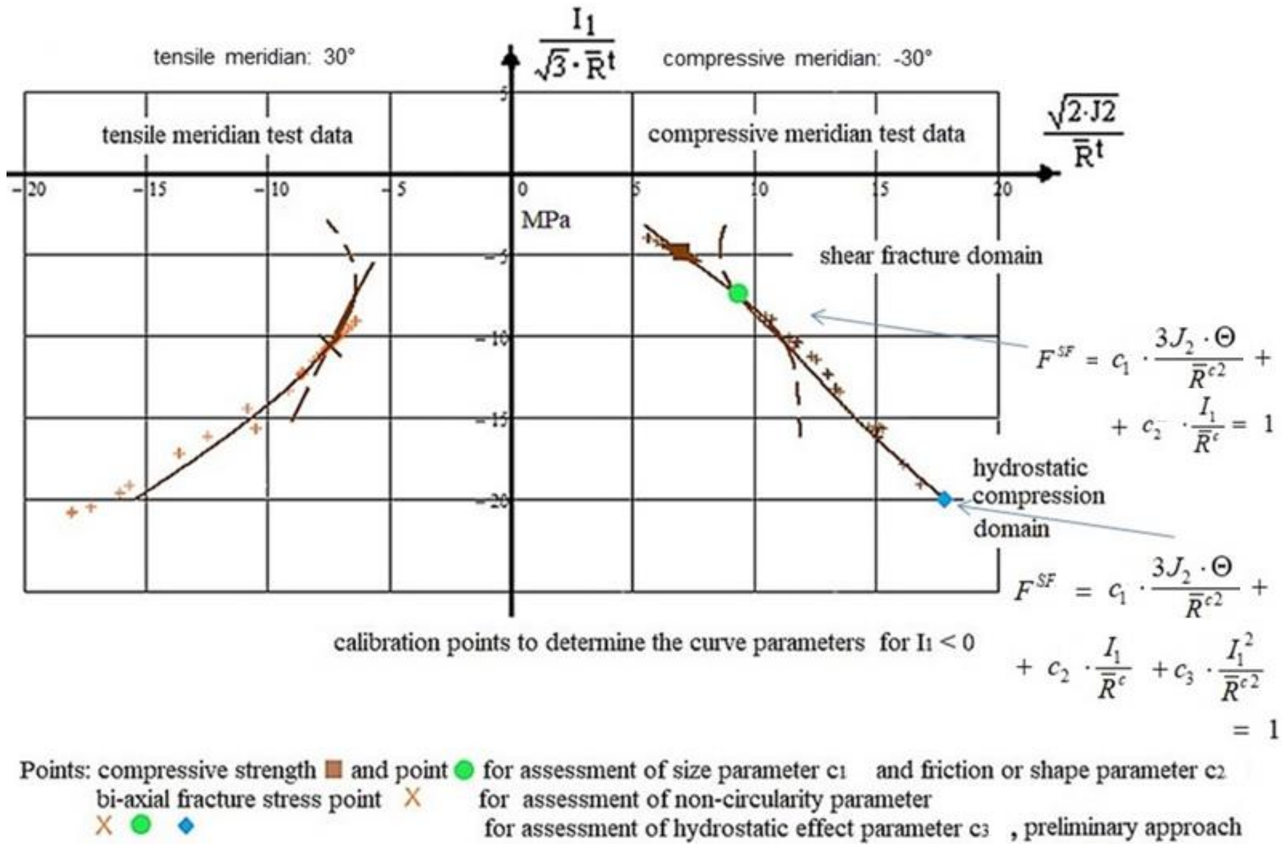

Fig.24-8 Ultra-High-Performance-Concrete (UHPC):
[Test data: Dr. Speck, IfM, TU-Dresden]. From this general data set as sub-sets the meridian data sets (constant Lode angles) have been extracted by the author

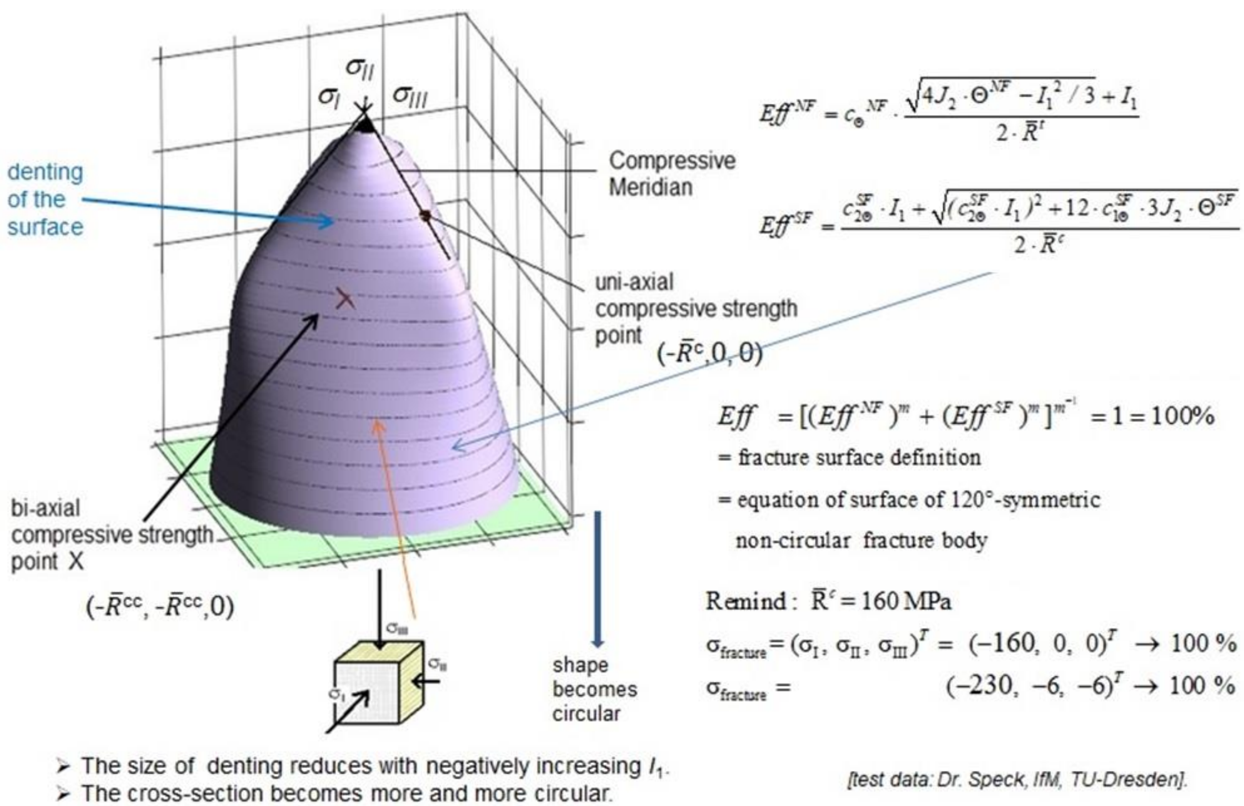

Fig.24-9, UHPC: Fracture body showing decay of denting with a negative I_1

Fig.24-10 shows a graph bi-axial compressive strength over uniaxial compressive strength. It turns out that with increasing uniaxial strength the bi-axial strength approximates the uniaxial strength.
The author tries to explain this: The effect of redundancy under hydrostatic loading can be interpreted as an out-smoothing of stress concentrations. In the case of Normal Concrete this effect becomes more chances according to being more roughly grained than UHPC. This explains why the bi-axial strength capacity increase of a roughly grained Normal Concrete is higher than for UHPC.

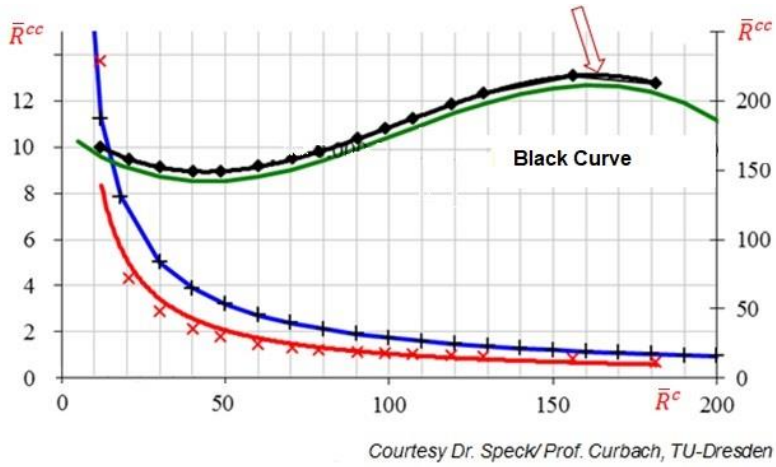

Fig.24-10: compressive strength capacity ratio of concrete $\bar{R}^{cc} / \bar{R}^{c}$ *(R = f),*

$\bar{R}^{cc} / \bar{R}^{c}$ (Normal Concrete) $>$ $\bar{R}^{cc} / \bar{R}^{c}$ (UHPC)

In *Fig.24-11* are depicted the 2 mode domains and its transition zone obtained with the interaction formula. This task concentrated about performing an interaction in the principal plane $I_1 > -2R^{cc}$.

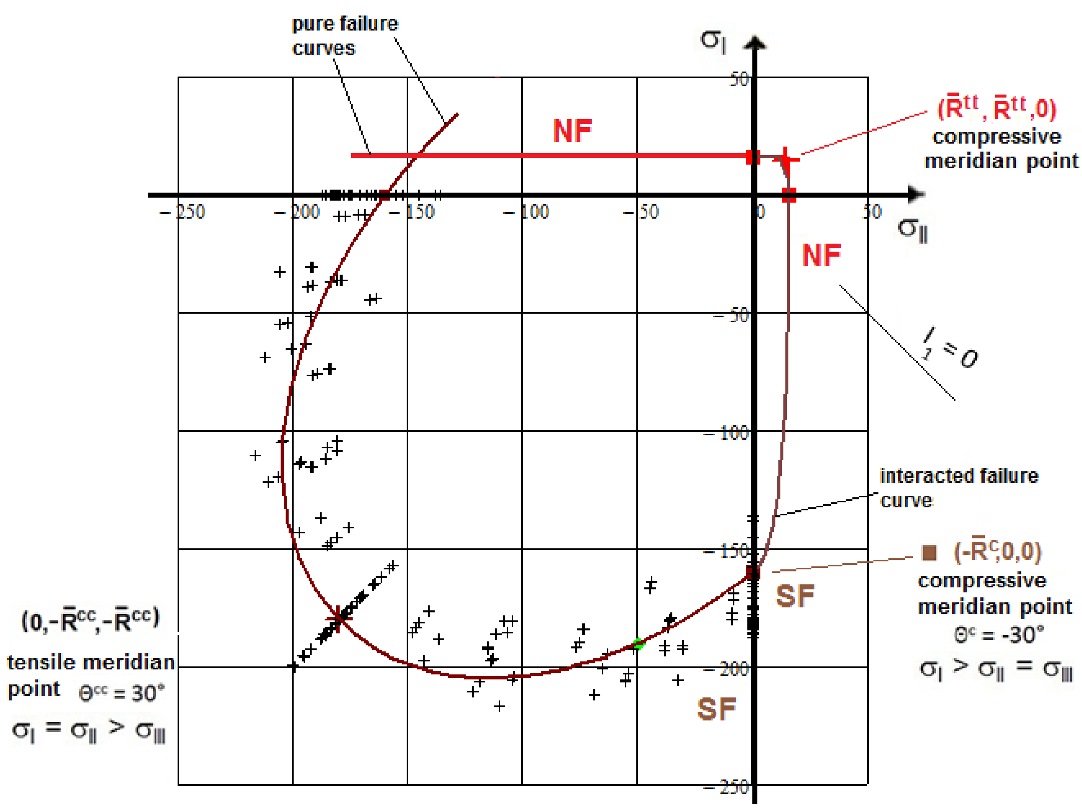

Fig.24-11, UHPC: Principal stress plane with measured test data and evaluated strength points

3D-Visualization of 2D compression test data: Porous Foam Rohacell 71 IG

With the Rohacell Hero (Evonik) a PMI (Poly-Methacryl-Imide) structural foam of an increased tensile fracture strain a light material is available which may replace the expensive honeycombs. Given is 'only' a 2D-Test Data Set and therefore just a realistic mapping in the Principal Stress Plane is possible data set used (*thanks to Dr. Kolupaev for the test data set*) reads:

$$\bar{R}^t = 1.8;\ \bar{R}^{tt} = 1.25;\ \bar{R}^{ttt} = 1.01;\ \bar{R}^c = 1.65;\ \bar{R}^{cc} = 1.4;\ \bar{R}^{ccc} = 1.53,\ \max I_1 = 3.03;$$

$$\min I_1 = -4.58,\ d^{NF} = -0.71;\ d^{CrF} = 0.21;\ c^{CrF} = 1.03, s^{cap} = -0.27;\ s^{bot} = 0.87,$$

$$\vartheta^{NF} = -0.57;\ \vartheta^{CrF} = 0.52; \Theta^{NF} = 1.2;\ \Theta^{CrF} = 1.07, m = 2.5.$$

The *Figs.* 24-12 and 24-13 show the application of the respective SFC for Rohacell.

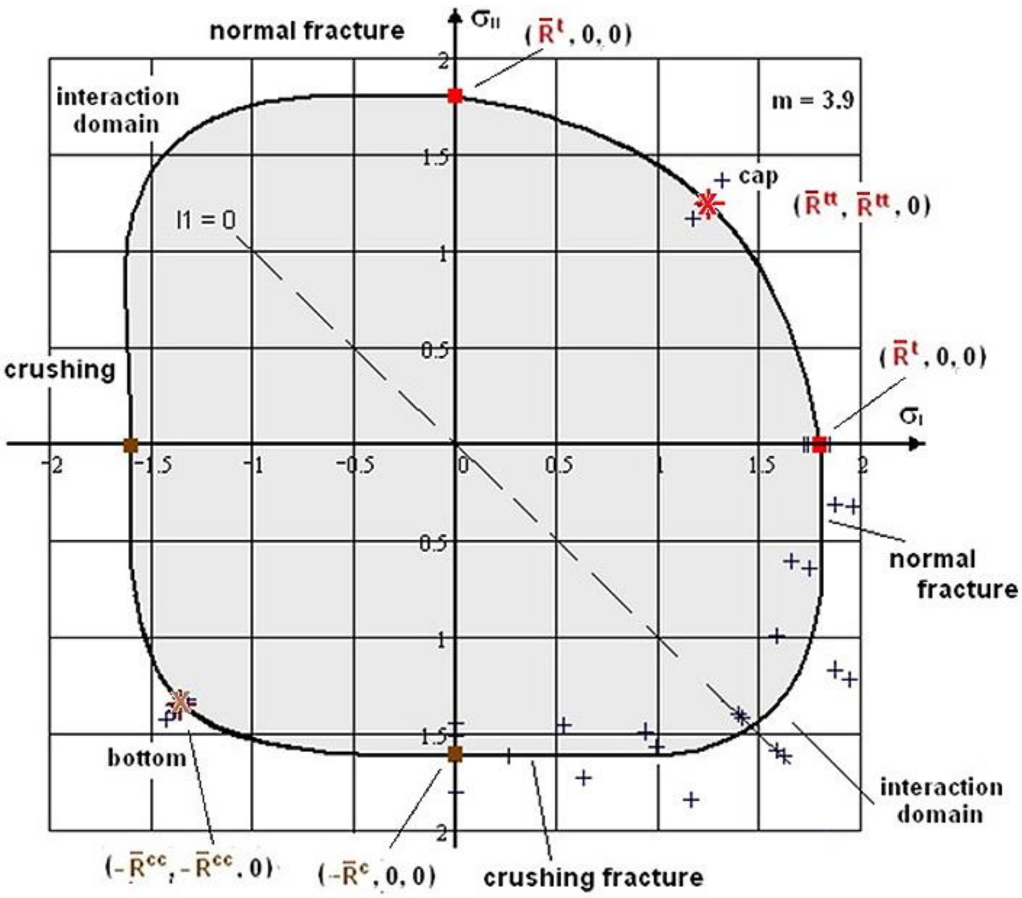

Fig.24-12, Foam Rohacell 71 IG: Mapping of 2D-test data in the Principal Stress Plane. MathCad plot [test data: courtesy V. Kolupaev, LBF Darmstadt]

LL:

* *120°-rotational symmetry is inherent for isotropic materials*
* *R^c lies on the CM, R^t on the TM and R^τ in the transition zone between the two modes F^σ and F^τ. This indicates, that an estimation of R^τ, obtained by just an extrapolation from R^c, will be questionable*
* *The failure body possesses inward dents for $I_1 > 0$ and outward dents for $I_1 < 0$ in contrast to porous concrete stone, where it is also inward. These dents become smaller with increasing $|I_1|$.*
* *There is a pretty large scatter of the compressive strength data in the 2D-figure*
* *Mapping of the course of test data with the SFCs worked very well*

** Fracture body shows a decay of denting with increasing negative I_1*

** The higher the strength ratio SR = R^c/R^t becomes, the more the Cohesive Strength value narrows R^t !*

** The strong influence of IFF1 is fully demonstrated.*

An extrapolation from the compression strength - just applying F^τ - cannot be accurate !

** A smaller μ value is more conservative.*

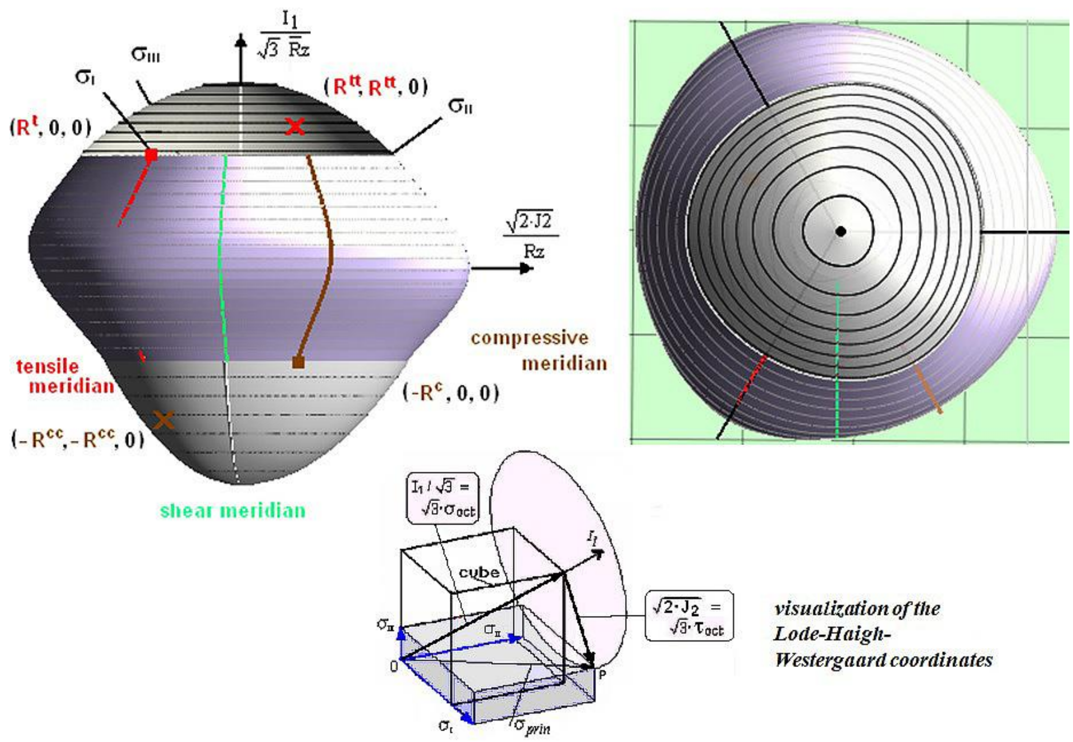

Fig.24-13, Rohacell 71 IG: Fracture body with its different meridians (left) and view from top (right

25 Accurate Mohr-Coulomb Curve and Cohesive shear Strength R^τ of Brittle Isotropic materials

Aim: *Enabling the correct understanding of the cohesive strength value as a* *bi-axial* *fracture quantity.*

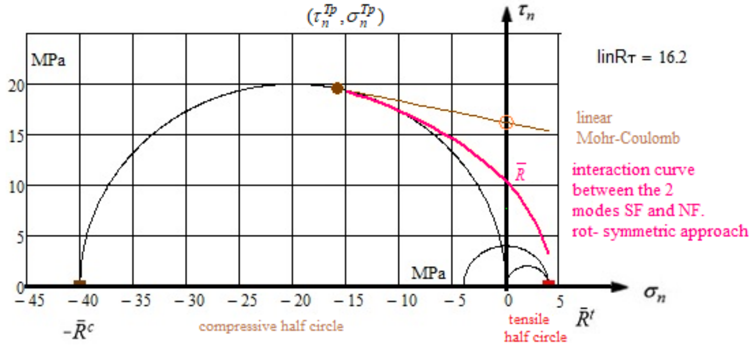

Fig.25-4: Joint display of the magenta failure curve in principal stresses (left) and in Mohr stresses (right). Fracture angle increase Θ_{fp}° , , scaled by twenty (left) and ten (right), is incorporated . 120°-rotational-symmetric model and improved mapping of the measured failure curve due to f_d

The Mohr half-circles are incorporated

This chapter is going to be reworked, because the fracture angle course is missing in the curve above.

25.1 Accurate Mohr-Coulomb Curve and Cohesive shear Strength R^τ

As the author had to design with all the three basic material families isotropic, transversely-isotropic and orthotropic for him a conflict comes up, if the used index-letters are not material-dedicated, self-explaining and not generally used in mechanics. This caused him *as civil engineer* to publish his Glossar.

In order to not disturb the co-working engineering family in construction the fiber-reinforced polymer matrix-linked terminology (world-wide applying the suffixes $_{1,\,2}$) should be also used with fiber-reinforced mineral matrix-linked Carbon Concrete (*another field of the author*).

The following analogous letters will be intentionally proposed to use $c \rightarrow R^\tau$, $\sigma_1 \rightarrow \sigma_{II}$. As some researchers in construction still began, when viewing Mohr-Coulomb friction: According to general mechanics they attribute usually positive marked compressive stresses a negative sign. Hence, the positive direction is to display rightward, *Fig. 25-1 (left)*. (Historically, civil engineers basically were more faced by compression and mechanical engineers by tension. This explains the different sign choice).

Fig.25-1 outlines the Mohr entities together with the transformation matrix for transforming principal stresses into Mohr stresses.

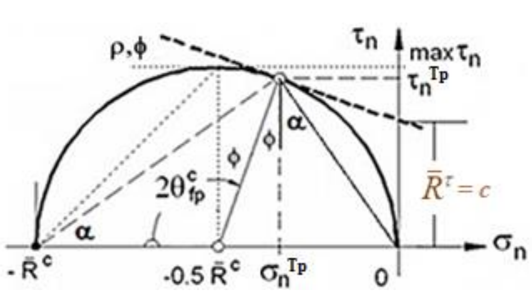

$$\begin{Bmatrix} \sigma_\lambda \\ \sigma_n \\ \sigma_t \\ \tau_n \\ \tau_{t\lambda} \\ \tau_{t\lambda} \end{Bmatrix} = \begin{bmatrix} 1 & 0 & 0 & 0 & 0 & 0 \\ 0 & c^2 & s^2 & 2sc & 0 & 0 \\ 0 & s^2 & c^2 & -2sc & 0 & 0 \\ 0 & -sc & sc & (c^2 - s^2) & 0 & 0 \\ 0 & 0 & 0 & 0 & c & -s \\ 0 & 0 & 0 & 0 & s & c \end{bmatrix} = \begin{Bmatrix} \sigma_I \\ \sigma_{II} \\ \sigma_{III} \\ 0 \\ 0 \\ 0 \end{Bmatrix}$$

With $\eta = \sigma_{II} - \sigma_{III}$ and $\sigma_\lambda,\ \tau_{t\lambda},\ \tau_{n\lambda} = 0$, the used addition theorems read: $\tau_{nt} \equiv \tau_n$

$$\sigma_n - \sigma_t = c^2 \cdot \eta - s^2 \cdot \eta = C \cdot \eta\ ,\ \ \mathrm{S} = \sqrt{1 - C^2},\ C = c^2 - s^2 = 2c^2 - 1 = 1 - 2s^2,$$

$$\sigma_n + \sigma_t = \sigma_{II} + \sigma_{III} = I_1,\ \sigma_t = \sigma_n - C \cdot \eta\ ,$$

$$\tau_n = -s \cdot c \cdot \sigma_{II} + s \cdot c \cdot \sigma_{III} = -0.5 \cdot \sqrt{1 - C^2} \cdot \eta, \qquad c = \cos\phi,\ \ s = \sin\phi,$$

$$\sigma_n = c^2 \cdot \sigma_{II} + s^2 \cdot \sigma_{III} = \frac{(C+1) \cdot \sigma_{II} + (1-C) \cdot \sigma_{III}}{2}.$$

Fig. 25-1: Transformation of Principal Structural Stresses into Mohr Stresses and helpful Addition Theorems

Assumption of O. Mohr

His basic assumption was: *"The strength of a material is determined by the (Mohr) stresses on the fracture plane"*. This means for the linear Mohr-Coulomb (M-C) formulation $\tau_n = \bar{R}^\tau - \mu \cdot \sigma_n$. Herein, the value μ is the intrinsic friction value of the material and $\bar{R}^\tau$ the so-called cohesion strength. The other two shear stresses $\tau_{t\lambda}$, $\tau_{n\lambda}$ are zero, Fig.25-1 (right). The normal stress σ_t must be accounted for in the investigation but will finally have no influence, which has to be proven when following Mohr and this must be shown. According to Mohr, the stresses σ_n and τ_n are the only fracture-responsible stresses, the normal stress σ_λ can be set zero.

SFCs regarding the 120"-rotational symmetry of the isotropic fracture body

$$F^{NF} = \frac{\sqrt{4J_2 - I_1^2/3} + I_1}{2 \cdot \bar{R}^t} \qquad , \qquad F^{SF} = c_2^{SF} \cdot \frac{I_1}{\bar{R}^c} + c_1^{SF} \cdot \frac{6 \cdot J_2}{2 \cdot \bar{R}^{c2}} \cdot \Theta^{SF}$$

$$I_1 = (\sigma_I + \sigma_{II} + \sigma_{III})\ ,\ 6J_2 = (\sigma_I - \sigma_{II})^2 + (\sigma_{II} - \sigma_{III})^2 + (\sigma_{III} - \sigma_I)^2$$

$$27J_3 = (2\sigma_I - \sigma_{II} - \sigma_{III}) \cdot (2\sigma_{II} - \sigma_I - \sigma_{III}) \cdot (2\sigma_{III} - \sigma_I - \sigma_{II}),$$

$$I_1 = (\sigma_n + \sigma_t + \sigma_\lambda)\ ,\ 6J_2 = (\sigma_n - \sigma_t)^2 + (\sigma_t - \sigma_\lambda)^2 + (\sigma_\lambda - \sigma_n)^2 + 6 \cdot \left(\tau_{nt}{}^2 + \tau_{n\lambda}{}^2 + \tau_{t\lambda}{}^2\right)$$

$$\Theta^{SF} = \sqrt[3]{1 + d^{SF} \cdot sin(3\vartheta)} = \sqrt[3]{1 + d^{SF} \cdot 1.5 \cdot \sqrt{3} \cdot J_3 \cdot J_2^{-1.5}},\ \ \sigma_t = \sigma_n - C \cdot \eta,\ \eta = \sigma_{II} - \sigma_{III}.$$

According to Mohr the invariants reduce to: $I_1 = (\sigma_n + \sigma_t),\ 6J_2 = (\sigma_n - \sigma_t)^2 + \sigma_t{}^2 + \sigma_n{}^2 + 6 \cdot \tau_{nt}{}^2$

$27J_3$: ä

Note on the Mohr-Coulomb Criterion (see 26.1)

Exemplarily, a paper a recently published in *Scientific Reports (2024) nature portfolio [Stress-dependent Mohr–Coulomb shear strength parameters for intact rock* [*Li24*] a critical assessment of the M-C criterion is performed. This report shall be not scientifically reworked here. The summarizing private elaboration at hand just tries to inform about the author's procedure to derive an accurate Mohr-Coulomb Envelope including Cohesive Strength. Basis of the procedure is the knowledge, that the M-C Envelope, spanning from the Touch point $(\tau_n^{Tp}, \sigma_n^{Tp}) \rightarrow (\tau_n = R^\tau, \sigma_n = 0)$, is affected by the shear failure mode together with the tensile failure mode and thus belonging to a transition zone, the mode interaction domain.

Solution Procedure for derivation of an improved M-C curve

Searched is an equation for the unknown fracture angle measure $C(\Theta_{fp})$. This is performed by equating the slopes in the so-called touch point: *A first slope equation* $d\tau_{nt} / d\sigma_n$ *is given by the derivation of the Mohr-model* (stress transformation of structural stresses to Mohr stresses) *according to the angle of inclination = slope angle in the Touch Point, marked* ^{Tp}. *Secondly, one has to find an equation for one of the stresses* σ_{III} *or* σ_{II}. *The differentiation of the SFC delivers this equation.*

The accurate derivation of the Cohesive Strength R^τ *and the M-C curve* $\tau_n(\sigma_n)$ *and further of the fracture angle* Θ_{fp} *requires to consider both the activated modes, according to Cuntze's model of the two activated modes, because* R^τ *lies in the transition zone of the two modes SF and NF.*

Differentiation of the Mohr stress relationship generating one of the two required equations

One equation used is that the tangent of the derived Mohr stress curve is identical to the tangent of the SFC-linked Mohr envelope. An angle-differentiation in the Touch point delivers a relationship for the friction value, below:

$$\frac{d}{d\Theta}\sigma n = \frac{d}{d\Theta}\left(c^2\cdot\sigma II + s^2\cdot\sigma III\right) = -2s\cdot c\cdot(\sigma II - \sigma III) \;;\; \frac{d}{d\Theta}\tau nt = \left[\frac{d}{d\Theta}(-s\cdot c\cdot\sigma II + s\cdot c\cdot\sigma III) = \left(-c^2 + s^2\right)\cdot\sigma II - \left(-c^2 + s^2\right)\cdot\sigma III\right]$$

$$\frac{d}{d\sigma n}\tau nt = \frac{\left(-c^2 + s^2\right)\cdot\sigma II - \left(-c^2 + s^2\right)\cdot\sigma III}{-2s\cdot c\cdot(\sigma II - \sigma III)} = \frac{c^2 - s^2}{2\cdot c\cdot s} = \frac{C}{S} = \frac{C}{\sqrt{1 - C^2}} = \tan\rho = \mu$$

$$\cot an(2\cdot\Theta fp) = \frac{\cos(2\cdot\Theta fp)}{\sin(2\cdot\Theta fp)} = \frac{C}{S} \;;\; \tan(\rho) = -\cot\left(2\cdot\Theta cfr\cdot\frac{\pi}{180}\right) \quad \rho = -\operatorname{acot}\left(2\cdot\Theta cfr\cdot\frac{\pi}{180}\right)$$

Strength Failure Criteria considering the 120°-rotational Symmetry of isotropic materials

The generation of a realistic, decaying Mohr-Coulomb curve $\tau_n(\sigma_n)$ requires the determination of the slope *along* the full curve, not a constant value $C = C^c$ in the touch *point* only, being sufficient for the determination of the friction value μ. This means, instead of the single F^{SF}-formulation the SF-NF-interaction managing *Eff*-formulation is to apply when moving from the structural stress formulation to a Mohr stress one.

Table 25-1 shows the transformation of the *Eff*s from principal stresses into Mohr stress-based ones. *Table 25-2* will later show the full procedure.

Table 25-1: Formulation of Mohr stress-based Effs. TM tensile meridian, CM compressive meridian

$$Eff^{NF} = c^{NF} \cdot \frac{\sqrt{4J_2 \cdot \Theta^{NF} - I_1^{\,2}/3} + I_1}{2 \cdot \bar{R}^t}, \quad \text{for Normal Concrete can be set } c^{NF} = \Theta^{NF} = 1,$$

$$Eff^{NF} = 1 \cdot \frac{\sqrt{4 \cdot [(\sigma_n - \sigma_t)^2 + \sigma_t^{\,2} + (-\sigma_n)^2 + 6 \cdot \tau_n^{\,2}] \cdot 1/6 - (\sigma_n + \sigma_t)/3} + (\sigma_n + \sigma_t)}{2 \cdot \bar{R}^t} .$$

$$Eff^{SF} = \frac{\sqrt{(c_{2\Theta}^{SF} \cdot I_1)^2 + 12 \cdot c_{1\Theta}^{SF} \cdot J_2 \cdot \Theta^{SF}}}{2 \cdot \bar{R}^c} + \frac{c_2 \cdot I_1}{2 \cdot \bar{R}^c} \text{ with } \Theta^{SF} \to \Theta^{CM} = \sqrt[3]{1 + d^{SF} \cdot (-1)},$$

$$Eff^{SF} = \frac{\sqrt{c_{2\Theta}^{SF\,2} \cdot (\sigma_n + \sigma_t)^2 + c_{1\Theta}^{SF} \cdot \Theta^{SF} \cdot 2 \cdot [(\sigma_n - \sigma_t)^2 + \sigma_t^{\,2} + (-\sigma_n)^2 + 6 \cdot \tau_n^{\,2}]}}{2\bar{R}^c} + c_2 \cdot \frac{\sigma_n + \sigma_t}{2\bar{R}^c}.$$

with $c_{1\Theta}^{SF} \cdot \Theta^{CM} = 1 + c_2$, $\Theta^{CM} = \Theta^{SF} = \sqrt[3]{1 + d^{SF} \cdot \sin(3\vartheta)} = \sqrt[3]{1 - d^{SF}}$.

Fig.25-2 displays the 2nd quadrant of the bi-axial failure curve formulated in structural stresses. This fully represents the Mohr-Coulomb curve domain. The joint mode situation of the Mohr-Coulomb curve - capturing the transition zone between the pure mode domains NF and SF - requires the application of the interaction equation $(Eff^{NF})^m + (Eff^{SF})^m = 1$. It spans over the regime $0 < \sigma_{III} < \bar{R}^t$, *the transition zone of the modes,* and covers Lode angles $-30° < \vartheta < +30°$.

Improved Mapping of Failure Stress data with Derivation of a more realistic $\Theta_{fp}°(\vartheta)$

As still experienced with the UD-materials, in a chapter before, also here it is to face that a SFC is 'just' a practical approach and therefore cannot sufficiently well map all domain parts. In any case, the given SFC calculates a conservative Reserve Factor, the SFC is on the safe side. In Design-Verification the Eff^{SF} contribution to *Eff* is not a problem because the interaction is a conservative procedure. Stimmt das noch However, when searching a local fracture angle $\Theta_{fp}°$ in the transition zone a correction is to be material-dependently applied to numerically determine a better value for $\Theta_{fp}°$ if one is interested in.

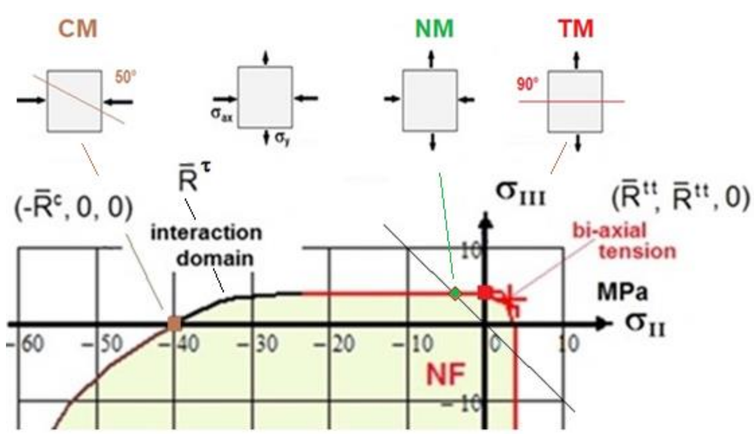

Fig.25-2: Second quadrant and associated stress states, transition zone between the 2 mode domains SF, NF

A characteristic point of the transition zone between the tensile domain and the compressive domain is when the first invariant becomes zero (see the bias grey line in *Fig.25-2*):

$$I_1 = \sigma_I + \sigma_{II} + \sigma_{III} = 0, \text{ means pure shear. For } \sigma_{II}^{\,c} = \sigma_{III}^{\,c} \rightarrow \sigma_I^{\,t} = 2 \cdot \sigma_{III}^{\,c}.$$

Mathematically-caused, the Eff^{SF}-curve and the $Eff^{SF\Theta}$–curve become positive in the pale colored curve part and numerically contribute its effort portion to the total effort. This is physically not accurate.

The Eff^{SF}-curve outlines the local shortcoming of the FMC-based choice of the SF-formula. Negative values of Eff^{SF} are sorted out by a McCauley-procedure, but occurring small positive values have to be made inactive in the low negative σ_{II} domain. Searching a procedure it is helpful to know how the pure mode efforts of the activated modes NF and SF share its influence with σ_{II}. *Fig.25-3* shows the courses of the efforts Eff^{NF} (= Eff^{σ}) and Eff^{SF} (= Eff^{τ}) representing the mode components of a *measured* fracture stress curve. Physical demands are given at the cohesion strength point with $\Theta_{fp}°= 90°$ for $\sigma_{III} = R^t$ and $Eff^{\tau} = 0$ for $\sigma_{II} = 0$).

The shear material stressing effort $Eff^{\tau} = Eff^{SF}$ must physically become zero at the tensile strength point (0, R^t).

According to the fact that the compression strength point is located on the compressive meridian and the tensile strength point on the tensile meridian the different Lode angle ϑ is to consider in order to achieve an accurate approach when investigating the Mohr-Coulomb envelope curve. This requires to consider the 120°-rotationally-symmetric $Eff^{SF\Theta}$.

26 Mapping 3D Test Results of Concrete and Rocks obtained on the Meridians TM, CM

Aim: *Provision of a test data evaluation formula for the test meridian, being a cross-section of a physically to be defined fracture body surface.*

26.1 General

Sufficient strength of tunnels and dam slopes are vital Design Verification requirements in geo-engineering. In order to achieve this, the course of the measured fracture data on Tensile (TM) and Compressive Meridian (CM) is to map. For this design task several SFC approaches are applied:

"Linear Mohr-Coulomb shear curve"

Shear stresses below the curve mean 'No fracture', or 'Stress states' below the τ^n- curve are not dangerous. This well-known simple SFC reads: $\tau^n(\sigma_I, \sigma_{III}) = \sigma \cdot tan\phi + c$.

→ a value for cohesive shear strength c and friction angle $\phi(\mu)$ are required.
This is an extrapolation from the compressive strength point.

"Linear Mohr-Coulomb criterion in geo-mechanics"

In order to achieve Design Verification in several numerical Rock mechanics Codes the use of the widely applied 'Mohr-Coulomb (M-C) Criterion' is recommended in order to map the course on that meridian where the tests have been run, on TM or CM. Due to Mohr, the intermediate stress has no influence. The criterion below says that a stress below the M-C curve is conservative.

$\sigma_1 = \sigma_3 \cdot tan^2(\Phi) + 2 \cdot c \cdot tan(\Phi)$, applying $\Phi = \pi/4 + \phi/2$

where c = cohesive shear strength and ϕ = internal friction angle,

σ_1 = most negative principal stress $\rightarrow \sigma_{III}$, σ_3 = most positive principal stress $\rightarrow \sigma_I$,

which are transferred to the mathematical principal stress convention $\sigma_I > \sigma_{II} > \sigma_{III}$.

Final formulation is: $\sigma_{III} = \sigma_I \cdot tan^2(\Phi) + 2 \cdot c \cdot tan(\Phi)$.

However in application, a difficult to be answered question arises: Which parameters are to insert? This concerns the fracture angle ϕ and the cohesive strength R^τ .

→ a value for cohesive shear strength c and friction angle are required.
This also is usually an extrapolation from the compressive strength point.

In *Fig.26-1* the derivation of the associated input data set is provided. Concerning R^τ it is referred to a previous chapter where the cohesive strength has been investigated.

"Cuntze's FMC-based SFCs regarding the common acting of SF and NF"

The SFC model, spanning up the isotropic fracture body, is shown in *Table 26-1*.

As still described before, the first part of the SFC in *Table 26-1* represents the shape change, the second the friction effect, the third the volume change and Θ^τ the 120°-symmetry of isotropic materials. Mapping the test data in the very high negative compression domain of UHPC could require a fifth part, which may be dedicated to a further effect, discontinuous densification including a failure body hoop reduction and later widening.

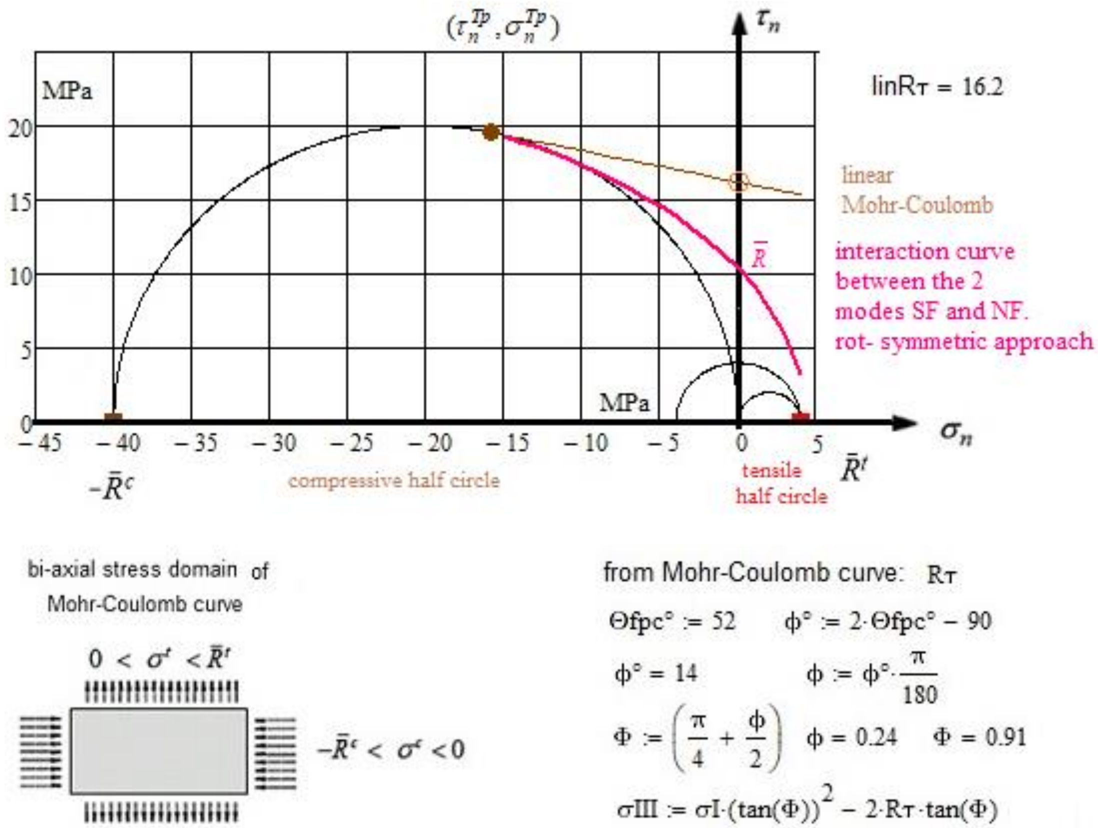

Fig.26-1, example Normal Concrete: (left) Derivation of a data set for the M-C criterion. Properties applied for UHPC: linR$^\tau$ = 70MPa, ϕ°= 14°. (right) Model dependent cohesive strength values (from Normal Concrete)

The SFC contains five un-known parameters. For their determination, mathematically at minimum, five reliable test points on the surface of the fracture body are to provide by tests along the TM and CM. Better fitting procedures could be applied.

Good Mapping requires to capture physics and to apply SFCs being as simple as possible.

Cuntze's approach includes a multifold mapping task, which can be a compromise, only:

(1) Mapping the 2D test data in the principal stress plane, considering the friction effect.

(2) Mapping the 3D test data along the tensile test meridian (TM) or / and along the compressive test meridian (CM) of these two axial (180°-opposite) cross-sections of the fracture body with TM $(\sigma_I, \sigma_{II} = \sigma_{III}) \rightarrow \sigma_I(2\sigma_{III})$ and CM $(\sigma_I = \sigma_{II}, \sigma_{III}) \rightarrow 2\sigma_I(\sigma_{III})$.

All subfigures, principal stress plane and meridian cross-sections must be able to be derived from the well mapped fracture body and this with sufficient precision.

→ cohesive shear strength $c = R^\tau$ and friction angle ϕ are not required.
Points on the fracture body surface are used to fix the model parameters.

Table 26-1: SFC model Cuntze

shape change	friction	volume change

$$I_1 < 0: \quad F^{SF} = F^{\tau} = c_1^{SF} \cdot \frac{6J_2 \cdot \Theta^{SF}}{2 \cdot \bar{R}^{c2}} \quad + \quad c_2^{SF}(\mu) \cdot \frac{I_1}{\bar{R}^c} \quad + + c_3 \cdot \left(\frac{I_1}{\bar{R}^c}\right)^2 + c_4 \cdot \left(\frac{I_1}{\bar{R}^c}\right)^3 \quad = \quad 1$$

'Mises Cylinder' formula

Above SFC is here normalized by the compressive strength $\bar{R}^c$. J_2 is the 'Mises' invariant.

$$I_1 = (\sigma_I + \sigma_{II} + \sigma_{III}) = f(\sigma), \quad 6J_2 = (\sigma_I - \sigma_{II})^2 + (\sigma_{II} - \sigma_{III})^2 + (\sigma_{III} - \sigma_I)^2 = f(\tau)$$

$$27J_3 = (2\sigma_I - \sigma_{II} - \sigma_{III}) \cdot (2\sigma_{II} - \sigma_I - \sigma_{III}) \cdot (2\sigma_{III} - \sigma_I - \sigma_{II}),$$

$$3 \cdot \sigma_{oct} = \sigma_I + \sigma_{II} + \sigma_{III} \; ; \; 9 \cdot \tau_{oct}^{\ 2} = 6J_2 = 4 \cdot (\tau_{III}^{\ 2} + \tau_I^{\ 2} + \tau_{II}^{\ 2}), \; \tau_{II} = max\,\tau(mathem.)$$

$\sigma_I, \sigma_{II}, \sigma_{III}$ are principal stresses, $\sigma_I > \sigma_{II} > \sigma_{III}$ are mathematical stresses (> more positive)

with $I_1 = (\sigma_I + \sigma_{II} + \sigma_{III})$, $6 \cdot J_2 = (\sigma_I - \sigma_{II})^2 + (\sigma_{II} - \sigma_{III})^2 + (\sigma_{III} - \sigma_I)^2$

Consideration: 120°-rotational symmetry of isotropic materials: $d^{SF} \equiv d_\tau$ *later*

$$\Theta^{SF}(J_3, J_2) = \sqrt[3]{1 + d^{SF} \cdot sin(3\vartheta)} = \sqrt[3]{1 + d^{SF} \cdot 1.5 \cdot \sqrt{3} \cdot J_3 \cdot J_2^{-1.5}}$$

with the non-circularity function Θ^{SF} including d^{SF} as non-circularity parameter.

Compr. Meridian: $\Theta^{SF} = \sqrt[3]{1 - d^{SF}}$, Tensile Meridian: $\Theta^{SF} = \sqrt[3]{1 + d^{SF}}$, Neutral Meridian: $\Theta^{SF} = 1$.

Reminder: All isotropic materials possess a more or less significant 120°-rotational symmetry of the fracture body depicted in Haigh-Lode-Westergaard coordinates, see *Fig.26-2*. Thereby, the well-known invariant J_3 is an excellent function to map this type of rotational symmetry (caused by $R^{cc} \neq R^c$ or $R^{tt} < R^t$ and to determine the Lode angle ϑ. Well-known is that the tests are run on the CM and on the TM. Therefore, the angle is given: for CM ϑ = *-30°* and for TM ϑ = *30°*.

Fig.26-2 presents the course of test data tested on Tensile Meridian + and Compr. Meridian +.

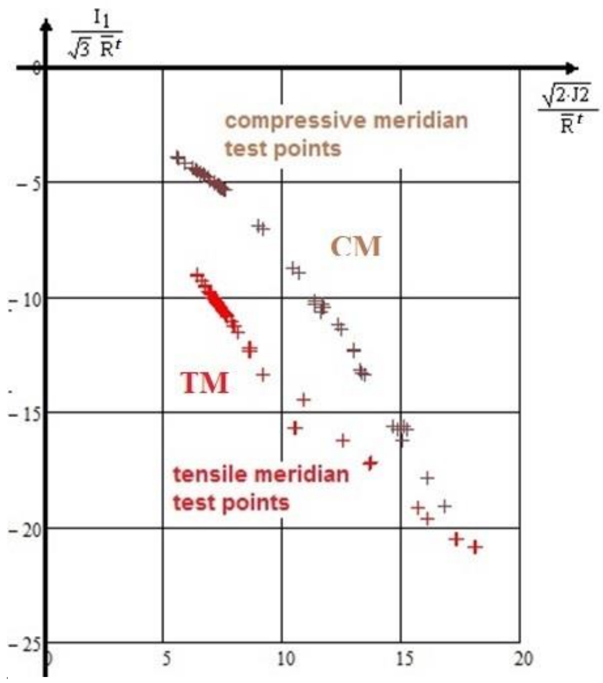

Fig.26-2, UHPC:
Compressive and tensile meridian test points.

Intentionally depicted on the positive abscissa to outlne the difference stemming from the brittle isotropic material's inherent 120°-rotational symmetry of the onset-of-fracture failure body

The tricky procedure how to obtain the required model parameters c_i is shown in *Table 26-2* by three steps. For the cohesive strength, required by the extrapolation approaches, numerical values are determined in the third step. Different models deliver different values improved models deliver a lower value, because these consider both damaging modes SF and NF.

26.2 Ultra-High-Performance-Concrete UHPC (relatively dense)

UHPC principally behaves similarly to Normal Concrete unless the normalized hydrostatic compression does not become larger than $I_1 / R^t \cdot \sqrt{3} \approx -10$ (> -300 MPa), see *Fig.26-2*.

In contrast to Normal Concrete with usually relatively low hydrostatic pressure loadings the UHPC experiences a hydrostatically activated effect, 'densification with volume shrinkage'. Therefore, the volume change must be considered by I_1^2. This explains why for the less 'dense' Normal Concrete R^{cc}/R^c is higher than with UHPC according to the possible higher densification. Combined with this a 'healing' of the flaw effects can be faced.

The fracture body of a theoretically dense concrete matrix possesses in the high hydrostatic compressive domain ($I_1 < 0$) an open fracture surface due to the densification. Practically however, the fracture body does only exist once and cannot be stressed twice. Further, the bi-axial compressive strength $R^{cc} \equiv f^{cc}$ (internationally used letter in construction, stems from the German term Festigkeit) may be not only linked to SF but also to NF due to the Poisson's ratio activated tensile strain in the axial direction despite $\sigma_{ax} = 0$.

The author had to search out of the huge test data set from IMb Dresden, which test points belong to TM and which to CM. When searching these data sets the full bunch of obtained 3D test data the respectively, had to be processed. Such a separation uses the Lode angle or meridian angle ϑ values: Which test point belongs more to the tensile meridian $\sin(3\vartheta) = 1$ or to the compressive meridian $\sin(3\vartheta) = -1$, see *Table 26-3* and *Fig.26-4*. For the shear meridian (neutral meridian NM) angle is valid $\sin(3\vartheta) = \vartheta = 0$.

$$F^{\tau} = c_1 \cdot \frac{6J_2 \cdot \Theta^{SF}}{2 \cdot \bar{R}^{c2}} + c_2(\mu) \cdot \frac{I_1}{\bar{R}^c} + c_3 \cdot \left(\frac{I_1}{\bar{R}^c}\right)^2 + c_4 \cdot \left(\frac{I_1}{\bar{R}^c}\right)^3 = 1$$

5 unknowns at least brequire 5 fix stress state failure points on the failure surface

$$\{\sigma\} = (\,,\,,\,)^T : (-\bar{R}^c, 0, 0),\ (-\bar{R}^{cc}, -\bar{R}^{cc}\, 0, 0),\ (\sigma_I^{frict}, \sigma_I^{frict}, 0),\ (\bar{R}^c, 0, 0),\ (\bar{R}^c, 0, 0)$$

with the values in MPa = N/mm^2: $\bar{R}^c = 175$, $\bar{R}^{cc} = 183$, $\sigma_I^{frict} = -195$, $\sigma_{II}^{frict} = -50$,

Points: $\sigma_I^{TM} = -40$, $\sigma_{II}^{TM} = \sigma_{III}^{TM}$, $\sigma_{III}^{TM} = -375$; $\sigma_I^{CM} = -61$, $\sigma_{II}^{CM} = \sigma_I^{CM}$, $\sigma_{III}^{CM} = -420$,

$m = 2.7.$

Table 26-3 presents the essential numbers of some measured failure stress states. The table indicates the Lode angle $\vartheta°$. On basis of redundancy effects it may be concluded that with increasing hydrostatic pressure both the meridians run into a common scatter band → circle shape of the hoop. Then, the effect of flaws generating micro-damaging in this heterogeneous material reduces. Thereby, the fracture body becomes more and more cylindrical.

Table 26-3: Characteristic material data when evaluating UHPC fracture tests. E = 20000 MPa, ν = 0.2, $\tau_{max} = \sigma_I - \sigma_{III}$

	Stress state in MPa	$I_1/\sqrt{3}$ $/R^t$	$\sqrt{2 \cdot J2}$ $/ R^t$	τ_{max} in MPa	(σ_{hyd}; σ_{ax}) in MPa	$\vartheta°$	ε_{ax} el in 10^{-3}	remarks
R^{tt}	(14, 14, 0)	1	0.7	-	-	-30	0.6	two-fold NF
R^c	(0 , 0, -160)	-5.8	8.2	80	(-0; -160)	-30	-8	Eff_{SF}
	(-6, -6,-230)	-8.7	11.4	111	(-6; -224)	-30	-11	
Compr essive	(-16,-16,-272)	-11.0	13.1	128	(-16; -256)	-30	-13	
	(-35,-35,-350)	-15.2	16.1	157	(-35; -315)	-30	-17	
	(-83,-83, -490)	-23.7	20.8	204	(-83; -407)	-30	-23	
comput.	**(-23,-23,-305)**	-12.6	14.4	141	(-23; -282)	-30	-15	
R^{cc}	(0,-175,-175)	-12.6	8.9	88	(0;-)	+30	3.5	two-fold SF
Tensile	(-2,-210,-210)	-15.2	10.6	104	(-2; -)	+30	4.1	
	(-24,-310,-310)	-23.2	14.6	143	(-24; -)	+30	5.0	
R^t	(-54,-388,-388)	-30	17	167	(-54; -)	+30	5.1	
	(16, 0, 0)	0.6	0.8	-	-	+30	0.8	Eff_{NF}
shear	(9, -9, 0)	0	0.8	9	-	0	0.5	$Eff_{NF} > Eff_{SF}$
change	(0,-52,-193)	-8.8	8.8	97	-	-15	-9.1	

Fig. 26-4 links multi-axial stress states to the Lode angles -30° (CM) and +30° (TM). Only stress states on the two meridians can be really depicted in the cross-sections. All other test points lie on the fixed hoop radius on a Lode angle different to +30° and -30°. These points are marked by o.

Table 26- 2, example Normal Concrete: Procedure to obtain model parameters. Material properties in § 24

1 ***Relationship of friction parameter and value considering the simple Two Parameter Model***

$F^{\tau} = c_2 \cdot \frac{I_1}{\bar{R}^c} + c_{1\Theta\tau} \cdot \frac{6 \cdot J_2 \cdot \Theta^{SF}}{2 \cdot \bar{R}^{c2}} = 1 \leftarrow$ insertion of the compression point $c_2 \cdot \frac{-\bar{R}^c}{\bar{R}^c} + c_{1\Theta\tau} \cdot \frac{6 \cdot \bar{R}^{c2} / 3 \cdot \Theta^{SF}}{2 \cdot \bar{R}^{c2}} = 1$

($c_{2\Theta} = c_2$, because the friction parameter does not depend on 120°-rotational symmetry)

$\Rightarrow c_{1\Theta} = \frac{1 + c_2}{\Theta^{CM}}$ with non-circularity function $\Theta^{CM} = \sqrt[3]{1 - d_\tau}$ (if rotationally-symmetric, $d_\tau = 0$, $\Theta^{SF} = 1$),

Estimation of c_2 also by a guess of friction value μ from $c_2 \approx (3\mu + \sqrt{1+\mu^2}) / (-3\mu + \sqrt{1+\mu^2})$.

Estimation of c_2 possible by a guess of friction value μ from $c_2 \approx (3\mu + \sqrt{1+\mu^2}) / (-3\mu + \sqrt{1+\mu^2})$.

2 ***Combined Determination of non-circularity parameter d_τ, c_2 and $c_{1\Theta\tau}$*** (Mathcad Coding)

If no test value available, this requires an estimate for $\bar{R}^{cc}$ (lies on the Tensile Meridian).

$\sigma If := -11.5 \quad \sigma IIIf := -73 \quad Rc = 43 \quad Rcc = 49$

Vorgabe $\quad c1\Theta\tau := 5 \quad d\tau := 0.6 \quad c2 := 4$

compression strength point Rc on CM

$c1\Theta\tau \cdot \frac{3J2c \cdot \sqrt[3]{1 - d\tau}}{Rc^2} + c2 \cdot \frac{I1c}{Rc} = 1$

point (-Rcc, -Rcc) on TM

$c1\Theta\tau \cdot \frac{3J2cc \cdot \sqrt[3]{1 + d\tau}}{Rc^2} + c2 \cdot \frac{I1cc}{Rc} = 1$

Insertion of a far 3D point on TM

$$\boxed{\frac{c2 + 1}{\sqrt[3]{1 + d\tau \cdot (-1)}} \cdot \frac{\left[(\sigma If - \sigma IIIf)^2 + (\sigma IIIf - \sigma If)^2\right] \cdot \sqrt[3]{1 + d\tau \cdot (1)}}{2Rc^2} + c2 \cdot \frac{\sigma If + 2\sigma IIIf}{Rc} = 1}$$

$A\tau := \mathrm{Suchen}(c1\Theta\tau, d\tau, c2)$

$A\tau = \begin{pmatrix} 12.462 \\ 0.633 \\ 7.922 \end{pmatrix} \quad c1\Theta\tau := A\tau_0 \quad d\tau := A\tau_1 \quad c2 := A\tau_2$

$c1\Theta\tau = 12.46 \quad d\tau = 0.633 \quad c2 = 7.92$

$Cc := \frac{-1}{3} \cdot \frac{(c2 - 1)}{c2 + 1} \quad \boxed{\mu := -\frac{Cc}{\sqrt{1 - Cc^2}}} \quad Cc = -0.26 \quad \mu = 0.21$

3 ***Estimation of the Cohesive Strength*** for application of the Mohr-Coulomb Criterion

touch point coordinates: $\sigma nTp := c^2 \cdot (-Rc) \quad \tau nTp := -s \cdot c \cdot (-Rc) \quad c := \sqrt{\frac{Cc}{2} + \frac{1}{2}} \quad s := \sqrt{\frac{1}{2} - \frac{Cc}{2}}$

$\sigma nTp = -16 \quad \tau nTp = 21$

Simple Mohr-Coulomb: $linR\tau := [\tau nTp + \mu \cdot (\sigma nTp)]$ C = Cc = constant along the M-C curve $\boxed{linR\tau = 17.4}$

Linear M-C Extrapolation: $\quad \sigma t := -Cc \cdot (-Rc)$

$c1 := c2 + 1 \quad R\tau := \sqrt{-\frac{-Rc^2 + c2 \cdot \sigma t \cdot Rc + c1 \cdot \sigma t^2}{3 \cdot c1}} \quad c1\Theta\tau = 12.5 \quad Cc = -0.26 \quad \boxed{R\tau = 13}$

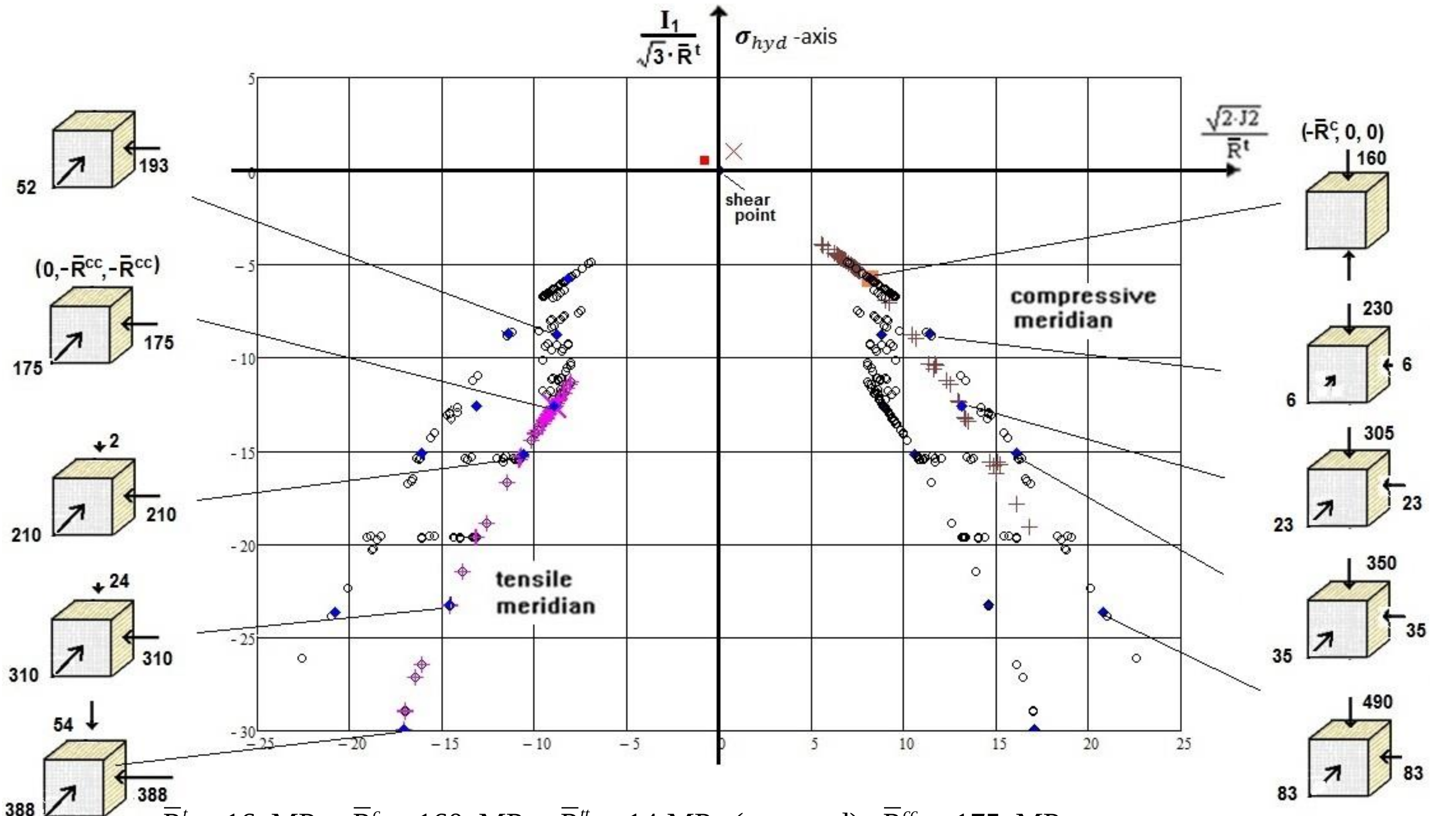

$\bar{R}^t = 16$ MPa, $\bar{R}^c = 160$ MPa, $\bar{R}^{tt} = 14$ MPa (assumed), $\bar{R}^{cc} = 175$ MPa

Fig.26-4, UHPC: Compressive and tensile meridian of the fracture body with associated stress states. (left) mirrored tensile meridian test points + *with compressive meridian ones* +*; (right) all 3D test points are marked by* **o** *(hoop ring), visualizing to be located at different meridians* ϑ.
Vice versa mirrored TM and CM meridian points

.

Fig.26-5 displays the mapping quality in the principal stress plane. For comparison the elliptical curve, as the bias cross-section of a cylinder is integrated. The figure indicates that there is no Mises cylinder is given, the 120°- rotational symmetry acts.

Fig.26-6 (left) displays the mapping of the TM and the CM data course on the cross section of the fracture body.
Fig.26-6 (right) depicts the mapping of the TM data set in a diagram using the rock mechanics coordinates (σ_I, σ_{III}) for TM and $(2\sigma_I, \sigma_{III})$ for CM. How the effortful programming has been performed is compiled in Table 26-4. Unfortunately Mathcad did not compute the CM curve. The 'Mohr-Coulomb (M-C) Criterion', using the calculated UHPC-parameters, produces a straight line. The author could not find any explanation for this unacceptable mapping.
According to the 180°-material symmetry the TM curve could be mirrored from the CM curve by switching from Θ^{CM} to Θ^{TM}.

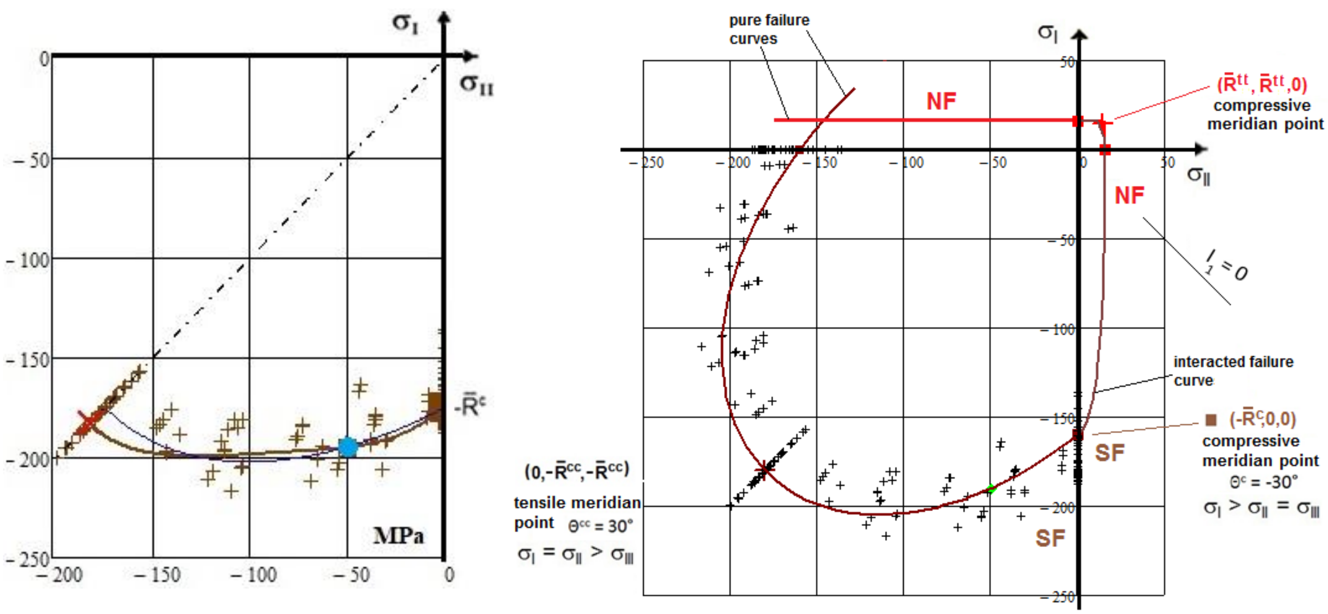

Fig.26-5, UHPC: (left) Mapping the course of 2D test data in the principal stress plane. The blue fix point serves for friction quantification, mapping course of test data in the SF-domain only (normalization by R^c.) *considering the alternating Lode angle θ*

(right) Full principal stress plane view, mapping interaction NF with SF in their transition zone (normalization by R^t).

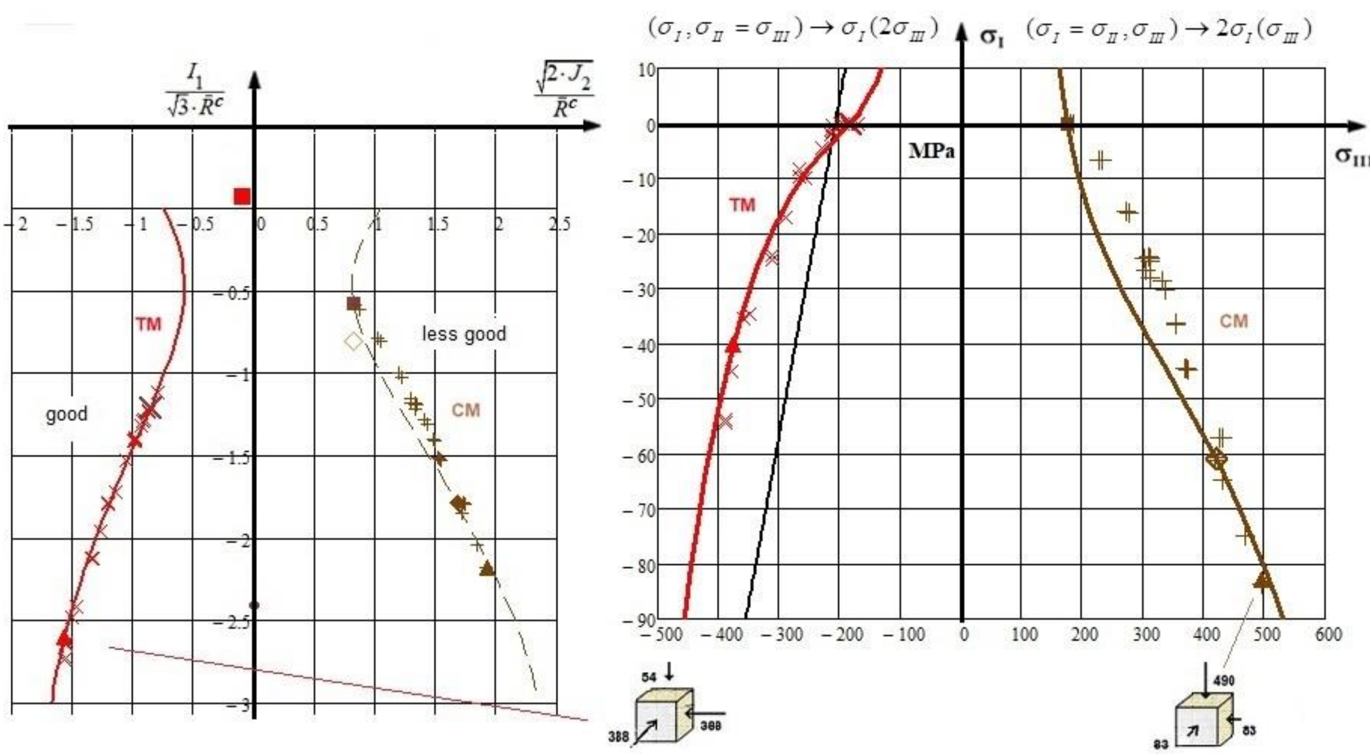

Fig. 26-6, UHPC: (left) mapping display of the two test data sets in Haigh-Lode-Westergaard coordinates. (right) Display using a confining stress coordinate

Eventually, *Table 26-4* presents the determination of the 5 UHPC model parameters.

Table 26-4,UHPC: Determiantion of the SFC model parameters

$$F\tau = \frac{c1 \cdot 6J2 \cdot \Theta\tau}{2Rc^2} + c2 \cdot \frac{I1}{Rc} + c3 \cdot \left(\frac{I1}{Rc}\right)^2 + c4 \cdot \left(\frac{I1}{Rc}\right)^3 = 1$$

$$I1 = \sigma I + \sigma II + \sigma III \qquad J2 = \frac{(\sigma I - \sigma II)^2 + (\sigma II - \sigma III)^2 + (\sigma III - \sigma I)^2}{6}$$

$$J3 = \frac{(2 \cdot \sigma I - \sigma II - \sigma III) \cdot (2 \cdot \sigma II - \sigma I - \sigma III) \cdot (2\sigma III - \sigma I - \sigma II)}{27}$$

$$\Theta\tau = \sqrt[3]{1 + d\tau \cdot 1.5 \cdot 3^{0.5} \cdot J3 \cdot J2^{-1.5}} = \sqrt[3]{1 + d\tau \cdot \sin(3\theta)}$$

$$\Theta\tau TM = \sqrt[3]{1 + d\tau \cdot \sin(3\theta t)} = \sqrt[3]{1 + d\tau} \qquad \Theta\tau CM = \sqrt[3]{1 + d\tau \cdot \sin(3\theta c)} = \sqrt[3]{1 - d\tau}$$

$$\theta = \frac{1}{3} \cdot \mathrm{asin}\left[1.5 \cdot 3^{0.5} \cdot \frac{(2 \cdot \sigma I - \sigma II) \cdot (2 \cdot \sigma II - \sigma I) \cdot (-\sigma II - \sigma I)}{27} \cdot \left(\frac{2 \cdot \sigma I^2 - 2 \cdot \sigma I \cdot \sigma II + 2 \cdot \sigma II^2}{6}\right)^{-1.5}\right]$$

Vorgabe $\quad c1 := 2$

$$\boxed{c1 \cdot \frac{3 \cdot J2c \cdot \sqrt[3]{1 - 1 \cdot d\tau}}{Rc^2} + c2 \cdot \frac{I1c}{Rc} + c3 \cdot \left(\frac{I1c}{Rc}\right)^2 + c4 \cdot \left(\frac{I1c}{Rc}\right)^3 = 1}$$

$$\boxed{c1 \cdot \frac{3 \cdot J2cc \cdot \sqrt[3]{1 + 1 \cdot d\tau}}{Rc^2} + c2 \cdot \frac{I1cc}{Rc} + c3 \cdot \left(\frac{I1cc}{Rc}\right)^2 + c4 \cdot \left(\frac{I1cc}{Rc}\right)^3 = 1}$$

$$\boxed{c1 \cdot \frac{3 \cdot J2f \cdot \sqrt[3]{1 + 1 \cdot d\tau \cdot \sin(3\theta f)}}{Rc^2} + c2 \cdot \frac{I1f}{Rc} + c3 \cdot \left(\frac{I1f}{Rc}\right)^2 + c4 \cdot \left(\frac{I1f}{Rc}\right)^3 = 1}$$

$$\boxed{c1 \cdot 3 \cdot \frac{J2vc1}{Rc^2} \cdot \sqrt[3]{1 - 1 \cdot d\tau} + c2 \cdot \frac{I1vc1}{Rc} + c3 \cdot \left(\frac{I1vc1}{Rc}\right)^2 + c4 \cdot \left(\frac{I1vc1}{Rc}\right)^3 = 1}$$

$$\boxed{c1 \cdot 3 \cdot \frac{J2v}{Rc^2} \cdot \sqrt[3]{1 + 1 \cdot d\tau} + c2 \cdot \frac{I1v}{Rc} + c3 \cdot \left(\frac{I1v}{Rc}\right)^2 + c4 \cdot \left(\frac{I1v}{Rc}\right)^3 = 1}$$

$$A\tau := \mathrm{Suchen}(c1, d\tau, c2, c3, c4)$$

Table 26-5 follows with the derivation of the mapping curves in confining stress coordinates from the model parameters for the full UHPV fracture body.

- ***Engineering mapping has basically to capture physics, must be simple and understandable and shall use measurable parameters.***
- ***Therefore the SFC-models applied for mapping can be good compromises, only.***

Table 26-5: Relationships to derive mapping with the confining stress coordinates

TM **Transfer to confing stress coordinates** **CM**

$\boxed{\sigma II = \sigma III}$ $$J2 = \frac{(\sigma I - \sigma II)^2 + (\sigma II - \sigma III)^2 + (\sigma III - \sigma I)^2}{6}$$ $\boxed{\sigma II = \sigma I}$

$(\sigma It - \sigma IIt)^2 + (0)^2 + (\sigma IIIt - \sigma It)^2$ same function $0^2 + (\sigma IIc - \sigma IIIc)^2 + (\sigma IIIc - \sigma Ic)^2$

$\boxed{J2 = \frac{Rc^2 \cdot x^2}{2}}$ $$J2 := \frac{\left[(\sigma I - \sigma III)^2 + (\sigma III - \sigma I)^2\right]}{6}$$ for TM and CM equal !

$\boxed{I1t = \sqrt{3} \cdot Rc \cdot yt}$ $$x^2 = \frac{\left[(\sigma I - \sigma III)^2 + (\sigma III - \sigma I)^2\right]}{3 \cdot Rc^2}$$

$I1 = \sigma I + \sigma II + \sigma III$ $yt = \frac{I1t}{\sqrt{3} \cdot Rc} = \frac{\sigma It + 2\sigma IIIt}{\sqrt{3} \cdot Rc}$ $\sigma IIIt = \frac{\sqrt{3} \cdot Rc \cdot yt}{2} - \frac{\sigma It}{2}$ $yc = \frac{\sigma Ic + 2\sigma IIIc}{\sqrt{3} \cdot Rc}$

$$xTM = \sqrt{\frac{\left[\left[\sigma It - \left(\frac{\sqrt{3} \cdot Rc \cdot y}{2} - \frac{\sigma It}{2}\right)\right]^2 + \left(\frac{\sqrt{3} \cdot Rc \cdot y}{2} - \frac{\sigma It}{2} - \sigma It\right)^2\right]}{3 \cdot Rc^2}} = \sqrt{\frac{\frac{1}{2} \cdot (3 \cdot \sigma It - \sqrt{3} \cdot Rc \cdot y)^2}{3 \cdot Rc^2}}$$

$$xCM = \sqrt{\frac{\left[\left[\sigma Ic - (\sqrt{3} \cdot Rc \cdot y - 2 \cdot \sigma Ic)\right]^2 + \left(\sqrt{3} \cdot Rc \cdot y - 2 \cdot \sigma Ic - \frac{\sigma Ic}{2} - \sigma Ic\right)^2\right]}{3 \cdot Rc^2}} = \sqrt{\frac{2 \cdot (3 \cdot \sigma Ic - \sqrt{3} \cdot Rc \cdot y)^2}{3 \cdot Rc^2}}$$

Values for x are given by inserting the y-coordinate into the SFC

$j := 0, 1 .. 40$ $y_j := \frac{-j}{10} - 1$ y runs negative

$$xTM_j = \sqrt{\left[-\frac{2 \cdot \left[c2 \cdot Rc^2 \cdot I1_j - Rc^3 + c3 \cdot Rc \cdot (I1_j)^2 + c4 \cdot (I1_j)^3\right]}{3 \cdot Rc^3 \cdot c1 \cdot \Theta\tau TM}\right]} \qquad xCM_j = \sqrt{\left[-\frac{2 \cdot \left[c2 \cdot Rc^2 \cdot I1_j - Rc^3 + c3 \cdot Rc \cdot (I1_j)^2 + c4 \cdot (I1_j)^3\right]}{3 \cdot Rc^3 \cdot c1 \cdot \Theta\tau CM}\right]}$$

Finally the y-value is inserted into the confing stress version of x xTM, xCM are known

Vorgabe $\sigma It := -100$

$$xTM = \sqrt{\frac{\left[\left[\sigma It - \left(\frac{\sqrt{3} \cdot Rc \cdot y}{2} - \frac{\sigma It}{2}\right)\right]^2 + \left(\frac{\sqrt{3} \cdot Rc \cdot y}{2} - \frac{\sigma It}{2} - \sigma It\right)^2\right]}{3 \cdot Rc^2}}$$

$V(xTM, y) :=$ Suchen(σIt) $\sigma It_j := V(xTM_j, y_j)$ $\sigma IIIt_j := \frac{\sqrt{3} \cdot Rc \cdot y_j}{2} - \frac{\sigma It_j}{2}$

Mathcad did not compute σIc_j however the formula can be simplified and σI extracted

$$\sigma It_j := \frac{\sqrt{6} \cdot Rc \cdot xTM_j}{3} + \frac{\sqrt{3} \cdot Rc \cdot y_j}{3} \qquad \sigma Ic_j := \frac{\sqrt{3} \cdot Rc \cdot y_j}{3} + \frac{\sqrt{2} \cdot \sqrt{3} \cdot Rc \cdot xCM_j}{6}$$

$$\sigma IIIt_j := \frac{\sqrt{3} \cdot Rc \cdot y_j}{2} - \frac{\sigma It_j}{2} \qquad \sigma IIIc_j := \sqrt{3} \cdot Rc \cdot y_j - 2 \cdot \sigma Ic_j$$

LL:
** Of course, concerning all part figures 2D and 3D shows that mapping is always a compromise.*

* *Further, a display using a confining stress (TM: $\sigma_{II}= \sigma_{III}$, CM: $\sigma_{I}= \sigma_{II}$) as coordinate leads to another mapping figure than the Haigh-Lode-Westergaard coordinates give*
* *Using just TM or CM test data incorporates a bottleneck concerning a reliable physical fracture body*
* *Fracture initiation in solid mechanics is given, if the stress vector touches the surface of the fracture body which represents the surface of all failure 1D-, 2D- and 3D-failure stress vectors.*
* *The fracture body surface is defined by a material stressing effort Eff = 100% = 1.*
* *Reliable mapping requires an approach which shall be physically-based and 'practical'. Such an approach should equally well map (1) the course of test data fixing the 3D fracture body, (2) the course of test data in the Principal Stress plane (bias 2D cross-section of the 3D fracture body), and (3) of the test data course along the two 3D-test meridians TM and CM.*
* *All theoretical approaches have their applicability limits and the very difficult 3D-testing as well.*
* *Of course, general 3D-failure stress states may not lie on TM (30°) or CM (-30°) but on another Lode angle around the hoop.*
* *The fracture body of a dense isotropic material has an open bottom fracture surface!*
* *The fracture planes of TM and CM are different.*
* *Both, the different course of the test data points compared to the also incorporated ellipse in the principal stress plane and the difference of the TM and the CM-curve document the inherent 120°-rotational symmetry of isotropic materials.(360°/3= 120° is given, because all 3 principal stresses are of equal mechanical importance, see Fig.14-9.*

*25.3 **Rock Material***, example Sandstone

AS for concrete the properties for Underground Rock Failure Stress Analysis are also provided by tests on the tensile and the compressive meridian.

Tensile domain:
Also in rock materials in the vicinity of excavations and boreholes tensile stresses will occur. Further, an undesirable brittle sudden failure is to prevent when a bore-hole is drilled. Therefore, a tensile strength proof requires a tensile strength $\bar{R}^t$ for the distinct rock material.
An estimation for the tensile strength value delivers the Brazilian splitting test (*indirect* tensile strength test) because a classical tensile test specimen is merely to obtain. A solid cylinder or disk (short cylinder) test specimens is used for the initially crack-free (intact) material, see *Fig.26-7.* The evaluation is performed via the formula $f_{sp} = \bar{R}^t = 2 \cdot q / (\pi \cdot d \cdot \ell)$ [*The constructor.or*g].

This 'indirect' measurement caused researchers to predict a value by using a Mohr-Coulomb-based SFC but the determined value is doubtful. In this context the author fully supports Mingqing You [*You15*] that a tensile strength R^t is a separate parameter and cannot be estimated by models working in the tensile-compressive transition zone. A real value for $\bar{R}^t$ is only to obtain by a uniaxial tensile stress test $\{\sigma\} = (\sigma^t_{ax} = F^t / A,\ 0,\ 0)^T$

Compressive domain:
Usual test series for concrete material (*see the concrete applications before)* are performed along the compressive meridian and not so often along the tensile meridian. For the general demonstration of the strength capacity, however, the full fracture failure body is required because all mixed 3D-compressive stress states are principally possible and to determine the surface of the fracture body. In rock mechanics the stress situation is linked to stress states along the compressive meridian. This explains why no bi-axial strength $\bar{R}^{cc}$ is provided in rock literature an entity that enables to

describe the 120°-symmetry. Mapping just the course of test data along a meridian simplifies the task: Just the functional description of the test meridian remains of interest.

A stress state in a material, formulated in Mohr's *mathematical* stresses, reads

$\{\sigma\} = (\sigma_I , \sigma_{II} , \sigma_{III})^T$ with σ_I becoming the smallest failure stress (most positive)

$\sigma_I > \sigma_{II} > \sigma_{III}$ mathematically and σ_{III} the largest compressive failure stress (most negative).

Tensile stresses must be signed positive in this context, otherwise confusion becomes extreme!

For the tensile meridian follows $\{\sigma\} = (\sigma_I , \sigma_{II} , \sigma_{III} = \sigma_{II})^T$ with $\sigma_I = \sigma^t_{ax} - p_{hyd}$

and the compressive meridian $\{\sigma\} = (\sigma_I = \sigma_{II} , \sigma_{II} , \sigma_{III})^T$ with $\sigma_{III} = \sigma^c_{ax} - p_{hyd}$.

The tensile meridian captures $\bar{R}^{cc}$ (and $\bar{R}^t$, in the domain of the Normal Fracture mode) and the compressive meridian captures $\bar{R}^c$ (and $\bar{R}^{tt}$, in the domain of the Normal Fracture mode).

In rock mechanics, a part of civil engineering, hydrostatic pressure is used, when testing concrete and UD material, but is to replace by the so-called Confining Pressure CP. This makes to introduce some definitions of rock mechanics terms: *Here, tensile stress is usually still negative, but not always. This makes literature interpretations difficult!*

- Multi-axial rock compressive strength capacity [*You15*]
  (the stress-sketch in Figure 1 of [Lan19] must be corrected. It does not fit to the provided failure stress states. In Fig.26-7 this is corrected)
  $\sigma_{III} \equiv \sigma_S \equiv \sigma_1$ termed here min or principal stress
- 1D uniaxial strengths: UTS $= \bar{R}^t$, UCS $= \bar{R}^c$
  Unfortunately the author found different meanings: In engineering design dimensioning UTS means Ultimate Tensile Strength and not Uniaxial Tensile Strength and UCS ultimate compressive strength *(still also applied in 'geo engineer'! Why is it not* ***generally*** *used in rock mechanics?)* and not for instance Unconfirmed Compressive Strength [*Wikipedia*]. UCS stands for the maximum axial compressive stress that a specimen can bear under zero Confining Pressure (*compressive stress*), which means it is nothing else than the usual simple standardized technical compression strength $\bar{R}^c$ in engineering.
- ✓ Confining pressure CP: maximum level of hydrostatic compression applied in a tri-axial compression test of a concrete, a rock material or a neat resin test specimen defined by
  $\{\sigma\} = (\sigma_{ax}{}^t$ - CP , -CP, -CP) or with $\sigma_{ax}{}^c$ (tensile meridian)
  $\{\sigma\} = (\sigma_{ax}{}^c$ - CP , -CP,, -CP) (*induced by test rig brushes in case of concrete*)
- ✓ Confining lithostatic pressure: CP = p_{hyd} + overlying weight.

The author would like to conclude: *using usual mathematical stresses and taking a look at Fig.25-16*

- Sealed, polished dog-bone test specimens deliver the failure stress points
  ($-\bar{R}^{ccc}, -\bar{R}^{ccc}, -\bar{R}^{ccc}$) no pore pressure, ($-\bar{R}^c$, 0, 0) , ($\bar{R}^t$, 0, 0) and
  further multi-axial compressive failure stresses on the compressive meridian.
- A bi-axial compressive failure stress ($-\bar{R}^{cc}$,-, 0) is obtainable by the dog-bone test specimen for $\sigma_1 = 0$ or $\sigma_{ax}{}^t = -CP$. However, the author did not find one single bi-axial strength value $\bar{R}^{cc}$ in the papers he examined!
  However, the UHPC fracture stress data set, thankfully left by IFM Dresden, brought a

statistically good base which should have a similar tendency as rock material

- A bi-axial tensile failure stress $(\bar{R}^{tt}, \bar{R}^{tt}, 0)$ can be obtained by cube test specimens prepared by a good gluing in order to load the needed bi-axial tensile stresses.

Test procedure: The confining pressure CP is achieved and then kept constant during the test. The axial stress σ_1 is increased at a certain rate until the test specimen fails at $\max\sigma_1$. It is to consider whether the porosity of the rock or the soil material and the saturation plays a role.

Fig.26-7 presents fracture pictures of the investigated Berea sandstone. Essential is that the fracture angle increases with CP.

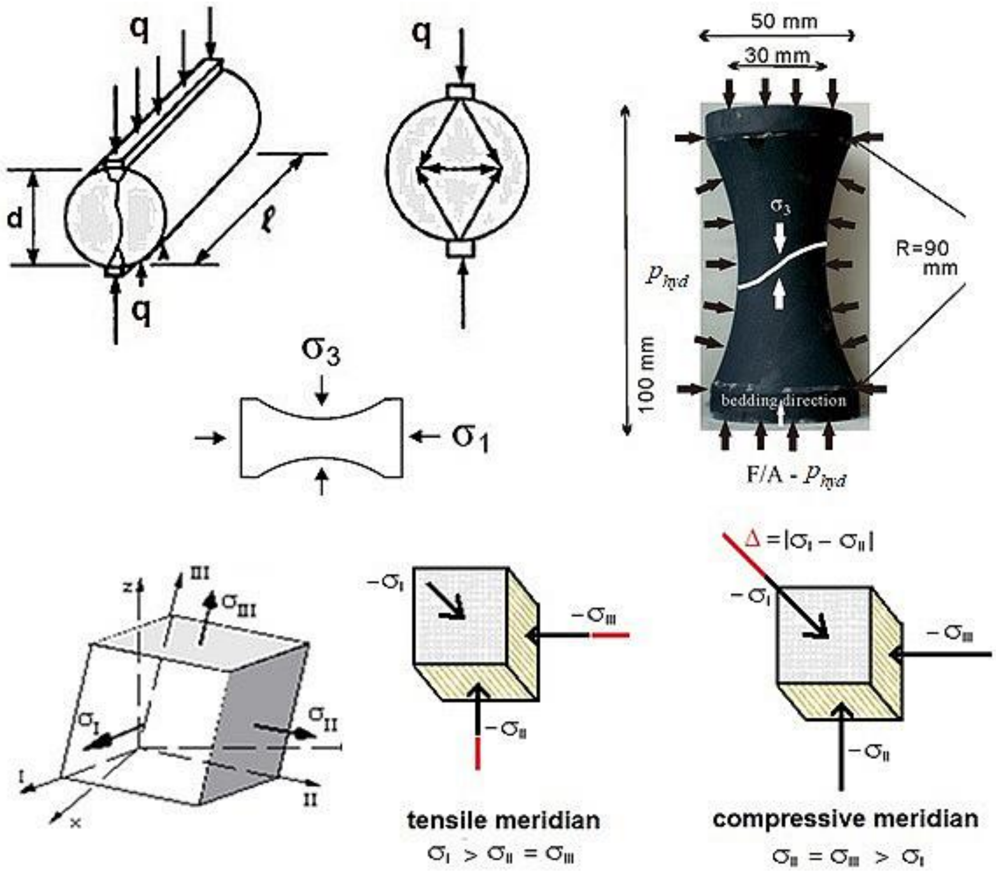

Fig. 26-7: Brazilian cylinder or disk (short length) for an indirect estimation of $\bar{R}^t$ and dog-bone (sealed, highest preparation effort, grinding from solid block with axial bedding layers) test specimen for direct measurement of tri-axial fracture stress states along compressive meridian including the tension-compression domain.
(Δ depicts the differential stress entity causing shear stress with shear deformation)

Similarly to other brittle materials the task always is the full (onset-of-)fracture body surface capturing NF and SF and not just $I_1 < 0$ and thereby regarding the intrinsic 120°-rotational symmetry. The TM and CM test data points are two oppositely located cross-sections of the body. The classical type of visualization is to use the Haigh-Lode-Westergaard coordinates (see *Fig.24-13 bottom*) which count equally in all directions. A visualization by using a confining stress cannot lead to the same mapping curve (see Fig. 26.6).

LL: *The interpretation of the concrete-diagrams above leads to the following results:*

- *Using just TM or just CM test data incorporates a bottleneck concerning the achievement of a reliable physical fracture body*
- *The use of the geo-Mohr-Coulomb Criterion leads to a straight mapping of the course of test data along the tensile meridian. The model of the author captures the curved course*
- *Engineers in other disciplines become pretty stressed because we civil engineers unfortunately use construction design tools which still call tensile stresses negative stresses. This completely disturbs the logic of the well-known 'civil engineer' A. Mohr in context with his use of mathematical stresses!*

Fig.26-8, Sandstone: Fracture pictures of Berea sandstone from [Lan19].

A dramatic situation, depicted in the figure below, led to my most dangerous car trip, on gravel roads, along gorges up to 1000 m deep, from the Central Himalaya down to the plain and back up into the high mountains. AND, this with just <u>one</u> driver from 7 until 23 o'clock.

Personal experience with a dangerous shear strength value and an associated critical sliding angle, leading to a land slide at the West-East Main road of Bhutan.
A video clip taken by me would show how huge rocks were 'travelling' down.

27 UD-Strength Failure criteria: Which one should I take?

Aim: *Assisting the user not to follow the FE Manual recommendation "Take the worst result of all".*

In the future, we will be forced to compute 3D-based reserve factors in static component Design Verification. The 2D-based Classical Laminate Theory for unidirectional fiber-reinforced matrices is not sufficient for this. For these reasons, the author has tried to compare those SFCs that were 'contributing' to the World Wide Failure Exercises (WWFE) for UD materials, namely Tsai-Wu, Hashin, Puck and Cuntze. The comparison carried out (*generally too little test data is available*) looks at the necessary input, shows the received failure envelopes for three 2D stress combinations and tries to evaluate the results, so that FE Manual recommendations "*Take the worst result of all*" is not to be followed anymore!

Regarding the chapters before, the SFCs of Hashin and Tsai-Wu will be presented, only, and some missing things of Puck's SFC.

27.1 SFC Hashin

* Hypothesis 2, valid for Cuntze's FMC-bases SFC-formulations:

"*For UD-material the SFCs should be invariant under any rotation around the fiber direction*."

Hashin with the Hypothesis 2 also proposed an invariant-based global quadratic approach with two different stress invariants:

$$I_1 = \sigma_1,\ I_2 = \sigma_2 + \sigma_3,\ I_3 = \tau_{31}{}^2 + \tau_{21}{}^2,\ I_4 = \tau_{23}{}^2 - \sigma_2 \cdot \sigma_3,\ I_5 = 4\tau_{23}\tau_{31}\tau_{21} - \sigma_2 \cdot \tau_{31}{}^2 - \sigma_3 \cdot \tau_{21}{}^2).$$

Table 27-1 compiles the four SFCs of Zvi Hashin.

Table 27-1: Four SFCs, for FF1, FF2, IFF1 and IFF2

$\{\sigma\} = (\sigma_1, \sigma_2, \sigma_3, \tau_{23}, \tau_{31}, \tau_{21})^{\mathrm{T}}$, $\{\bar{R}\} = (\bar{R}_{\parallel}^t, \bar{R}_{\parallel}^c, \bar{R}_{\perp}^t, \bar{R}_{\perp}^c, \bar{R}_{\perp\parallel};\ \bar{R}_{23})^{\mathrm{T}}$; 6 strengths, principally
Interaction of the 4 modes necessary.
Hypothesis 1: $F\left(\{\sigma^A\}, \{\bar{R}^A\}, \theta_{\mathrm{fp}}\right) = 1$, Puck's way
Hypothesis 2: $F\left(\{\sigma\}, \{\bar{R}\}\right) = 1$, Cuntze's way, *below*
FF1, $\sigma_1 > 0: \left(\frac{\sigma_1}{\bar{R}_{\parallel}^t}\right)^2 + \frac{\tau_{31}^2 + \tau_{21}^2}{\bar{R}_{\perp\parallel}{}^2}$; FF2, $\sigma_1 < 0: \left(\frac{-\sigma_1}{\bar{R}_{\parallel}^c}\right)^2 = 1$,
IFF1, $\sigma_2 + \sigma_3 > 0: \frac{(\sigma_2 + \sigma_3)^2}{\bar{R}_{\perp}^t} + \frac{(\tau_{23}{}^2 - \sigma_2 \cdot \sigma_3)}{\bar{R}_{23}{}^2} + \frac{(\tau_{31}^2 + \tau_{21}^2)}{\bar{R}_{\perp\parallel}{}^2} = 1$,
IFF2, $\sigma_2 + \sigma_3 < 0: \left(\frac{\bar{R}_{\perp}^{c\,2}}{4 \cdot \bar{R}_{23}{}^2} - 1\right) \cdot \frac{(\sigma_2 + \sigma_3)}{\bar{R}_{\perp}^c} + \frac{(\sigma_2 + \sigma_3)^2}{4 \cdot \bar{R}_{23}{}^2} + \frac{(\tau_{23}{}^2 - \sigma_2 \cdot \sigma_3)}{\bar{R}_{23}{}^2} + \frac{(\tau_{31}^2 + \tau_{21}^2)}{\bar{R}_{\perp\parallel}{}^2} = 1$,
Interlaminar failure: $\sigma_3 > 0: \left(\frac{\sigma_3}{R_3^t}\right)^2 = 1$; $\sigma_3 < 0: \left(\frac{-\sigma_3}{R_3^c}\right)^2 = 1$.

* Hypothesis 1, valid for Puck's Action Plane IFF formulation:

"In the event that a failure plane under a distinct fracture angle can be identified, the failure is produced by the normal and shear stresses on that plane".

Hashin proposed this modified Mohr-Coulomb IFF approach but did not pursue this idea due to numerical difficulties (*A. Puck succeeded on this way*).

Question: What about the determination of $\bar{R}_{23} \neq \bar{R}^{\tau}_{23}$? *See Technical Terms, please.*

27.2 SFC Tsai-Wu, global SFC

A general anisotropic tensor polynomial expression of Zakharov and Goldenblat-Kopnov with the parameters F_i, F_{ij} as strength model parameters was the basis of the Tsai-Wu SFC $\sum_{i=1}^{6}(F_i \cdot \sigma_i) + \sum_{j=1}^{6}\sum_{i=1}^{6}(F_{ij} \cdot \sigma_i \cdot \sigma_j) = 1$. From this tensor formulation, Tsai-Wu used the linear and quadratic terms, see *Table 27-2*:

Table 27-2: 3D SFCs of Tsai-Wu

$\{\sigma\} = (\sigma_1, \sigma_2, \sigma_3, \tau_{23}, \tau_{31}, \tau_{21})^{\mathrm{T}}$, $\{\bar{R}\} = (\bar{R}^t_{\parallel}, \bar{R}^c_{\parallel}, \bar{R}^t_{\perp}, \bar{R}^c_{\perp}, \bar{R}_{\perp\parallel};\ \bar{R}_{23})^{\mathrm{T}}$, 6 strengths

$$F(\{\sigma\},\{\bar{R}\}) = 1. \ \textit{The interaction is global SFC} - \textit{inert}$$

$$F_i \cdot \sigma_i + F_{ij} \cdot \sigma_i \cdot \sigma_j = 1 \quad \text{with} \quad (\text{i,j} = 1,2..6) \quad \text{or executed}$$

$$F_{11} \cdot \sigma_1^2 + F_1 \cdot \sigma_1 + 2F_{12} \cdot \sigma_1 \cdot \sigma_2 + 2F_{13} \cdot \sigma_1 \cdot \sigma_3 + F_{22} \cdot \sigma_2^2 + F_2 \cdot \sigma_2 +$$
$$+ 2F_{23} \cdot \sigma_2 \cdot \sigma_3 + F_{33} \cdot \sigma_3^2 + F_{33} \cdot \sigma_3^2 + F_3 \cdot \sigma_3 + F_{44} \cdot \tau_{23}^2 + F_{55} \cdot \tau_{13}^2 + F_{66} \cdot \tau_{12}^2 = 1$$

with the strength model parameters

$$F_1 = 1/\bar{R}^t_{\parallel} - 1/\bar{R}^c_{\parallel},\ F_{11} = 1/(\bar{R}^t_{\parallel} \cdot \bar{R}^c_{\parallel}),\ F_2 = 1/\bar{R}^t_{\perp} - 1/\bar{R}^c_{\perp},\ F_{22} = 1/(\bar{R}_{\perp} \cdot \bar{R}^c_{\perp}) = F_{33},$$

$$F_{13} = F_{12},\ F_{55} = F_{66} = 1/\bar{R}^2_{\perp\parallel},\ 2F_{23} = 2F_{22} - 1/\bar{R}^2_{23},\ F_{44} = 2 \cdot (F_{22} + F_{23})$$

and - *in order to avoid an open failure surface* - the so-called interaction term

$$F_{12} = \bar{F}_{12} \cdot \sqrt{F_{11} \cdot F_{22}} \quad \text{with} \quad -1 \leq \bar{F}_{12} \leq 1; \quad \text{usually applied } F_{12} = -0.5.$$

Question, again: What about the determination of $\bar{R}_{23}$ and the value for F_{12} for 3D applications?

27.3 SFC Puck

Some history:

**As early as 1969 A. Puck recognized to separate FF from IFF (not Hashin as is sometimes said). Since the mid-eighties Puck from Uni Kassel, Cuntze from MAN and colleagues of the DLR-Braunschweig looked together for an improved IFF-SFC.*

* *H. Schuermann, Uni Darmstadt, found the article [Has80] with the Hashin Hypothesis 1 which Puck could successfully execute. Cuntze recommended to use the matrix formulation to mathematically simpler convince the reader, which was more successful than his excellently written model description.*

* *Beside several dissertation works, Puck's IFF model was further developed in a founded research project 1994. Results were published in VDI Progress Reports Series 5 Vol.506, VDI-Verlag, Düsseldorf, 1997, [VDI97]. The investigations for this book gave valuable results for Puck's book, 1996.*

* *Due to the still highly established Puck IFF model Cuntze invited Puck to put his SFC into the [VDI 2014]*

German Guideline, Sheet 3, Development of Fibre-Reinforced Plastic Components, Analysis.

Puck's so-called Action Plane IFF Conditions (1991) base on Mohr-Coulomb and Hashin.

In his interaction approach for the 3 IFF modes Puck interacted the 3 Mohr stresses σ_n, τ_{nt}, τ_{n1} on the IFF fracture plane, see *Fig.27-4*. He uses parabolic or elliptic polynomials to formulate a so-called master fracture body in the (σ_n, τ_{nt}, τ_{n1}) space. Thereby he assumes that a compressive σ_n cannot cause fracture on its action plane and that the stress σ_1 does not have any influence on the angle of the IFF fracture plane. The stresses on the fracture plane are decisive for fracture: A tensile stress σ_n supports the fracture, while in contrast a compressive stress makes the material 'stronger'. In other words: A compressive σ_n impedes IFF which is caused by the action plane shear stresses τ_{nt} and τ_{n1}, or – in other words - cannot cause fracture on its action plane. Fracture-responsible are only those stresses which act on a common action plane.

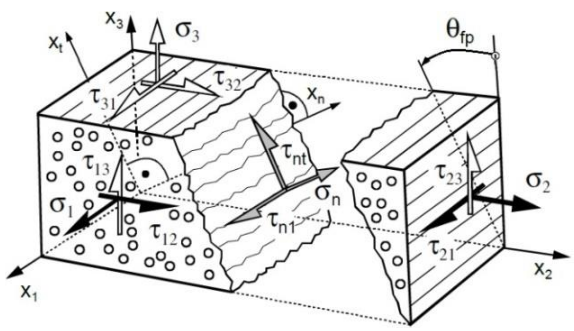

Fig.27-4, UD-composite element: Lamina and action plane stresses at an inclined failure angle θ_{fp} (from [Lut05, SAMPE])

Fig.27-5 presents Puck's 3 IFF modes: mode A (= IFF1), mode B (≡ IFF3), mode C (≡ IFF2. The modes A and B lead to transversal fracture planes with $\theta_{fp} = 0$, whereas in mode C inclined planes occur O°< θ_{fp} < 55° (for CFRP). The determination of the unknown IFF action plane angle θ_{fp} is

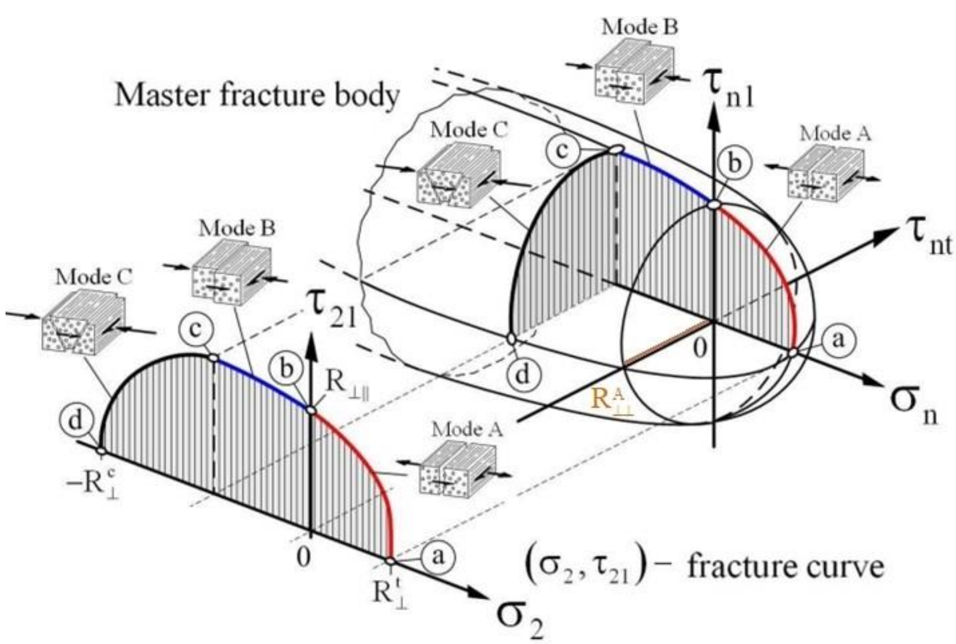

Fig.27-5: Master fracture body with Puck's IFF modes and action plane stresses (σ_n, τ_{nt}, τ_{n1}). *(left) Lamina stresses and main IFF cross section of the fracture body in lamina stresses* (σ_2, τ_{21}) *[courtesy H. Schürmann]*

performed by a search process in the domain -90°< θ_{fp} < 90. For the in-plane stress state $\tau_{21}(\sigma_2)$ which is dominant in many structural components, Puck found an analytic solution for the angle of the fracture plane [*Puc02*]: $\cos\theta_{\mathrm{fp}} = \sqrt{\frac{1}{2+2\cdot p^c_{\perp\perp}}\cdot\left[\left(\frac{\bar{R}^A_{23}}{\bar{R}_{\perp\|}}\right)^2\cdot\left(\frac{\tau_{21}}{\sigma_2}\right)^2+1\right]}$.

In *Table 27-3* Puck's Action Plane Mohr-Coulomb-linked (global) IFF SFCs discriminate 3 IFF domains and are completed by the simple maximum stress modes FF1 and FF2. Two IFF fracture plane resistances (superscript ^{A}) directly are technical strengths.

Table 27-3: SFCs for FF1, FF2, IFF1, IFF2 and IFF3

$\{\sigma\} = (\sigma_1,\sigma_2,\sigma_3,\tau_{23},\tau_{31},\tau_{21})^{\mathrm{T}}$, $\{\bar{R}\} = (\bar{R}^t_\|,\bar{R}^c_\|,\bar{R}^t_\perp,\bar{R}^c_\perp,\bar{R}_{\perp\|};\ \bar{R}^A_{23})^{\mathrm{T}}$, 6 strengths, principally

In Mohr's action plane stresses the IFF-SFC reads $F\left(\sigma_n,\tau_n,\bar{R}_\sigma,\bar{R}_\tau,\theta_{\mathrm{fp}}\right)=1$,

$F\left(\{\sigma^A\},\{\bar{R}^A\},\theta_{\mathrm{fp}}\right)=1$ with $\{\bar{R}\} = (\bar{R}^t_\|,\bar{R}^c_\|,\bar{R}^A_\perp=\bar{R}^t_\perp,\bar{R}^A_{23},\bar{R}^A_{\perp\|}=\bar{R}_{\perp\|})^{\mathrm{T}};\ Puck:\bar{R}^A_{23}\neq\bar{R}_{23}!$

$$\text{FF1},\ \sigma_1>0:\ \left(\frac{\sigma_1}{\bar{R}^t_\|}\right)^2;\qquad \text{FF2},\ \sigma_1<0:\ \left(\frac{-\sigma_1}{\bar{R}^c_\|}\right)^2=1,\quad \text{(maximum stress criteria)}$$

and due to the IFF hypotheses, two different eqations are provided [*Puc* 96, *p*.118]

$$\text{IFF:}\quad \sigma_n>0:\ \varepsilon=\left(\frac{\tau_{nt}}{\bar{R}^A_{23}}\right)^2+\left(\frac{\tau_{n\ell}}{\bar{R}^A_{\perp\|}}\right)^2+\left(\frac{\sigma_n}{\bar{R}^A_\perp}\right)=1,\quad \tau_n=\sqrt{\tau_{nt}{}^2+\tau_{n1}{}^2}$$

$$\text{IFF:}\quad \sigma_n<0:\ \varepsilon=\left(\frac{\tau_{nt}}{\bar{R}^A_{23}-p_{\perp\perp}{}^{c}\cdot\sigma_n}\right)^2+\left(\frac{\tau_{n\ell}}{\bar{R}^A_{\perp\|}-p_{\perp\|}{}^{c}\cdot\sigma_n}\right)^2=1,\quad [Puc96,\ p.143]$$

$\Rightarrow$ from originally assumed 6 material strengths down to 5 action plane resistancies which capture all 3 sub-modes IFF1, IFF2 and IFF3.

The following transfer relationship is to apply above ($_{fp}$ = failure plane)

$$\begin{Bmatrix}\sigma_n(\theta_{fp})\\ \tau_n(\theta_{fp})\\ \tau_{n\ell}(\theta_{fp})\end{Bmatrix}=\begin{bmatrix}c^2 & s^2 & 2sc & 0 & 0\\ -sc & sc & c^2-s^2 & 0 & 0\\ 0 & 0 & 0 & s & c\end{bmatrix}\cdot\begin{Bmatrix}\sigma_2\\ \sigma_3\\ \tau_{23}\\ \tau_{31}\\ \tau_{21}\end{Bmatrix},\quad c=\cos\theta_{fp}\ \text{and}\ s=\sin\theta_{fp}.$$

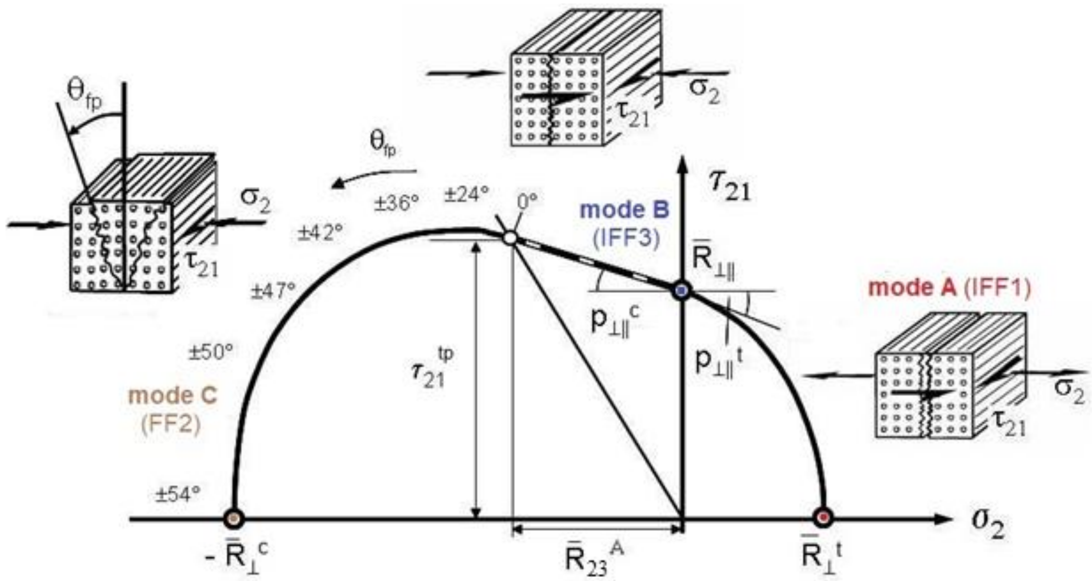

Fig. 27-6: Fracture modes of the (σ_2, τ_{21})-failure envelope; index ^{tp} marks the touchpoint between mode B and C, [Lut13, Puc96]

*Table 27-4: 2D-IFF [VDI2014***]**

Mode A (= IFF1) : $\varepsilon = \frac{1}{\bar{R}_{\perp\|}} \cdot \sqrt{\left(\frac{\bar{R}_{\perp\|}}{\bar{R}_{\perp}^{t}} - p_{\perp\|}^{t}\right)^2 \cdot \sigma_2{}^2 + \tau_{21}^2} + p_{\perp\|}^{t} \cdot \sigma_2;$

Mode B (≅ IFF3) : $\varepsilon = \frac{1}{\bar{R}_{\perp\|}} \cdot \sqrt{p_{\perp\|}^{c\ 2} \cdot \sigma_2{}^2 + \tau_{21}^2} + p_{\perp\|}^{c} \cdot \sigma_2;$

Mode C (≅ IFF2) : $\varepsilon = \frac{\tau_{21}^2}{4 \cdot \left(\bar{R}_{\perp\|} + p_{\perp\|}^{c} \cdot \bar{R}_{23}^{A}\right)^2} \cdot \frac{\bar{R}_{\perp}^{c}}{-\sigma_2} + \frac{-\sigma_2}{\bar{R}_{\perp}^{c}}$

ε is also termed f_{E} $[Lut05,\ VDI2014]$

$$\tau_{21}^{\mathrm{tp}} = \bar{R}_{\perp\|} \cdot \sqrt{1 + 2 \cdot p_{23}^{c}}, \quad \sigma_2^{\mathrm{tp}} = -\bar{R}_{23}^{A}\ , \quad \bar{R}_{23}^{A} = \left[\bar{R}_{\perp\|} \cdot \sqrt{1 + 2 \cdot p_{\perp\|}^{c} \cdot \bar{R}_{\perp}^{c} / \bar{R}_{\perp\|}} - 1\right] / 2 \cdot p_{\perp\|}^{c},$$

* The action plane resistance $\bar{R}_{23}^{A}$ depends on the chosen fracture body model such as the parabolic Mohr envelope and not just the linear Mohr approach.

* Assumption on coupling the inclination parameters: $p_{23}^{c} = p_{\perp\|}^{c} \cdot \bar{R}_{23}^{A} / \bar{R}_{\perp\|}$.

R_{23}^{A} is found in the horizontal cross-section of Puck's Master failure body. It is a IFF-Mohr model-linked quantity and consequently a given model strength parameter and not a technical strength. It finally did vanish therefore as a measurable technical strength. Puck's R_{23}^{A} is a model parameter and defined by Puck's Mohr-Model using two strength and the so-called inclination parameters *p*, depicted in Fig.6.

Practically, 5 independent failure activing stresses are left, which would support Cuntze's material symmetry-based 'generic' number of 5 he elaborated for UD materials.

Of course, an interaction of IFF with the two FF modes is also with Puck mandatory in order to capture the combined (joint) failure danger. This procedure is documented in detail in the VDI 2014, sheet 3. One reason to do that is that experiments demonstrate micro-damage activation at the ends of broken filaments. Puck terms this 'weakening of the matrix' and uses a so-called weakening factor. Applying Cuntze's interaction equation *Eff* = 1 this is automatically performed in the foreseen comparison.

27.4 Comparison of the obtained different SFC Failure Envelopes

In consequence of the rare test data sets just 2D-models of Tsai-Wu, Hashin, Puck and Cuntze could be numerically investigated.

A comparison is only possible if the interaction can be equally performed for each model and the same interaction. This could be realized for the 4 models by a transfer to the single 2D-*Eff*-formulation, example Tsai-Wu:

$$\frac{\sigma_1{}^2/Eff^2}{\bar{R}_{||}{}^t\cdot\bar{R}_{||}{}^c}+\frac{\sigma_1}{Eff}\cdot\left(\frac{1}{\bar{R}_{||}{}^t}-\frac{1}{\bar{R}_{||}{}^c}\right)+\frac{2F_{12}\cdot\sigma_1\cdot\sigma_2/Eff^2}{\sqrt{\bar{R}_{||}{}^t\cdot\bar{R}_{||}{}^c\cdot\bar{R}_{\perp}{}^t\cdot\bar{R}_{\perp}{}^c}}+\frac{\sigma_2{}^2/Eff^2}{\bar{R}_{\perp}{}^t\cdot\bar{R}_{\perp}{}^c}+\frac{\sigma_2}{Eff}\cdot\left(\frac{1}{\bar{R}_{\perp}{}^t}-\frac{1}{\bar{R}_{\perp}{}^c}\right)+\frac{\tau_{12}^2/Eff^2}{\bar{R}_{\perp||}}=1$$

The investigation focuses mapping of the curves of test data by SFCs. In these formulations each single strength is an average strength consequently indicated by a bar over.

The following figures present the failure envelopes of investigated three plane stress combinations.

SFC Failure Envelopes

Fig.27-6 visualizes, how the four models map the most interesting cross-section of the UD fracture body, namely $\tau_{21}(\sigma_2)$.

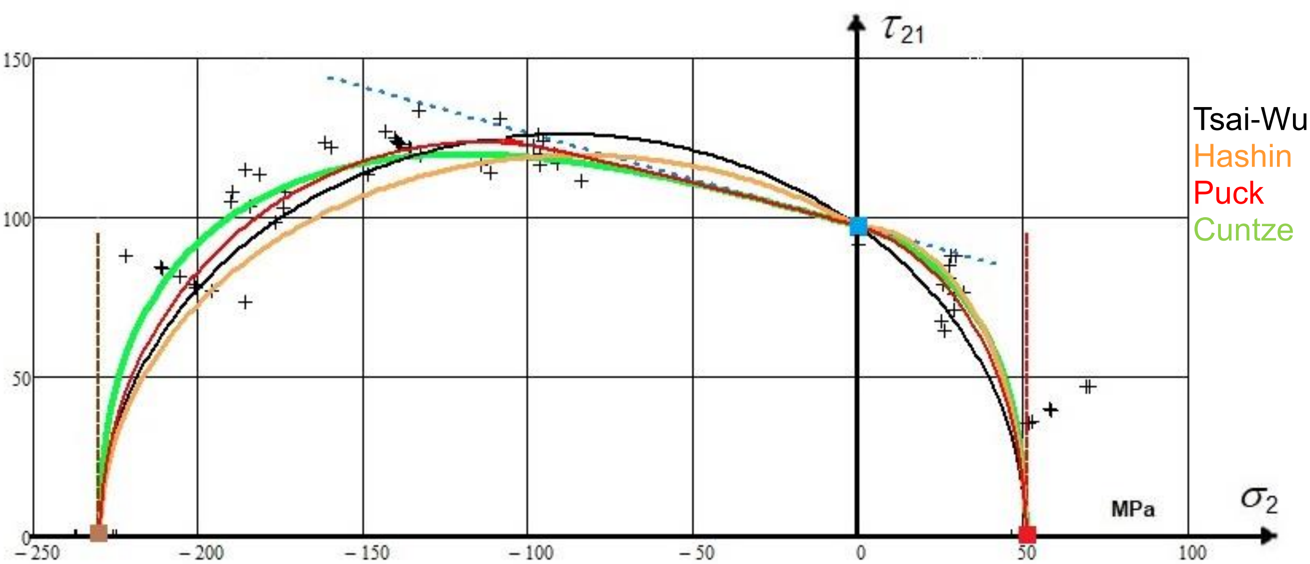

Fig. 27-6: CFRP test results (MAN Technologie research project with A. Puck, IKV Aachen et al.)
$\{\bar{R}\} = (1280,\ 800,\ 51,\ 230,\ 97)^T$ MPa, $\mu_{\perp||} = 0.3$ [*VDI 97*]

Fig.27-7 depicts the failure envelope σ2(σ1), being the WWFE Test Case 3. In this test case below, just the 4 strength values were provided together with the not $R_{\perp}^{c}$ -matching test data of a Russian test data provider showing a test discrepancy (*passed away, no request possible*) in the fourth quadrant of *Fig.27-7*. However, the tendency of the two different (*assumed*) test sets can be carefully used for validation.
The global Tsai-Wu SFC lies fully outside, which would be of high effect for stability analysis. The test data set in the quadrant III was provided by M.. Knops, IKV Aachen, [*Kno03*].
Mapping tells, that modal modelling is the better choice.

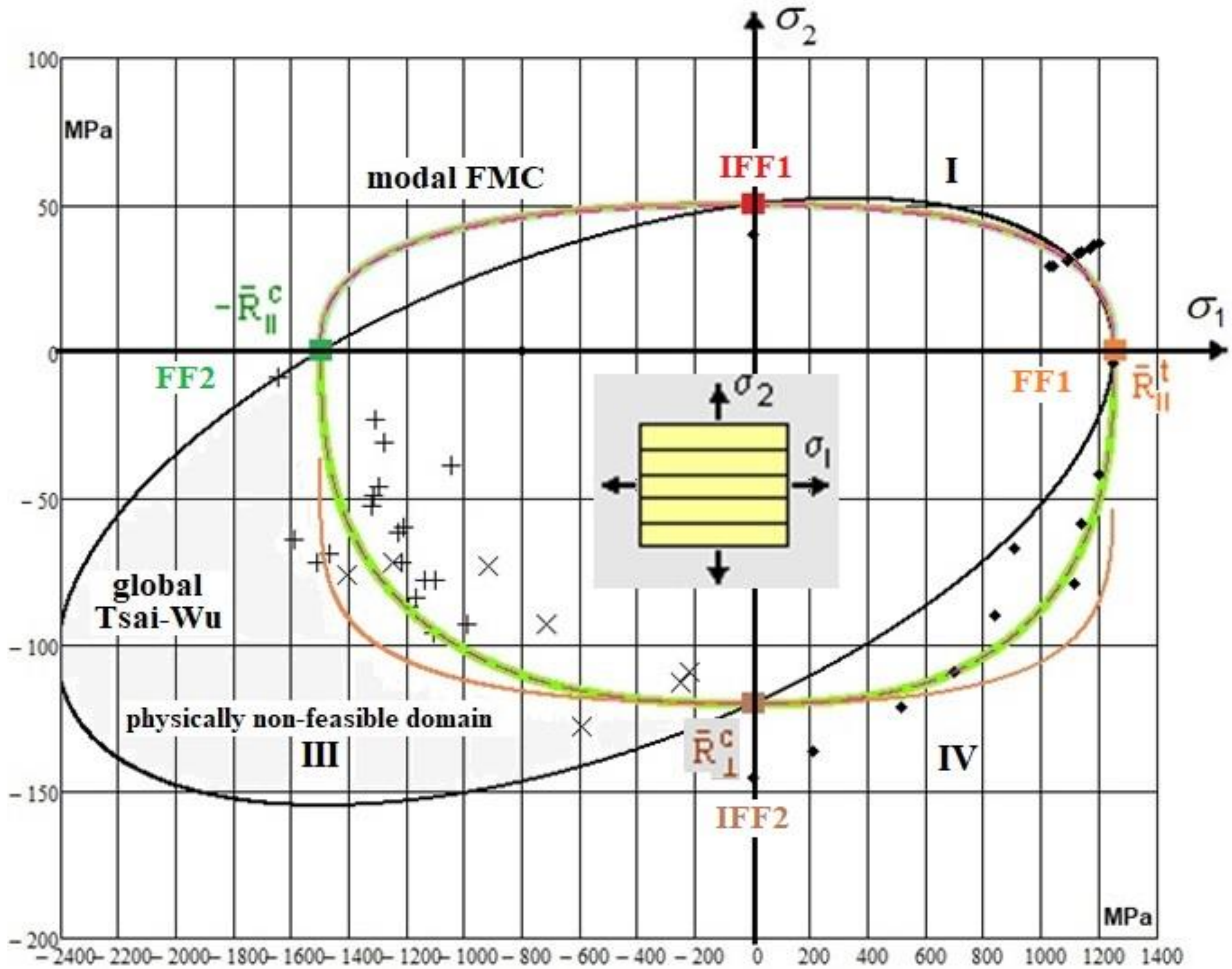

Fig.27-7, WWFE-I, TC3: Hoop wound tube lamina. E-glass/MY750 Ep.

$$\{\bar{R}\} = (1280,\ 800,\ 51,\ 230,\ 97)^T$$

In order to be able to generate above different envelopes the author had to harmonize terminology and to make them to apply his interaction formula for the modal SFC ones.

This limited the amount of further numerical comparisons. τ21(σ1) could be investigated.

From *Fig.27-8* can be concluded that the envelope of Puck and Cuntze lie upon another. Modal Hashin and Global Tsai-Wu are lying inside.

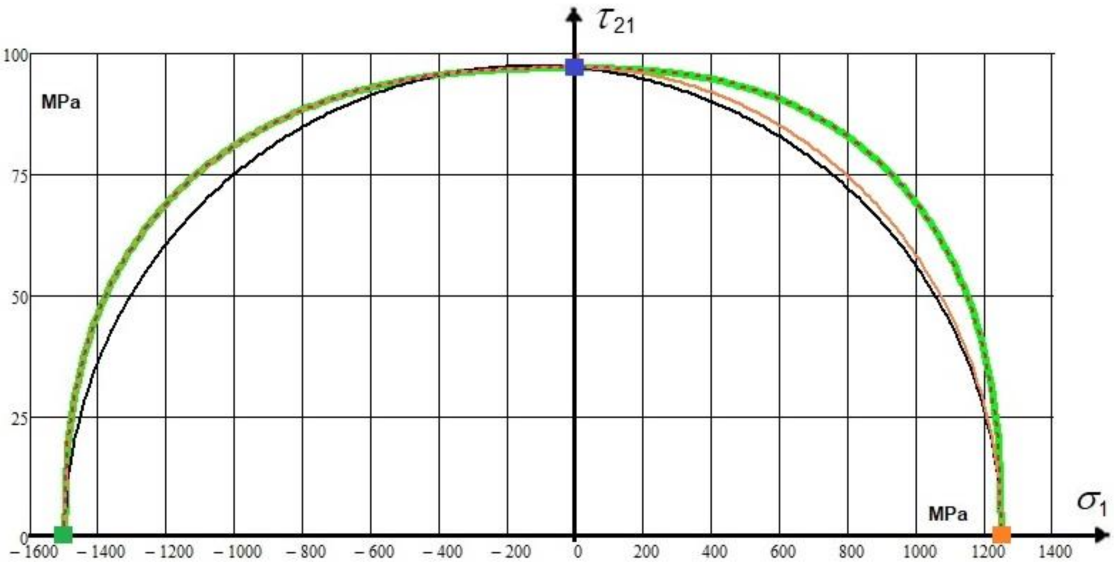

Fig.27-8: $\{\bar{R}\} = (1280,\ 800,\ 51,\ 230,\ 97)^T$

27.5 Computation of a SFC-linked Reserve Factor

Principally, in order to avoid either to be too conservative or too un-conservative, a separation is required of the always needed 'analysis of the average structural behavior' in Design Dimensioning (*using average properties and average stress-strain curves*) in order to obtain optimum structural information (= 50% expectation value) from the mandatory single Design Verification analysis of the final design, where statistically minimum values for strength and minimum, mean or maximum values for the task-demanded other properties are applied as Design Values. There it is to demonstrate that '*A relevant Limit State is not met yet'*.

A very simple example of the Design Verification of a critical UD lamina in a distinct wall design shall depict the *RF*-calculation procedure: BeispielCHECK

Asssumption: Linear analysis permitted, design FoS $j_{\text{ult}} = 1.25$

* Design loading (action): $\{\sigma\}_{\text{design}} = \{\sigma\} \cdot j_{\text{ult}}$

* 2D-stress state: $\{\sigma\}_{\text{design}} = (\sigma_1, \sigma_2, \sigma_3, \tau_{23}, \tau_{31}, \tau_{21})^T \cdot j_{\text{ult}} = (0,\ -76,\ 0,\ 0,\ 0,\ 52)^T$ MPa

* Residual stresses: 0 $\left(\textit{effect vanishes with increasing micro-cracking}\right)$

* Strengths (resistance) : $\{\bar{R}\} = (1378,\ 950,\ 40,\ 125,\ 97)^T$ MPa average from mesurement

statistically reduced $\{R\} = (R_{||}^t, R_{||}^c, R_{\perp}^t, R_{\perp}^c, R_{\perp||})^T = (1050,\ 725,\ 32,\ 112,\ 79)^T$ MPa

* Friction value(s) : $\mu_{\perp||} = 0.3,\ (\mu_{\perp\perp} = 0.35)$, Mode interaction exponent: $m = 2.7$

$$\{Eff^{\text{mode}}\} = \left(Eff^{||\sigma},\ Eff^{||\tau},\ Eff^{\perp\sigma},\ Eff^{\perp\tau},\ Eff^{\perp||}\right)^T = \left(0.88,\ 0,\ 0,\ 0.21,\ 0.20\right)^T$$

$$Eff^{\,m} = (Eff^{||\sigma})^m + (Eff^{||\tau})^m + (Eff^{\perp\sigma})^m + (Eff^{\perp\tau})^m + (Eff^{\perp||})^m = 100\%\ .$$

The results above deliver the following material reserve factor $f_{\text{RF}} = 1/Eff$

* $Eff^{\perp\sigma} = \dfrac{\sigma_2 + |\sigma_2|}{2 \cdot \bar{R}_{\perp}^t} = 0,\quad Eff^{\perp\tau} = \dfrac{-\sigma_2 + |\sigma_2|}{2 \cdot \bar{R}_{\perp}^c} = 0.60,\quad Eff^{\perp||} = \dfrac{|\tau_{21}|}{\bar{R}_{\perp||} - \mu_{\perp||} \cdot \sigma_2} = 0.55$

$$Eff = [(Eff^{\perp\sigma})^m + (Eff^{\perp\tau})^m + (Eff^{\perp||})^m]^{1/m} = 0.80.$$

$\Rightarrow\quad f_{\text{RF}} = 1/Eff = 1.25 \rightarrow$ RF = f_{RF} (if linearity permitted) $\rightarrow$ MoS = $RF - 1 = 0.25 > 0$!

The certification–relevant load-defined Reserve Factor *RF* corresponds in the linear case to the material reserve factor f_{RF}. Its value here is $RF = 1.25 > 1$ → Laminate wall design is verified!

The multiple Lessons Learned and conclusions are incorporated in the following list:

LL

- ✓ *Considering FE-results and necessary properties: We must more and more 3D-design! However properties, especially for composites is 3D-property data test sets, are seldom sufficiently available*
- ✓ *So-called global SFCs couple physically different failure modes whereas the modal SFCs describe each single failure mode and therefore will better map the course of test data*
- ✓ *First-Ply-Failure (FPF) envelopes are searched by these SFCs, which means determination of 'Onset-of-damage' and includes both Inter Fiber Failure (IFF) and Fiber Failure (FF). Last Ply Failure (LPF) usually requires a non-linear analysis, which can be used to save a design*
- ✓ *Material symmetry seems to require for UD materials a 'generic' number of 5, valid for strengths and elasticity properties and the distinct SFCs.*
- ✓ *In this context: The Standard 3D SFCs of Tsai-Wu and Hashin employ the so-called cohesive (shear) strength* R_{23} *and regard it as a technical strength and not as a general strength quantity. The mystery behind the various interpretations is tried to be unlocked by the author. Because most of the published applications are 2D-ones the employed SFCs do not require* R_{23} *and its determination by tests needed not to be presented*
- ✓ *Often, SFCs employ just strengths and no friction value. This is physically not accurate and the undesired consequence in Design Verification is: RF may be not on the safe side*
- ✓ *SFCs are 'just' necessary but not sufficient for the prediction of strength failure. Basically, due to internal flaws, also an energy criterion is to apply. The novel approach 'Finite Fracture Mechanics (FFM)' offers a hybrid criterion to more realistically predict the stress-based crack initiation in brittle isotropic and UD materials.*
- ✓ *The physically clear-based quantity Eff gives an impressive interpretation of the failure envelope or what 100% strength capacity in 3D stress states physically really means.*
- ✓ *From the nevertheless well performed WWFEs the author had to learn that provided test results can be far away from the reality like an inaccurate theoretical model. Theory creates a model of the reality and one experiment shows 'just' one realization of the reality. Test article analysis is mandatory to interpret the test results and for a simulation-based improvement of the design. Only well-understood experiments can verify the design assumptions made!*
- ✓ *Assuming 6 strength quantities seems to violate material symmetry. Cuntze's SFC set just employs 5 measurable strengths and 2 friction parameters.*

The SFC models of Puck and Cuntze are most probably those SFC models, which are best validated by 2D and the few 3D UD experiments.

28 Technical Terms, Laminate Description, Material Stressing Effort *Eff*

Aim: *Bridging mutual understanding between engineering disciplines.*

28.1 Terms

Some terms for a better common understanding and for the application of SFCs comparison shall be added. This is the more necessary for composites:

- Analysis: Computation that uses fixed model parameters, such as of the final design
- Fracture body: smoothed surface of the ends of the multi-axial failure stress vectors
- Failure condition: Condition on which a failure becomes effective, meaning $F = 1$ for one limit state
- Failure criterion: Distinctive feature defined as a condition for one of the 3 states F < = > 1
- Failure Mode Concept (FMC)**:** invariant, failure mode-based general concept to generate strength failure conditions (SFCs) for single failure modes. It is a 'modal' formulation in contrast to 'global' concepts where all failure modes are mathematically linked and a concept for materials that can be homogenized (smeared). Applicability of a SFC ends if homogenization as pre-requisite of modeling is violated
- Fracture body: smoothed surface of the ends of the multi-axial failure stress vectors
- First-Ply-Failure (FPF): usually First Inter-Fiber-Failure IFF in a lamina of the laminate. FPF failure envelopes are searched by the SFCs. This means determination of 'Onset-of-damage' and includes both Inter Fiber Failure (IFF) and Fiber Failure (FF)
- Lamina: Designation of the single UD ply as computational element of the laminate, used as laminate subset or building block for laminate modeling. It might capture several equal plies.
- Last-Ply-Failure (LPF) in the laminate: usually requires a non-linear laminate analysis, which can be used to save a design
- Material Stressing Effort $\sigma = R \cdot Eff$ (not material utilization in the usual sense of manufacture waste minimization): artificial term, generated in the UD World Wide Failure Exercises in order to get an English term for the meaningful German term Werkstoffanstrengung. The SCF is stress-based and not strain –based. In the linear case it is directly valid $f_{\text{Res}} = RF = 1/\ Eff$. (in his book Puck originally used the term effort ε and further exposure). $Eff_{\max} = 100\% = 1$
- *Ply, layer*: Physical element from a winding, tape-laying process etc
- Properties: 'Agreed' values to achieve a common and comparable design basis. Must be provided with average value and coefficient of variation
- Reserve Factor *RF*: load-defined value $RF_{\text{ult}} = \textit{final failure load} \ / \ \textit{design ultimate load DUL}$
- (material Reserve factor f_{Res}: $f_{\text{Res}} = \textit{strength design allowable R / stress at design load DUL}$
- R : general strength, strength design allowable for Design Verification;
- $\bar{R}$: average strength in model validation for mapping tasks, marked by the statistical 'bar over'
- Simulation: Process, that consists of several analysis loops and lasts until the system is imitated in the Design Dimensioning process. The model parameters are adjusted hereby to the 'real world' parameter set
- Strength quantities: $\{R\} = (R_{\parallel}^{t}, R_{\parallel}^{c}, R_{\perp}^{t}, R_{\perp}^{c}, R_{\perp\parallel};\ R_{23})^{\text{T}} \ \Leftarrow \ (\text{X}, X', Y, Y', S_{12}; \text{S}_{23})^{\text{T}}$ Tsai
- Stress components: They should exactly read stress tensor components or simpler just stresses (*only a shear stress can be composed of a tensile component jointly acting with a compressive stress component*)

• Technical strength, standard-measurable: for clarity symbolically indexed $R_{\perp}^{c}, R_{\perp||}$;

• General strength quantity: indexed by numbers like $R_{\perp\perp} \to R_{23}$.

It seems necessary to again cite for the two different composite domains two long-time used terms:

Material composite (Werkstoffverbund): structural-mechanically a composed 'construction of different materials.

Note: A not smearable 'conglomerate' is usually the Fiber-grid-Reinforced-Concrete.

Composite material (Verbundwerkstoff): combination of constituent materials, different in composition.

For the strength properties it is to discriminate in the English language:

Yield stress (unfortunately termed yield strength, despite of the fact that it is not set as a strength property for Design Verification): material property corresponding to the point at which the material begins to deform plastically (in German Streckgrenze Re), is end of proportionality σ_{prop}

Proof stress: point at which the material exhibits 0.2% of plastic deformation, known as stress at 0.2% strain- offset and set as yield strength property $R_{p0.2}$. (in German Fließgrenze or 0.2% -Dehngrenze).

Repetition: ***Shear Strength Quantities in Spatial Analysis of isotropic and anisotropic materials***

These are an essential input with UD materials however also with isotropic mineral materials.

For 3D-analysis two specific shear strength quantities are applied, see *Fig. 28-1*:

* An approach-formalistic τ_{23}/R_{23} linked shear fracture stress $\tau_{23}^{\text{fracture}} = R_{23} \leq R_{\perp}^{t}$,

used with Tsai-Wu and in the invariant approach of Hashin and further

* A Mohr-based approach linked so-called cohesive strength $R_{23}^{\tau} = \tau_n(\sigma_n = 0)$, used within an Hashin approach and in consequence, principally also with Puck. Since Puck formulated a full IFF-SFC $R_{23}^{\tau} \Rightarrow R_{23}^{A}$, defined by all 3 IFFs interacting approach , he could model-associated dedicate his action plane resistance a relation with other model parameters.

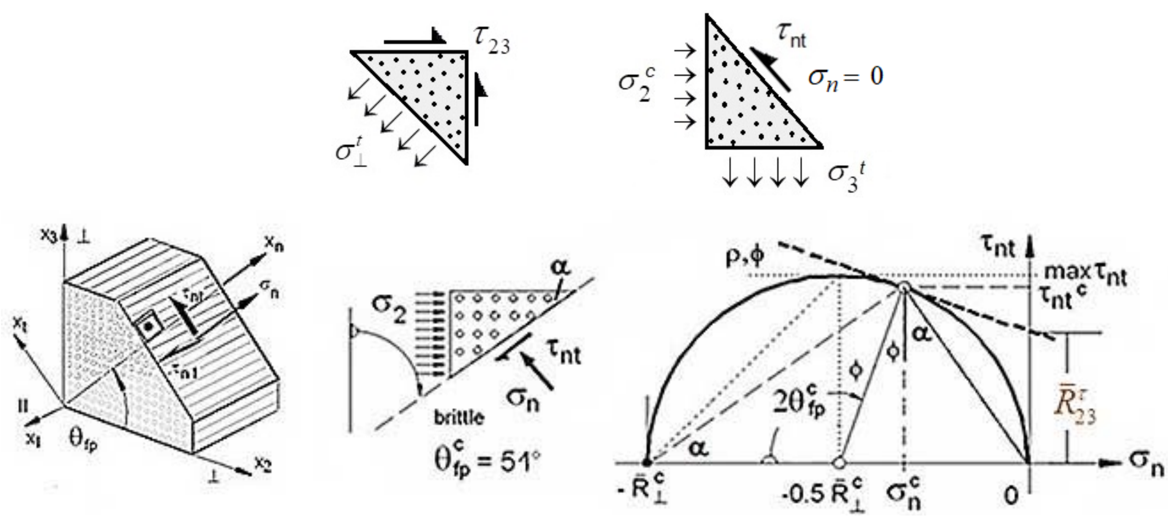

Fig. 28-1: (up) Difference of transversal shear fracture stress and cohesive strength. (below) Mohr-Coulomb curve characteristics

28.2 Indexing and Material Notations

Indexing is a chaos in the disciplines: It seems to be that the author could find (*some years ago for the planned novel ESA –Material Handbook*) a physically clear indexing system for the 3 material family models isotropic, transversely-isotropic UD and orthotropic materials (fabrics etc.). This indexing captures all material properties and allows a switching between.

The author's Glossar on 'Technical Terms' (Springer) hopefully shall be a contribution to a better mutual understanding of 'constructive' engineers from the building industry and engineers from mechanical engineering and further, of engineers from the textile, manufacturing and material discipline as well in order to better manage the more and more interdisciplinary future project tasks.

Notes on designations: As a consequence to isotropic materials (European standardization) the letter R has to be used for strength. US notations for UD material with letters X (*direction* $_1$, $\|$) and Y (*direction 2*, $\perp$) confuse with the structural axes' descriptions X and Y. R_m := '*resistance maximale*' (French) = tensile fracture strength (superscript ^{t} is usually skipped because in mechanical engineering design runs in the tensile domain, which is opposite to civil engineering, where fiber reinforcement is coming up viewing carbon concrete). See further [*Cuntze Glossar*]. In the following Table, on basis of investigations of the VDI-2014 Working Group and on investigations for above Materials Handbook, Cuntze proposed internationally not confusing terms for strengths and physical properties. These self-explaining symbolic designations read for UD- materials:

Property type	**UD quantities**	**'generic' number**
fracture strength properties	$\{R\} = (R_{\|}^t, R_{\|}^c, R_{\perp}^t, R_{\perp}^c, R_{\perp\|})^{\mathrm{T}}$,	5
+ friction properties	$\mu_{\perp\|}$, $\mu_{\perp\perp}$	2
elasticity properties	$\{E\} = (\mathrm{E}_{\|}, E_{\perp}, G_{\|\perp}, \nu_{\perp\|}, \nu_{\perp\perp})$	5
hygrothermal properties	$\{\alpha\} = \mathrm{CTE}\ (\alpha_{\|}^T, \alpha_{\perp}^T)$; $\mathrm{CME}\ (\alpha_{\|}^M, \alpha_{\perp}^M)$	2 ; 2

Notes on composites and matrices:

(1) The constituents retain their identities in the composite; that is, they do not dissolve or otherwise merge completely into each other although they act in concert. Composite materials provide improved characteristics not obtainable by any of the original constituents acting alone.

(2) Normally the constituents can be physically identified, and there is an interface between them.

(3) Composites include fibrous materials, fabrics, laminated (layers of materials), and combinations of any of them.

(4) Composite materials can be metallic, non-metallic or a hybrid combination thereof. Carbon concrete is one example.

(5) Approximately homogenizable to a smeared material are short fiber-reinforced FRC, SMC, UD-ply = UD-lamella. The lamella is smearable and therefore it can be modelled as a 'composite material'.

(6) Layered materials and foam materials are also forms of composite materials.

(7) Cement-based mortar is a 'smearable' composite material (the construction organization RILEM has a problem here, because they do not discriminate 'material composite' from 'composite material')

Table 28-1: Notations of material properties

9	**general orthotropic**	R_1^t	R_2^t	R_3^t	R_1^c	R_2^c	R_3^c	R_{12}	R_{23}	R_{13}
5	**UD, ≅ non-crimp fabrics**	$R_{\parallel}^t$ NF	$R_{\perp}^t$ NF	$R_{\perp}^t$ NF	$R_{\parallel}^c$ SF	$R_{\perp}^c$ SF	$R_{\perp}^c$ SF	$R_{\parallel\perp}$ SF	$R_{\perp\perp}$ NF	$R_{\parallel\perp}$ SF
6	**fabrics**	R_W^t	R_F^t	R_3^t	R_W^c	R_F^c	R_3^c	R_{WF}	R_{F3}	R_{W3}
9	**fabrics general**	R_W^t	R_F^t	R_3^t	R_W^c	R_F^c	R_3^c	R_{WF}	R_{F3}	R_{W3}
5	**mat**	R_{1M}^t	R_{1M}^t	R_{3M}^t	R_M^c	R_{1M}^c	R_{3M}^c	R_M^τ	R_M^τ	R_M^τ
2	*ductile* **isotropic**	R_m SF	R_m SF	R_m SF	deformation-limited			R_m^τ	R_m^τ	R_m^τ
	brittle	R_m NF	R_m NF	R_m NF	R_m^c SF	R_m^c SF	R_m^c SF	R_m^σ NF	R_m^σ NF	R_m^σ NF

9	*general orthotr.*	E_1	E_2	E_3	G_{12}	G_{23}	G_{13}	ν_{12}	ν_{23}	ν_{13}	**comments**
5	*UD, ≅ non-crimp fabrics*	$E_{\parallel}$	$E_{\perp}$	$E_{\perp}$	$G_{\parallel\perp}$	$G_{\perp\perp}$	$G_{\parallel\perp}$	$\nu_{\parallel\perp}$	$\nu_{\perp\perp}$	$\nu_{\parallel\perp}$	$G_{\perp\perp} = E_{\perp}/(2+2\nu_{\perp\perp})$ $\nu_{\perp\parallel} = \nu_{\parallel\perp} E_{\perp} / E_{\parallel}$ 3 is perpendicular to quasi-isotropic 2-3-plane
6	*fabrics*	E_W	E_F	E_3	G_{WF}	G_{W3}	G_{W3}	ν_{WF}	ν_{W3}	ν_{W3}	*Warp = Fill*
9	*fabrics general*	E_W	E_F	E_3	G_{WF}	G_{W3}	G_{F3}	ν_{WF}	ν_{F3}	ν_{W3}	*Warp ≠ Fill*
5	*mat*	E_M	E_M	E_3	G_M	G_{M3}	G_{M3}	ν_M	ν_{M3}	ν_{M3}	$G_M = E_M/(2+2\nu_M)$ 1 is perpendicular to quasi-isotropic mat plane
2	*isotropic*	E	E	E	G	G	G	ν	ν	ν	$G=E/(2+2\nu)$

9	general orthotropic	α_{T1}	α_{T2}	α_{T3}	α_{M1}	α_{M2}	α_{M3}
5	UD ≅ non-crimp fabrics	$\alpha_{T\parallel}$	$\alpha_{T\perp}$	$\alpha_{T\perp}$	$\alpha_{M\parallel}$	$\alpha_{M\perp}$	$\alpha_{M\perp}$
6	fabrics	α_{TW}	α_{TW}	α_{T3}	α_{MW}	α_{MW}	α_{M3}
9	fabrics general	α_W	α_F	α_F	α_{MW}	α_{MF}	α_{M3}
5	mat	α_{TM}	α_{TM}	α_{TM3}	α_{MM}	α_{MM}	α_{MM3}
2	isotropic for comparison	α_T	α_T	α_T	α_M	α_M	α_M

Table of structural properties

Strength properties: *NF:= Normal Fracture, SF:= Shear Fracture, R:= strength, σ, τ := indicate the fracture responsible normal or shear stress acting on the fracture 'plane'.*
Hygro-thermal properties*: T:= Thermal, M:= Moisture and Mat. λ , c : not listed.*
Elasticity properties: *E:=Young's modulus, ν:=Poisson's ratio, G:=shear modulus. ||:= parallel to the fiber, ⊥ := transversal to the fiber direction; W:= Weft, F:= Fill, M:= Mat . $\nu_{\parallel\perp}$:= (here!) larger Poisson's ratio.*
1:= lamina fiber direction, 2:= lamina transverse fiber direction across the width or the plane, 3:= through-thickness direction; x ,y := principal in-plane laminate directions, z:= thickness direction (interlaminar)

28.3 Upcoming construction standards in Germany with comments

Standards in Germany are finalized, see *Fig.28-2*:

- polymer matrix: BÜV 10 update
- mineral matrix: novel DAfStb-Richtlinie “Betonbauteile mit nicht-metallischer Bewehrung“.

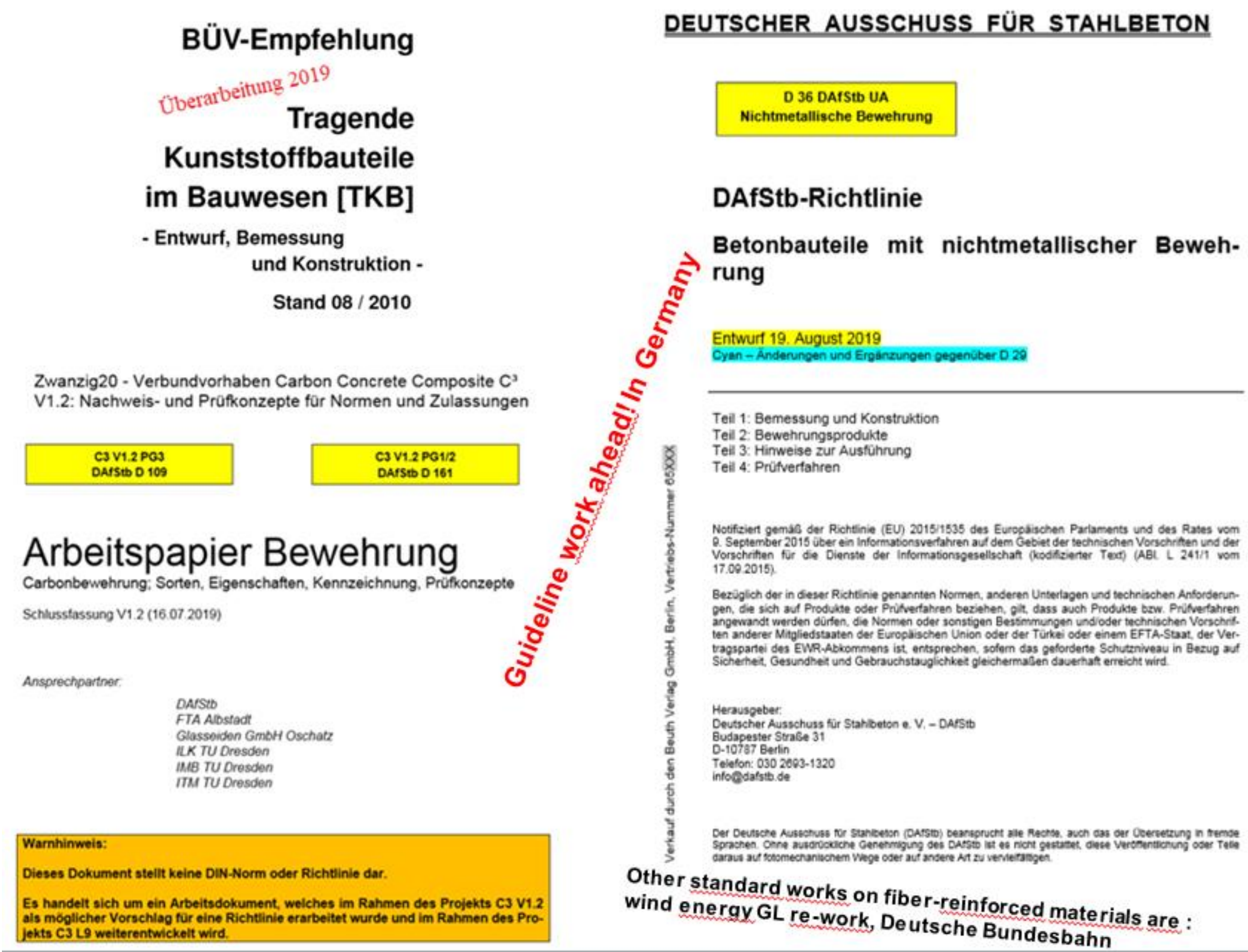

Fig.28-2: Guideline work ahead in Germany, BÜV10 update and D 36 novel

Comments of the author after a careful investigation of the two standard proposals, about 2020:

The DAfStb guideline “Concrete components with non-metallic reinforcement” is intended for fiber-reinforced components with concrete matrix.

*For engineers it is confusing not to clearly say which fiber material group the guideline is for. The fiber type CF, GF sets the limits of application.

*Originally for the *open* fiber grid the name lamella for a *dense* non-crimp fabric was used. The lamella however was still intensively used in construction repair of corroding steel-concrete ceilings (see *Fig.28-3*)

*The suffix $_{nm}$ could be replaced by the indices of the polymer matrix world, namely for the pure fiber$_f$ and the cured fiber strand $_{||}$.

*Why sticking further to the old German-originated letter *f* (strength). Still at the GruSiBau-time (*about 1985, development of the excellent partial safety factor concept*) the author used the international letter *R* for the resistance entity strength in construction. Using the letter *R* – internationally and partly nationally still started - makes life of engineers over the technical fences simpler, internationally at least.

The BÜV-recommendation for load-carrying composite parts in construction is intended for fiber-reinforced components with polymer matrix.

*Above two upcoming standards are not harmonized regarding the designations amongst themselves and w.r.t. terms half a century internationally used in timber construction and also with polymer matrices. This is all the sadder for the author, because he edited the VDI 2014, sheet 3 guideline - initiated by civil engineers !- but not used in construction. The European Codes hopefully will improve this unfortunate situation.

***LL**: Harmonization of denotations remains an urgent on-going task .*

Surprising picture, Sambia 2011:
Learning from Crocodile and hippo??

Desire of the author: “It were good for both the dicsciplines, mechanical and civil engineering, to act side-by-side such as croco and hippo document

Fig.28-4 presents a proposal for an ordering scheme.

Production of optimal structural components firstly requires an optimum design which includes the connections / joints and possible materials.
Then the locally best materials are to determine and to sort out - regarding production -
to ensure the required optimum component properties considering sustainability.

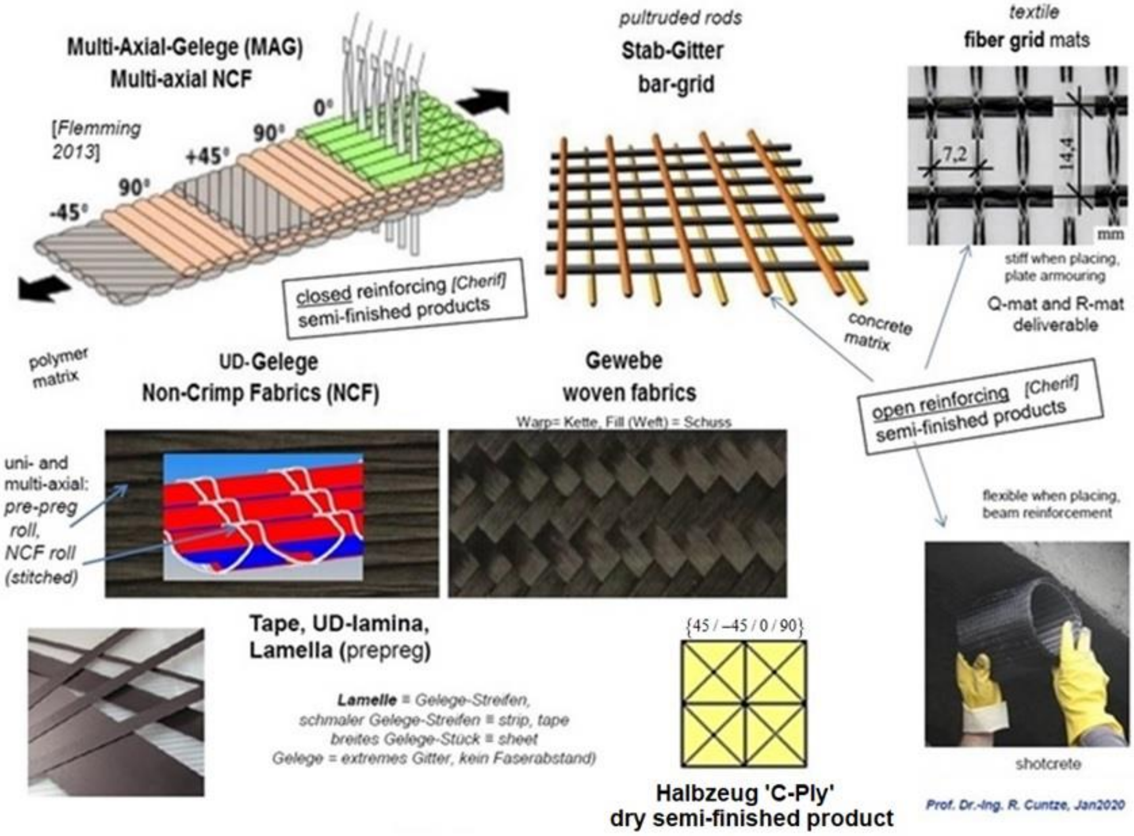

Fig.28-3: Basic fiber-reinforcing products in Engineering

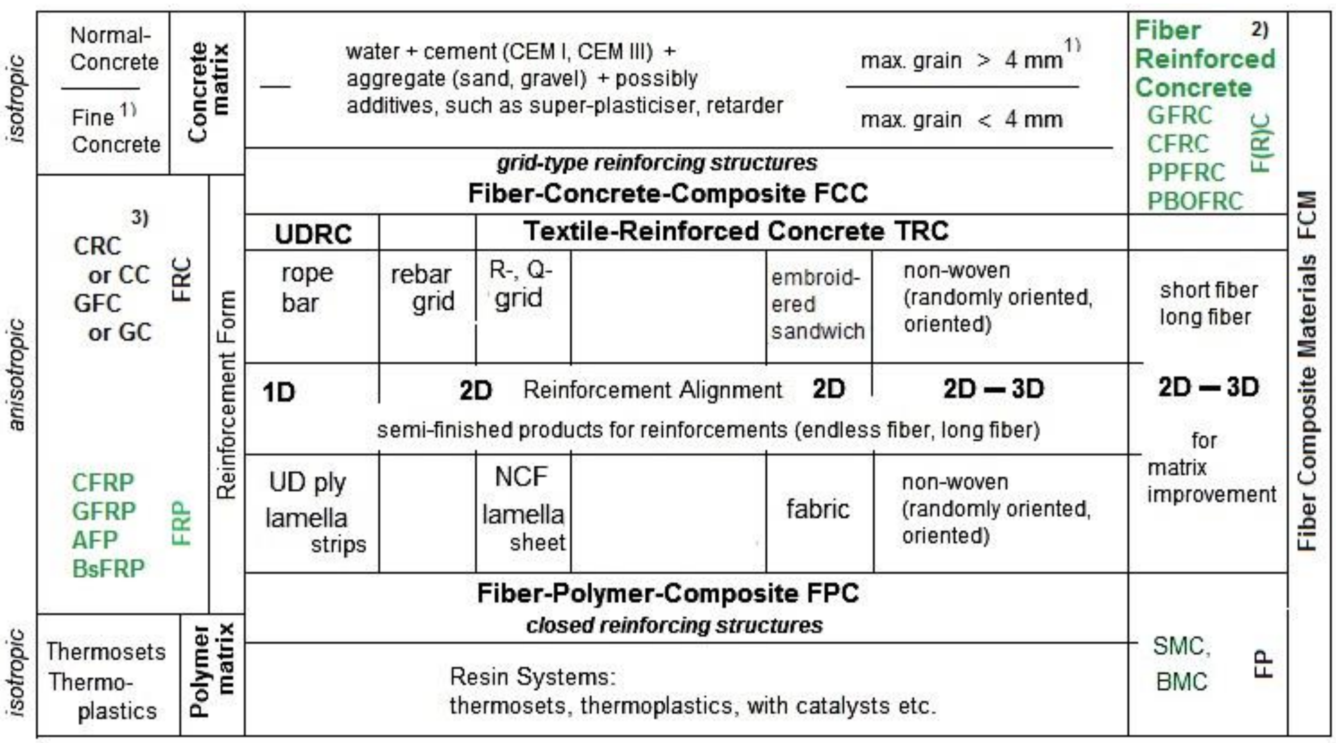

Fig.28-4: Ordering scheme proposal for Fiber-Composite Materials FCM, construction-linked such as Fiber-Reinforced Polymer FRP, Fiber-Reinforced Concrete FRC, CFRC:= CarbonFiber–Reinforced Concrete, Bi-Directionally Reinforced Concrete BDRC, UHP-(short)Fiber-Reinforced Concrete, HPFRC. Green couloured are still fixed notions.Matrix types of the Reinforcements FRPm = Fiber-Reinforced Polymer matrix, Fiber-Reinforced-Mineral matrix FRMm. International subscipts f = filament, m = matrix; superscripts t = tension, c = compression

29 Miscelleaneous

In this chapter some results of the author's works are collected, which have been discussed in his various working groups.

29.1 Construction-linked Additive Fabrication AF

Classification of fabrication processes: Subtractive processes (waste), Formative processes and Additive processes (automatically digitized fabrication now) [*VDI 2403*]. *The term manufacture is not accurate: Manus* and *facere → means made by hand*.

1. In subtractive processes, the geometry to be created is created by defining the removal of individual volume regions. Typical representatives of this group of manufacturing processes are machining processes such as turning, drilling or milling. (timber construction etc.)
2. Formative processes refer to the production of geometries by forming in compliance with volume constancy. Formative manufacturing processes are deep drawing, forging or primary forming.
3. Additive fabrication processes create a geometry by joining together volume elements (so-called "voxels"), such as the standard processes concreting, bracketing, plastering a wall etc.

The engineer's desire is to obtain accurate process names in the additive fabrication point 3, the term 3D-print does not give a clear process information. Therefore some basic definitions

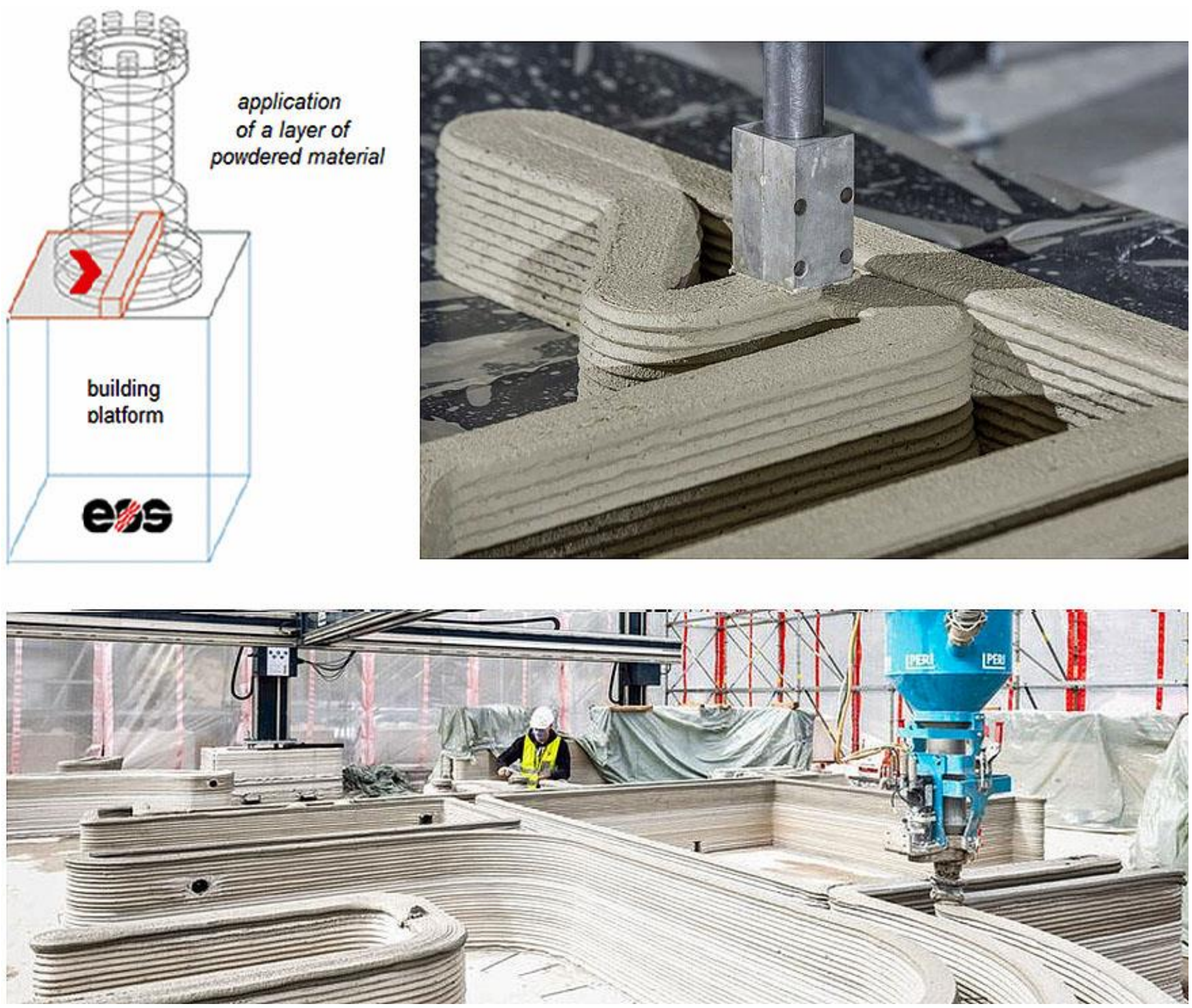

Fig.29-1: Particle-bed technique (up left), Mortar strand depositing (up, right);
(below) Peri GmbH 2021,building a two-story house in Beckum

are provided for construction. The two basic digitized additive fabrication processes in construction are to term:

(3a) P**owder bed process:** *true original 3D horizontal slice printing in construction*
Total cross-section including the 'openings' is produced in a powder bed layering process. Layer thickness is usually << 1 mm. (*for formwork production, usually*). Technique Selective Laser Sintering, does pretty well correspond with the printing definition '*Procedure, to apply something by pressure like printing a book'*.

(3b) **Extruded mortar-strand deposit process:** *is no 3D printing* in the original sense
Total cross-section including 'openings' is produced in a 'path tracking operation'. Layer thickness is several mm, depending on the strand thickness. Technique Extruded mortar strand deposit.

LL:

* *Any material that can be glued, welded or melted can be used in AF. For industrial purposes, metals, plastics, sand and ceramics are common materials, but the process is to adapt*
* *The extrusion process is for walls and other compressed load-bearing building structures!. That's why there is no fully '3D-printed house' existing.*
* *Cost-effective conventional ceiling slabs are still required*
* *Any material that can be glued, welded or melted can be used in AF. For industrial purposes, metals, plastics, sand and ceramics are common materials, but the process is to adapt.*

29.2 Buckling analysis versus Strength analysis

This chapter provides introductory information about buckling of columns (beams), plates, panels and shells. It shortly addresses just essential features in stability analysis (*speaking stability is more positive than buckling*).

This chapter is just dealing with static stability problems. It covers a very basic background in order to guide the practicing designer to better understand the manuals of commercial analysis software.

The following contents basically stems from the creation of the ESA Buckling Handbook, ECSS-E-HB-32-24A. Cuntze was first convenor and founder of the team as well as a co-author of the later prepared HSB 40100-04] from R. Cuntze and J. Broede. Noteworthy: In the HSB, section 40000, for a wide spectrum of columns, rods, rings and deep beams design sheets are found. The same is given in the chapter plates where the available design sheets on anisotropic plates provided by J. Broede and colleagues are outstanding sheets.

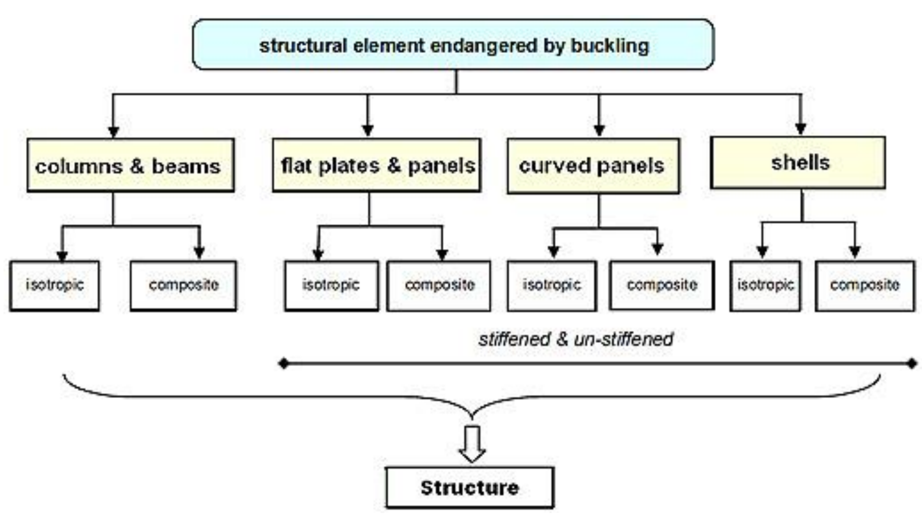

Fig.29-2: Breakdown of buckling of endangered structural elements [Cuntze, ECSS]

Different levels of analysis complexity are treated in the literature above. Going in steps from the lower level of complexity to the higher level of complexity (which will be denoted as a "hierarchical approach") the structural analyst is able to carry out and finally to successfully interpret analyses at the highest level of complexity, typically finite element computations (see [*CUN22*]).

In structural design the following subjects must be demonstrated: *Material* Strength, applying SFCs, strength criteria, and *Structural* Strength, applying buckling resistance conditions. *Fig.23-3* compiles these subjects.

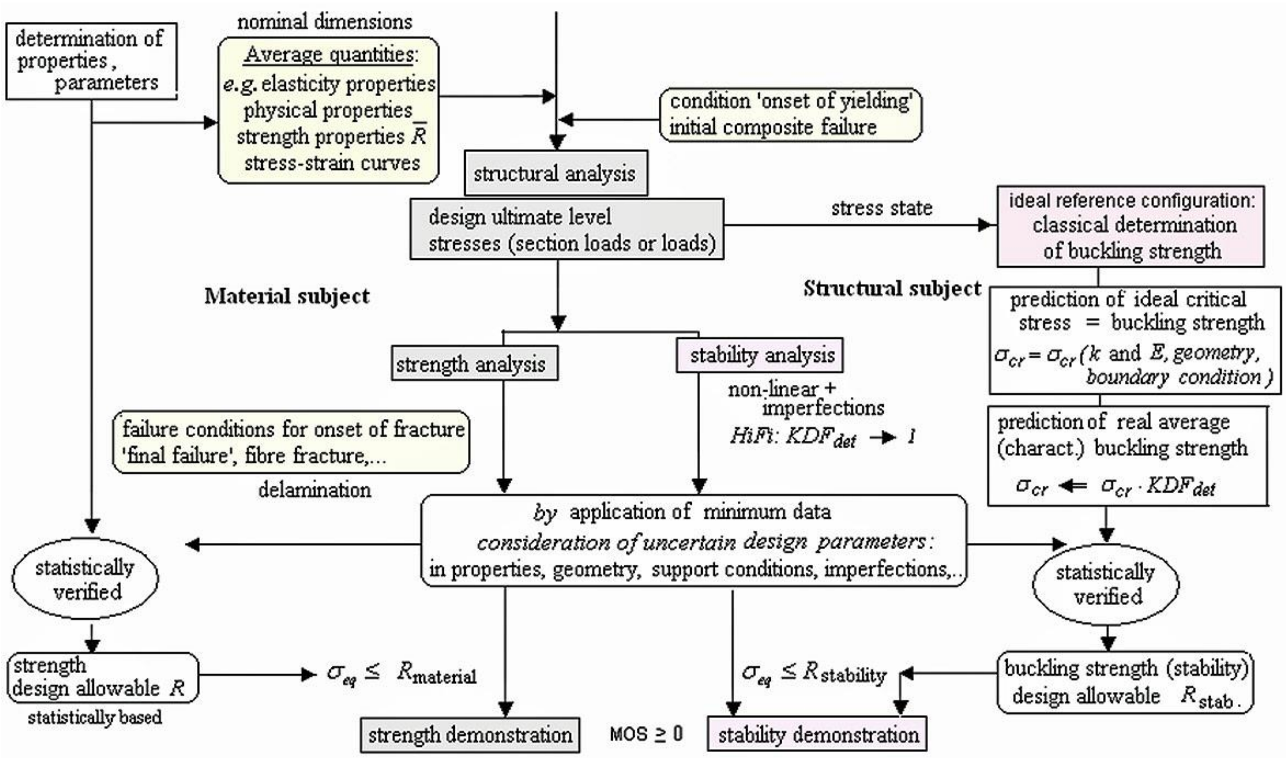

Fig. 29-3: Visualization of the (actually) required deterministic input demands.
KDF usually corrects difference of calculation model to experiment (50% expectance value), k:=buckling factor (from handbook tables), MoS:=Margin of Safety

Using such an engineering procedure the engineer is able to analyze the stability of (large) structures composed of structural elements, also referred to in literature as structural components or structural items. The term structural element includes typical elements such as columns and beams, plates, panels, and shells. In practice these structural elements often contain structural details, e.g. shells containing openings or reinforcements. The associated "basic" structural elements, the elements without structural details are denoted in the ECSS as "Typical Structural Elements".
Non-axial symmetric shells and truss systems are not addressed in the book.

29.3 Annex

If one might be interested one can find information on the following subjects in the author's life compilation [*CUN22*] especially on the various projects at MAN the author was involved:

- Influence of low Cross-sectional Shear Rigidity and Rotatory Inertia on the Critical Speeds of Shafts with Uniformly Distributed Mass (1984 for centrifuges
- The Influence of Cross-sectional Shear Flexibility and Rotatory Inertia on the Natural Frequencies of Beams with Uniformly Distributed Mass (1983)
- Natural Frequencies of a Cracked Beam for Production Quality-testing of Rotor blades
- Design of the Metallic Energy storage Flywheel for the floating crane ship Swartow (1982)
- Design of Fiber-reinforced Gas-Ultra-Centrifuges, GUZ (1971-1986
- A New concept of a Composite Flywheel due to novel fiber-reinforced materials (1988)
- Increasing the Limit of Usability of CFRP Tubes by Built-in-Stresses (1993)
- Structural Reliability, Factors of Safety and Design Values, §12
- Some Winding Theory of Filament Wound Pressure Vessels, §20.

The author's annual books piled up over the decades.

The author's
Annual booklets
with their
technical project-records
from
1970 up to 2023

29.3 Some Final Notes from Personal Experience

- ✓ Mechanics remains one very essential basis when developing light-weight structural components and Artificial Intelligence (AI) with its algorithms is a helpful supporting tool
- ✓ Only System Engineering with experienced engineers using mechanics and the necessary other disciplines - together with AI - enables to produce qualified products
- ✓ At the end someone has to sign that the developed structure will work and by that will take over responsibility. This experienced person is the absolutely necessary 'plausibility checker' for the obtained analysis and test results including generic AI-supported results.
- ✓ Bridge disciplines and materials by showing up similarities to simplify engineering life!

- ✓ In the present multi-physics applications product development is the work of several experienced engineers. Otherwise one does not deliver qualified 'Multiple function structural products'.
- ✓ In the case of bending of FRPlastic- and FRConcrete-parts carbon fibers can be only exploited using pre-tensioning and thereby compressing the tension-sensitive matrices Plastic or Concrete
- ✓ Viewing SFCs, one must be careful with conclusions reported in literature (unpleasant personal experience): SFC model *modifications* - created by another author - are used under the name of the originator and then poorly rated, however, the modification was not reported!
- ✓ Experienced engineers know: "Check your test together with test data evaluation. Check your analysis including assumptions."
- ✓ There is a rationale to take a distinct $\sigma - \varepsilon$ curve: From risk analyses and decision theory the best prediction will be achieved by applying the *mean(σ,ε)-curve* = 50% probability !
- ✓ Certification by Analysis, only: Here, simulation can optimize the output of the usually only permitted minimum number of physical tests, and enabling to better manage risk and improve prediction.

30 Glossary book, Contributions to Handbooks, Guidelines etc.

30.1 "Technical terms for composite components in civil engineering and mechanical engineering"

The construction industry is an industry in which the topic of high-performance fibre composites is not yet established on the one hand, but where there is enormous application potential on the other. Against this backdrop, Carbon Composites e.V. (CCeV) in Augsburg has founded a specialist department "CC Bau (construction)".

For CC Bau, this repositioning meant that Fibre-Reinforced Plastic (FRP) - and the various fiber-reinforced concrete matrices had to be covered. i.e. 'fibre-reinforced concrete'. The latter envolves endless '(roving)-Reinforced Concrete' (RC) as well as '(short) Fibre Reinforced Concrete' (FRC).

The following matrix applications must therefore be captured: *(1) Polymer matrix-related,* such as Glass fibre plastic pipes and containers, wind rotor blades and pedestrian bridges in GlassFRP and CarbonFRP as well, and *(2) Concrete matrix-related,* such as textile 'fibre grid' (mat) -reinforced concrete bridges and machine foundations, overhead line masts, industrial floors, multi-storey car parks, silos, prefabricated garages, transformer houses, offshore applications, tubbings, sandwich façade panels, un-tensioned and tensioned bending panels, FRP shells and bridges.
Further, a big topic is the rehabilitation with FRP-'lamellas' (tapes, strips) such as the reinforcement of a ceiling plate (slab), because of increased moments, using CFRP-lamellas applied by surface bonding,

Carbon Fibers in the construction industry reduce the concrete amount, which is positive for the CO_2 footprint due to the reduced clinker production required and are sustainable due to their non-corroding behaviour in contrast to steel."

Purpose of this Glossary: Borders between engineering disciplines are disappearing, more and more. It can also be noticed that in the different fields of the fiber-using industry there are different "speeches" and that technical terms are sometimes used very differently. Several groups of engineers would therefore have to be connected conceptually so that they understand each other correctly when making decisions. These are 'constructive' engineers from building industry and mechanical engineering and further, engineers from the textile and material range as well as from manufacturing. This glossary focuses especially on carbon fibers CF and concrete matrices. At the beginning it presents a first scheme of order for the different, interconnected disciplines. At the end, a picture gallery illustrates technological details and applications. This gallery just includes carbon applications from construction industry because these are less known.	

30.2 “Handbook for the German Ministry of Defense on a Safety Concept for Fiber Reinforced Plastic Structures".

Koblenz, 1992 (in German) and a Guideline Draft
Cuntze R., Rackwitz R., Gollwitzer S., Plica S. and Stoeffler G.

30.3 “ VDI 2014 Sheet 1-3” (1980 - 2006)

Editor of the VDI 2014, sheet 3, (2006) and contributor to sheets 1 and 2

Working Group VDI 2014, Meeting members: *Moser, Cuntze, Lutz*

ICS 59.100, 83.140.20 — **VDI-RICHTLINIEN** — September 2006

VEREIN DEUTSCHER INGENIEURE	Entwicklung von Bauteilen aus Faser-Kunststoff-Verbund Berechnungen Development of FRP components (fibre reinforced plastics) Analysis	VDI 2014 Blatt 3 / Part 3 Ausg. deutsch/englisch Issue German/English

Frühere Ausgabe: 04.97 Entwurf, deutsch
Former edition: 04/97 Draft; in German only

Die deutsche Version dieser Richtlinie ist verbindlich.

No guarantee can be given with respect to the English translation. The German version of this guideline shall be taken as authoritative.

Inhalt — Seite

Vorbemerkung . . . 3
1 Anwendungsbereich . . . 3
2 Abkürzungen, Begriffe, Symbole, Indizierung . . . 4
3 Berechnungsablauf . . . 12
3.1 Allgemeines . . . 12
3.2 Auslegungsphilosophie . . . 14
3.3 Berechnungsprogramme . . . 15
4 Modellierung der Schicht . . . 16
4.1 Allgemeines . . . 16
4.2 Eben beanspruchte Schicht . . . 18
4.2.1 UD-Schicht (faserparalleles KOS) . . . 18
4.2.2 G-Schicht und M-Schicht . . . 20
4.2.3 Drehung der UD-Schicht in das Laminat-KOS . . . 21
4.2.4 Berücksichtigung der Schubspannungen aus Querkraft bei UD-Schichten . . . 22
4.3 Räumlich beanspruchte Schichten . . . 23
4.3.1 Mechanische Beanspruchung (faserparalleles KOS) . . . 23
4.3.2 Mechanische Beanspruchung einer UD-Schicht (gedrehtes KOS) . . . 25
4.4 Einfluss von Beanspruchungsarten/-dauer . . . 26
4.4.1 Kurzzeitbeanspruchung . . . 26
4.4.2 Ruhende Langzeitbeanspruchung . . . 26
4.4.3 Schwingbeanspruchung . . . 30
4.4.4 Stoßbeanspruchung . . . 31
4.5 Festigkeitskriterien . . . 31
4.5.1 Allgemeines . . . 32
4.5.2 Bruchbedingungen für UD-Schichten . . . 36
4.5.3 G-Schicht . . . 44
4.5.4 M-Schicht . . . 45
4.5.5 Einzusetzende Festigkeitswerte . . . 46
4.6 Anwendung von Berechnungsprogrammen . . . 46
4.6.1 UD-Schicht . . . 46
4.6.2 G-Schicht . . . 48

Contents — Page

Preliminary note . . . 3
1 Scope . . . 3
2 Abbreviations, terminology, symbols, superscripts and subscripts . . . 4
3 Analytical procedure . . . 12
3.1 General comments . . . 12
3.2 Design philosophy . . . 14
3.3 Computer programs . . . 15
4 Modelling the lamina . . . 16
4.1 General comments . . . 16
4.2 Two-dimensionally loaded lamina . . . 18
4.2.1 UD lamina (parallel-to-fibre COS) . . . 18
4.2.2 WF lamina and M lamina . . . 20
4.2.3 Rotation of the UD lamina into the laminate . . . 21
4.2.4 Inclusion of shear stresses from transverse forces in case of UD laminae . . . 22
4.3 Laminae subject to three-dimensional loading . . . 23
4.3.1 Mechanical loading (parallel-to-fibre COS) . . . 23
4.3.2 Mechanical loading of a UD lamina (rotated COS) . . . 25
4.4 Influence of loading type and duration . . . 26
4.4.1 Short-term load . . . 26
4.4.2 Long-term static load . . . 26
4.4.3 Cyclic load . . . 30
4.4.4 Impact load . . . 31
4.5 Strength criteria . . . 31
4.5.1 General comments . . . 32
4.5.2 Fracture conditions for UD lamina . . . 36
4.5.3 WF lamina . . . 44
4.5.4 M lamina . . . 45
4.5.5 Strength values to be used . . . 46
4.6 Application of calculation programs . . . 46
4.6.1 UD lamina . . . 46
4.6.2 WF lamina . . . 48

VDI-Gesellschaft Kunststofftechnik

VDI-Handbuch Kunststofftechnik
VDI-Handbuch Konstruktion

VEREIN DEUTSCHER INGENIEURE	Entwicklung von Bauteilen aus Faser-Kunststoff-Verbund **Zuverlässigkeit und Sicherheit**	VDI 2014 Blatt 4 (4. Entwurf) Zusammengestellt R. Cuntze, MAN

Development of FRP components
(fibre reinforced plastics)
Reliability and Safety

Einsprüche bis ??.??.1995 an
Verein Deutscher Ingenieure
VDI-Gesellschaft Kunststofftechnik
Postfach 10 11 39
40002 Düsseldorf

Inhalt Seite

Vorbemerkung ....

1. Anwendungsbereich, Nutzen ....

2. Abkürzungen, Begriffe, Symbole ....

3. Nachweis ....
- 3.1 Allgemeines zu Rechnerischem und Experimentellem Nachweis ....
- 3.2 Mechanische Modellierung (Grenzzustände)
- 3.3 Experimenteller Nachweis ....

4. Traditionelles Sicherheitskonzept (TSK) ....
- 4.1 Allgemeines, charakteristische Werte ....
- 4.2 Unsichere Eingangsgrößen beim Rechnerischen Nachweis ....
- 4.3 Sicherheitsfaktoren (Auslegung) und Sicherheitsmargen (rechn. und experim. Nachweis)
- 4.4 Kritik am TSK ....

5. Probabilistisches Sicherheitskonzept (PSK) ....
- 5.1 Allgemeines ....
- 5.2 Einwirkungsgrößen, Widerstandsgrößen und stochastische Konstruktionsparameter ....
- 5.3 Teilsicherheitsfaktoren (semiprobabilistische Vorgehensweise) ....
- 5.4 Stochastische Modellierung und Logische Modellierung des Versagenssystems ....
- 5.5 Berechnung von Versagenswahrscheinlichkeit oder Zuverlässigkeit ....

6. Bestimmung von Kennwerten ....
- 6.1 Definition und Verwendung von Dimensionierungskennwerten ....
- 6.2 Ermittlung der statistischen Parameter aus Meßdaten ....
- 6.3 Ermittlung Charakteristischer Werte ....

7. Produktsicherung ....
- 7.1 RAMS-orientierte Entwicklung ....
- 7.2 Qualitätssicherungskonzept und Integritätskontrolle mit Prüfmethoden ....
- 7.3 Versuche zur Erzielung der Strukturzuverlässigkeit des FKV-Bauteils ....

Literatur ....

Anhang 1 Schätzverfahren, Statistische Tests, Updating Verfahren, Bayes ....

Vorbemerkung

Die Richtlinie enthält Empfehlungen für das Entwickeln von Bauteilen aus Faser-Kunststoff-Verbunden (FKV), die aus einzelnen faserverstärkten Schichten bestehen, bei denen Fasern in einer Kunststoff-Matrix eingebettet sind. Die Bauteilentwicklung wird dargestellt, wobei die Berechnungen eingehender behandelt werden. Die Richtlinie will durch Systematisieren und Vereinheitlichen der Bauteildimensionierung auch die Zulassungsverfahren und die Qualitätssicherung erleichtern. Sie ist in vier Teile gegliedert:

- Blatt 1 Grundlagen
- Blatt 2 Konzeption und Gestaltung....................
- Blatt 3 Berechnung....................
- Blatt 4 Zuverlässigkeit und Sicherheit.

Beispielsammlung: s. VDI Report??

VDI-Gesellschaft Kunststofftechnik

VDI-Handbuch Kunststofftechnik

30.4 “German Aeroautical Handbook” (‘*Airbus design folder’*)

HSB HANDBUCH STRUKTUR BERECHNUNG	General description	Issue E Year 2018 Page 1 of 21

Luftfahrt-Technisches Handbuch (LTH)

HSB

HANDBUCH STRUKTUR BERECHNUNG

Fundamentals and Methods
for
Aeronautical Design and Analyses

issued by

iasb INDUSTRIE-AUSSCHUSS-STRUKTUR-BERECHNUNGSUNTERLAGEN

Prepared: Dr. M. Schagerl	Checked: Dr. M. Magin	Date: 22.11.2018	IASB / IVW

Digitally signed by Michael Magin
Date: 2020.10.20 00:13:05 CEST

Design sheet contributor 1972-2015

Co- reworker and Co-translator of the ’Airbus’ structural handbook into English (2004)

IASB 1972-2024

30.5 “ Weekly course: Development of Fibre Reinforced Plastic Components” (1986, 1989)

SHORT COURSE

DEVELOPMENT OF FIBRE REINFORCED PLASTIC COMPONENTS

Pretoria

16th to 18th April 1986

repeated 1989

Presented by : Dr R G Cuntze

Course Organizer : P A Coetzer

30.6 ESA/ESTEC Contributions: Since 1970 for the ESA/ESTEC Material Handbook and down **Organizer of below Working Group (WG), convenor and contributor"**

ECSS-E-HB-32-24A
24 March 2010

EUROPEAN COOPERATION
ECSS
FOR SPACE STANDARDIZATION

Space engineering

Buckling of structures

ECSS Secretariat
ESA-ESTEC
Requirements & Standards Division
Noordwijk, The Netherlands

This Handbook has been authored and agreed upon by:

J. Arbocz, TU Delft
C. Bisagni, Politecnico di Milano
A. Calvi, ESA-ESTEC (Convenor)
E. Carrera, Politecnico di Torino
R. Cuntze, formerly MAN-Technologie
R. Degenhardt, DLR Braunschweig and PFH Göttingen
N. Gualtieri, Thales Alenia Space
H. Haller, Intales
N. Impollonia, Università di Catania
M. Jacquesson, CNES
E. Jansen, TU Delft
H.R. Meyer-Piening, ETH Zuerich
H. Oery, RWTH Aachen
A. Rittweger, Astrium EADS
R. Rolfes, Leibniz Universitaet Hannover
G. Schullerer, MT Aerospace
G. Turzo, CNES
T. Weller, Technion, Haifa
J. Wijker, Dutch Space

The valuable contributions of the following persons are acknowledged:

C. Huehne, DLR Braunschweig; D. Petry, Astrium EADS; H. G. Reimerdes, RWTH Aachen; K. Rohwer, DLR Braunschweig; R. Zimmermann, DLR Braunschweig.

The ECSS-E-HB-32-24 has been prepared by merging the volunteer contributions of the authors. Comments concerning the technical content of this handbook will be welcomed by the European Cooperation for Space Standardization, Noordwijk, the Netherlands, www.ecss.nl.

	BUREAU OF LIGHTWEIGHT STRUCTURES **MINUTES OF MEETING**	**Date :** Feb. 02/03 2006

Location **: INTALES at Technical University Innsbruck (A)**

Object **: ECSS-E-30-24 Buckling Handbook (BH): 4th** ***meeting***

Meeting Place and Time:

- First day: Start at 9.15 , End at 18.00
- Second day: Start at 9.00 , End at 15.30.

List of Participants:

Name	Acronym	Company	Remark
	Full members and supporting members		
Johan Arbocz	JA	TU Delft	-
Paul Arendsen	PA	NLR, Holland	-
Gerd Bertrand	GB	AIRBUS-Germany, Hbg.	no response.
Vincent Billey	VB	EADS-ST LM	02/03-
Chiara Bisagni	CB	Politec Milano	02/03
Adriano Calvi	AC	ESTEC	02/03
Erasmo Carrera	EC	Politec Torino	-
Ralf Cuntze	RC (convenor)	Bureau Cuntze	02/03
Richard Degenhardt	RD	DLR, BS	02/03
Bodo Geier	BG	DLR, BS	-
Nunziatino Gualtieri	NG	ALENIA Spazio	02/03
Herbert Haller	HH (secretary)	INTALES, Innsbruck	02/03
Eelco L. Jansen	EJ	TU Delft	02/03
Marie Jacquesson	MJ	CNES DLA (EVRY)	02/03
Ali Limam	AL	INSA Lyon	-
H. R. Meyer-Piening	HRMP	ETH Zuerich	02/03
Huba Oery	HO	RWTH Aachen	-
Dirk Petry	DP	ASTRIUM EADS	02/03
Hans G. Reimerdes	HGR	RWTH Aachen	-
Michael Rotter	MR	Univ. Edinburgh	02/03
Andreas Rittweger	AR	EADS Bremen	never response
Raimund Rolfes	RR	Uni Hannover	02/03
Günther Schullerer	GS	MT-Aerospace Augsburg	02/03
Guy Turzo	GT	CNES Toulouse	02/03
Jaap Wijker	JW	Dutch Space	-
Rolf Zimmermann	RZ	DLR, BS	retired
	New and visiting members		
			-

Diffusion : participants + non-attending WG members + T. Henriksen + Athena Tilson.

Thanks to Herbert for providing us with such a nice weather.

1 of 7

Again, my thanks for the fruitful and effective discussions, for taking over work for the preparation of the BH draft, and to Michael for helping to substantiate 'our' *ECSS* handbook by inputting 'things' from 'his' civil engineering *ECCS* standard/handbook (of mixed type)!

Further Meetings planned:

5th Meeting: End of April, Bremen, EADS (Dr. Rittweger) + AIRBUS (Mr. H. Wellen)
Discussion of *Large Structure Examples,* permitted for being published in our Buckl. Hdbk.
To be fixed by RC with Rittweger and Wellen! Desired: April, 18-20
6th Meeting: planned: June 26-27, Edinburgh (Prof. M. Rotter)
7th Meeting planned: Sept. 21-22, Milano (Prof. C. Bisagni)
8th Meeting planned: first advent week (In 2006 is the latest possible begin!), Dec. 4-8 !, Munich, DP
9th Meeting ....

DISCUSSION POINTS AND RESULTS

1) **Welcome, Introduction of new WG Member** Prof. Michael Rotter

2) **Discussion of MoM, 3rd Meeting, Hannover** No comment.

3) **Discussion on next meetings** Results see above.

4) **Discussion of Action Items List (AIL), 3rd Meeting, Hannover** Status of Actions
- A19: Linked to A46 are linked concerning strategy. A common agreement is suggested. Impact from later presentation by Michael Rotter to be included.
- A49: The tracking of doc: Marking for example by letter "X" and date for the version (whole doc). Result of discussion:
  Name of doc.: (Sub)Chapter Title.(acronym date)
  Example ***§1_3 Analysis Methods (NG11oct2005).***
- A62: CB tries further to get agreement from system engineer an input for §3.2
  - A64: CB did some analyses and the action is closed for CB. HH tries to do some analyses till next meeting
- A70 RC provides MR and PA with info till 15.2.06
- A77 will be taken over by EJ. RC will inform TW until the next meeting

5) **Discussion of contents of Website Folders of the Buckling Handbook.**
All folders of the BH Website have been looked at and actual uploaded contents discussed.
- Direct actions are directed to the AIL
- The Hdbk draft will be uploaded as .pdf file.

6) **References**
- The reference list will be attached to each chapter
- The references will be handled by full authors name for preparation
- The citation will be changed to numbers after checking procedure of WG, tbc see A91, for final draft to be delivered before Public Review
- Equations, Tables, Figures: follow the referencing system of the other ECSS-handbooks
- Paragraphs: As it is.

2 of 7

7) **Checking/Reviewing of a Working Document = DRR folder** (proposition from NG)
Presentation by RC
- The DRR folder within a chapter folder is the area for submission of review results.
- In order to not forget any correction proposal, comment etc. the official Document Review Record (DRR) form sheet for ECSS Standards shall be taken, see Website: DRR for E-30-24, template and for one example(of RC), see *DRRs folder for corresponding ECSS Standards.*

Procedure if you wish to write a DRR, on chapter 2.3 e.g.,
- Download the template from the *Template Folder*
- Update the completed file named, e.g. ***DRR2_3 FlatPanels (EJ11oct2005)_RC date*** , as seen above, where RC here means the initials of the author of the DRR
- Upload the document to the folder Working Documents
  §2.3 Flat Panels
  Chapter DRRs.

8) **+ How to get on** BH **Website?** Repetition for PA.
GOOGLE→ECSS→Log in→My Team

9) **Presentation of Company INTALES** by HH

10) **Presentation about Shell Structures** (Analysis, Failure modes, ECCS Handbook) by MR.
Prof. Rotter was invited to present in Innsbruck his institute + past ECCS activities + how ECCS may contribute to ECSS BH.
There are valuable parts/ideas/figures/tables. However, the (legal) possibility of implementation of which will have to be considered by us when taking over something.

11) **Example for BEAM buckling** presented by HRMP
Variable cross section values – Finite Diff. on Excel Sheet
Example transferable to a solid propellant launcher on launch pad

12) **Commitment of RC and RD as compilers for §1.7**

13) **Full TOC urgently needed.**
Therefore, RC needs the not yet structured SUB-TOCs of the respective compilers in order to complete the Handbook TOC

14) **Paul Andresen may take over §2.4 Flat Panels** (information from EJ)

15) **Drafting of §1.8**
To A92: RR encourages JW to begin drafting.
Also ask the contributors to give their statements by 1st march 2006.

16) **Proposal for § 1.7 „Manufacturing Aspects"** (see Website §1.7). Presentation by RC
The proposal, necessary for the upcoming discussions of RC + RG with manufacturing engineers, has been discussed, simplified and uploaded:
New: §1.7 Buckling implications of manufacturing and assembling processes
1.7.1 Sensitive parameters for buckling
1,7.2 Metallic materials

3 of 7

1.7.3 Composite materials.

17) **GT shall provide a presentation on the development of a launcher** for Bremen

18) **Discussion: Should software be annexed to the handbook** for design reasons, only?
* Software: - not certified 'little' programs, no maintenance (author may be addressed)
- Teaching software and checking tools for the more sophisticated FE codes
- Not foreseen for production aspects

* Description of Software: Scope, Theory, Limitations
* Simple Program Structure.

Final Conclusion of Discussion: Decision will be taken at 5th meeting in Bremen. Majority voted for an annex of little programs on EXCEL sheets etc. ..

19) **Lack of support by ECSS Secretariat** (reported by AC)
Due to this lack the WG members are asked to produce the Figures and Tables as far as possible on their own.
Discussion on a support, again, when the preliminary Hdbk draft will be finalized for Public Review.

20) ***Which are the 'design limit states' to be applied in the non-linear buckling analysis?***
Load reached at stop of a numerical computation; deformation or strain as a usability limit state; initiation of global yielding or of local yielding; initiation of inter-fibre fracture in a lamina of the laminate; delamination; or ??
To be discussed at Bremen.

21) **TOC Structure of** ***Large Examples***
A structure for the body text of the Large Examples was presented by RC (see Website §3.1) and discussed. GT recommends to give Test-Analysis Correlation an own chapter.
This structure may be improved by WG members in order to find a more general structure. Of course, the structure can be tailored by each chapter compiler, if necessary.

22) **Virtual Testing shall be mentioned in the handbook**

23) **TOC Structure of** ***Structural Element examples***
A structure for the body text of these examples was presented by RC (see Website § 2.5, shared area) and discussed. The application was for a CFRP cylinder at DLR Braunschweig.
This structure may be improved in order to probably find a more generally applicable structure. Of course, the structure can be tailored by each chapter compiler if necessary.

24) **Subgroup fixations**
- Ali Limam, Paul Arendsen and Michael Rotter will take over work.
- Rolf Zimmermann still contributes to the sub chapters he addressed before his retirement.

Best regards, *Ralf & Herbert. 07/02/06*

4 of 7

ECSS-E-30 24 BUCKLING-HANDBOOK (BH) **ACTION ITEMS LIST**

Status: November, 08/09, 2006 at MT Aerospace, Augsburg for next meeting

Action		Description	Actionee	Deadline	Status
1.	**27/04/05 Noordw.**	use of verbs	EG	30/05/05	closed
2.	27/04/05	sketch on validation/verification to Work Docs	RR	15/05/05	closed
3.	28/04/05	putting MoM attachments on website	AT	asap	ongoing
4.	28/04/05	WG BH member list	RC	15/05/05	closed
5.	28/04/05	review of NWI (basis for Work Plan discussion)	all	20/06/05	closed
6.	28/04/05	plausibility check list for analyses	RC	08/07/05	closed
7.	28/04/05	input glossary/definitions from SRUCTURAL	NG	15/07/05	closed
8.	28/04/05	clarification of *Consideration of operational aspects*	AC, MK	20/06/05	closed
9.	28/04/05	clarification of the meaning "Documentation of lessons learned during design, manufacturing, verification and operations	NG, MK	20/06/05	closed
10	28/04/05	copy right problem (we use source data)	EG, AC	20/06/05	response text required
11	28/04/05	recommend. to fill in the date on 1st page of Hdbk ?	RC	20/06/05	closed
12	28/04/05	asking INSA colleagues for their vacant time	RC	20/06/05	closed
13	28/05/05	provision of ASTM website on "council on codes & standards, committee 60"	AC	20/06/05	closed, on website
14	28/04/05	fill in the Report Form for EP	RC	July 05	closed
15	28/04/05	volunteers for contributions, part 1 through 3	all	20/06/05	closed
16	28/04/05	collection: contributions to sub-chapters	all	20/06/05	closed
17	28/04/05	downloading possibility from our website: for members, only	Athena	asap	closed
18	28/04/05	template for handbook from secretariat	EG. AC	20/06/05	**open**
19	28/04/05	flow chart How to run buckling	HH	20/06/05	closed
20	28/04/05	search for further volunteers for checking (especially those which cannot attend the meetings)	all	20/07/05	ongoing
21	**23/06/05 Noordw.**	asking HRMP for a Part 3structure example or a Part 2 structural element example	RC	01/09/05	closed
22	23/06/05	contributions from EADS-ST France (Aerospatiale) required for §3.1	VB	15/09/05	closed
23	23/06/05	issue of an address list incl. acronyms (add to next MOM)	RC	15/09/05	closed
24	23/06/05	does ESTEC perform Structure buckling tests?	AC	15/09/05	closed
25	23/06/05	interviewing Dr. Vollrath, VDI, for taking VDI2014 Guideline as a Reference Doc and its§6.2, Stability, as a Work Doc	RC	01/09/05	closed
26	23/06/05	example Part 3: from Columbus receivable? NO!	NG	15/09/05	closed
27	23/06/05	giving V. Billey and B. Geier full access to website	Athena	asap	closed
28	23/06/05	processing and distributing of a Work Plan draft	RC	01/08/05	closed
29	23/06/05	adding NASA docs to website AC provides link	EJ, AC	21/07/05	closed
30	23/06/05	interviewing Dr. Clormann, MAN Technologie, for examples Part 3 (Lox-Tank, Front Skirt, Booster,..);	RC	15/09/05	Closed and linked to A32
31	24/06/05	interviewing Hr. Wellen, (fuselage shells, composite bulkhead,..), §3.3	RC, GV	15/09/05 **11/2006**	**pending**
32	24/06/05	interviewing Dr. Rittweger, EADS-ST Bremen for examples, Part 3 (link to A 30 !)	RC	15/09/05	closed (AR agreed)
33	24/06/05	interviewing Prof. Schwarmann, Airbus, for examples at Bremen and Hamburg	RC	15/09/05	closed

AIL Ottobrunn 04/07/06 1 of 8 16.11.2006

34	24/06/05	attempting to put GARTEUR results on website: BG checks potential contributions (Nov. Hannover)	BG, RD	15/02/06	closed
35	24/06/05	upload Koiters article on curvature parameter	EJ	01/08/05	closed
36	24/06/05	PDF draft of BH to website before each meeting	RC	10/09/05	ongoing
37	24/06/05	presentation on COCOMAT (design verification, glossary, philosophy,..)	AK	2nd meet.	closed
38	24/06/05	wrt. definitions adding BG article on Structural Behaviour to Work Doc	BG	01/08/05	closed
39	24/06/05	setting up and distributing a list of the Work Docs (although still on website)	HH		closed
40	24/06/05	setting up and distributing a list of the Reference Docs (although on website)	HH		closed
41	24/06/05	finding a specialist incl. compiler for § Manufacturing Aspects (see SMH group)	GT, RC, RD, all	asap **09/2006**	**pending**
42	24/06/05	informing RMP wrt Zürich on meeting requirements	RC	01/08/05	closed
43	24/06/05	implementing *DRD Buckling* as Work Doc	NG	01/08/05	closed
44	24/06/05	wrt "Engin. language": Can we get a PDF of Bush-Almroth?? If yes, add to Reference Docs	EJ	01/08/05	closed
45	24/06/05	wrt accurate property input for all materials (ductile aerospace metals, usually brittle composites, ductile GLARE hybrid composite, etc.): generate a table for the elasticity properties for the strength properties for the hygrothermal properties	RC RC RC	01/09/5	closed
46	**15/09/05 Zuerich**	handbook flow chart at beginning is required	HH	asap	closed
47	15/09/05	checking whether the ECSS ordering terms for the Handbook (not a standard!!): *paragraph, section, chapter* are correctly used ???	EG	asap	closed
48	15/09/05	DRD on Buckling is added to website	RC	01/08/05	closed
49	15/09/05	Tracking of *Buckling HB* draft changes	ECSS + WG, AC	asap 15/01/06	**Still under discussion**
50	15/09/05	Preparation of general list of symbols (collecting from members) as basis for discussions, this list will be enhanced if necessary	RC	1/11/05	closed
51	15/09/05	Input for action 50, Send to RC (nothing received)	all	23/09/05	closed
52	15/09/05	Discussion between NG + RR about §1.1 to finalize this point	NG, RR	30/09/05	closed
53	15/09/05	Ask HGR and HO to make a TOC §1.4 to be discussed at 3rd meeting	RC	15/10/05	closed
54	15/09/05	§1.5.1 (new), §1.5.3 proposal for draft	RC	4/11/05	closed
55	15/09/05	§1.5.2 proposal for draft	CB	4/11/05	closed
56	15/09/05	§1.6.3 proposal for draft (see A100)	JB, RD	15/10/05	closed
57	15/09/05	Ask JB for contribution to §1.7 (JB cancelled membership)	GT	15/10/05	closed
58	15/09/05	Comments about §1.9 to CB	MJ, GT	15/10/05	closed
59	15/09/05	Information from RC to compilers: Tanchum Weller for §2.3 , Bodo Geier for §2.4, Jerome Buffe for several chapters in PARTs 1 to 3.	RC	23/09/05	closed

2 of 8

30.7 “MAN-Project leader of the funded Research on UD Fracture Criteria”, SFC Puck

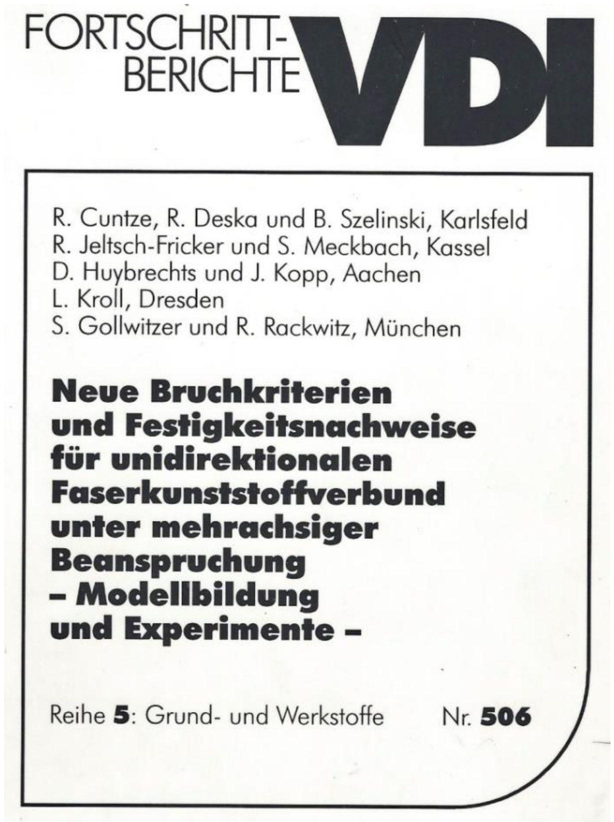

FORTSCHRITT-BERICHTE VDI

R. Cuntze, R. Deska und B. Szelinski, Karlsfeld
R. Jeltsch-Fricker und S. Meckbach, Kassel
D. Huybrechts und J. Kopp, Aachen
L. Kroll, Dresden
S. Gollwitzer und R. Rackwitz, München

Neue Bruchkriterien und Festigkeitsnachweise für unidirektionalen Faserkunststoffverbund unter mehrachsiger Beanspruchung – Modellbildung und Experimente –

Reihe **5**: Grund- und Werkstoffe Nr. **506**

	
Meckbach, Jeltsch-Fricker, Rackwitz	***Lothar Kroll, Alfred Puck***

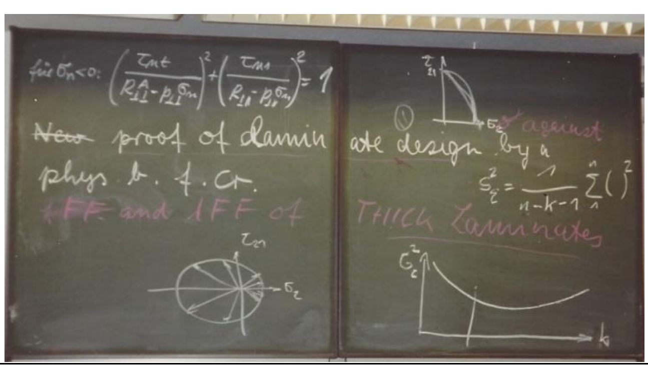

BETONTAGE CONCRETE SOLUTIONS

COMPOSITES UNITED | BAU

CC Bau-Forum

"Carbonbeton-Anwendungen in der Praxis - auf der Baustelle und im Fertigteilwerk"

Transformation von praktischem Anwendungswissen.

Zielgruppe: Hersteller, Sanierer, Vertreter der Betonbranche

am 25. Februar, Donnerstag, als Podium integriert bei den Ulmer Betontagen vom 23. - 26.02.2021

25 min Vortrag + 5 min Diskussion. Folien: deutsch oder englisch. Vortrag: falls möglich möglich deutsch

08:30	*Kaffeepause – Networking*
09:00	**Einführende Worte** *Prof. Dr.-Ing. habil. Ralf Cuntze, CU Bau, Augsburg. Composites United e.V. CUeV (formerly CCeV)*
09:15	**Digitale Entwicklung – von der Faser zum textilen Gelege.** *Roy Thyroff, rothycon – Roy Thyroff Consulting, Naila*
09:30	**Carbonbeton: Zwischen Theorie & Praxis.** *Dipl.-Ing. Oliver Heppes, GOLDBECK Bauelemente Bielefeld SE*
12:10	**Größer, stärker, wirtschaftlicher - Carbonbewehrungen in neuen Dimensionen.** *Dipl.-Ing. Stephan Gießer, Solidian, Albstadt*
12:40	***Mittagspause und Besuch der Ausstellung***
14:00	**Tragwerksplanung des C³–Ergebnishauses „CUBE" – Bemessung, Nachweisführung und Zulassung im Einzelfall.** *Dipl.-Ing. Hendrik Ritter, Assmann Beraten und Bauen, Dresden*
14:30	**Modulare Brückenbauwerke aus Carbonbeton** *M.Sc. Sven Bosbach, Lehrstuhl und Institut für Massivbau, RWTH Aachen*
15:00	**Bauen mit CPC-Carbonbetonplatten, einer komplett neuen Bauweise in Beton – Verfahren, Konstruieren, Bemessen.** *Prof. Joseph Kurath, ZHAW Winterthur, Schweiz*
15:30	**Stadtbahnbrücke Stuttgart: CFK-Zugglieder finden Akzeptanz.** *Prof. Dr. Urs Meier, EMPA, Dübendorf, Schweiz*
16:00	**Ausgewählte Ingenieurbauwerke - nachträgliche Bauteilverstärkung mit Carbon-Faser-Kunststoffen „CFK" (geklebte Lamellen).** *Dr.-Ing. Horst Peters, HPTL Carbon GmbH, Ditzingen*

Ihr Ralf Cuntze und der weitere Vorstand des Netzwerks CU Bau

Weitere Termine 2020 / 2021 des Netzweks CU Bau:

- 19.11. 2020: CU Thementag „Richtlinien, bauaufsichtliche Zulassungen und Bauartgenehmigungen für die potenziellen Anwender Architekten, Tragwerksplaner und Bauherrn". Zoom-Konferenz
- 17.03.2021: Thementag aller Arbeitsgruppen des Netzwerks CU BAU mit TU Chemnitz. Zoom-Konferenz?
- 30.03.2021: 4. Thementag der AG „Automatisierte Fertigung im Bauwesen inkl. Serielles Bauen". Zoom-Konferenz?

Das Netzwerk CU Bau, besteht aus 4 Arbeitsgruppen: Bemessung und Nachweis (Prof. Ralf Cuntze), Faserverbundarmierter Beton (Dr. Ingelore Gaitzsch), Faserverstärkte Kunststoffe (Prof. Jens Ridzewski), Automatisierte Fertigung im Bauwesen inkl. Serielles Bauem (Cuntze)

Agenda Carbonbeton-Forum Ulmer Betontage Cuntze 21okt20

Probably the first World-Wide Conference on Wind Energy

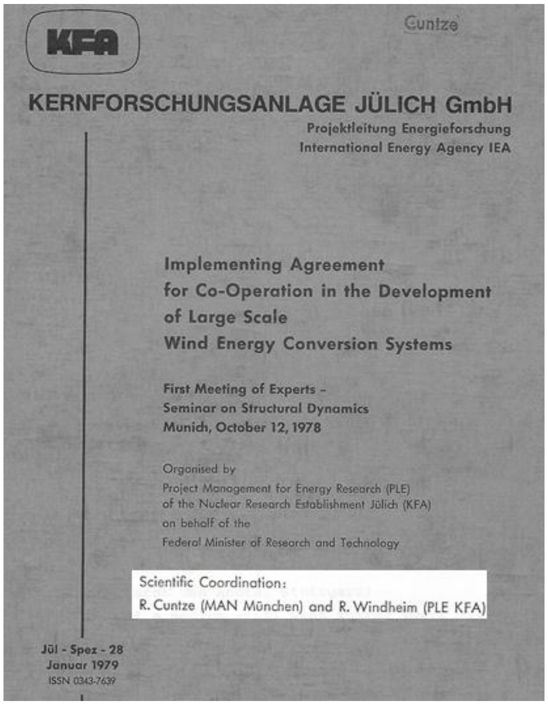

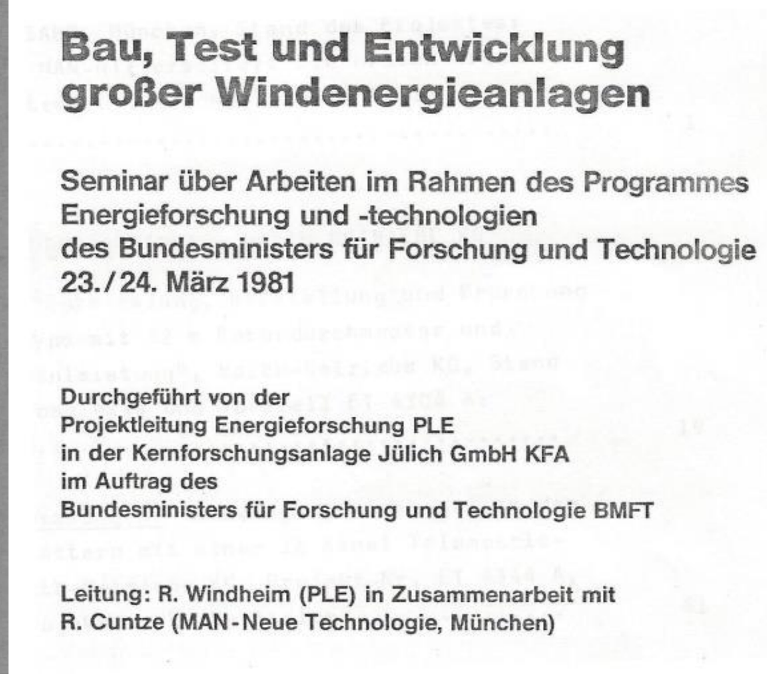

(left) International wind energy conference at MAN (1978),
(right) Seminar Research project from KFA Jülich GmbH (1981)
(below) contributors

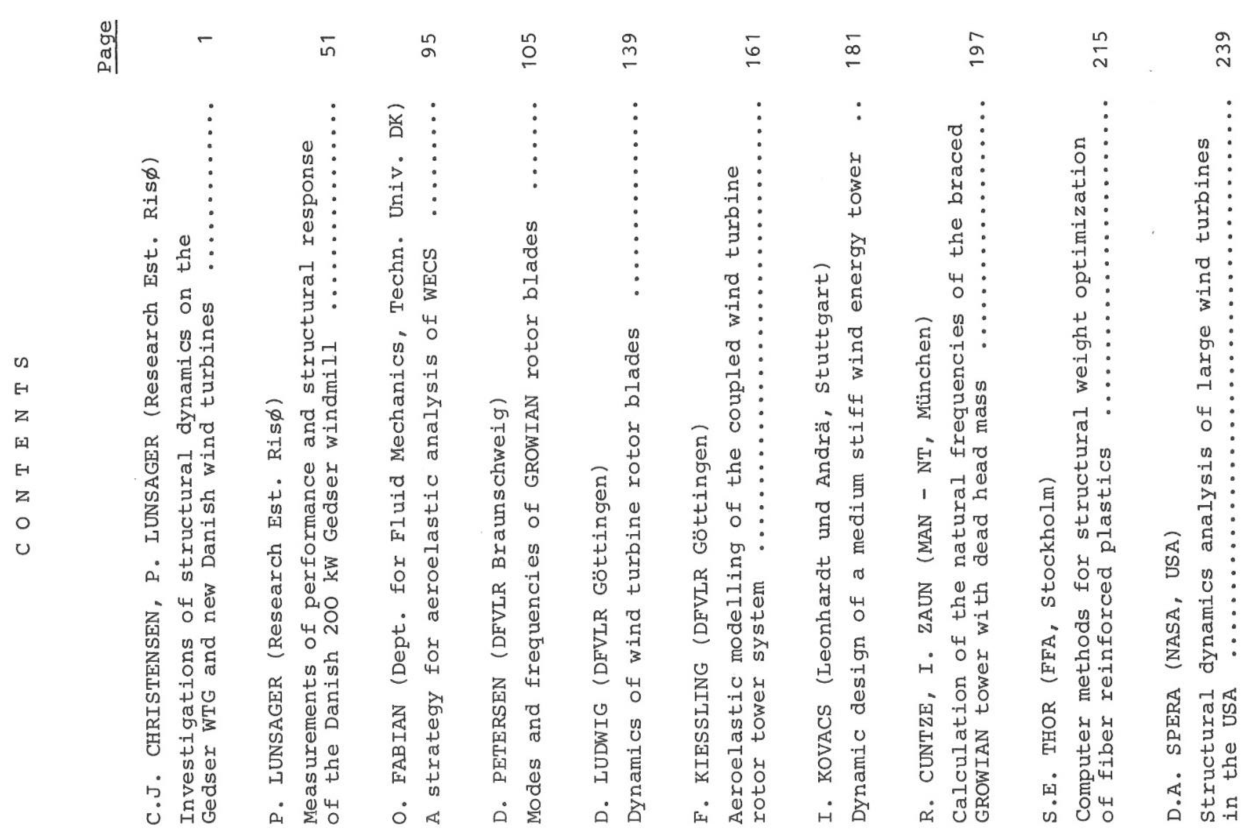
C O N T E N T S

Page

C.J. CHRISTENSEN, P. LUNSAGER (Research Est. Risø)
Investigations of structural dynamics on the Gedser WTG and new Danish wind turbines 1

P. LUNSAGER (Research Est. Risø)
Measurements of performance and structural response of the Danish 200 kW Gedser windmill 51

O. FABIAN (Dept. for Fluid Mechanics, Techn. Univ. DK)
A strategy for aeroelastic analysis of WECS 95

D. PETERSEN (DFVLR Braunschweig)
Modes and frequencies of GROWIAN rotor blades 105

D. LUDWIG (DFVLR Göttingen)
Dynamics of wind turbine rotor blades 139

F. KIESSLING (DFVLR Göttingen)
Aeroelastic modelling of the coupled wind turbine rotor tower system 161

I. KOVACS (Leonhardt und Andrä, Stuttgart)
Dynamic design of a medium stiff wind energy tower .. 181

R. CUNTZE, I. ZAUN (MAN - NT, München)
Calculation of the natural frequencies of the braced GROWIAN tower with dead head mass 197

S.E. THOR (FFA, Stockholm)
Computer methods for structural weight optimization of fiber reinforced plastics 215

D.A. SPERA (NASA, USA)
Structural dynamics analysis of large wind turbines in the USA 239

31 References (Cuntze since 2000) and Acknowledgement

31.1 References

[Awa78] Awaji H and Sato S: *A Statistical Theory for the Fracture of Brittle Solids under Multiaxial Stresses*. Int. J. of Fracture 14 (1978), R 13-16

[Cun00] Progressive failure of 3D-stressed laminates: Multiple nonlinearity treated by the Failure Mode Concept. Recent Developments in Durability Analysis of Composite Structures. Balkema, ISBN 90 5809 103 1

[Cun01] *Assessment of Load- and Strain-controlled States of Stress in 'Hot Spots' – on the way to an Industrial Approach for 'Gurson Materials'*. Europ. Conf. on Launcher Technology Strascourg , De1.11-14, 2001

[Cun03] Cuntze R and Memhard D*: Evaluation of the Tension Rod Test for Ductile Material Behavior*. European Conference on Spacecraft Structures, Materials & Mechanical Testing CNES, DLR; ESA, ISU: Toulouse, 11-13 December, 2002. Conference Proceedings

[Cun06] *Failure Conditions for Isotropic Materials, Unidirectional Composites, Woven Fabrics - their Visualization and Links*. https://www.ndt.net › cdcm2006 › papers › cuntze, PDF

[Cun13] *Comparison between Experimental and Theoretical Results using Cuntze's Failure Mode Concept model for Composites under Tri-axial Loadings – Part B of the WWFE-II*. Journal of Composite Materials", Vol.47 (2013), 893-924

[Cun12] *The Predictive Capability of Failure Mode Concept-based Strength Criteria for Multidirectional Laminates*. Part B, Composites Science and Technology 63 (2004), 487-516

[Cun17] *Fracture Failure Bodies of Porous Concrete (foam-like), Normal Concrete, Ultra-High-Performance-Concrete and of the Lamella - generated on basis of Cuntze's Failure-Mode-Concept (FMC*). NWC2017, June 11-14, NAFEMS, Stockholm *

[Cun19] *Technical terms for composite components in civil engineering and mechanical engineering*. Fachbegriffe mit Erklärung und Definition. In: Fachbegriffe für Kompositbauteile – Technical terms for composite parts. 171 pages, Springer Vieweg, Wiesbaden (2019). Pre-print downloadable*

[CUN22] *Life-Work Cuntze - a compilation*. 2022/2023. *The Failure-Mode-Concept FMC, a physical and theoretical Material Symmetry-driven basis to generate Strength Criteria, that gave a reason to look after a 'more closed' Strength Mechanics Building, and in addition Very Much on Structural Materials, Techniques and Design including work-life experiences of the author in many engineering fields*. (about 850 pages), downloadable from https://www.carbon-connected.de/Group/Prof.Ralf.Cuntze

[Cun23a] *Design of Composites using Failure-Mode-Concept-based tools— from Failure Model Validation to Design Verification*. Mechanics of Composite Materials, Vol. 59, No. 2, May, 2023, pp. 263-282*

[Cun23b] *Minimum Test Effort-based Derivation of Constant-Fatigue-Life curves - displayed for the brittle UD composite materials.* Springer, Advanced Structured Materials, Vol.199, 107–146, draft *

[Cun23c] *Comparative Characterization of Four Significant UD Strength Failure Criteria (SFC) with focusing a direct use of Friction Values, use of 'Strength' and 'Proportional Loading'. 54 pages**

[Cun23d] *Gedanken eines faseranwendungserfahrenen Ingenieurs zum Umgang mit Faser-Mikro-bruchstücken und Feinstäuben bei Herstellung und Recycling faserverstärkter Bauteile*. Composites United construction (CU Bau) *

[Cun24b] *Ceramic Strength Models for Monolithic (isotropic), Transversely-isotropic UD and Fabric Materials**

[Cun24c] Cuntze R and Kappel E: *Benefits, applying Tsai's Ideas 'Trace', 'Double-Double' and 'Omni Failure Envelope' to Multiply UD-ply composed Laminates.* 60 pages *

[Cun24a] Cuntze R and Kappel E: *Why not designing multidirectional laminates with in-plane Strength Design Sheets applying the UD criteria of Tsai-Wu and Cuntze*? Part 1, Analytical foundation in Mechanics of Composite Materials (MCM), Vol. 60, No. 5, November, 2024; Part 2 , Application in MCM , November 2024

[Fla82] Flaggs D L and Kural, MH: *Experimental Determination of the In Situ Transverse Lamina Strength in Graphite Epoxy Laminates.* J. Comp. Mat. Vol 16 (1982), 103-116

[Har93b] Hart-Smith L J: *An Inherent Fallacy in Composite Interaction Failure Curves*. Designers Corner, Composites 24 (1993), 523-524

[Has80] Hashin Z: *Failure Criteria for Unidirectional Fiber Composites*. J. of Appl. Mech. 47 (1980), 329-334

[Hin02] Hinton M J , Kaddour A S and P.D. Soden P D: *A comparison of the predictive capabilities of current failure theories for composite laminates, judged against experimental* ***evidence*** (it would have been very nice). Composites Science and Technology 2002 (62), 1725-97

[Hah15] Hahne C: Zur Festigkeitsbewertung von Strukturbauteilen aus Kohlenstofffaser-Kunststoff-Verbunden unter PKW-Betriebslasten“, Shaker Verlag, Dissertation 2015, TU-Darmstadt, Schriftenreihe Konstruktiver Leichtbau mit Faser-Kunststoff-Verbunden, Herausgeber Prof. Dr.-Ing Helmut Schürmann

[HSB 02000-01] Cuntze R: *Essential topics in the determination of a reliable reserve factor*. 2012, HSB sheet, 20 pages. HSB = (luftfahrttechnisches) Handbuch für Strukturberechnung (*German aerospace handbook*). Edited by the industrial committee (*working group*!) IASB = IndustrieAusschuss für StrukturBerechnung

[Jai20] Jain N and Koch D: *Prediction of Failure in Ceramic Matrix Composites Using Damage-Based Failure Criterion*. J. Compos. Sci. 2020, 4, 183; doi:10.3390/jcs4040183

[Kaw04] Kawai M: *A phenomenological model for off-axis fatigue behavior of uni-directional polymer matrix composites under different stress ratios*. Composites Part A 35 (2004), 955-963

[Kno03] Knops M: *Sukzessives Bruchgeschehen in Faserverbundlaminaten*. Diss. 2003. Aachen, Institut für Kunststoffverarbeitung

[Leg02] Leguillon D: *Strength or Toughness? –A criterion for crack onset at a notch*. Europ. J. of Mechanics A/Solids 21 (2002), 61 – 72 end. Ist. D. sci. Lett., Cl. Mat. Nat.18, 705-714 (1885

[Li24] Li H, Pel L, You Z and Smeulders D: *Stress-dependent Mohr-Coulomb shear strength parameters for intact rock*. Nature.com/scientific reports

[Lut06] Lutz G: *The Puck theory of failure in laminates in the context of the new guideline VDI 2014, Part* 3. NDT.net https://www.ndt.net › cdcm2006 › papers › lutzii, PDF

[Puc96] Puck A: *Festigkeitsanalyse von Faser-Matrix-Laminaten - Modelle für die Praxis.* München, Carl Hanser Verlag, 1996

[Tsa71] Tsai S W and Wu E M: *A General Theory of Strength for An-isotropic Materials*. Journal Comp. Materials 5 (1971), 58-80 S.

[You15] You M: *Strength criterion for rocks under compressive-tensile stresses and its application*. J. of Rock Mechanics and Geotechnical Engineering 7 (2015), 434-439

31.2 Thanks and Acknowledgement

Many Thanks to: My parents Helmy and Werner for my *inherited tenacity* to endure this hobby alongside the job, my first wife Jutta and to my second wife Maria for tolerating my private, very time-consuming scientific hobby.

The professores

- *Hans Kauderer, E. Doeinck, Theo. Lehmann, Frederick-Henry Schroeder and Kurt Magnus for my knowledge of mechanics, which of course is still imperfect. Theo Lehmann and F-H Schroeder were my doctoral supervisors.*
- *Theo Lehmann, as well as the purple-robed jaguar driver Zerna, especially for the tensor analysis knowledge, which I was later able to use in the fiber laying winding technique*
- *Bodo Heimeshoff and Huba Öry for the self-critical way of working, which is later called 'self-testing' in ISO 9000. Bodo Heimeshoff and Harry Grundmann, who were my habilitation fathers in 1978*
- *Alfred Puck for many valuable discussions and his indirect initiation of my Failure Mode Concept (FMC) idea*
- *Rüdiger Rackwitz for the knowledge of structural reliability, applied in my FMC idea*
- *Karl-Heinz Schwalbe for my fracture mechanics knowledge*
- *Ms. Rita Jeltsch-Fricker for "Getting on the Right Mathematical Path" in a large MAN research project on A. Puck's Action Plane Stress criterion*
- *The honorary professor-reviewers Werner Hufenbach, Hans Eschenauer and finally Mr. Fahlbusch of the Bundeswehr University for the realization of the honorary professorship at the UniBw at Neubiberg*

Thanks to all those who are not named, especially MAN colleagues and the members of the Aerospace-Technical Industry Committee for Structural Calculation (IASB), who contributed to both my professional and my scientific work.

Without the encouragement of Wilfried (Prof. Becker, TU Darmstadt) I would not have made it through the laborious work in the last two decades.

Yes, and where wouldn't I have gotten stuck everywhere in Mathcad-code calculations if it there would not have been Dipl.-Ing. Bernd Szelinski, who was usually able to eliminate Mathcad-attributable difficulties, such as changed letters, characters or that vectors were no longer read. It's a pity that such a great calculation program has such shortcomings and errors are incorrectly noted or it doesn't calculate and doesn't give a suspicion of error. Sometimes, another solution way could be gone.

Not to forget Dr.-Ing. Andreas Freund, with whose Mathcad skills I was only able to make the numerical entry into WWFE-I, culminating in a joint paper on WWFE-I A. Thank you Bernd and Andreas.

And, to my scientific friends and partners:

Bodo Heimeshoff, Walter Wunderlich, Gottfried Ehrenstein, Huba Öry, Alfred Puck, Helmut Schürmann, Steve Tsai, Urs Meier, Rüdiger Rackwitz, Wilfried Becker, Holm Altenbach, Werner Hufenbach, Volker Ulbricht, Rolands Rikards, Lothar Kroll, Siegfried Schmauder etc.

Looking at my Lessons Learned ***LL:***

Much Experience is required in Design! But what is experience?

Experience is not what happens to you; it's what you do with what happens to you.

Aldous Huxley